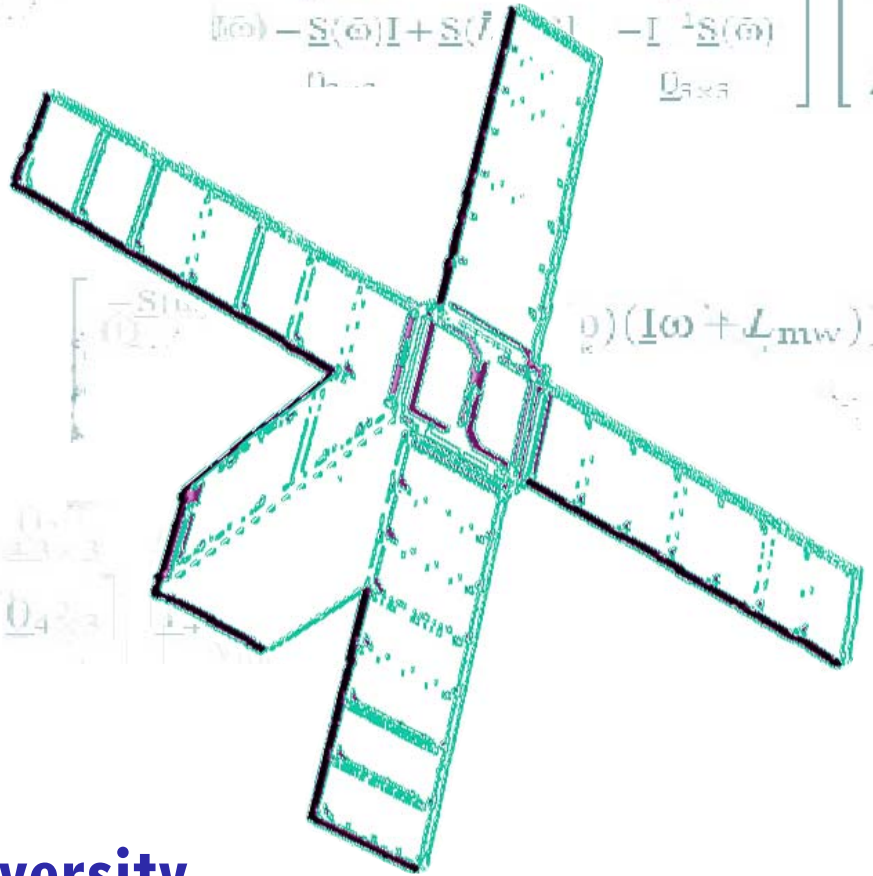


Robust Disturbance Rejecting Attitude Control

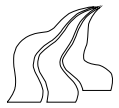
- for the North Sea Observer Satellite

$$\begin{bmatrix} \dot{\tilde{q}}_{1:3} \\ \dot{\tilde{\omega}} \\ \dot{\tilde{L}}_{mw} \end{bmatrix} = \begin{bmatrix} -S(\tilde{\phi}) \\ 0_{3 \times 3} \\ 0_{3 \times 3} \end{bmatrix} + \begin{bmatrix} \frac{1}{2} I_{3 \times 3} \\ I(0) - S(\tilde{\phi})I + S(I) \\ 0_{3 \times 3} \end{bmatrix} \begin{bmatrix} \tilde{q}_{1:3} \\ \tilde{\omega} \\ \tilde{L}_{mw} \end{bmatrix} - \begin{bmatrix} 0_{3 \times 3} \\ -I^{-1}S(\tilde{\phi}) \\ 0_{3 \times 3} \end{bmatrix} \begin{bmatrix} \tilde{q}_{1:3} \\ \tilde{\omega} \\ \tilde{L}_{mw} \end{bmatrix}$$

$$\begin{bmatrix} \dot{\tilde{q}}_{1:3} \\ \dot{\tilde{\omega}} \\ \dot{\tilde{L}}_{mw} \end{bmatrix} = \begin{bmatrix} -S(\tilde{\phi}) \\ 0_{3 \times 3} \\ 0_{3 \times 3} \end{bmatrix} + \begin{bmatrix} 0_{3 \times 3} \\ 0_{3 \times 3} \\ 0_{3 \times 3} \end{bmatrix} \begin{bmatrix} \tilde{q}_{1:3} \\ \tilde{\omega} \\ \tilde{L}_{mw} \end{bmatrix} - \begin{bmatrix} 0_{3 \times 3} \\ -I^{-1}S(\tilde{\phi}) \\ 0_{3 \times 3} \end{bmatrix} \begin{bmatrix} \tilde{q}_{1:3} \\ \tilde{\omega} \\ \tilde{L}_{mw} \end{bmatrix}$$



Aalborg University
Department of Control Engineering
10th Semester - Master Thesis
IAS - 06 gr 1032



TITLE:

Robust Disturbance Rejecting
Attitude Control for the North Sea
Observer Satellite

PROJECT PERIOD:

Control Engineering, Master Thesis,
From: February 1st, 2006
To: June. 1st, 2006

PROJECT GROUP:

IAS - 06gr1032

GROUP MEMBERS:

Martin Green
Martin Nygaard Kragelund
Mads Sletten Kristensen

SUPERVISORS:

Jan Dimon Bendtsen
Lars Alminde

NUMBER OF COPIES: 8

TOTAL PAGE COUNT: 181

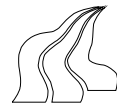
Abstract:

This report documents the development of an Attitude Control System (ACS) for the North Sea Observer (NSO), which is a pico-satellite complying with a triple CubeSat configuration. The primary payload of the satellite is a high resolution camera, which is to be used to monitor shipping routes in the North Sea, and search for oil spills from seagoing vessels in these waters. By correlating with shipping trajectories it will be possible to identify the leaking vessel. Furthermore, the NSO features a deployable solar cell array to enhance power producing capabilities.

The ACS utilises three momentum wheels and three magnetorquers to achieve active three-axis torque control.

Models of the ACS actuators, the space environment and satellite dynamics and kinematics have been developed to produce a viable simulator for controller evaluations. A general operational mode diagram has been produced and two modes have been selected for further development of attitude stabilising controllers for pointing purposes. A general control structure has been developed for the chosen modes, and controllers have been designed for each part of the control structure. The controllers comprise an optimal attitude controller, a robust angular rate controller with disturbance estimation using a Kalman filter, and a momentum wheel desaturating controller based on the common cross product law. Furthermore, a camera pointing controller has been designed for pointing purposes.

The ability of these controllers in collaboration to stabilise the attitude of the satellite has been evaluated using SIMULINK implementations. The evaluations revealed that an angular accuracy of 0.0174 [°] in the stabilised attitude could be obtained within a 95 [%] confidence interval, however the camera pointing controller introduced an error of 2 [°].



TITEL:

Robust Disturbance Rejecting
Attitude Control for the North Sea
Observer Satellite

PROJEKTPERIODE:

Afdeling for Proceskontrol, Kandidat
Afhandling,
Fra: 1. Februar, 2006
Til: 1. Juni, 2006

PROJEKTGRUPPE:

IAS - 06gr1032

GRUPPEMEDLEMMER:

Martin Green
Martin Nygaard Kragelund
Mads Sletten Kristensen

VEJLEDERE:

Jan Dimon Bendtsen
Lars Almindé

PUBLIKATIONER: 8

SIDEANTAL: 181

Synopsis:

Denne rapport dokumenterer udviklingen af et Attitude Control System (ACS) til en satellit kaldet North Sea Observer (NSO), som er en pico-satellit der opfylder en triple Cubesat konfiguration. Hovednyttelasten er et høj-opløsningskamera, som skal anvendes til at overvåge sejlreder i Nordsøen, for at finde olieudslip fra fartøjer i disse farvande. Sammen med information om skibes sejlruter, vil det være muligt at finde frem til det lækkende fartøj. Derudover vil NSO også medføre udfoldelige solcellepaneler, til forhøjelse af strømproduktionen.

ACS anvender tre momenthjul og tre spoler til treakses momentkontrol.

Modeller af aktuatorer, rummiljøet og satellittens dynamik og kinematik er udledt for at konstruere et simulationsmiljø, hvori regulatorer kan evalueres. Et generelt diagram over satellittens tilstande er blevet udviklet og to tilstande er blevet udvalgt til videre udvikling af attitude-stabiliserende regulatorer. En generel regulatorstruktur er blevet udviklet til disse tilstande og regulatorer er blevet designet til hver del af strukturen. Disse regulatorer omfatter en optimal attitude regulator, en robust regulator til satellittens vinkelhastighed med et Kalman filter til at estimere forstyrrelser, og en regulator til at aflaste impulsmoment fra momenthjulene under anvendelse af en krydsprodukt lov. Endvidere er der blevet udviklet en retningsstyrende regulator, hvis formål er at få satellitten til at pege på et bestemt punkt på jorden.

Disse regulatorers evne til at stabilisere satellittens attitude i fællesskab er blevet undersøgt, under anvendelse af et simulationsmiljø implementeret i SIMULINK. Undersøgelserne viste at satellittens attitude blev stabiliseret med en nøjagtighed på $0.0174 [^{\circ}]$ i et 95 [%] konfidensinterval, dog tilføjede den retningsstyrende regulator en fejl på $2 [^{\circ}]$.

Preface

This report is the product of a master thesis in Control Engineering as part of the Intelligent Autonomous Systems specialisation master programme at Aalborg University. The objective of this project is to develop an Attitude Control System for a pico-satellite called the North Sea Observer, hereby enabling satellite operators to point the satellite payload in any desired direction.

The report is organised in ten main chapters and thirteen appendices, which contains elaborations of elements in the report. Furthermore, a single annex with correspondences is present. In the following a brief introduction to the chapters is given. The purpose of this, is to provide the reader with an overview of the entire development process before investigating the design.

Chapter 1 This chapter provides an insight into the NSO satellite, the history behind it, and introduces the project. Furthermore, the Attitude Determination and Control System is described. This provides an introduction to a reader who is not familiar with the NSO, the satellite system, and its implications to this project.

Chapter 2 This chapter contains the modeling of the NSO and the space environment. It is addressed to the reader with interest in the models describing the satellite behavior and the modeling of the exerted disturbances. A reader familiar with these subjects could proceed to Chapter 3.

Chapter 3 This chapter presents the overall functionality and control design for the different modes of the satellite. Furthermore, once the overall design has been described, the delimitations for the control design are specified and the control structure is presented. It is addressed to the reader with interest in a description of the operational modes of the NSO and the control structure used in the subsequent design.

Chapter 4 This chapter describes the initial contemplations upon which to base further controller design. The linear model is analysed for its accuracy compared to the non-linear implementations, and it is analysed for system controllability. Furthermore, an analysis for stability conditions is conducted to ease controller verifications. This chapter is addressed to the reader with interest in the important steps preluding controller synthesis.

Chapter 5 This chapter describes the design of the angular velocity controller, which task is to reject disturbance torques and handle uncertainties in the inertia matrix. The angular velocity controller is an essential part of the attitude control system and this chapter is, therefore, considered an essential part of this report.

Chapter 6 This chapter describes the design of the desaturation controller for the NSO.

It is addressed to the reader with interest in the essential theory and design, regarding the method developed for desaturation of the NSO momentum wheels.

Chapter 7 This chapter describes the design of the attitude controller, which incorporates optimal control theory. It is addressed to the reader with interest in the theory and design of the attitude controller designed for the NSO, and is considered essential reading.

Chapter 8 This chapter describes how the reference input for the attitude controller can be generated, such that a specific location on the Earth can be tracked. This chapter is addressed to the reader with interest in the development of the Earth location tracking control and is an essential part of this report.

Chapter 9 In this chapter the complete robustly controlled system designed in this report is evaluated. The results obtained are compared to the results obtained by using a similar control structure, but with simple substitutions in each of the controllers in the structure. This chapter is addressed to the reader with interest in the final evaluation of the developed control structure, on which the final conclusions will be drawn.

Chapter 10 This chapter presents conclusions on the results obtained in the project and discusses perspectives concerning future projects on robust disturbance rejecting control for small satellites like the NSO, and is addressed to any reader.

The product of this project is a SIMULINK implementation of the controllers and models described in the report, and it is included on the enclosed CD-ROM together with other relevant materials. An overview of the contents of the CD-ROM can be found in Appendix M on page 163.

The nomenclature describes the notation used throughout the report and can be found on page 167.

The following syntax is used in the report for citations and references. Citations are enclosed in square brackets and state the author(s) and the year of publishing, e.g. [Adams 1978]. The bibliography can be found on page 86. References are made as follows: Figures and sections are referred to by stating the chapter and the index number, e.g. Figure 4.2 or Section 4.2. References to equations are enclosed in parentheses, e.g., (4.42).

Special thanks to Professor Jakob Stoustrup for the useful guidance that he provided in the robust control design phase of this project, and to Morten Bisgaard for his artistic contribution. To our supervisors a special thanks, for their persistent and devoted guidance, is also in order. Also thanks to Executive Secretary Jette Damkjær for the support she has provided during the semester, and her continuous colourful presence.

Project participants:

Martin Green

Martin Nygaard Kragelund

Mads Sletten Kristensen

AAU, June 1st, 2006

Contents

1	Introduction	1
1.1	System Description	2
1.2	Description of Objective	5
1.3	Requirements for the ACS	6
2	Modeling	7
2.1	Ephemeris	7
2.2	Reference Frames	9
2.3	Disturbance Modeling	12
2.4	Actuator Modeling	20
2.5	Satellite Dynamics and Kinematics	22
2.6	System Equations	26
3	Control Structure	27
3.1	Mode Selection	27
3.2	Controller Design Delimitation	30
4	Model Analysis	31
4.1	Linear Model Accuracy	31
4.2	Controllability	33
4.3	Lyapunov Stability	38
5	Angular Velocity Controller	43
5.1	Control Structure	43
5.2	Disturbance Estimation	44
5.3	Robust Control	45
5.4	Evaluation	52
6	Desaturation Control	55
6.1	Controller Choice	56
6.2	The Common Cross Product Law	56
6.3	Controller Design	58
6.4	Evaluation	59
7	Attitude Control	61
7.1	Optimal Control	61
7.2	Controller Design	62
7.3	Evaluation	64
8	Pointing Controller	67

8.1 Attitude Reference Calculation	67
8.2 Implementation Assumptions and Limitations	69
8.3 Evaluation	69
9 System Evaluation	71
9.1 Attitude Manoeuvres	71
9.2 Reliability	74
9.3 Target Acquisition	75
10 Closure	77
10.1 Conclusion	77
10.2 Discussion	79
10.3 Future Work	80
Bibliography	86
Appendix	87
A Inertia Matrix Calculation	87
B Tasks and Requirements	91
C Quaternions	95
D Worst Case Disturbance Torques	99
E Magnetorquer Model	103
F Magnetorquer Design	107
G Momentum Wheel Model	111
H Rotations	117
I Linearisation	123
J Kalman Filter	131
K Evaluation	135
L Simulation Environment	157
M Content of Enclosed CD-ROM	163
Annex	164
1 Email from Neil Melville	165
Nomenclature	166
List of Tables	170
List of Figures	171
Index	179

CHAPTER 1

Introduction

This chapter provides an insight into the NSO satellite, the history behind it, and introduces the project. Furthermore, the Attitude Determination and Control System is described. This provides an introduction to a reader who is not familiar with the NSO, the satellite system, and its implications to this project.

The North Sea Observer (NSO) is a mind child of the rapid expansion in student satellite activities at Aalborg University (AAU). The university started its involvement in student satellite development, with the first Danish student satellite called AAU CubeSat¹. The goal of this satellite was to take photographic images of the Earth, using its on-board camera.

The AAU CubeSat mission was a partial success, as students were able to get "hands-on" experience with space technology and contact was established with the satellite, but no pictures were taken.

In September 2003 the next CubeSat project at Aalborg University was initiated. The satellite is named AAUSAT-II, and a preliminary launch date is set for late 2006. The payload on this satellite is a gamma ray burst detector developed by the Danish National Space Center (DNSC), which is used to measure radiation from gamma ray bursts in space [Wikipedia 2006]. The satellite is currently in phase C-D² of the ECSS standard classification [ESTEC April 1996].

The two described satellites both follow the CubeSat concept developed by California Polytechnic State University, San Luis Obispo and Space Systems Development Laboratory at Stanford University [California Polytechnic State University 2005]. This concept allows the satellite to have a mass of maximum 1 [kg] and the dimensions of 10 [cm] × 10 [cm] × 10 [cm], hence the name CubeSat.

The NSO will be the next generation satellite from AAU, and will feature a triple CubeSat configuration with the dimensions of 30 [cm] × 10 [cm] × 10 [cm] and a mass of maximum 3 [kg]. The primary objective of NSO will be to monitor shipping routes in the North Sea, using a high resolution digital camera, and search for oil spills from seagoing vessels in these waters. Due to mandatory Automatic Identification System (AIS) transponder technology on board ships, it will be possible to correlate oil spill findings with the trajectory of ships to identify the culprit [Navigation Center 2005].

The NSO will reuse some of the existing subsystem technologies developed for AAUSAT-II, but will feature a new deployable solar array on each lateral side panel. The possibility of a

¹AAU Cubesat was launched on June 30th 2003 together with DTU-SAT from the Danish Technological University.

²Detailed definition and production/ground qualification testing.

launch of the NSO is already in the negotiation stage, with a possible launch on the approval flight for the medium sized VEGA³ launch vehicle, currently under development within the European Space Agency (ESA). The approval flight of VEGA is currently scheduled for late 2007 or early 2008, and it will launch the NSO into Low Earth Orbit (LEO). An artists impression of the NSO in orbit can be seen in Figure 1.1. The NSO is currently in the feasibility phase (A) of the ECSS standard classification [ESTEC April 1996].



Figure 1.1: The North Sea Observer in orbit with the solar arrays deployed. Removing the solar arrays from the figure, illustrates the situation where the solar arrays are collapsed.
©Morten Bisgaard.

The satellite will rely on a high-precision, low economical cost Attitude Determination and Control System (ADCS), to limit the rotational velocity of the satellite and enable pointing of the on-board camera towards a location in the North Sea. The attitude control part of this system will have the main task of decelerating the satellite from a spin, but also maintaining or changing the attitude of the satellite. The system will function based on on-board estimates of the satellite attitude and using its on-board actuators, in the form of reaction wheels and magnetorquers.

1.1 System Description

In this section the outline of the system configuration is presented. This includes assumptions regarding the dimensions and inertia of the satellite, modes for the ADCS system and a description of the sensors and actuators on board the satellite.

³Vettore Europeo di Generazione Avanzata or Advanced Generation of European Vector

1.1.1 Mechanical Properties

The satellite complies with the specifications regarding the triple CubeSat concept, thus the dimensions, when the solar arrays are collapsed, are as stated previously. However, the NSO allows for deployment of four solar arrays, which have to be considered e.g. when calculating the inertia of the satellite. Due to the fact that no mechanical subsystem has been developed yet the inertia matrix calculation for the satellite has been approximated with the following assumptions:

- The solar arrays have the dimension $30 \text{ [cm]} \times 10 \text{ [cm]} \times 0.2 \text{ [cm]}$.
- The combined mass of the solar arrays is 0.5 [kg] , i.e. 0.125 [kg] each.
- The satellite body has no loss in dimensions, when the solar arrays have been deployed.

Regarding these two cases an inertia matrix has been calculated, for when the solar arrays are collapsed and deployed. These calculations are found in Appendix A, which also indicates that the satellite body and the solar arrays have been approximated as solid bricks. The following inertia matrices, calculated around the combined Center of Mass (CoM), have been obtained for the collapsed and deployed situation respectively

$$\mathbf{I}_{\text{sat}_c} = \begin{bmatrix} 0.025 & 0 & 0 \\ 0 & 0.025 & 0 \\ 0 & 0 & 0.005 \end{bmatrix} \text{ [kgm}^2\text{]} \quad (1.1)$$

$$\mathbf{I}_{\text{sat}_d} = \begin{bmatrix} 0.0423 & 0 & 0 \\ 0 & 0.0423 & 0 \\ 0 & 0 & 0.0283 \end{bmatrix} \text{ [kgm}^2\text{]}. \quad (1.2)$$

These matrices are used throughout the report, e.g., for calculating disturbance torques.

1.1.2 Modes of the ADCS

The ADCS has two main tasks one is to decelerate the satellite from an initial spin once it separates from the launch vehicle, and the other is to enable pointing with the satellite. However, the pointing task could be divided into sub-tasks depending on the operating situations. The following modes has been defined as the preliminary primary modes:

Detumbling: After separation from the launch vehicle the ADCS shall stabilise the satellite from random tumbling. This is called the detumbling mode.

Pointing: Once the satellite is firmly stabilised the ADCS can enter the pointing mode, where the camera must be pointed towards a specific location on the Earth at all times, when this location is within line of site. This procedure will be referred to as a pointing manoeuvre.

Desaturation: The momentum wheels on board the satellite suffers from saturation limits during pointing. This mode shall therefore be available in conjunction with the pointing modes to desaturate these actuators.

Sun Pointing: This mode shall be active when no other tasks are performed by the ADCS and shall ensure that the largest area with solar cells points towards the Sun.

Pointing with electromagnetic actuation: This mode utilises actuators with no saturation limit. Thus, the desaturation mode is not required to operate.

1.1.3 Sensors and Actuators for the ADCS

In order to determine and control the attitude of the satellite it has been equipped with different sensors and actuators. The sensors are used in the attitude determination, and the actuators can change and maintain the attitude of the satellite. It is assumed that the actuators on the NSO will be of similar nature to the ones used on AAUSAT-II, being magnetorquers and momentum wheels. No orbital manoeuvring is therefore possible. In the following a short description of the sensors and actuators on board the NSO is given.

Momentum wheel: The momentum wheel consists of a motor and a flywheel. Once the flywheel starts to rotate it transfers angular momentum from the satellite to the flywheel. Due to the fact that this type of actuator suffers from saturation limits, they are normally used in conjunction with other actuators. Three momentum wheels are implemented perpendicular to each other to allow for 3-axis angular momentum transfer.

Magnetorquer: A magnetorquer is a coil, which generates a magnetic field when carrying a current. The magnetic field generated by the coil interacts with the Earth's magnetic field, thus unloading angular momentum from the satellite to the Earth, which allows for control. A total of three orthogonal magnetorquers provides the possibility to achieve control on all spatial axes.

Sun sensor: This sensor is used to estimate the position of the Sun relative to the satellite.

Gyro: A gyro measures the angular velocity of the satellite or the angle of rotation from an inertial reference point. This is without any use of external references.

Magnetometer: This sensor measures the direction and magnitude of the magnetic field present, which constitutes that it can only be used in the vicinity of the Earth (LEO). Due to the fact that the satellite is equipped with magnetorquers, coordination between magnetic field measurements and actuation with the magnetorquers is important.

In Figure 1.2 the system configuration for the ADCS is shown. Both the actuators and the sensors have interfaces, which transmit and receive information to and from the on-board computer (OBC). The OBC is the main computer on the satellite, which provides processing facilities for other subsystems on the satellite, e.g., the ADCS.

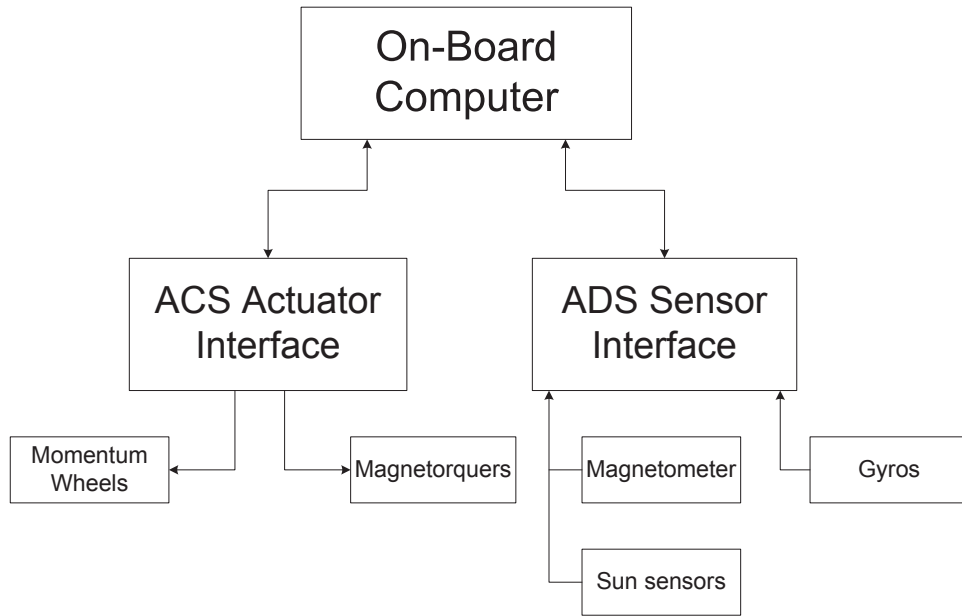


Figure 1.2: Overall system configuration for the NSO Attitude Determination and Control System.

Adopting the sampling capabilities from the ADCS of AAUSAT-II, it is possible to utilise a maximum sampling frequency of $1 \cdot 10^3$ [Hz]. The definitive sampling frequency, for controller synthesis will be specified during the controller design for the NSO.

1.1.4 System Feasibility

Originally the Danish company Gatehouse was brought in to investigate the feasibility of tracking oil spills with a camera from a triple cubesat. However, no results were presented in time for testing of the controllers presented in this report. Therefore, a preliminary estimate of the accuracy required has been performed, with no regards to satellite link budgets or image formats, as this is not considered within the project scope. Choosing a camera resolution of 1240×1024 [pixel], restricting oil spills to a minimum size of 4×4 [pixel] and assuming an orbit height of 700 [km], it is possible to detect square oil spills of a size of minimum 150 [m]. This, in turn, sets a requirement for the satellite to point the on-board camera within an accuracy of 1.57 [$^\circ$].

1.2 Description of Objective

This report deals with the development of an Attitude Control System (ACS) for the NSO, that will incorporate the development of specialised controllers for specific tasks in the satellite mission and include the design of a managing algorithm. A specified and conclusive satellite mission has not yet been established and is not considered a task to be undertaken in this project. However, to ensure that the NSO is capable of fulfilling its task of taking pictures of the oil spills in the North Sea, a number of requirements must now be defined.

1.3 Requirements for the ACS

The collective capability to acquire and maintain a specified attitude is dependent on the complete ADCS system. However, by considering the precision of a previous developed ADS, the requirements for the ACS are derived in Appendix B, where it is stated that:

1. The ACS shall be able to detumble the satellite from $0.1 \text{ [rad/s]} \approx 5.73 \text{ [°/s]}$ to 0.117 [°/s] or below, within two orbits.
2. The ACS shall be able to rotate the satellite at an angular velocity of at least 0.26 [°/s] .
3. The ACS shall be able to point the camera-axis at a location on the Earth with a maximum deviation from the correct direction of 0.57 [°] , within a 95 [%] confidence interval.

CHAPTER 2

Modeling

This chapter contains the modeling of the NSO and the space environment. It is addressed to the reader with interest in the models describing the satellite behavior and the modeling of the exerted disturbances. A reader familiar with these subjects could proceed to Chapter 3.

In this project the modeling developed for the AAUSAT-II by [Group 05gr833 2005] will be used as a basis. However, most of the modeling have been reevaluated to comply with the NSO structure and the space environment. This chapter contains the modeling of disturbances, such as aerodynamic drag, gravity gradient, solar radiation and magnetic residual. Furthermore, the satellite behaviour has also been modeled, i.e., derivation of the satellite dynamics and kinematics. Only the disturbances and satellite dynamics and kinematics are derived in this chapter, as it is assumed that the rotational and translational movement are not correlated, i.e., no orbit changing manoeuvres are considered.

The satellite will be considered a rigid body during the modeling, as the flexible modes of the solar arrays are assumed to be of high frequency, and as the solar arrays are locked in place making the complete structure a single rigid body. The deployed state of the solar arrays are not considered during modeling, as the derived models are valid with both collapsed and deployed solar arrays.

Furthermore, the actuators available for the attitude control system are modeled, i.e., models of the magnetorquers and momentum wheels are derived, and the actuators are dimensioned in accordance with the disturbance torques present.

2.1 Ephemeris

In order to describe the orbit of a satellite, the notion of ephemeris is introduced. Ephemeris describes the position of celestial objects in an inertial coordinate system, i.e., in the modeling ephemeris is used to determine the position of the satellite with regards to the Earth. An example of a satellite orbit is depicted in Figure 2.1 and an orthogonal view of the orbit is shown in Figure 2.2.

Vernal equinox (γ) is the line connecting the center of the Earth and the center of the Sun where the ecliptic, which is the plane of the Earth's orbit around the Sun, crosses the equator from north to south. Due to the precession and nutation of the Earth the direction of vernal equinox must be associated with a specific year to give an unambiguous definition of the direction in space.

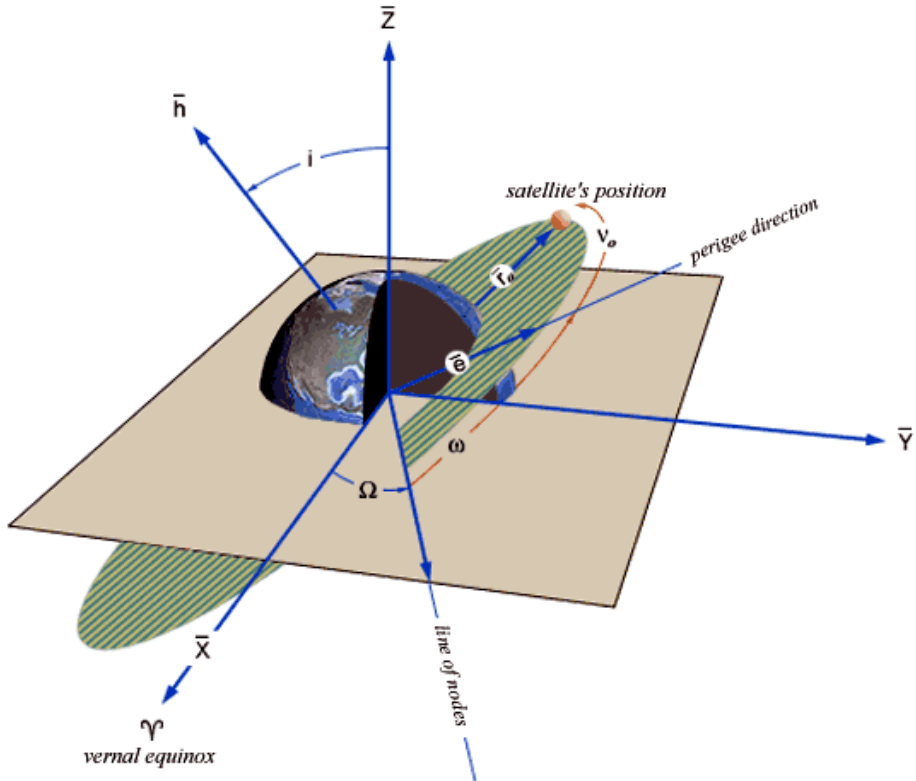


Figure 2.1: Illustration of orbit parameters for a satellite.

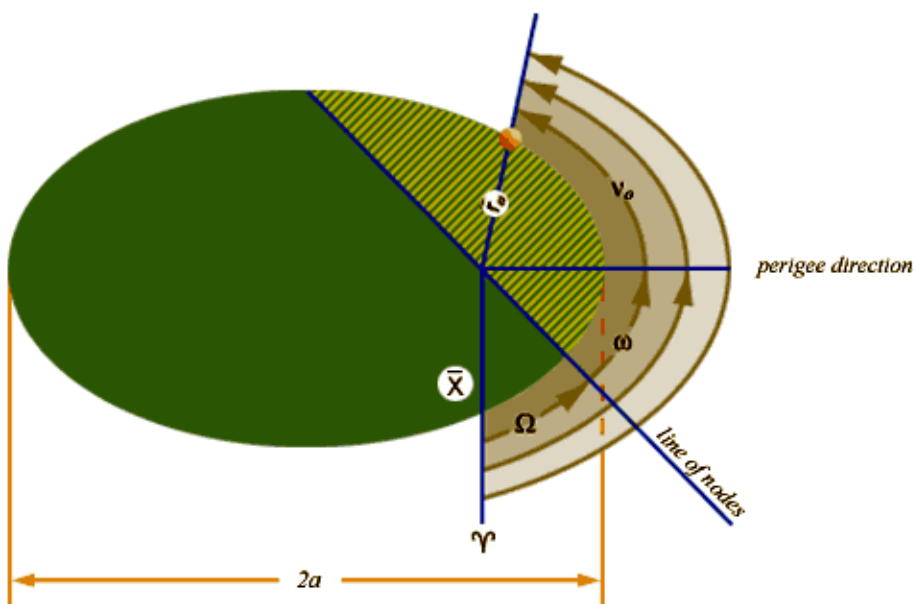


Figure 2.2: Orthogonal view of a satellite orbit.

Line of nodes is the line through the two points of intersection between the satellite orbit and the reference plane, typically the equatorial plane of the Earth. The point in the orbit where the satellite crosses from south to north is called the ascending node.

Longitude of ascending node (Ω) is the angle from vernal equinox to the ascending node. Note that this angle lies in the equatorial plane.

Perigee direction is the point in the orbit closest to the center of mass of the primary (the center of the Earth).

Argument of perigee (ω) is the angle from the ascending node to the perigee direction.

Inclination (i) is the angle from the equatorial plane to the orbit plane.

2.2 Reference Frames

To ease the modeling of the satellite dynamics and kinematics a number of reference frames is defined, as the satellite can be observed from different points of view. The reference frames used in this project is defined as right-handed 3-dimensional cartesian coordinate systems, described by three mutually perpendicular unit vectors. The reference frames used are:

- Earth Centered Inertial reference frame - ECI
- Earth Centered Earth Fixed reference frame - ECEF
- Satellite Body Reference Frame - SBRF
- Controller Reference Frame - CRF

Earth Centered Inertial Reference Frame

An inertial reference frame is needed to have a non-accelerating point of view, in which Newton's laws of motion applies. As the NSO will be launched into LEO the Earth will be the primary object, and therefore an Earth Centered Inertial reference frame (ECI) system is used as the inertial reference frame.

The ECI reference frame is illustrated in Figure 2.3. It is defined as a right handed cartesian coordinate system, having its origo in the center of the Earth. The x-axis is in the direction of vernal equinox, γ , the z-axis is perpendicular to the equatorial plane with the positive direction going through the geographic North Pole of the Earth, and the y-axis is the cross product between the z-axis and the x-axis.

Earth Centered Earth Fixed Reference Frame

Some calculations can be simplified by using a reference frame that rotates with the Earth. This means that locations on the Earth's surface such as ground stations are fixed in this frame. For this purpose the Earth Centered Earth Fixed (ECEF) reference frame is introduced.

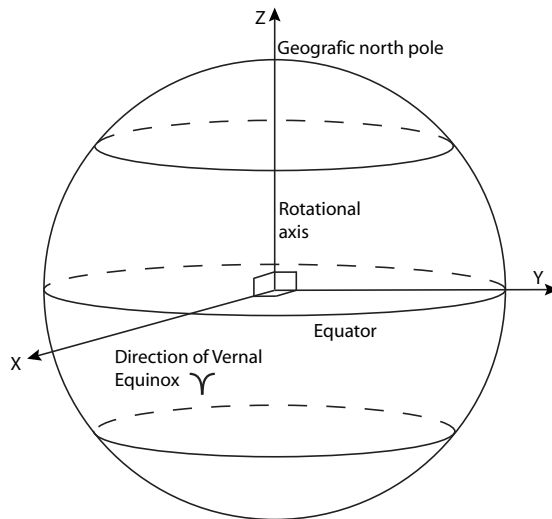


Figure 2.3: The Earth Centered Inertial reference frame.

The ECEF is illustrated in Figure 2.4. It is defined with origo in the center of the Earth. The z-axis is the Earth rotational axis and the positive direction is through the North Pole. The x-axis is in the direction of the intersection between the equatorial plane (0 latitude) and the Greenwich meridian (0 longitude). The y-axis is the cross product between the z- and x-axis, thus forming a right handed cartesian coordinate system.

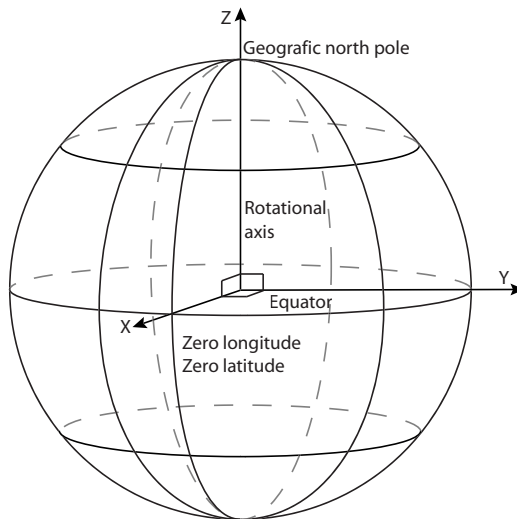


Figure 2.4: The Earth Centered Earth Fixed reference frame.

Satellite Body Reference Frame

The Satellite Body Reference Frame (SBRF) is fixed with respect to the body of the satellite. It is used to determine the orientation of the on-board instrumentation. As the NSO has a camera it is convenient to define the SBRF with one of the axis parallel to

the line of sight of the camera. The SBRF has its center in the corner of the satellite, where the magnetorquers, meet and the z-axis is perpendicular to the line of sight of the camera. The axes form a right-handed coordinate system with the axes perpendicular to the satellite sides. The SBRF is depicted in Figure 2.5.

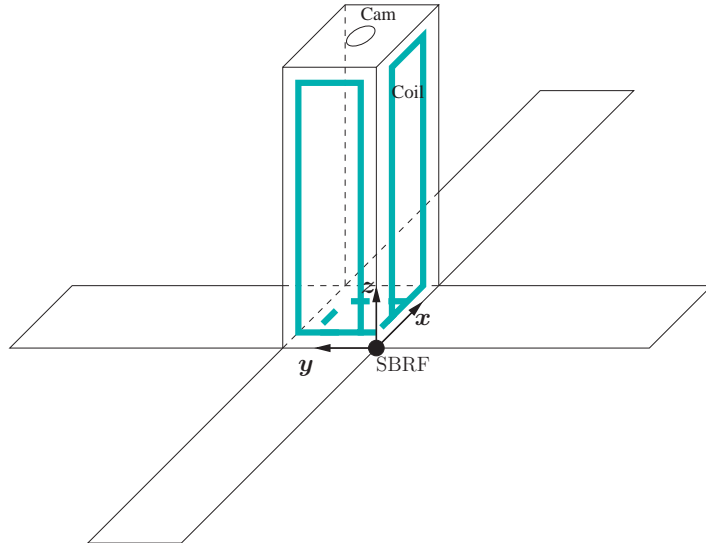


Figure 2.5: The NSO Satellite Body Reference Frame.

Controller Reference Frame

Figure 2.6 illustrates the Controller Reference Frame (CRF), which is convenient for calculations involving the satellite dynamics as all products of inertia are eliminated.

The origo of the CRF is in CoM of the satellite and the axes are defined with respect to the principal axes of the satellite. The x-axis is the major axis of inertia, the y-axis the minor axis of inertia and the z-axis is the cross product between the x-axis and the y-axis, thus forming a right handed cartesian coordinate system.

Because the satellite is non-spherical and have a non-uniform mass distribution, the CoM will not always coincide precisely with the geometrical center of the satellite. The mass distribution of the satellite must be computed in order to determine CoM and the principal axes, which are required for defining the CRF.

The principal axes can be found by calculating the eigenvalues of the inertia matrix. The major axis is the eigenvector corresponding to the largest eigenvalue. The intermediate axis is the eigenvector corresponding to the intermediate eigenvalue, and the minor axis is the eigenvector corresponding to the smallest eigenvalue [Wie 1998, page 331-339]. The inertia matrix, comprised of the eigenvectors, can be used to describe the rotation from SBRF to CRF. As the assumptions made during the calculation of the inertia matrix results in a diagonal inertia matrix no rotation from SBRF to CRF exist. However, this rotation is included in the modeling, such that a real inertia matrix can be included later.

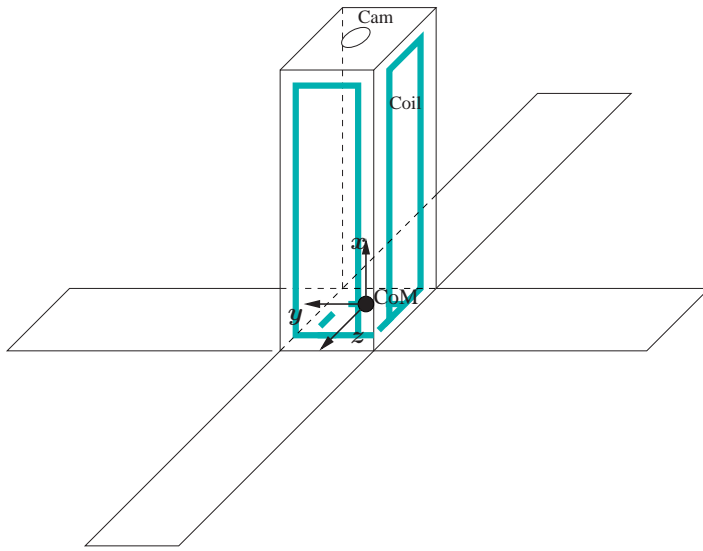


Figure 2.6: The NSO Controller Reference Frame w.r.t. the principal axes, with the origo placed in the CoM.

2.2.1 Coordinate System Transformations

Rotations of coordinate systems can be described by quaternions. Quaternions provide a singularity-free representation of kinematics and provide a convenient product rule for successive rotations. In Appendix C quaternions are defined as used in this report, and their fundamental algebraic properties are described. A rotation of a vector, \mathbf{v} , from reference frame A to reference frame B represented by ${}^B_A\mathbf{q}$ yields

$$\begin{bmatrix} {}^B\mathbf{v} \\ 0 \end{bmatrix} = {}^B_A\mathbf{q}^{-1} \begin{bmatrix} {}^A\mathbf{v} \\ 0 \end{bmatrix} {}^B_A\mathbf{q}. \quad (2.1)$$

There are certain advantages in using quaternions as a representation of rigid body rotation; the quaternions eliminate the redundancy and singularities, that appear when expressing rigid body rotation with the attitude matrix or Euler angles. Furthermore, the quaternion representation only consists of products and sums, and it does not contain any trigonometric functions like the attitude matrix and Euler angles representation. This makes the rigid body rotation expressed in quaternions more suited for software implementation, as it is less computationally demanding.

2.3 Disturbance Modeling

This section describes the main disturbance torques affecting the attitude of the satellite. The four major disturbances are considered, which are aerodynamic, gravity gradient, radiation and magnetic residual disturbances [Wertz 1978, page 566]. Calculations of the worst case disturbances can be found in Appendix D, and are summarised in Table D.1 on page 101.

2.3.1 Aerodynamic Disturbance

For a satellite in LEO the main disturbance is exerted by aerodynamic drag [Wertz 1978, page 573]. The drag arises from the friction between the satellite and the atmosphere, and act in the opposite direction of the velocity vector of the satellite.

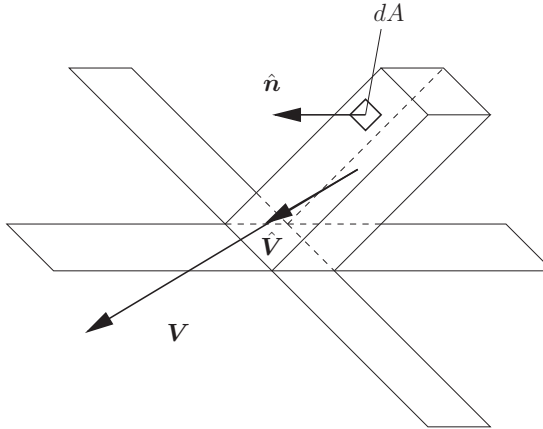


Figure 2.7: Aerodynamic drag force on an infinitesimal surface element of the NSO.

Figure 2.7 illustrates the force, $d^S \mathbf{F}_A$, acting on an infinitesimal surface element, dA , with the normal vector $\hat{\mathbf{n}}$. The force is given by

$$d^S \mathbf{F}_A = -\frac{1}{2} \rho_{\text{air}} C_D \|{}^S \mathbf{V}\|^2 ({}^S \hat{\mathbf{n}} \cdot {}^S \hat{\mathbf{V}}) {}^S \hat{\mathbf{V}} dA, \quad (2.2)$$

where ${}^S \hat{\mathbf{V}}$ is a unit vector in the direction of the translational velocity of the satellite, ${}^S \mathbf{V}$, ρ_{air} is the atmospheric density, and C_D is the drag coefficient [Wertz 1978, page 573]. The atmospheric density is dependent of the altitude and solar activity, which introduce variation both due to the ≈ 11 year solar cycle and the night - day cycle. The solar activity is described by the $F10.7$ value, which measures the radio emission at a wavelength of 10.7 [cm]. From the $F10.7$ value SPENVIS¹ can be used to predict the air density.

Figure 2.8 from [Schatten 2006, page 8] illustrates the expected solar activity during solar cycle 24. In the beginning of 2008, the expected value of $F10.7$ is 70, which yields a mean air density of approximately $100 \cdot 10^{-15} \frac{\text{kg}}{\text{m}^3}$. The output from SPENVIS is depicted in Figure 2.9, which illustrates the variation due to the day-night cycle.

Since there is no measured value available for C_D , the following assumptions can be used:

- All momentum of the air molecules is transferred to the satellite.
- The velocity of the air molecules is negligible compared to that of the satellite.
- The velocity of the surface element, dA , is the same as the velocity of the satellite's CoM.
- Molecules leaving the surface element does not introduce momentum transfer.

¹The SPace ENVironment Information System (SPENVIS) is an online tool for calculating different environment parameters including the air density and is developed by Belgian Institute for Space Aeronomy in collaboration with ESA - www.spenvis.oma.be

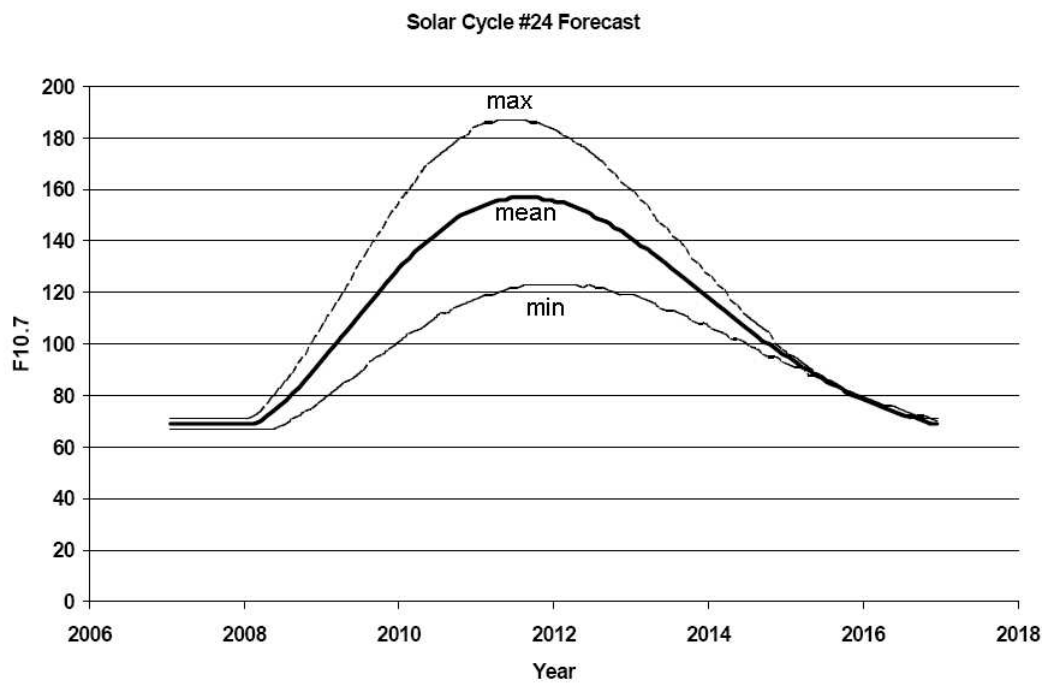


Figure 2.8: The expected $F_{10.7}$ value during the next solar cycle (cycle 24).

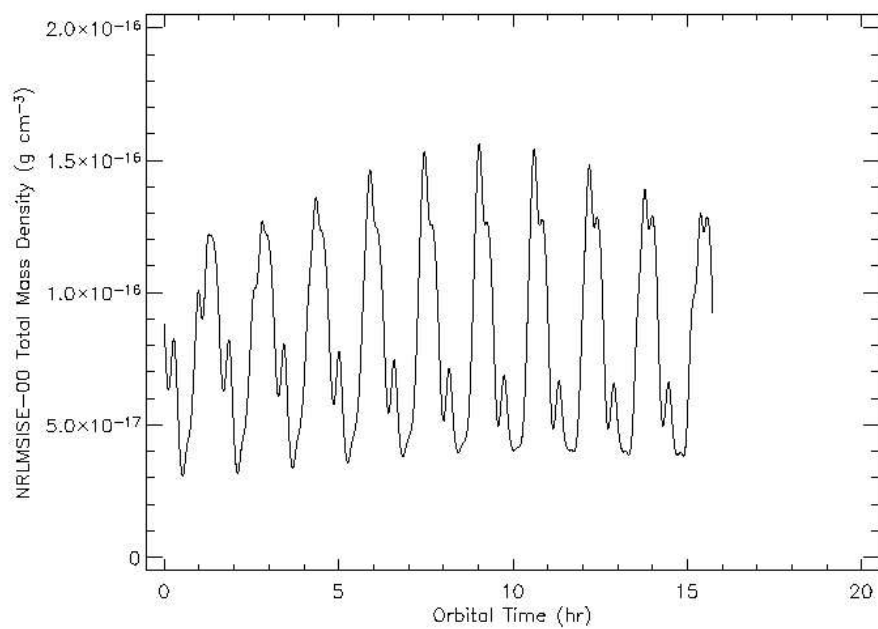


Figure 2.9: The air density in an orbit height of 500 [km]. This plot is generated by SPENVIS.

According to [Hughes 1986, page 248-260] these assumptions are equivalent to $C_D = 2$ [.].

By integrating (2.2) over the exposed area, the total aerodynamic drag can be calculated. For objects with a simple and symmetric structure this can be simplified to

$$^S\mathbf{F}_A = -\frac{1}{2}\rho_{\text{air}} C_{DA} \| ^S\mathbf{V} \|^2 ^S\hat{\mathbf{V}}, \quad (2.3)$$

where A is the total exposed area of the satellite, measured in a plane perpendicular to the translational motion [Serway & Beichner 2000, page 165-166]. This means that the aerodynamic torque, $^S\mathbf{N}_A$, acting on the satellite due to $^S\mathbf{F}_A$, can be written as

$$^S\mathbf{N}_A = ^S\mathbf{R}_{\text{Acp}} \times ^S\mathbf{F}_A, \quad (2.4)$$

where $^S\mathbf{R}_{\text{Acp}}$ is a vector from the CoM to the Center of Pressure² (CoP) on the satellite. The CoP is the geometrical center of the exposed cross sectional area.

In order to find the geometrical center of the exposed area, the exposed sides of the satellite are projected onto a plane perpendicular to the velocity vector of the satellite. In the case where three sides of the satellite are exposed the enclosed projected area becomes a hexagon, if the satellite, with collapsed solar arrays, is considered. According to [Adaweb 2006] the geometrical center can be calculated by adding the vectors describing the position of each vertex in the hexagon. The result is then divided by the number of vertices in the hexagon yielding the position of the geometrical center. Furthermore, by projecting the geometrical center of the satellite onto the plane the calculated and the projected geometrical center coincide.

The exposed cross sectional area of the satellite is calculated by projecting the satellite body and solar arrays onto a plane perpendicular to the velocity vector, and calculating the combined area in this plane. This task poses some difficulties as the satellite body and the solar arrays cast “shadows” on each other, when the velocity vector is not parallel with one of the axes in the SBRF.

Figure 2.10 depicts the satellite body and solar arrays projected onto the plane, where A_{s_1} and A_{s_2} are the shadow areas, \mathbf{z}_{sat} is the z-axis of the satellite projected onto the plane and $\mathbf{x}_{\text{array}_1}, \mathbf{y}_{\text{array}_1}$, $\mathbf{x}_{\text{array}_2}$, and $\mathbf{y}_{\text{array}_2}$ are vectors describing the individual solar array dimensions in the plane. The area of the satellite body in the plane is calculated by taking the norm of the cross-product, i.e.,

$$A_{\text{sat}} = \| \mathbf{x}_{\text{sat}} \times \mathbf{y}_{\text{sat}} \| + \| \mathbf{x}_{\text{sat}} \times \mathbf{z}_{\text{sat}} \| + \| \mathbf{y}_{\text{sat}} \times \mathbf{z}_{\text{sat}} \| . \quad (2.5)$$

The area of the solar arrays is found by

$$A_{\text{array}} = 2 (\| \mathbf{x}_{\text{array}_1} \times \mathbf{y}_{\text{array}_1} \| + \| \mathbf{x}_{\text{array}_2} \times \mathbf{y}_{\text{array}_2} \|) . \quad (2.6)$$

The calculation of the shadow area is divided into three cases, dependent on how \mathbf{z}_{sat} intersects the vectors defining the solar arrays, i.e., as a triangle, a square or a triangle subtracted from a square (the three cases are illustrated in Figure 2.10 by \mathbf{z}_{sat} , $\mathbf{z}_{\text{sat}_1}$ and $\mathbf{z}_{\text{sat}_2}$, respectively). Considering A_{s_1} the following is used. If \mathbf{z}_{sat} is parallel with $\mathbf{y}_{\text{array}_1}$ then the shadow area, A_{s_1} , is calculated as a square. If \mathbf{z}_{sat} intersects $\mathbf{y}_{\text{array}_1}$ before

²In the same way that the weight of all the satellite components act through a single point, the Center of Mass, the aerodynamic forces act through a single point called the Center of Pressure.

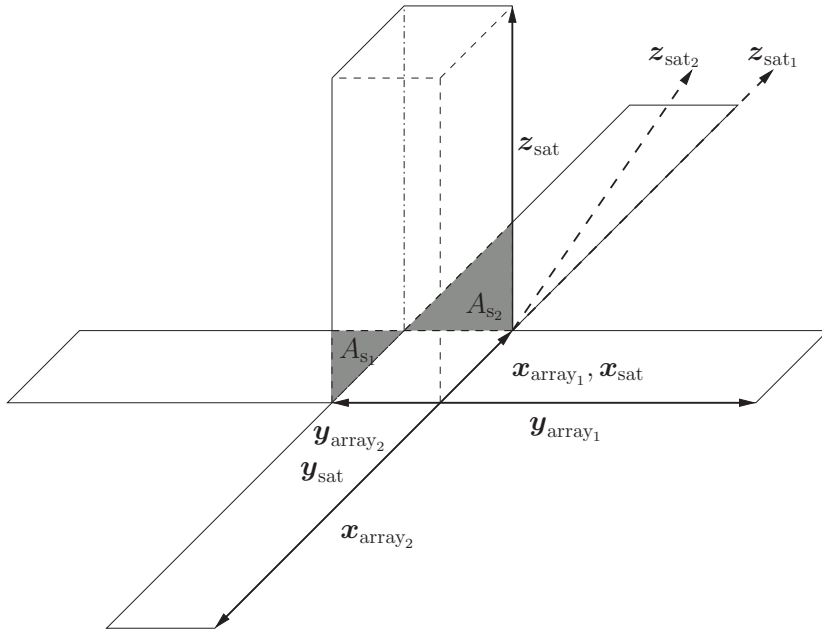


Figure 2.10: Illustration of the satellite body and solar arrays projected onto a plane perpendicular to the velocity vector of the satellite.

$\mathbf{x}_{\text{array}_1}$, the area is calculated as a triangle. Otherwise, the area is calculated as a triangle subtracted from a square. By denoting \mathbf{z}_{sat} projected onto $\mathbf{x}_{\text{array}_1}$ and $\mathbf{y}_{\text{array}_1}$ as $\mathbf{z}_{x_{\text{array}_1}}$ and $\mathbf{z}_{y_{\text{array}_1}}$ respectively, the algorithm can be described as

$$\begin{aligned}
 & \text{if}(\|\mathbf{z}_{y_{\text{array}_1}}\| > \|\mathbf{y}_{\text{array}_1}\|) \\
 & \quad \mathbf{k} = \mathbf{y}_{\text{array}_1} \\
 & \text{else} \\
 & \quad \mathbf{k} = \mathbf{z}_{y_{\text{array}_1}} \\
 & \text{if}(\|\mathbf{z}_{x_{\text{array}_1}}\| > \|\mathbf{x}_{\text{array}_1}\|) \\
 & \quad A_{s_1} = \frac{1}{2} \|\mathbf{x}_{\text{array}_1} \times \mathbf{k}\| \\
 & \text{else} \\
 & \quad A_{s_1} = \|\mathbf{x}_{\text{array}_1} \times \mathbf{k}\| - \frac{1}{2} \|\mathbf{z}_{x_{\text{array}_1}} \times \mathbf{k}\|. \tag{2.7}
 \end{aligned}$$

A_{s_2} can be found in a similar manner.

The torque generated by the aerodynamic disturbance is depicted in Figure 2.11 as a function of the attitude change. The attitude is changed, such that the direction of the velocity vector of the satellite rotates from parallel with the z-axis of the satellite, through the plane of the solar arrays to parallel with the z-axis again (opposite direction). The angle specified in the figure is from the solar array plane to the velocity vector.

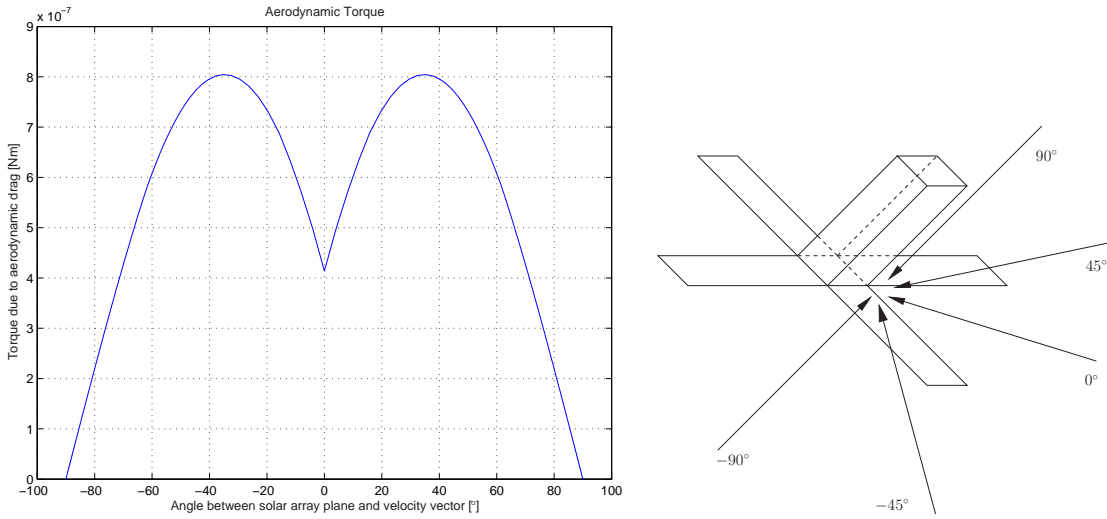


Figure 2.11: The norm of the aerodynamic torque on the NSO with deployed solar arrays as a function of the attitude.

As depicted in the figure the torque is symmetrical on each side of the solar array plane, which is expected as it is the vector from CoP to CoM, that defines the direction of rotation. Thereby, when the vector is perpendicular with the velocity vector, the torque is zero (that is at $\pm 90^\circ$ in the figure). Furthermore, the decrease in torque around an angle of 0° is ascribed to a decrease in the exposed area of the satellite.

2.3.2 Gravity Gradient Disturbance

The NSO is non-spherical and has a non-uniform mass distribution. Therefore, it will experience a gravitational torque due to gravitational forces from celestial objects. Considering only the Earth's gravitational force and assuming that the force field is spherical, the gravitational force between the Earth, with mass $m_E = 5.9742 \cdot 10^{24} [\text{kg}]$, and a satellite of a mass m_{sat} , at a distance, $\|{}^S\mathbf{R}_{\text{sat}}\|$, from the Earth's center, has a magnitude of

$$\|{}^S\mathbf{F}\| = G \frac{m_E m_{\text{sat}}}{\|{}^S\mathbf{R}_{\text{sat}}\|^2}, \quad (2.8)$$

where G is the gravitational constant, which is $66.726 \cdot 10^{-12} [\frac{\text{Nm}^2}{\text{kg}^2}]$. If m_1 and m_2 , in Figure 2.12, are two equal mass elements of the satellite, they will not experience the same gravity. This is due to the fact, that the gravity depends on the inverse square of the distance between the mass elements and the Earth's center. In the scenario depicted in Figure 2.12, F_2 will be greater than F_1 and the satellite will experience a counter-clockwise torque around the CoM.

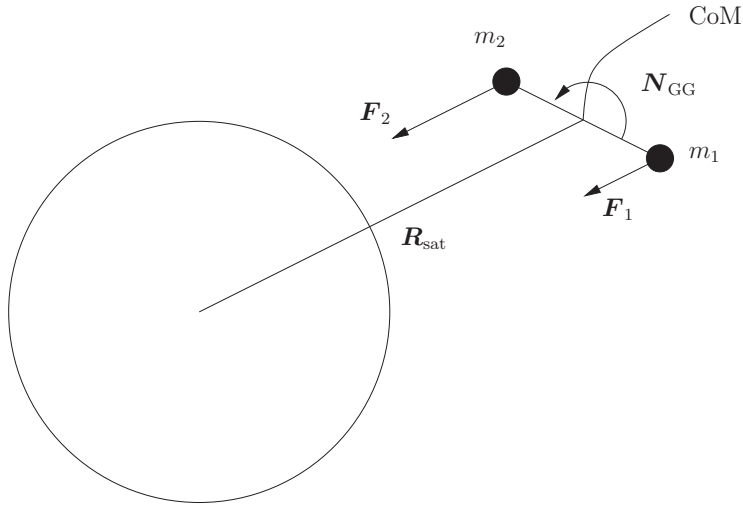


Figure 2.12: Illustration of the gravity gradient torque.

Assuming the satellite consists of a single body, the equation for the torque can be expressed as [Wertz 1978, page 567]

$${}^S\mathbf{N}_{GG} = \frac{3Gm_E}{\| {}^S\mathbf{R}_{sat} \|^3} \left[{}^S\hat{\mathbf{R}}_{sat} \times ({}^S\mathbf{I} {}^S\hat{\mathbf{R}}_{sat}) \right], \quad (2.9)$$

where ${}^S\mathbf{R}_{sat}$ is a vector from the center of the Earth to the satellite and ${}^S\mathbf{I}$ is the moment of inertia matrix.

2.3.3 Radiation Disturbance

Radiation hitting the surface of the satellite will cause a torque around the CoM. There are several radiation sources exerting this torque, but the major ones are direct solar radiation and solar radiation reflected by the Earth and its atmosphere, i.e. the Earth's albedo. Direct solar radiation is generally the only one considered [Wertz 1978, page 571]. Depending on how the light is reflected on the satellite's surface, three different cases are considered. These are specular, diffuse and absorption. The force exerted by specular reflection can be described as [Hughes 1986, page 260-263]

$$d^S\mathbf{F}_{rs} = -2P(-{}^S\hat{\mathbf{n}} \cdot {}^S\hat{\mathbf{S}})^2 {}^S\hat{\mathbf{n}} dA, \quad (2.10)$$

where P is the momentum flux from the Sun given by $4.4 \cdot 10^{-6}$ [kg/ms²], ${}^S\hat{\mathbf{n}}$ is a vector normal to the surface area element, dA , pointing outwards, and ${}^S\hat{\mathbf{S}}$ is a unit vector in the direction from the incident radiation. The diffuse reflection yields a force of

$$d^S\mathbf{F}_{rd} = -P {}^S\hat{\mathbf{S}} \cdot {}^S\hat{\mathbf{n}} ({}^S\hat{\mathbf{S}} - \frac{2}{3} {}^S\hat{\mathbf{n}}) dA, \quad (2.11)$$

and the force from absorption can be described as

$$d^S\mathbf{F}_{ra} = -P {}^S\hat{\mathbf{S}} \cdot {}^S\hat{\mathbf{n}} {}^S\hat{\mathbf{S}} dA. \quad (2.12)$$

The total force exerted on a surface is often a combination of these three, which can be calculated assuming that each force exerts a fraction, C_{rs} , C_{rd} and C_{ra} of the total force limited by $C_{rs} + C_{rd} + C_{ra} = 1$. Furthermore, it is possible to consider the cross-sectional area perpendicular to ${}^S\hat{\mathbf{S}}$, A , which yields

$$\begin{aligned} {}^S\mathbf{F}_R &= C_{rs} \int_A d{}^S\mathbf{F}_{rs} + C_{rd} \int_A d{}^S\mathbf{F}_{rd} + C_{ra} \int_A d{}^S\mathbf{F}_{ra} \\ &= \left(C_{rs} \left(-2P \left(-{}^S\hat{\mathbf{n}} \cdot {}^S\hat{\mathbf{S}} \right)^2 {}^S\hat{\mathbf{n}} \right) + C_{rd} \left(-P {}^S\hat{\mathbf{S}} \cdot {}^S\hat{\mathbf{n}} \left({}^S\hat{\mathbf{S}} - \frac{2}{3} {}^S\hat{\mathbf{n}} \right) \right) \right. \\ &\quad \left. + C_{ra} \left(-P {}^S\hat{\mathbf{S}} \cdot {}^S\hat{\mathbf{n}} {}^S\hat{\mathbf{S}} \right) \right) A \\ &= \left(2C_{rs} + \frac{5}{3}C_{rd} + C_{ra} \right) AP {}^S\hat{\mathbf{S}} \\ &= C_R AP {}^S\hat{\mathbf{S}}, \end{aligned} \quad (2.13)$$

where $C_R = 1.5$ is considered in this report. According to [Wertz 1978, page 65] C_R is in the range $0 \leq C_R \leq 2$; $C_R < 1$ for translucent materials, $C_R = 1$ for absorbing materials and $C_R > 1$ for reflecting materials. The area, A , is calculated as in aerodynamic torque. The disturbance torque from radiation can be expressed as

$${}^S\mathbf{N}_R = {}^S\mathbf{R}_{Rcp} \times {}^S\mathbf{F}_R, \quad (2.14)$$

where ${}^S\mathbf{R}_{Rcp}$ is a vector from the CoM of the satellite to the radiation CoP. The radiation CoP is the geometrical center as with aerodynamic torque.

2.3.4 Magnetic Residual Disturbance

The magnetic field of the Earth interacts with the residual magnetic dipole of the satellite, which causes a torque around the CoM of the satellite. The residual magnetic dipole of the satellite is caused by the current running through the wires and PCBs on the satellite. The magnetic disturbance can, according to [Wertz 1978, page 575], be expressed as

$${}^S\mathbf{N}_{mag} = {}^S\mathbf{M}_{sat} \times {}^S\mathbf{B}, \quad (2.15)$$

where ${}^S\mathbf{M}_{sat}$ is the magnetic residual dipole of the satellite and ${}^S\mathbf{B}$ is the magnetic field vector. A magnetic residual dipole of the NSO, ${}^S\mathbf{M}_{sat} = [0, 0, 22.5 \cdot 10^{-6}]^T [\text{Am}^2]$, has been guesstimated from a current loop on the edge of a PCB in the satellite. This yields a maximum torque of $1.6 \cdot 10^{-9} [\text{Nm}]$, which is considered negligible. The residual magnetic dipole of the satellite is, however, not used in the model, as the final configuration is not known and it is possible to cancel the torque by positioning the wires and PCBs accordingly, or adding a permanent magnet to obtain ${}^S\mathbf{M}_{sat} \approx \mathbf{0}$ [Hughes 1986, page 264].

2.3.5 Total Disturbance Torque

The total disturbance torque can now be derived as

$$\begin{aligned} {}^S\mathbf{N}_{\text{ext}} &= {}^S\mathbf{N}_{\text{drag}} + {}^S\mathbf{N}_{\text{GG}} + {}^S\mathbf{N}_{\text{R}} \\ &= {}^S\mathbf{R}_{\text{Acp}} \times {}^S\mathbf{F}_A \\ &\quad + \frac{3\mu}{\| {}^S\mathbf{R}_{\text{sat}} \|^3} \left({}^S\hat{\mathbf{R}}_{\text{sat}} \times ({}^S\mathbf{I} {}^S\hat{\mathbf{R}}_{\text{sat}}) \right) \\ &\quad + {}^S\mathbf{R}_{\text{Rcp}} \times {}^S\mathbf{F}_R. \end{aligned} \quad (2.16)$$

Given the worst case disturbance torques calculated in Appendix D, the torque generated by magnetic residuals has been omitted. Moreover, no model of the residual magnetic dipole of the satellite is available.

The disturbance models described in this section have been implemented in SIMULINK as depicted in Appendix L.

2.4 Actuator Modeling

In this section the models for the attitude control actuators on board the satellite will be described. The on-board actuators on the NSO are of similar nature to the ones on AAUSAT-II, i.e., magnetorquers and momentum wheels. The momentum wheels will be used for fast and small changes in the satellite attitude and the magnetorquers for desaturation³ of the momentum wheels, or for slower larger changes in attitude. All sensors and actuators mounted on the satellite will, to variable degrees, be subject to misalignments. These misalignments can be remedied prior to launch by conducting measurements and subsequent adjustments, either to the mechanical securement or to the actuator hardware. Therefore, this subject will not be treated any further in this project.

2.4.1 Magnetorquer Model

The magnetorquers used on the NSO are rectangular coils placed on the side panels with the dimensions guesstimated to be 70 [mm] \times 70 [mm] for the coil on the z -side with 865 windings, and 210 [mm] \times 70 [mm] for the remaining two sides with 435 windings each, if feasible with the final satellite mechanics. The coil dimensions are chosen to maximise the coil area in order to reduce the magnitude of the current required in the coil. The coil material is chosen to be copper wire with a diameter of 0.2 [mm]. When placed in a magnetic field and carrying a current the coils will produce a torque stemming from the forces created by the current flowing in the magnetic field.

The modeling of the magnetorquers requires significant explanations, which is why the full derivation of the magnetorquer model and dimensioning is performed in Appendix E and only the results are presented here.

³Unloading of accumulated angular momentum.

From Appendix E it is known that the total torque exerted on the coil is described by

$$\begin{aligned}\mathbf{N}_{\text{Total}} &= ni_{\text{mt}} A_{\text{mt}} \hat{\mathbf{n}} \times \mathbf{B} \quad \Rightarrow \\ \mathbf{N}_{\text{Total}} &= \mathbf{M}_{\text{mt}} \times \mathbf{B},\end{aligned}\tag{2.17}$$

where n is the number of windings of the coil, i_{mt} is the current in the coil, A_{mt} is the area spanned by the coil, $\hat{\mathbf{n}}$ is a unit normal vector to the coil plane, which direction is determined by using the right-hand rule, and \mathbf{B} is the magnetic field vector. The term $ni_{\text{mt}} A_{\text{mt}} \hat{\mathbf{n}}$ is often expressed as the magnetic dipole moment, \mathbf{M}_{mt} .

Taking into account the electro mechanic properties of the coil the transfer function from the impressed voltage on the ADCS PCB to the generated magnetic dipole moment is

$$\frac{\mathbf{M}_{\text{mti}}(s)}{v_{\text{mt}}(s)} = \frac{nA_{\text{mt}}}{R_{\text{mt}}}, \quad i = \{x, y, z\},\tag{2.18}$$

where R_{mt} is the coil resistance, and is dependent on the coil temperature which is assumed consistent with the satellite internal temperature. The coil resistance is given by

$$R_{\text{mt}} = \frac{nC\sigma_{0\text{cu}}(1 + \alpha_{0\text{cu}}(T - T_0))}{A_{\text{wire}}},\tag{2.19}$$

where $\sigma_{0\text{cu}} = 1.7 \cdot 10^{-8} [\Omega\text{m}]$ is the resistivity of copper at 293 [K], $\alpha_{0\text{cu}} = 3.9 \cdot 10^{-3} [\text{K}^{-1}]$ is the resistivity temperature coefficient, C is the circumference of coil, T is the temperature, T_0 is the resistivity base temperature being 293 [K] and A_{wire} is the wire cross sectional area. The effect of the coil inductance is not included in the model as it is shown to be negligible in Appendix E.

Using the magnetorquer parameters a model of the magnetorquers has been implemented in SIMULINK as depicted in Figure L.6 in Appendix L.

2.4.2 Momentum Wheel Model

The NSO is equipped with three momentum wheels consisting of a flywheel mounted on a DC-motor (Maxon RE 10). When the flywheel is accelerated by the motor the change in angular momentum generates a torque, which makes the satellite rotate. The momentum wheels are aligned parallel to the axes of the SBRF.

Similar to the magnetorquer modeling the modeling of the momentum wheels require significant explanations, which are performed in Appendix G. Here a model of the electrical properties is firstly derived and subsequently a model of the mechanical properties, whereafter the momentum wheel dimensioning is performed. To create an accurate model of the entire momentum wheel system, the modeling also includes the modeling and design of a hardware PID-controller on the ADCS PCB. The effect of the motor coil inductance is not included in the model as it is shown to be negligible in Appendix G.

From Appendix G the transfer function for the entire momentum wheel system is known to be describable by the closed loop of the PID-controller and motor model yielding

$$\begin{aligned}
 \frac{\omega_{\text{mw}}(s)}{\omega_{\text{mw}_{\text{ref}}}(s)} &= \frac{b_1 s^2 + b_2 s + b_3}{a_0 s^3 + a_1 s^2 + a_2 s + a_3}, \quad \text{where} \\
 b_1 &= C_p C_t I_{\text{mw}} R_{\text{mw}} \\
 b_2 &= C_p C_t (\mu_f R_{\text{mw}} + C_t C_s) + C_i C_t I_{\text{mw}} R_{\text{mw}} \\
 b_3 &= C_i C_t (\mu_f R_{\text{mw}} + C_t C_s) \\
 a_0 &= I_{\text{mw}}^2 R_{\text{mw}}^2 \\
 a_1 &= C_p C_t I_{\text{mw}} R_{\text{mw}} + 2I_{\text{mw}} R_{\text{mw}} (\mu_f R_{\text{mw}} + C_t C_s) \\
 a_2 &= C_p C_t (\mu_f R_{\text{mw}} + C_t C_s) + C_i C_t I_{\text{mw}} R_{\text{mw}} + \mu_f^2 R_{\text{mw}}^2 \\
 &\quad + C_t^2 C_s^2 + 2\mu_f R_{\text{mw}} C_t C_s \\
 a_3 &= C_i C_t (\mu_f R_{\text{mw}} + C_t C_s), \tag{2.20}
 \end{aligned}$$

where ω_{mw} is the angular velocity of the rotor, I_{mw} is the inertia of the momentum wheel, R_{mw} is the resistance in the motor coils, μ_f is the viscous friction coefficient in the motor, C_t is the motor torque constant, C_s is the motor speed constant, C_p is the hardware controller proportional gain and C_i is the hardware controller integral gain.

The values used in the momentum wheel modeling and dimensioning of the flywheel can be found in Appendix G in Table G.1. Furthermore, the tuning of the hardware controller resulted in a PI-controller with $C_p = 0.4$ [.] and a $C_i = \frac{C_p}{10}$ [.]. The D-term is left out to limit the noise susceptibility of the control loop.

In Figure L.7 in Appendix L the SIMULINK implementation of the momentum wheel model is illustrated.

2.5 Satellite Dynamics and Kinematics

This section contains the derivation of the dynamic and kinematic equations of the satellite. The dynamic differential equation of the satellite describes how torques acting on the satellite influence the rotational acceleration of the satellite. The kinematic differential equation of the satellite describes the time dependent relationship between different reference frames. This section is based on previous work performed by [Group 05gr833 2005] and on [Wertz 1978, page 516-523] and [Wie 1998, page 307-328]. Appendix C provides a description of the fundamental algebraic properties of quaternions, which are used for these equations.

2.5.1 Dynamic Equation of the Satellite

This section contains the dynamic differential equation of the satellite, which is based on Newton's laws of motion and Euler's laws of angular motion.

Euler's second equation for the satellite given in inertial coordinates can be expressed as

$$\frac{d^{\text{I}} \mathbf{h}}{dt} = {}^{\text{I}} \mathbf{N}_{\text{ext}}, \tag{2.21}$$

where \mathbf{h} is the angular momentum and \mathbf{N}_{ext} are the external torques acting on the satellite. These external torques are disturbance torques, which include aerodynamic drag, solar radiation, and gravity gradient cf. Section 2.3.

In order to express ${}^I\mathbf{h}$ in the CRF the following equation is used

$${}^C\mathbf{h} = {}_I\underline{\mathbf{C}} {}^I\mathbf{h}, \quad (2.22)$$

where ${}_I\underline{\mathbf{C}}$ is a rotation matrix from ECI to CRF. Taking the derivative w.r.t. time yields

$$\begin{aligned} {}^C\dot{\mathbf{h}} &= {}_I\underline{\mathbf{C}} {}^I\dot{\mathbf{h}} + {}_I\underline{\mathbf{C}} {}^I\mathbf{h} \\ &= {}^C\dot{\mathbf{h}} + {}_I\underline{\mathbf{C}} {}^I\mathbf{h}. \end{aligned} \quad (2.23)$$

Using the translation theorem and [Wertz 1978, page 515], yields the subsequent expression for the change in angular momentum given in the CRF

$${}^C\dot{\mathbf{h}} = {}^C\mathbf{N}_{\text{ext}} - \boldsymbol{\omega} \times {}^C\mathbf{h}. \quad (2.24)$$

Besides the disturbance torques the satellite is also influenced by control torques from the magnetorquers and momentum wheels. The control torques from the momentum wheels will be modeled in the dynamic differential equation of the satellite. Control torques from the magnetorquers will be modeled separately, however the contribution from the magnetorquers will be included in the dynamic differential equation.

Due to the fact that the satellite contains momentum wheels, it cannot be considered a strictly rigid body. With the angular momentum from the momentum wheels included, the total angular momentum of the satellite becomes

$$\mathbf{h} = \mathbf{h}_{\text{sat}} + \mathbf{h}_{\text{mw}}, \quad (2.25)$$

where \mathbf{h}_{mw} is the angular momentum of the momentum wheels and \mathbf{h}_{sat} is defined as

$$\mathbf{h}_{\text{sat}} = \underline{\mathbf{I}}_{\text{sat}} \boldsymbol{\omega}, \quad (2.26)$$

where $\underline{\mathbf{I}}_{\text{sat}}$ is the moment of inertia matrix.

Inserting (2.26) into (2.25) yields

$$\mathbf{h} = \underline{\mathbf{I}}_{\text{sat}} \boldsymbol{\omega} + \mathbf{h}_{\text{mw}} \quad \Leftrightarrow \quad (2.27)$$

$$\begin{aligned} \underline{\mathbf{I}}_{\text{sat}} \boldsymbol{\omega} &= \mathbf{h} - \mathbf{h}_{\text{mw}} \quad \Leftrightarrow \\ \boldsymbol{\omega} &= \underline{\mathbf{I}}_{\text{sat}}^{-1} (\mathbf{h} - \mathbf{h}_{\text{mw}}). \end{aligned} \quad (2.28)$$

Substituting (2.28) into (2.24) yields the change in total angular momentum of the satellite given by

$${}^C\dot{\mathbf{h}} = {}^C\mathbf{N}_{\text{ext}} - ({}^C\underline{\mathbf{I}}_{\text{sat}}^{-1} ({}^C\mathbf{h} - {}^C\mathbf{h}_{\text{mw}})) \times {}^C\mathbf{h}. \quad (2.29)$$

It is important that the dynamic equation of the satellite is calculated in the CRF, to avoid the effects of cross correlations. By choosing the CRF as consisting of the principal axes, the product of inertia becomes 0, thereby yielding the diagonal moment of inertia matrix [Wertz 1978, page 519]

$${}^C\underline{\mathbf{I}}_{\text{sat}} = \begin{bmatrix} I_{11} & 0 & 0 \\ 0 & I_{22} & 0 \\ 0 & 0 & I_{33} \end{bmatrix}. \quad (2.30)$$

Since the CRF will be used in the expression of the dynamic equation the superscript denoting the reference frame, will not be used in the further derivation of the dynamic equation. Inserting (2.27) and (2.28) in (2.29) yields

$$\begin{aligned}\underline{\mathbf{I}}_{\text{sat}}\dot{\boldsymbol{\omega}} + \dot{\mathbf{h}}_{\text{mw}} &= \mathbf{N}_{\text{ext}} - (\underline{\mathbf{I}}_{\text{sat}}^{-1}(\mathbf{h} - \mathbf{h}_{\text{mw}})) \times \mathbf{h} \quad \Leftrightarrow \\ \underline{\mathbf{I}}_{\text{sat}}\dot{\boldsymbol{\omega}} &= \mathbf{N}_{\text{ext}} - \dot{\mathbf{h}}_{\text{mw}} - \boldsymbol{\omega} \times (\underline{\mathbf{I}}_{\text{sat}}\boldsymbol{\omega} + \mathbf{h}_{\text{mw}}) \quad \Leftrightarrow \\ \dot{\boldsymbol{\omega}} &= \underline{\mathbf{I}}_{\text{sat}}^{-1}[\mathbf{N}_{\text{ext}} + \mathbf{N}_{\text{ctrl}} - \underline{\mathbf{S}}(\boldsymbol{\omega})(\underline{\mathbf{I}}_{\text{sat}}\boldsymbol{\omega} + \mathbf{h}_{\text{mw}})],\end{aligned}\quad (2.31)$$

where $\underline{\mathbf{S}}(\boldsymbol{\omega})$ is a skew symmetric matrix defined as

$$\underline{\mathbf{S}}(\boldsymbol{\omega}) = \begin{bmatrix} 0 & -\omega_3 & \omega_2 \\ \omega_3 & 0 & -\omega_1 \\ -\omega_2 & \omega_1 & 0 \end{bmatrix}, \quad (2.32)$$

and the control torque, \mathbf{N}_{ctrl} , is defined as

$$\mathbf{N}_{\text{ctrl}} = \mathbf{N}_{\text{mt}} - \mathbf{N}_{\text{mw}}, \quad (2.33)$$

where \mathbf{N}_{mt} is the torque contributed by the magnetorquers and the \mathbf{N}_{mw} is the torque applied to the momentum wheels, which is defined as

$$\mathbf{N}_{\text{mw}} = \dot{\mathbf{h}}_{\text{mw}}. \quad (2.34)$$

The equation derived in (2.31) will be used in the system equations for the satellite.

2.5.2 Kinematic Equation for the Satellite

There are different methods to represent the kinematic differential equation of the satellite. These are the direction cosine matrix (DCM), denoted the attitude matrix, Euler angles and quaternions. However, the attitude matrix representation suffers from redundancy and the Euler angles suffer from singularities, which is why this section contains the kinematic differential equation represented in terms of quaternions, which only have one redundant parameter.

In order to derive the kinematic differential equation in terms of quaternions the attitude matrix given by Euler's eigenaxis rotation theorem is used. This attitude matrix is derived in Appendix H and is expressed as

$$\underline{\mathbf{C}} = \begin{bmatrix} c\theta + e_1^2(1 - c\theta) & e_1e_2(1 - c\theta) + e_3s\theta & e_1e_3(1 - c\theta) - e_2s\theta \\ e_2e_1(1 - c\theta) - e_3s\theta & c\theta + e_2^2(1 - c\theta) & e_2e_3(1 - c\theta) + e_1s\theta \\ e_3e_1(1 - c\theta) + e_2s\theta & e_3e_2(1 - c\theta) - e_1s\theta & c\theta + e_3^2(1 - c\theta) \end{bmatrix}, \quad (2.35)$$

where $c\theta \equiv \cos(\theta)$, $s\theta \equiv \sin(\theta)$ and e_i are the direction cosines of the Euler axes, which are bounded by $e_1^2 + e_2^2 + e_3^2 = 1$.

Based on Appendix C the following definitions for the quaternions are used in deriving the kinematic differential equation.

$$\mathbf{q}_{1:3} = e \sin(\theta/2) \quad (2.36)$$

$$q_4 = \cos(\theta/2) \quad (2.37)$$

$$\mathbf{q} = (\mathbf{q}_{1:3}, q_4) \quad (2.38)$$

$$1 = q_1^2 + q_2^2 + q_3^2 + q_4^2. \quad (2.39)$$

It is now possible to express the attitude matrix, given in (2.35), in terms of quaternions, yielding [Wie 1998, page 318]

$$\underline{\mathbf{C}}(\mathbf{q}) = \begin{bmatrix} 1 - 2(q_2^2 + q_3^2) & 2(q_1q_2 + q_3q_4) & 2(q_1q_3 - q_2q_4) \\ 2(q_2q_1 - q_3q_4) & 1 - 2(q_1^2 + q_3^2) & 2(q_2q_3 - q_1q_4) \\ 2(q_3q_1 + q_2q_4) & 2(q_3q_2 - q_1q_4) & 1 - 2(q_1^2 + q_2^2) \end{bmatrix}. \quad (2.40)$$

The kinematic differential equation for the attitude matrix method, which is derived in Appendix H, yields

$$\dot{\underline{\mathbf{C}}} + \underline{\mathbf{S}}(\boldsymbol{\omega})\underline{\mathbf{C}} = 0, \quad (2.41)$$

where $\underline{\mathbf{C}}$ is the attitude matrix from one reference frame to another, $\dot{\underline{\mathbf{C}}}$ is the time derivative of the same attitude matrix and $\underline{\mathbf{S}}(\boldsymbol{\omega})$ is a 3×3 skew symmetric matrix containing the angular velocity.

From (2.41) the following vector composition for the angular velocity is given:

$$\omega_1 = \dot{C}_{21}C_{31} + \dot{C}_{22}C_{32} + \dot{C}_{23}C_{33} \quad (2.42)$$

$$\omega_2 = \dot{C}_{31}C_{11} + \dot{C}_{32}C_{12} + \dot{C}_{33}C_{13} \quad (2.43)$$

$$\omega_3 = \dot{C}_{11}C_{21} + \dot{C}_{12}C_{22} + \dot{C}_{13}C_{23}. \quad (2.44)$$

In order to express (2.42), (2.43) and (2.44) in terms of quaternions (2.40) is used. This yields the following equations

$$\omega_1 = 2(\dot{q}_1q_4 + \dot{q}_2q_3 - \dot{q}_3q_2 - \dot{q}_4q_1) \quad (2.45)$$

$$\omega_2 = 2(\dot{q}_2q_4 + \dot{q}_3q_1 - \dot{q}_1q_3 - \dot{q}_4q_2) \quad (2.46)$$

$$\omega_3 = 2(\dot{q}_3q_4 + \dot{q}_1q_2 - \dot{q}_2q_1 - \dot{q}_4q_3). \quad (2.47)$$

One more equation is needed in order to obtain 4 equations with 4 unknowns. By differentiating (2.39) the last equation is obtained

$$0 = 2(\dot{q}_1q_1 + \dot{q}_2q_2 + \dot{q}_3q_3 + \dot{q}_4q_4). \quad (2.48)$$

The four equations (2.45), (2.46), (2.47) and (2.48) can be combined into a matrix form, which yields

$$\begin{bmatrix} \omega_1 \\ \omega_2 \\ \omega_3 \\ 0 \end{bmatrix} = 2 \begin{bmatrix} q_4 & q_3 & -q_2 & -q_1 \\ -q_3 & q_4 & q_1 & -q_2 \\ q_2 & -q_1 & q_4 & -q_3 \\ q_1 & q_2 & q_3 & q_4 \end{bmatrix} \begin{bmatrix} \dot{q}_1 \\ \dot{q}_2 \\ \dot{q}_3 \\ \dot{q}_4 \end{bmatrix}. \quad (2.49)$$

Since the 4×4 matrix in (2.49) is orthonormal, the kinematic differential equation for the satellite in terms of quaternions is given in matrix form by [Wie 1998, page 327]

$$\begin{bmatrix} \dot{q}_1 \\ \dot{q}_2 \\ \dot{q}_3 \\ \dot{q}_4 \end{bmatrix} = \frac{1}{2} \begin{bmatrix} 0 & \omega_3 & -\omega_2 & \omega_1 \\ -\omega_3 & 0 & \omega_1 & \omega_2 \\ \omega_2 & -\omega_1 & 0 & \omega_3 \\ -\omega_1 & -\omega_2 & -\omega_3 & 0 \end{bmatrix} \begin{bmatrix} q_1 \\ q_2 \\ q_3 \\ q_4 \end{bmatrix} = \frac{1}{2} \begin{bmatrix} q_4\boldsymbol{\omega} - \boldsymbol{\omega} \times \mathbf{q}_{1:3} \\ -\boldsymbol{\omega}^T \mathbf{q}_{1:3} \end{bmatrix} = \frac{1}{2} \begin{bmatrix} -\underline{\mathbf{S}}(\boldsymbol{\omega}) & \boldsymbol{\omega} \\ -\boldsymbol{\omega}^T & 0 \end{bmatrix} \mathbf{q} = \frac{1}{2} \underline{\boldsymbol{\Omega}} \mathbf{q}. \quad (2.50)$$

2.6 System Equations

Based on the derived dynamic and kinematic differential equations for the satellite, it is possible to express the system equations as

$$\underbrace{\begin{bmatrix} \dot{\omega} \\ \dot{q} \end{bmatrix}}_{\dot{x}} = \underbrace{\begin{bmatrix} \underline{\mathbf{I}}_{\text{sat}}^{-1}(\mathbf{N}_{\text{ext}} + \mathbf{N}_{\text{ctrl}} - \underline{\mathbf{S}}(\omega)(\underline{\mathbf{I}}_{\text{sat}}\omega + \mathbf{h}_{\text{mw}})) \\ \frac{1}{2}\underline{\Omega}q \end{bmatrix}}_{f(\mathbf{x}, \mathbf{u}, \mathbf{w})} \quad (2.51)$$

$$\underbrace{\begin{bmatrix} \omega \\ q \end{bmatrix}}_{y} = \underbrace{\begin{bmatrix} \mathbf{1}_{3 \times 3} & \mathbf{0}_{3 \times 4} \\ \mathbf{0}_{4 \times 3} & \mathbf{1}_{4 \times 4} \end{bmatrix}}_{\underline{\mathbf{C}}_{\text{sat}}} \underbrace{\begin{bmatrix} \omega \\ q \end{bmatrix}}_{x}. \quad (2.52)$$

The system equations are constructed, based on the desire of an output containing the angular velocity, ω , and the attitude in terms of a quaternion, q . In order to keep the output matrix $\underline{\mathbf{C}}_{\text{sat}}$ simple, the angular velocity and the attitude quaternion are suitable choices for the state vector, \mathbf{x} . In (2.51) the states are given by a function, containing the state variables, the control signals and the disturbances denoted $f(\mathbf{x}, \mathbf{u}, \mathbf{w})$. In (2.52) the notation $\mathbf{1}_{3 \times 3}$ means a 3×3 identity matrix, i.e. the output matrix $\underline{\mathbf{C}}_{\text{sat}}$ becomes a 7×7 identity matrix. However, the system equations in (2.51) are non-linear, and in order to design e.g. optimal controllers the non-linear expression needs to be linearised, which yields

$$\underbrace{\begin{bmatrix} \dot{\tilde{q}}_{1:3} \\ \dot{\tilde{\omega}} \\ \dot{\tilde{h}}_{\text{mw}} \end{bmatrix}}_{\dot{\tilde{x}}} = \underbrace{\begin{bmatrix} -\underline{\mathbf{S}}(\bar{\omega}) & \frac{1}{2}\mathbf{1}_{3 \times 3} & \mathbf{0}_{3 \times 3} \\ \mathbf{0}_{3 \times 3} & \underline{\mathbf{I}}_{\text{sat}}^{-1}[\underline{\mathbf{S}}(\underline{\mathbf{I}}_{\text{sat}}\bar{\omega}) - \underline{\mathbf{S}}(\bar{\omega})\underline{\mathbf{I}}_{\text{sat}} + \underline{\mathbf{S}}(\bar{h}_{\text{mw}})] & -\underline{\mathbf{I}}_{\text{sat}}^{-1}\underline{\mathbf{S}}(\bar{\omega}) \\ \mathbf{0}_{3 \times 3} & \mathbf{0}_{3 \times 3} & \mathbf{0}_{3 \times 3} \end{bmatrix}}_{\underline{\mathbf{A}}_{\text{sat}}} \underbrace{\begin{bmatrix} \tilde{q}_{1:3} \\ \tilde{\omega} \\ \tilde{h}_{\text{mw}} \end{bmatrix}}_{\tilde{x}} + \underbrace{\begin{bmatrix} \mathbf{0}_{3 \times 3} & \mathbf{0}_{3 \times 3} \\ \underline{\mathbf{I}}_{\text{sat}}^{-1} & -\underline{\mathbf{I}}_{\text{sat}}^{-1} \\ \mathbf{0}_{3 \times 3} & \mathbf{1}_{3 \times 3} \end{bmatrix}}_{\underline{\mathbf{B}}_{\text{sat}}} \underbrace{\begin{bmatrix} \tilde{\mathbf{N}}_{\text{mt}} \\ \tilde{\mathbf{N}}_{\text{mw}} \end{bmatrix}}_{\tilde{\mathbf{u}}}. \quad (2.53)$$

Furthermore, the actuator models should be included so the designed controllers consider the dynamics of the entire system. A linearisation of the non-linear expression in (2.51), including the actuator models, is presented in Appendix I. This linearisation facilitates the possibility to express the system equations as

$$\begin{aligned} \dot{\mathbf{x}} &= \underline{\mathbf{A}}_{\text{sat}_\text{act}} \mathbf{x} + \underline{\mathbf{B}}_{\text{sat}_\text{act}} \mathbf{u} \\ \mathbf{y} &= \underline{\mathbf{C}}_{\text{sat}_\text{act}} \mathbf{x}, \end{aligned} \quad (2.54)$$

where the matrices $\underline{\mathbf{A}}_{\text{sat}_\text{act}}$, $\underline{\mathbf{B}}_{\text{sat}_\text{act}}$ and $\underline{\mathbf{C}}_{\text{sat}_\text{act}}$ are given in Appendix I and \mathbf{x} and \mathbf{u} are given as

$$\begin{aligned} \mathbf{x} &= [\tilde{q}_{1:3} \ \tilde{\omega} \ \tilde{h}_{\text{mw}} \ \mathbf{x}_{\text{mw}_x} \ \mathbf{x}_{\text{mw}_y} \ \mathbf{x}_{\text{mw}_z}]^T \\ \mathbf{u} &= [v_{\text{mt}_x} \ v_{\text{mt}_y} \ v_{\text{mt}_z} \ \alpha_{\text{ref}_x} \ \alpha_{\text{ref}_y} \ \alpha_{\text{ref}_z}]^T. \end{aligned} \quad (2.55)$$

In order to include the dynamics of the actuators the state vector has been augmented with four states for each momentum wheel. These have been defined in the vectors \mathbf{x}_{mw_x} , \mathbf{x}_{mw_y} and \mathbf{x}_{mw_z} . Including the actuator dynamics gives an input vector, which contains the voltage to each magnetorquer and the angular acceleration of the momentum wheels.

Control Structure

This chapter presents the overall functionality and control design for the different modes of the satellite. Furthermore, once the overall design has been described, the delimitations for the control design are specified and the control structure is presented. It is addressed to the reader with interest in a description of the operational modes of the NSO and the control structure used in the subsequent design.

3.1 Mode Selection

The different modes of the NSO satellite were presented in Chapter 1. This section identifies the interconnections of the modes presented earlier, and introduces some additional locations needed for describing the overall functionality and control design as a discrete event system.

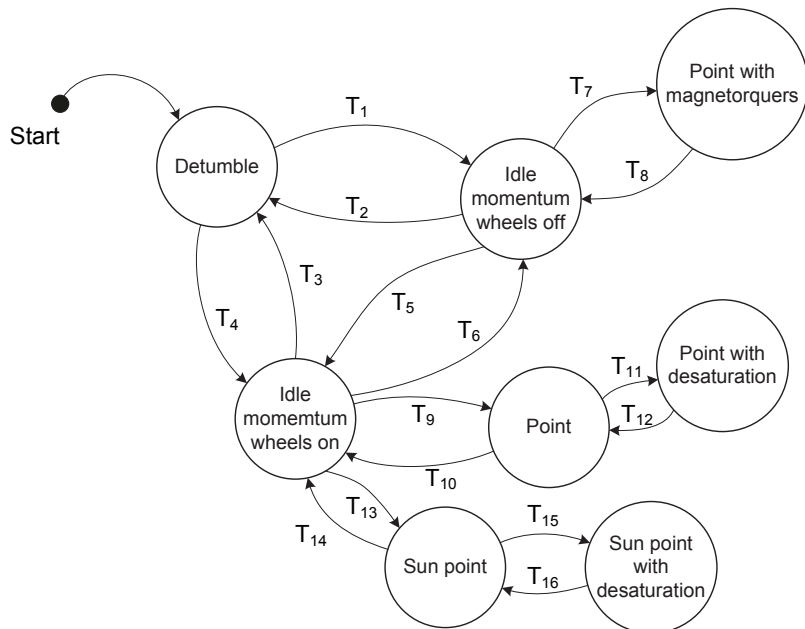


Figure 3.1: Operational modes of the ACS.

Figure 3.1 depicts the different modes of operation for the NSO satellite, along with the possible transitions from each mode. The different transitions are described in Table 3.1. In the situation where the solar arrays are deployed the modes of operation are the same, however, the controllers in the different modes might have to be changed due to the change

in inertia matrix of the satellite. Furthermore, some of the transitions specified in Figure 3.1 require commands from the ground station, which are uploaded to a flight plan on board the satellite. The flight plan contains the specified commands and a execution time for each command.

Transition	Description
T_1	This transition can only occur if $\ \omega\ \leq \ \omega_{\text{det}}\ $ and <code>mw_on = false</code> . Where <code>mw_on</code> is a variable specified in the flight plan.
T_2, T_3	In order to enable these two transitions the expressions $\ \omega\ > \ \omega_{\text{det}}\ + \omega_{\text{offset}}$ and $\dot{\omega}_{\text{mw}} = \mathbf{0}$ must be valid, where ω_{offset} is an offset scalar.
T_4	This transition is only possible if $\ \omega\ \leq \ \omega_{\text{det}}\ $ and <code>mw_on = true</code> . Here <code>mw_on</code> is a variable specified in the flight plan.
T_5, T_6	Transition T_5 is possible if <code>mw_on = true</code> and T_6 is possible if <code>mw_on = false</code> .
T_7, T_8	These two transition can only be enabled by specifying a variable in the flight plan. T_7 occurs when <code>mt_pointing = true</code> and T_8 occurs when <code>mt_pointing = false</code> .
T_9, T_{10}	Transitions T_9 and T_{10} only occurs when the variable <code>pointing</code> is either true or false. T_9 occurs when <code>pointing = true</code> and T_{10} occurs when <code>pointing = false</code> .
T_{11}, T_{12}	These transitions occur depending on the angular momentum of the momentum wheels.
T_{13}, T_{14}	In order to enable these two transitions the variable <code>sun_pointing</code> must be specified in the flight plan. T_{13} occurs when <code>sun_pointing = true</code> and T_{14} occurs when <code>sun_pointing = false</code> .
T_{15}, T_{16}	These transitions occur depending on the angular momentum of the momentum wheels.

Table 3.1: Description of the transitions depicted in Figure 3.1.

Detumbling

Once the NSO is separated from the launch vehicle an initial angular velocity is expected. This angular velocity characterises the detumbling mode, which has the objective of minimising the angular velocity around each axis of the satellite. The detumbling mode is introduced as initial angular velocity is not acceptable, when trying to establish communication with the satellite. Furthermore, a reduced angular velocity is also required in order for ADS to determine the attitude of the satellite facilitating the possibility of camera pointing operations.

The objective of the detumbling mode is to dissipate kinetic energy, thereby lowering the angular velocity of the satellite. In general, the controllers designed for detumbling have to be reliable and not rely on estimation filters to be active, which reduces the risk of failure in the controller. One controller that is widely used is the $\ddot{\mathbf{B}}$ -controller, [Wisniewski 1996] and [Graversen, Frederiksen & Vedstesen 2002], which uses the magnetorquers to dissipate kinetic energy, such that the satellite follows the geomagnetic field. Since the satellite is equipped with gyros another possibility for detumble control could be an optimal controller minimising the angular velocity of the satellite. This design is preferred as the gyros measure the angular velocity directly.

Idle Momentum Wheels on/off

From the detumbling mode it is possible to make transitions to two other locations. These are specified as idle modes and they enable the satellite to be in locations where no controllers are active. It has been necessary to introduce two locations due to the fact that it is not desirable to have the momentum wheels active, when pointing with only magnetorquers. In one location the momentum wheels are inactive and it is possible to make transitions to either pointing with magnetorquers or back to the detumbling mode if the angular velocity increases. Furthermore, it is possible to activate the momentum wheels by switching to the other location. From this location it is also possible to access the detumbling mode. The activation of the momentum wheels facilitates the possibility of making transitions to the two pointing modes, that utilises the momentum wheels for actuation.

Point with Magnetorquers

This mode is only reachable if the momentum wheels are inactive and the satellite has been detumbled. There are numerous control methods that could be applied to facilitate three axis stabilising attitude control using only magnetorquers [Wisniewski 1996]. The difficulty in this sort of attitude control is that the mechanical torque from the magnetorquers can only be produced in a plane perpendicular to the geomagnetic field vector. An interesting choice of control could be to utilise model predictive control, however, this is not further investigated in this project.

Pointing

As opposed to the pointing with only magnetorquers, this mode can only be accessed if the momentum wheels are active and the satellite has been detumbled. The objective of the pointing mode is to reduce the angular velocity even more than what was achieved in the detumbling mode. Furthermore, this mode must point the camera towards a specific location on the Earth, when this location is within line of sight. As for the magnetorquer pointing mode the pointing with momentum wheels could be implemented as an LQR-controller [Group 04gr830a 2004]. However, uncertainties in the dynamic and kinematic models, such as disturbances, entails implementation of robust control for the angular velocity. Since the pointing mode utilises momentum wheels for actuation an additional mode called desaturation has been introduced in order to avoid momentum wheel saturation. In the desaturation mode the pointing controller maintains the stability of the satellite, while the desaturation controller uses the magnetorquers to unload the angular momentum from the momentum wheels. Instead of using the magnetorquers for desaturation the use of estimated external disturbance torques could be considered. However, this is not investigated further in this report.

Sun Pointing

When no other tasks are preformed by the ADCS the sun pointing mode should be active in order to optimise the energy production. This optimisation is obtained by pointing the

largest area of solar cells towards the Sun. The objective of optimising the energy production in the satellite could be handled by an optimal controller, such as an LQR-controller. However, like the pointing mode, the sun pointing mode also utilises the momentum wheels for actuation. This entails the introduction of another desaturation mode, where the stability is maintained by the sun pointing controller.

As Figure 3.1 shows, this mode can only be activated if the momentum wheels are active and the satellite is detumbled. The utilisation of momentum wheels as actuators in this mode enables switching between the sun pointing mode and the pointing mode without switching the momentum wheels on and off. This minimises wear on the momentum wheels and energy is not used to activate them.

In the following section delimitations to the controller designs are stated and the control structure for final control design is presented.

3.2 Controller Design Delimitation

In Section 3.1 various modes were described along with potential controllers for handling the specific objective of the particular mode. The objective of this report will be limited to the design of a controller for the pointing mode. Furthermore, the design of a suitable desaturation controller is also included. The control structure for the pointing controller is depicted in Figure 3.2.

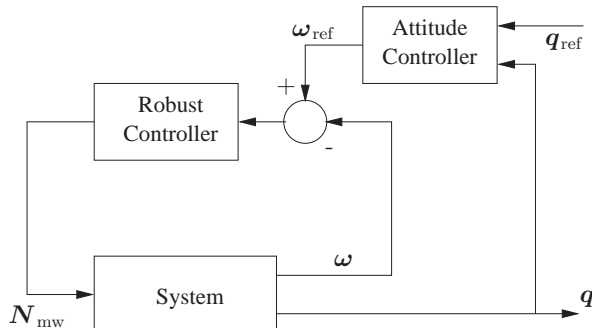


Figure 3.2: Control structure for the pointing mode. The attitude controller generates the angular velocity reference for a robust controller, which generates the control signal for the momentum wheels.

As noticed the control structure includes both a robust controller for controlling the angular velocity of the satellite and an attitude controller. The attitude controller uses the measured attitude of the satellite and a reference attitude to determine a reference for the angular velocity of the satellite. This reference is then used to calculate the error signal for the robust controller. The controllers designed for the pointing mode will also be usable in the sun pointing mode. Designing controllers for the pointing mode also entails utilisation of both the momentum wheels and the magnetorquers. The control structure presented in Figure 3.2 only maintain attitude stability. In order to facilitate pointing on a certain location on the Earth, the reference quaternion, q_{ref} , must be changed continuously.

CHAPTER 4

Model Analysis

This chapter describes the initial contemplations upon which to base further controller design. The linear model is analysed for its accuracy compared to the non-linear implementations, and it is analysed for system controllability. Furthermore, an analysis for stability conditions is conducted to ease controller verifications. This chapter is addressed to the reader with interest in the important steps preluding controller synthesis.

4.1 Linear Model Accuracy

To verify the validity interval of the linear model described in Section 2.6, the linear model is compared to the non-linear. Only the linear model without actuator dynamics is considered of significant importance, which is why they are also omitted when comparisons to the non-linear model are made.

In order to compare the two models they are both implemented in SIMULINK and simulated given the same input sequence. The input sequence is chosen to be a pulse sequence, with one pulse up and one pulse down, applied to only the x-axis. The input pulse size is chosen to be that of the maximal torque of the actuators, combined with the maximal disturbance torque, with a duration of 20 [s] each. The pulses are applied to the systems after 300 [s] and after 1300 [s]. The result of the simulation is evaluated on the values from the subtraction of the system output from each other. As directly subtracting the two simulated quaternions is not possible, the error quaternion, describing the rotation between the two resulting attitudes, is examined instead. The fourth element in \mathbf{q}_{err} is a direct indication of the error angle between the two attitudes, when looking at $2 \arccos(\mathbf{q}_{\text{err}}^4)$, which is equal to the rotation angle around the Euler eigenaxis.

In Figure 4.1 the difference between the linear and non-linear model is plotted. As seen in the figure the attitude in the models starts to deviate from each other quite fast, but the error in the angular velocity is negligible throughout the entire simulation. This means that the linear model is accurate for describing the angular velocity in a large interval, however the same is not true for the attitude. The attitude error is actually several sequential full rotations wrong after the simulation. This is attributed to the fact that the linear model for the attitude only uses the first three components of the quaternion. However, some variation does occur when different solvers are used in MATLAB. Using the `ode45` solver is recommended as it yields the most accurate result. The reason the error becomes stationary after the application of the last pulse, is that the models are nearly identical in terms of the angular velocity, which entails that the angular velocity drops to zero in both models, and therefore, no change in attitude can be observed. The same tendency has been observed with pulse input signals at different time instances and of different amplitudes,

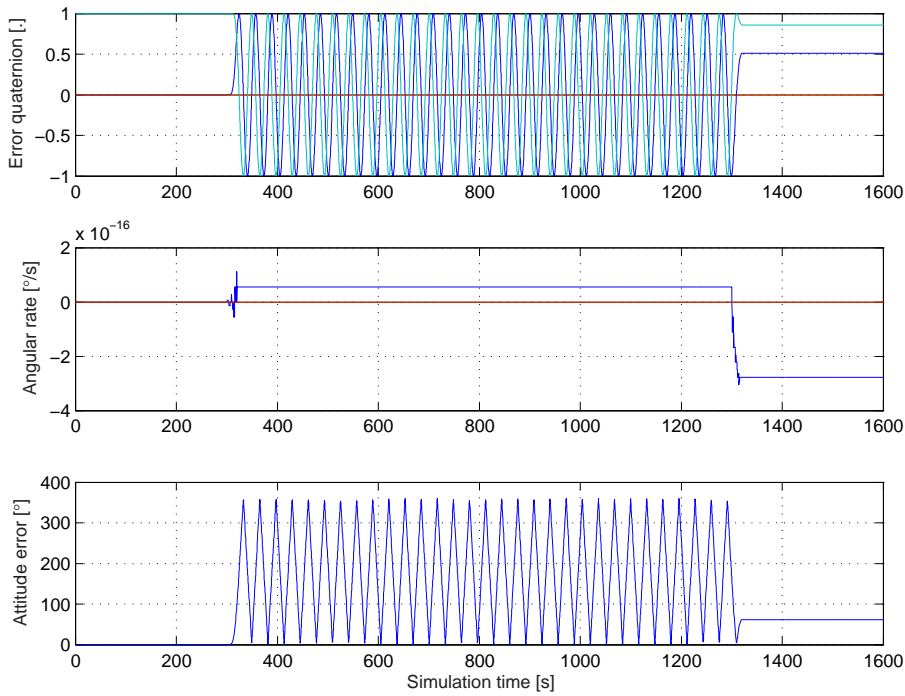


Figure 4.1: Model errors. The topmost plot describes the evolution of the error quaternion, the middle plot the error in the angular velocities and the bottom one the rotation error angle.

and the application of a sinusoid signal yields similar results.

To get an indication of the attitude validity interval of the linear model, the time interval around the first pulse start is examined. A closeup of this time interval is plotted in Figure 4.2.

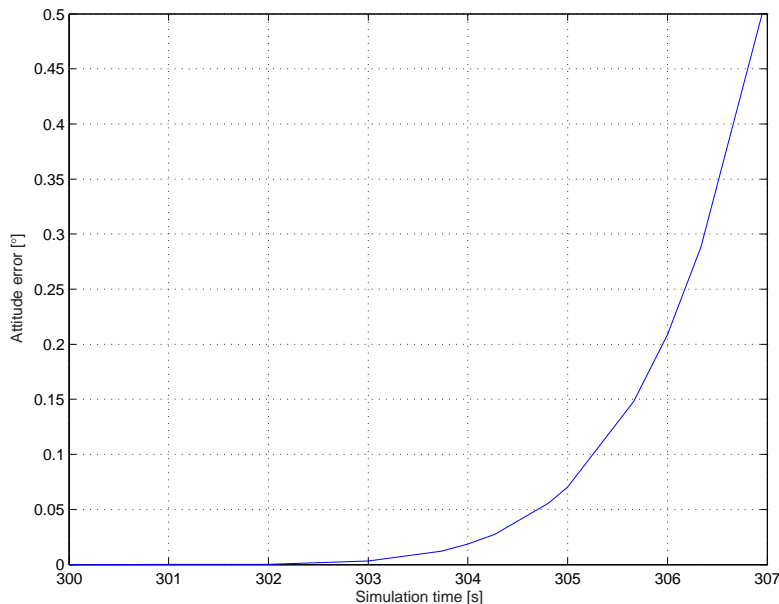


Figure 4.2: The rotation error angle between the two attitudes, from the linear and non-linear model respectively.

If a drift of maximum $0.2 [{}^\circ]$ is considered acceptable then the linear model has deviated from the acceptable limit within $6 [s]$. This means that the model is still considered usable if the control horizon of the attitude controller is shorter than $6 [s]$, i.e., the sampling frequency shall be greater than $10 \cdot \frac{1}{6} [\text{Hz}]$, when considering $10 [.]$ as an adequate sample multiple¹. Therefore, the sampling frequency of the attitude controller shall be greater than $1.7 [\text{Hz}]$. This property is also illustrated in general in Figure 4.3.

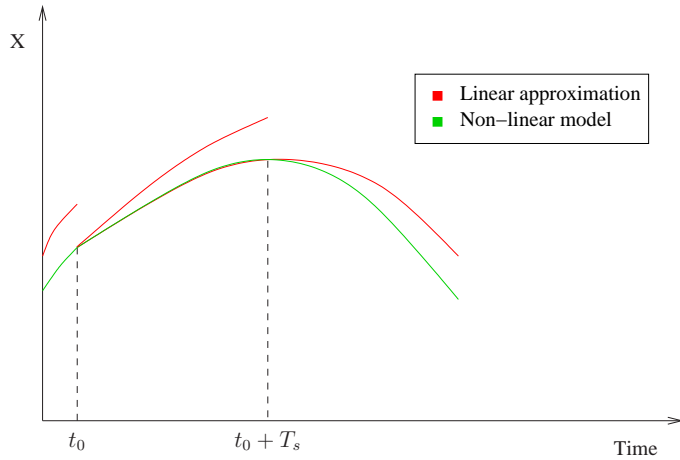


Figure 4.3: Illustration of model deviations with time, and the effect of sampling rate variations.
If a higher sampling rate is applied better precision is achieved, but elevation of the processing load is inevitable.

When remembering the control structure described in Section 3.2, it is therefore worth mentioning that the bandwidth of the angular velocity control loop must be no greater than $0.2 [\text{Hz}]$, when using a sampling rate of $2 [\text{Hz}]$ and a required sample multiple of $10 [.]$. A sample rate of no more than $2 [\text{Hz}]$ is considered feasible with most satellite controller applications, as restrictions on computational load is often an inhibitory element. The bandwidth of $0.2 [\text{Hz}]$ on the angular velocity control loop, furthermore, entails that the bandwidth of the attitude control loop must be less than $0.2 [\text{Hz}]$.

Following the preluding verification of the linear model, it is necessary to verify that the linearised model is controllable to facilitate controller synthesis.

4.2 Controllability

This section presents with a controllability analysis of the linear satellite model found in Section 2.6. The system is examined at the operating point, defined as $\bar{\omega} = [0 \ 0 \ 0]^T$ and

¹The sample multiple is reduced to $10 [.]$ from the conservative rule of thumb of $20 [.]$. This is also used elsewhere in the space industry, e.g., in the ESA guidance - navigation and control section.

$\bar{\mathbf{h}}_{\text{mw}} = [h_{\text{mw}1\text{bias}} \ h_{\text{mw}2\text{bias}} \ h_{\text{mw}3\text{bias}}]^T$, which yields

$$\begin{bmatrix} \dot{\tilde{\mathbf{q}}}_{1:3} \\ \dot{\tilde{\boldsymbol{\omega}}} \\ \dot{\tilde{\mathbf{h}}}_{\text{mw}} \end{bmatrix} = \left[\begin{array}{c|cc} \underline{\mathbf{0}}_{3 \times 3} & \frac{1}{2}\underline{\mathbf{1}}_{3 \times 3} & \underline{\mathbf{0}}_{3 \times 3} \\ \hline \underline{\mathbf{0}}_{3 \times 3} & \underline{\mathbf{I}}_{\text{sat}}^{-1} \mathbf{S}(\bar{\mathbf{h}}_{\text{mw}}) & \underline{\mathbf{0}}_{3 \times 3} \\ \underline{\mathbf{0}}_{3 \times 3} & \underline{\mathbf{0}}_{3 \times 3} & \underline{\mathbf{0}}_{3 \times 3} \end{array} \right] \begin{bmatrix} \tilde{\mathbf{q}}_{1:3} \\ \tilde{\boldsymbol{\omega}} \\ \tilde{\mathbf{h}}_{\text{mw}} \end{bmatrix} + \left[\begin{array}{cc} \underline{\mathbf{0}}_{3 \times 3} & \underline{\mathbf{0}}_{3 \times 3} \\ \hline \underline{\mathbf{I}}_{\text{sat}}^{-1} & -\underline{\mathbf{I}}_{\text{sat}}^{-1} \\ \underline{\mathbf{0}}_{3 \times 3} & \underline{\mathbf{1}}_{3 \times 3} \end{array} \right] \begin{bmatrix} \tilde{\mathbf{N}}_{\text{mt}} \\ \tilde{\mathbf{N}}_{\text{mw}} \end{bmatrix}. \quad (4.1)$$

As previously presented the control structure consists of an inner angular velocity control loop and an outer attitude control loop. The system is, therefore, divided into two subsystems; an angular velocity system and an attitude system. The controllability of the outer loop depends on the closed loop of the inner loop, and thus the developed angular velocity controller. The controllability of the attitude state, $\tilde{\mathbf{q}}_{1:3}$, will, therefore, be omitted at this point.

4.2.1 Angular Velocity System

The angular velocity system consists of the states $\tilde{\boldsymbol{\omega}}$ and $\tilde{\mathbf{h}}_{\text{mw}}$ in (4.1). When defining state controllability as the ability to bring a system from a given state to any final state within a finite time [Postlethwaite 2005, page 166], it is desirable to deal with a controllable system. Controllability of the angular system is verified by examining the state controllability matrix,

$$\underline{\mathcal{C}} = [\underline{\mathbf{B}} \ \underline{\mathbf{AB}} \ \underline{\mathbf{A}}^2\underline{\mathbf{B}} \ \dots \ \underline{\mathbf{A}}^{(n-1)}\underline{\mathbf{B}}]. \quad (4.2)$$

It can be noticed that it is possible to control the six states using both actuators ($\text{rank}(\underline{\mathcal{C}}) = 6$). However, the control torque from the magnetorquers, \mathbf{N}_{mt} , depends on the direction of the magnetic field (as explained in Section 2.4.1). Therefore, it is not possible to guarantee three axes control at all times, and the magnetorquer control input is omitted. This reduces the rank of $\underline{\mathcal{C}}$ to three and leaves the angular momentum of the momentum wheels uncontrolled, and requiring momentum management. This is the objective of the desaturation controller suggested in Section 3.2, and from the above this must be performed using the magnetorquers.

Input-Output Direction

In order to design the angular velocity controller it is important to know how the system responds to different input. One method to determine this, is to examine the singular values of the system which is a measure of the directional gains, and states how well conditioned the system is.

In MIMO systems an input vector in a certain direction might yield a larger gain than in a different direction [Postlethwaite 2005, page 71-80]. This is illustrated in Figure 4.4 for a 2×2 system, where the input vectors², \mathbf{v}_1 and \mathbf{v}_2 , define the unit circle.

²Note that \mathbf{v} is used to denote the input vectors, rather than \mathbf{u} as in control theory, as this section is based on the standard notation of SVD given in [Postlethwaite 2005, page 76].

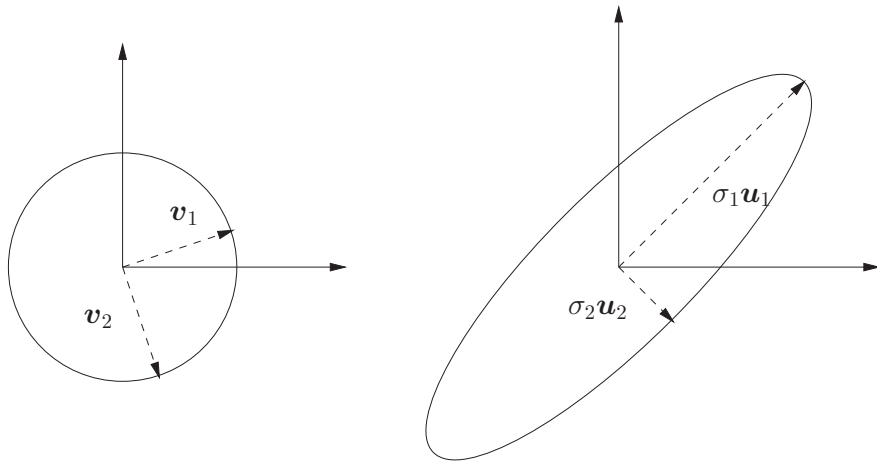


Figure 4.4: Input-output mapping of a 2×2 system.

The output is described by a set of output vectors, \mathbf{u}_1 and \mathbf{u}_2 , and a gain in each direction. From the input vectors, output vectors, and gains, it is possible to determine how the system will react to certain input. Furthermore, the ratio between the largest and smallest gain, called the condition number, can be used as a measurement for the complexity of the control problem. If the condition number, γ , is close to one the system is well conditioned and if $\gamma \gg 1$ the system is defined as ill-conditioned [Postlethwaite 2005, page 78], and can be hard to control. A small error in the input to an ill-conditioned system, can result in a large error on the output, e.g., to move the output in the \mathbf{u}_2 direction in Figure 4.4 requires a large control signal, and if an error occurs on the input resulting in an output direction \mathbf{u}_1 , it could yield a large undesired output.

The directional gains, the input, and output directions of a system can be found using the Singular Value Decomposition (SVD) of the transfer matrix, $\underline{\mathbf{G}}$. This yields

$$\underline{\mathbf{G}} = \underline{\mathbf{U}} \underline{\Sigma} \underline{\mathbf{V}}^T, \quad (4.3)$$

where $\underline{\mathbf{U}}$ contains the output direction vectors, $\underline{\Sigma}$ is a diagonal matrix containing the singular values or directional gains and $\underline{\mathbf{V}}$ contains the corresponding input direction vectors.

The angular velocity system is decomposed at $1 \cdot 10^{-3}$ [rad/s] and 1 [rad/s], and using `svd` in MATLAB

$$\underline{\mathbf{G}}_1 = \underbrace{\begin{bmatrix} -0.579 & 0.207 & -0.789 \\ -0.576 & -0.788 & 0.216 \\ -0.577 & 0.580 & 0.575 \end{bmatrix}}_{\underline{\mathbf{U}}} \underbrace{\begin{bmatrix} 26549 & 0 & 0 \\ 0 & 259 & 0 \\ 0 & 0 & 258 \end{bmatrix}}_{\underline{\Sigma}} \underbrace{\begin{bmatrix} 0.576 & 0.788 & 0.216 \\ 0.579 & -0.207 & -0.789 \\ 0.577 & -0.580 & 0.575 \end{bmatrix}}_{\underline{\mathbf{V}}^T} \quad (4.4)$$

$$\underline{\mathbf{G}}_2 = \underbrace{\begin{bmatrix} -0.036 & -0.688 & -0.725 \\ 0.026 & -0.726 & 0.688 \\ -0.999 & 0.006 & 0.045 \end{bmatrix}}_{\underline{\mathbf{U}}} \underbrace{\begin{bmatrix} 35 & 0 & 0 \\ 0 & 23.6 & 0 \\ 0 & 0 & 23.5 \end{bmatrix}}_{\underline{\Sigma}} \underbrace{\begin{bmatrix} -0.026 & 0.726 & 0.688 \\ 0.036 & 0.688 & -0.725 \\ 0.999 & -0.006 & 0.045 \end{bmatrix}}_{\underline{\mathbf{V}}^T}, \quad (4.5)$$

is obtained. This yields a condition number of $\gamma_1 = 103$ and $\gamma_2 = 1.5$ for $\underline{\mathbf{G}}_1$ and $\underline{\mathbf{G}}_2$ respectively.

Figure 4.5 depicts the singular values of the angular velocity system in the frequency range $1 \cdot 10^{-3}$ [rad/s] $< \omega < 10$ [rad/s]. The large values of γ suggests that the system is sensitive to uncertainties, which should, therefore, be considered in the control design.

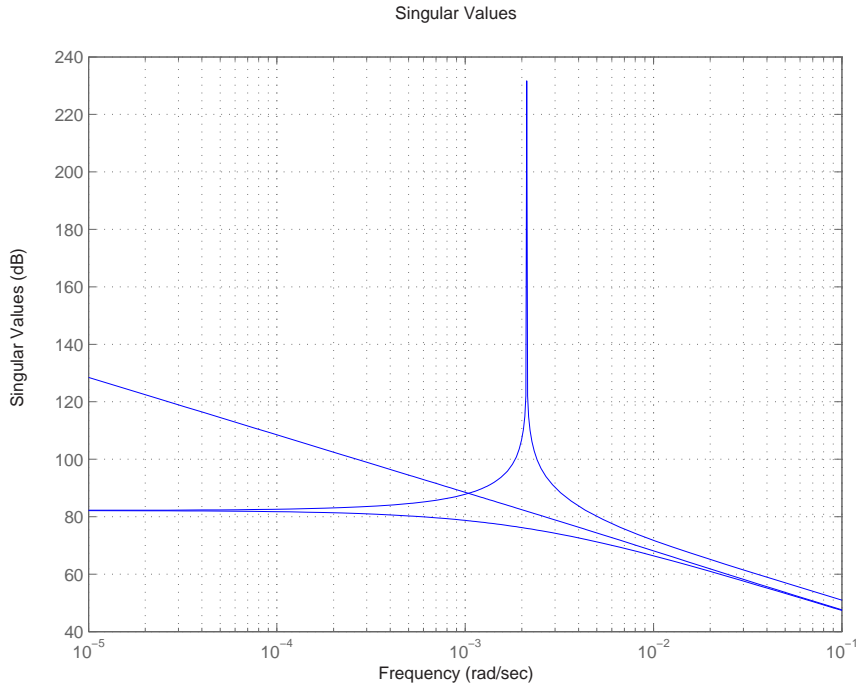


Figure 4.5: Singular values of the angular velocity system as a function of frequency. The spike, at approximately 0.1 [rad/s], is caused by two imaginary system poles.

4.2.2 Attitude Controllability

When looking at attitude controllability two possible scenarios exist: One using momentum wheels and one using magnetorquers. Both of them are subject to limitations due to the physical constraints of the actuators.

Momentum Wheels

Omitting the magnetorquers in the attitude control implies that the momentum wheels must be used to handle both attitude corrections and disturbance rejection. Assuming a stable attitude the total angular momentum of the satellite must be equal to the angular momentum of the momentum wheels, i.e.,

$$\mathbf{h}_{\text{total}} = \mathbf{h}_{\text{mw}}. \quad (4.6)$$

Disregarding the disturbances the law of conservation of angular momentum applies and states that the momentum wheels of the satellite must be able to store the angular momentum independent of the attitude, i.e.,

$$\dot{\mathbf{h}}_{\text{total}} = \mathbf{0}. \quad (4.7)$$

The momentum wheels have a limited operation range, especially as they are biased, and thus limited to rotate in one direction. This implies that the momentum wheels can only generate an angular momentum in the 1st octant of the SBRF. When the attitude of the satellite is stable (no rotation) and the momentum wheels are at the operating point, the

angular momentum of the satellite is expressed as

$${}^S\mathbf{h}_{\text{total}} = {}^S\mathbf{h}_{\text{mw}} = \frac{\| {}^S\mathbf{h}_{\text{mw bias}} \|}{\sqrt{3}} \begin{bmatrix} 1 \\ 1 \\ 1 \end{bmatrix}. \quad (4.8)$$

This implies that a rotation of more than 45° cannot be guaranteed without changing ${}^I\mathbf{h}_{\text{mw}}$ using the magnetorquers, as ${}^S\mathbf{h}_{\text{mw}}$ would then move outside the 1st octant. This is illustrated in Figure 4.6, and must be considered in the design of the attitude controller.

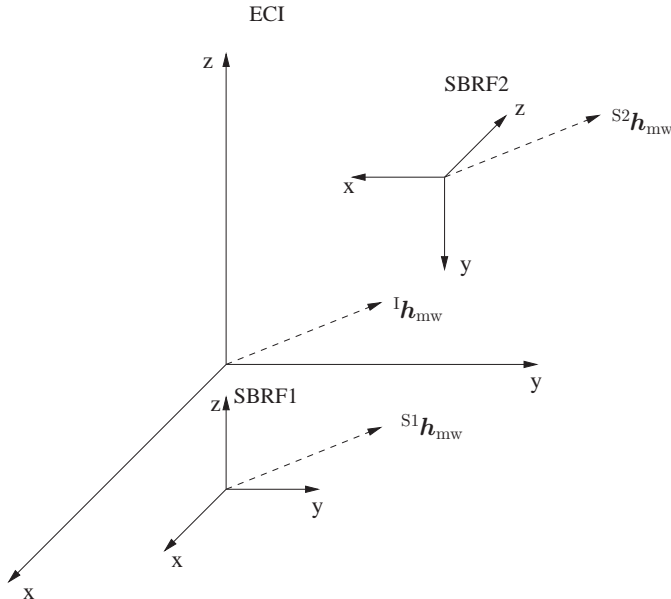


Figure 4.6: The angular momentum of the satellite is constant in an inertial coordinate system and the angular momentum of the momentum wheels must reside in the 1st octant of the SBRF.

Note that in this analysis it is assumed that the angular momentum of the individual momentum wheels coincide with the axis of the SBRF. A more favourable positioning might exist when considering an Earth pointing satellite. However, it is only the relative perpendicular positioning of the individual momentum wheels that causes a limitation of 45° .

Magnetorquers

When using the magnetorquers to desaturate the momentum wheels, it is necessary to consider the limitations inherent by the magnetorquers moving in the magnetic field. The torque produced by the magnetorquers is always perpendicular to the magnetic field vector. Assuming a constant attitude it is possible to determine which rotations are possible at different orbit positions. Figure 4.7 depicts the SBRF at two different positions in the magnetic field. When the satellite is located above the magnetic north pole, with the attitude shown in Figure 4.7, it is only possible to rotate around the x- and y-axes. When the satellite has moved approximately an $\frac{1}{8}$ of an orbit it is only possible to rotate around x-axis and z-axis (note that the magnetic vector field is illustrative and not necessarily correct). It is, therefore, not possible to guarantee three axis control at all times using the

magnetorquers, but over a quarter of an orbit it should be possible to perform three axis rotations.

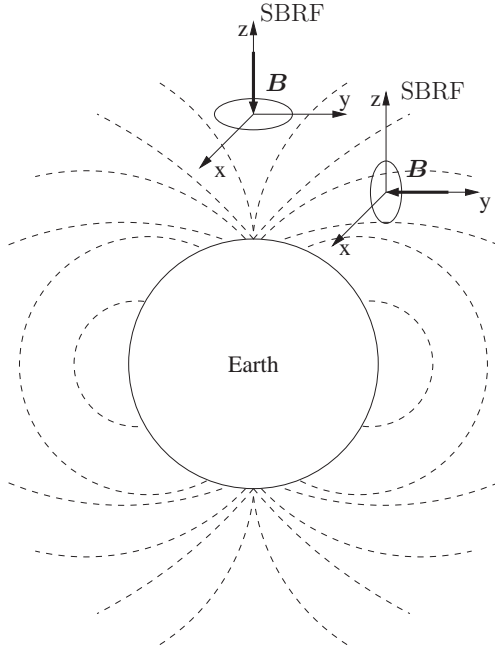


Figure 4.7: The control torques produced by the magnetorquers are always perpendicular to the magnetic field vector (indicated by the circle). Thus, it is not possible to perform three axis control at all times. Note that the magnetic vector field is illustrative and not necessarily correct.

4.3 Lyapunov Stability

In order to prove stability of the closed loop system with a designed controller, it is advantageous to examine the Lyapunov stability criteria for autonomous systems, as opposed to running exhaustive simulations. By choosing a positive definite continuously differentiable function, $\mathcal{V}(x)$, defined on a domain $\mathcal{D} \subset \mathbb{R}^n$ describing the closed loop system, φ , and examining the derivative of that function, it can be proved that φ , whose trajectories belong to that same domain, is stable in a neighbourhood of its equilibrium, $x = 0 \in \mathcal{D}$, [Khalil 2002, page 114]. This can be expressed as

Lyapunov Stability Theorem:

if $\exists \mathcal{V} : \mathcal{D} \rightarrow \mathbb{R}$ s.t. :

I: $\mathcal{V}(0) = 0$

II: $\mathcal{V}(x) > 0 \quad \forall x \in \mathcal{D}, x \neq 0$

III: $\dot{\mathcal{V}}(x) \leq 0 \quad \forall x \in \mathcal{D}$

then $x = 0$ is a stable equilibrium for φ .

And if IV: $\dot{\mathcal{V}}(x) < 0 \quad \forall x \in \mathcal{D}, x \neq 0$

then $x = 0$ is an Asymptotically Stable (AS) equilibrium for φ .

And if V: $\|x\| \rightarrow \infty \Rightarrow \mathcal{V}(x) \rightarrow \infty$

then $x = 0$ is a Globally Asymptotically Stable (GAS) equilibrium for φ .

An energy function is often found to be a suitable candidate for $\mathcal{V}(x)$, and it is often brought to the form $\mathcal{V}(\mathbf{x}) = \mathbf{x}^T \underline{\mathbf{Q}} \mathbf{x}$, where \mathbf{x} is the state vector and $\underline{\mathbf{Q}}$ is a constant matrix, which has the same definiteness as $\mathcal{V}(\mathbf{x})$.

When dealing with the NSO as a system it becomes apparent that it is not a pure autonomous mechanical system, as angular momentum is transferred to the internal momentum wheels. This implies that a complete stability analysis of the system using regular Lyapunov stability analysis is not feasible; however, certain assumptions can be made to remedy this. If the angular momentum of the non-rigid satellite system with momentum wheels is considered bounded and suppressed by a desaturation controller, the gyro effect from the residual constant angular momentum can be viewed as a constant disturbance on the satellite, even though it is exerted from the inside of the satellite. As introducing other disturbances on the satellite also will make the system non-autonomous, all disturbances are excluded. Analysing the Lyapunov stability of the complete system with momentum wheel effects, would require a hybrid system analysis approach, which is considered outside the scope of this report.

Angular Velocity System Stability

Considering the angular velocity part of the system as an autonomous system the Lyapunov candidate function is chosen to be the kinetic energy of the rotational motion of the rigid autonomous satellite system, which is defined as

$$\mathcal{V}(\mathbf{x}) = E(\boldsymbol{\omega}) = \frac{1}{2} \boldsymbol{\omega}^T \underline{\mathbf{I}}_{\text{sat}} \boldsymbol{\omega}, \quad (4.9)$$

where $\underline{\mathbf{I}}_{\text{sat}}$ and $\boldsymbol{\omega}$ are the inertia matrix and the angular velocity vector of the satellite respectively. No contribution is stated for the energy contribution of the momentum wheels, as the autonomous system is examined with the above assumptions. In order to incorporate the effects of the described control structure, the error state of the system, being the angular velocity reference given by the attitude controller subtracted from the actual state of the satellite system, is introduced. Thereby introducing the true state $\boldsymbol{\omega}_e = \boldsymbol{\omega} - \boldsymbol{\omega}_r$ and

differentiating (4.9), yields

$$\begin{aligned}
 \dot{E}(\boldsymbol{\omega}_e) &= \frac{1}{2} (\dot{\boldsymbol{\omega}}_e^T \underline{\mathbf{I}}_{\text{sat}} \boldsymbol{\omega}_e + \boldsymbol{\omega}_e^T \underline{\mathbf{I}}_{\text{sat}} \dot{\boldsymbol{\omega}}_e) \\
 &\Downarrow \text{using } \underline{\mathbf{I}}_{\text{sat}} = \underline{\mathbf{I}}_{\text{sat}}^T \\
 &= \frac{1}{2} (\dot{\boldsymbol{\omega}}_e^T \underline{\mathbf{I}}_{\text{sat}} \boldsymbol{\omega}_e + \dot{\boldsymbol{\omega}}_e^T \underline{\mathbf{I}}_{\text{sat}}^T \boldsymbol{\omega}_e) \\
 \dot{E}(\boldsymbol{\omega}_e) &= \dot{\boldsymbol{\omega}}_e^T \underline{\mathbf{I}}_{\text{sat}} \boldsymbol{\omega}_e. \tag{4.10}
 \end{aligned}$$

By inserting the non-linear dynamics of the satellite, w.r.t. the angular velocity, as found in (2.31), into (4.10) and disregarding the effects of disturbances and magnetorquers, the statement becomes

$$\begin{aligned}
 \dot{E}(\boldsymbol{\omega}_e) &= (\underline{\mathbf{I}}_{\text{sat}}^{-1} (-\mathbf{N}_{\text{mw}} - \underline{\mathbf{S}}(\boldsymbol{\omega}_e)(\underline{\mathbf{I}}_{\text{sat}} \boldsymbol{\omega}_e + \mathbf{h}_{\text{mw}})))^T \underline{\mathbf{I}}_{\text{sat}} \boldsymbol{\omega}_e \\
 &= (-\mathbf{N}_{\text{mw}} - \underline{\mathbf{S}}(\boldsymbol{\omega}_e)(\underline{\mathbf{I}}_{\text{sat}} \boldsymbol{\omega}_e + \mathbf{h}_{\text{mw}}))^T (\underline{\mathbf{I}}_{\text{sat}}^{-1})^T \underline{\mathbf{I}}_{\text{sat}} \boldsymbol{\omega}_e \\
 &= (-\mathbf{N}_{\text{mw}}^T - (\underline{\mathbf{S}}(\boldsymbol{\omega}_e) \underline{\mathbf{I}}_{\text{sat}} \boldsymbol{\omega}_e)^T - (\underline{\mathbf{S}}(\boldsymbol{\omega}_e) \mathbf{h}_{\text{mw}})^T) \boldsymbol{\omega}_e \\
 &= -\mathbf{N}_{\text{mw}}^T \boldsymbol{\omega}_e - (\underline{\mathbf{I}}_{\text{sat}} \boldsymbol{\omega}_e)^T \underline{\mathbf{S}}(\boldsymbol{\omega}_e)^T \boldsymbol{\omega}_e - \mathbf{h}_{\text{mw}}^T \underline{\mathbf{S}}(\boldsymbol{\omega}_e)^T \boldsymbol{\omega}_e \\
 &\Downarrow \text{using } \underline{\mathbf{S}}(\boldsymbol{\omega}_e)^T = -\underline{\mathbf{S}}(\boldsymbol{\omega}_e) \\
 \dot{E}(\boldsymbol{\omega}_e) &= -\mathbf{N}_{\text{mw}}^T \boldsymbol{\omega}_e + (\underline{\mathbf{I}}_{\text{sat}} \boldsymbol{\omega}_e)^T \underbrace{\underline{\mathbf{S}}(\boldsymbol{\omega}_e) \boldsymbol{\omega}_e}_0 + \mathbf{h}_{\text{mw}}^T \underbrace{\underline{\mathbf{S}}(\boldsymbol{\omega}_e) \boldsymbol{\omega}_e}_0 \\
 &= -\mathbf{N}_{\text{mw}}^T \boldsymbol{\omega}_e. \tag{4.11}
 \end{aligned}$$

Subsequently, it is now possible to prove stability of the system by inserting the desired control law in place of \mathbf{N}_{mw} , although, failing to prove stability does not necessarily imply instability. If a proportional controller with positive feedback is used in a full state feedback control law, (4.11) becomes

$$\begin{aligned}
 \dot{E}(\boldsymbol{\omega}_e) &= -(\underline{\mathbf{K}}_{\text{ang}} \boldsymbol{\omega}_e)^T \boldsymbol{\omega}_e \\
 &= -\boldsymbol{\omega}_e^T \underline{\mathbf{K}}_{\text{ang}}^T \boldsymbol{\omega}_e, \tag{4.12}
 \end{aligned}$$

where $\underline{\mathbf{K}}_{\text{ang}}$ is the proportional gain feedback matrix on the angular velocity. Thus, if $\underline{\mathbf{K}}_{\text{ang}}$ is positive definite then \dot{E} is negative definite, which, together with the fact that $E(\mathbf{0}) = \frac{1}{2} \mathbf{0}^T \underline{\mathbf{I}}_{\text{sat}} \mathbf{0} = 0$, proves that the closed loop satellite system is AS in a vicinity around $\boldsymbol{\omega}_e = \mathbf{0}$. Examining (4.12) and (4.9) it is also apparent that for $\|\boldsymbol{\omega}_e\| \rightarrow \infty$ the function $E(\boldsymbol{\omega}_e) \rightarrow \infty$ and $\dot{E}(\boldsymbol{\omega}_e) < 0$, which proves that the satellite system is also GAS in $\boldsymbol{\omega}_e = \mathbf{0}$.

Having proven stability for the described autonomous system, it shall now be mentioned that some jitter might occur in the equilibrium. This is ascribed to the non-rigid nature of the disturbances and internal angular momentum bias on the momentum wheels, which gyroscopic effect will force the satellite to rotate the angular momentum vector perpendicular to the orbital plane. So unless the satellite attitude is exactly prescribed in such a manner that this is fulfilled, the internal disturbance from the momentum wheels will effect the satellite in the equilibrium.

The stability of the satellite system with a controller with the prescribed definiteness, is perhaps best illustrated by a 3D-plot of the satellite angular velocity, as in Figure 4.8. Here the angular velocity system is controlled by a simple state feedback controller, and it can be seen that the angular velocity is driven towards zero in a spiraling trajectory.

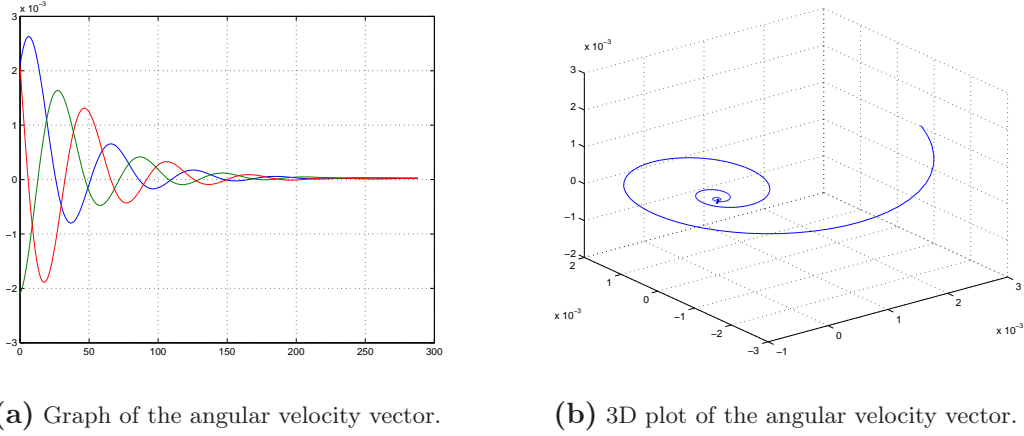


Figure 4.8: The angular velocity system controlled by a simple untuned state feedback positive definite controller gain matrix. Notice the spiraling tendency, where the trajectory converges towards the equilibrium.

Attitude System Stability

Now if a proportional controller is used for stabilizing the system in $\dot{\mathbf{q}}$ it is futile to examine the stability of this system, as the dynamic equation of the system will be on the form

$$\dot{\mathbf{q}} = \frac{1}{2} \underline{\Omega}(\omega) \underline{\mathbf{K}}_{\text{att}} \mathbf{q}, \quad (4.13)$$

where $\underline{\mathbf{K}}_{\text{att}}$ is a proportional gain feedback matrix on the attitude and $\underline{\Omega}(\omega)$ is a skew matrix dependent on the angular velocity of the satellite.

As long as $\underline{\Omega}(\omega)$ is not zero the change in attitude will be evident. However, as it has just been shown in (4.12), the angular velocity will be driven towards zero, and thus the skew matrix $\underline{\Omega}(\omega) \rightarrow \mathbf{0}$. This, in turn, will always decrease $\dot{\mathbf{q}}$ and the attitude will stabilise, leaving the satellite to point in the same direction in space. Although, the satellite attitude will be subject to the same jitter caused by disturbances, as previously described for the satellite angular velocity.

CHAPTER 5

Angular Velocity Controller

This chapter describes the design of the angular velocity controller, which task is to reject disturbance torques and handle uncertainties in the inertia matrix. The angular velocity controller is an essential part of the attitude control system and this chapter is, therefore, considered an essential part of this report.

The model analysis performed in Chapter 4 states requirements that must be considered in the design of the angular velocity controller. In Section 4.1 the maximum closed loop bandwidth of the angular velocity controller is specified to 0.2 [Hz]. The stability requirement to the closed loop system using state feedback was examined in Section 4.3, and requires the state feedback matrix, \mathbf{K}_{ang} , to be positive definite. The angular velocity controller should also follow a reference, $\boldsymbol{\omega}_r$, i.e., the control error, $\boldsymbol{\omega}_e = \boldsymbol{\omega} - \boldsymbol{\omega}_r$, should be minimised even in a case where external disturbance torques are present. Furthermore, some of the parameters in the linear satellite dynamics cannot be determined exactly and/or are subject to uncertainties due to the linearisation. The controller is, therefore, also required to be able to handle these uncertainties and input disturbances.

5.1 Control Structure

The preluding requirements suggest designing a robust controller that can handle both the input disturbances, i.e., the external disturbance torques, and the parametric uncertainties due to the imperfect knowledge of the system. However, as the disturbance torques are large, it is likely to yield a slow response of the closed loop system, since the controller is not allowed to be aggressively tuned. To avoid this, and decouple the effects of the external disturbance torques, the angular velocity controller is divided into a disturbance estimator and a robust controller, handling parametric uncertainties and the residual disturbance torques from the estimation error. The described control structure is depicted in Figure 5.1.

The estimated total disturbance torque is fed forward to attenuate the input disturbance to the satellite. According to [Peck 2003] the inertia matrix is difficult to measure or calculate, even when the satellite has been fully integrated. The parameter uncertainty considered in this report will, therefore, be inertia matrix components, which will be included in the robust controller design. The disturbance estimator and robust controller will be designed separately in the following two sections.

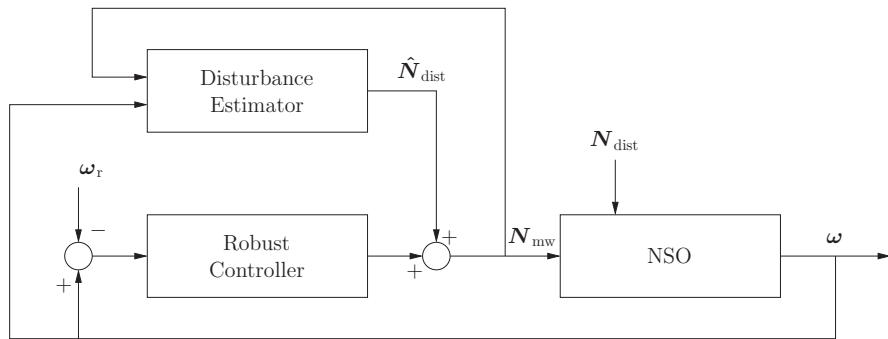


Figure 5.1: Block diagram of the angular velocity controller with estimation and feedforward of the external disturbance torques.

5.2 Disturbance Estimation

Estimation of the total disturbance torque is based on the angular velocity system from Section 4.2.1 and the fact that the total disturbance torque changes slowly. The environmental disturbance torque will, from a satellite point of view, change with the orbital rate when assuming a constant attitude, as can be derived in Section 2.3. The total torque can, therefore, be modeled as constant bias in the control torque, i.e., $\dot{\mathbf{N}}_{\text{dist}} = \mathbf{0}$. This yields an estimation of the disturbance torque, which is not dependent on the disturbance models. Thus, the model parameters, such as the air density, which has a large uncertainty as explained in Section 2.3.1, will not affect the estimation and no on-board disturbance models are required. The system considered in the disturbance estimation is defined as

$$\begin{bmatrix} \dot{\omega} \\ N_{\text{dist}} \end{bmatrix} = \begin{bmatrix} \mathbf{I}_{\text{sat}}^{-1} \mathbf{S}(\bar{h}_{\text{mw}}) & \mathbf{I}_{\text{sat}}^{-1} \\ \mathbf{0}_{3 \times 3} & \mathbf{0}_{3 \times 3} \end{bmatrix} \begin{bmatrix} \omega \\ N_{\text{dist}} \end{bmatrix} + \begin{bmatrix} -\mathbf{I}_{\text{sat}}^{-1} \\ \mathbf{0}_{3 \times 3} \end{bmatrix} N_{\text{mw}}, \quad (5.1)$$

where ω is the angular velocity of the satellite and N_{dist} and N_{mw} are the disturbance torque and the control torque from the momentum wheels respectively. The estimated total disturbance torque is fed forward to the momentum wheel control input to attenuate the input disturbance.

It is chosen to implement the disturbance estimation in a Kalman filter using the system in (5.1). The Kalman filter is depicted in Figure 5.2, and is further explained in Appendix J. The Kalman filter consists of a predictor step and a corrector step. The predictor predicts the next state, which is then corrected using the Kalman gain in the corrector.

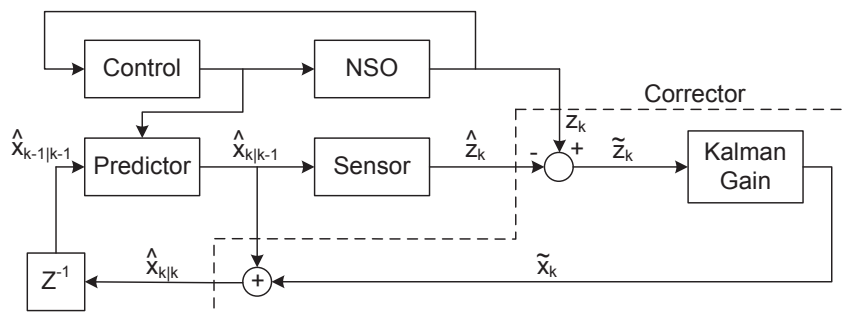


Figure 5.2: Block diagram of a Kalman filter.

The Kalman gain is calculated using the noise description of the measurement and the process, $\underline{\mathbf{R}}_{\text{ang}}$ and $\underline{\mathbf{Q}}_{\text{ang}}$ respectively. The noise descriptions are determined empirically, as $\underline{\mathbf{R}}_{\text{ang}} = 10^{-12} \cdot \mathbf{1}_{3 \times 3}$, and $\underline{\mathbf{Q}}_{\text{ang}} = 5 \cdot 10^{-15} \cdot \mathbf{1}_{6 \times 6}$ is defined, such that the system model is trusted more than the measurement, thus allowing a slow change in the state estimates. The Kalman filter is implemented using the function, `kalman(sys_ang,Q,R)` in MATLAB, and the implementation can be found in `kalman_estimator.m`.

An evaluation of the filter, presented in Appendix K, indicated that the mean estimation error is $31.2 \cdot 10^{-9}$ [Nm] and the standard deviation is $50.2 \cdot 10^{-9}$ [Nm], which corresponds to 2 [%] of the worst case disturbance torque, thus providing that the derived effect of the Kalman filter is achieved. The estimation error of a random simulation is depicted in Figure 5.3. The oscillations is assumed to be caused by the angular momentum bias in the momentum wheels.

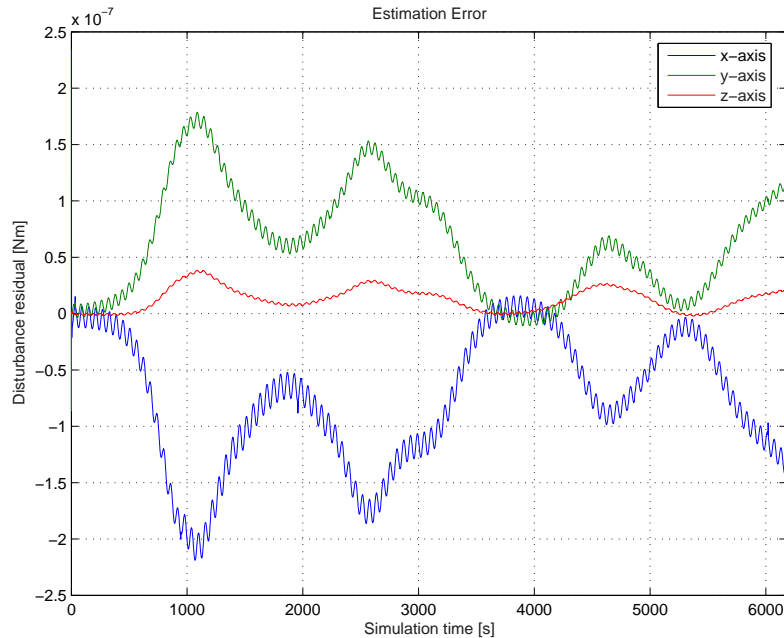


Figure 5.3: The estimation error between the modeled disturbance torque and the estimated torque, during one of the simulations. The small oscillations are assumed to be caused by the momentum wheel bias.

5.3 Robust Control

The estimation of the disturbance torques does yield a small residual error as described in the previous section. Therefore, the angular controller should be able to handle the remaining input disturbance. Furthermore, it is difficult to achieve precise knowledge of all the parameters in the model, which the controller should also be able to handle.

Figure 5.4 depicts a general control structure for an uncertainty system, where the system, $\underline{\mathbf{S}}$, is denoted the generalised plant and contains the nominal system. The uncertainties in the model are lumped into one uncertainty system, $\Delta_{\mathbf{S}}$, which combined with $\underline{\mathbf{S}}$ forms the perturbed system, $\underline{\mathbf{S}}_{\Delta}$.

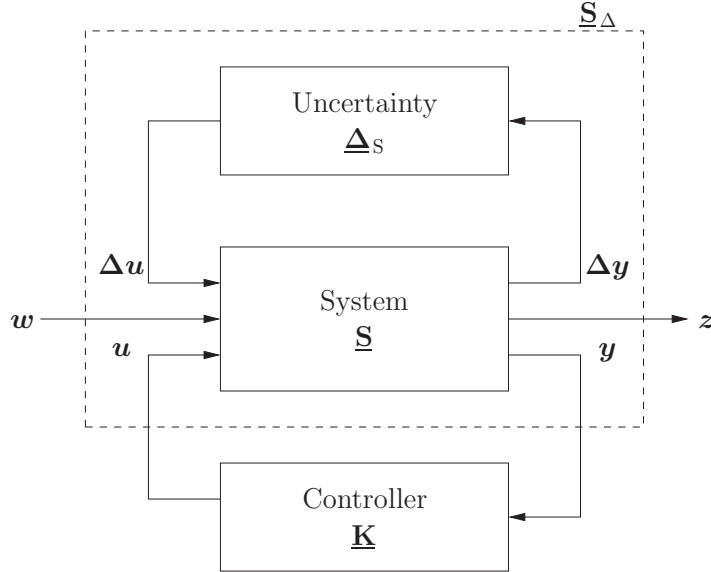


Figure 5.4: General control structure for cases with model uncertainties.

The objective of robust control is to find a controller, $\underline{\mathbf{K}}$, that minimises a norm of the transfer function from \mathbf{w} to \mathbf{z} [Postlethwaite 2005]. Partitioning the generalised system as

$$\underline{\mathbf{S}} = \begin{bmatrix} \underline{\mathbf{S}}_{11} & \underline{\mathbf{S}}_{12} \\ \underline{\mathbf{S}}_{21} & \underline{\mathbf{S}}_{22} \end{bmatrix}, \quad (5.2)$$

yields the transfer functions

$$\mathbf{z} = \underline{\mathbf{S}}_{11}\mathbf{w} + \underline{\mathbf{S}}_{12}\mathbf{u} \quad (5.3)$$

$$\mathbf{y} = \underline{\mathbf{S}}_{21}\mathbf{w} + \underline{\mathbf{S}}_{22}\mathbf{u}, \quad (5.4)$$

which, combined with the controller equation,

$$\mathbf{u} = \underline{\mathbf{K}}\mathbf{y}, \quad (5.5)$$

specify the closed loop from \mathbf{w} to \mathbf{z} . Inserting (5.5) in (5.4) yields

$$\begin{aligned} \mathbf{y} &= \underline{\mathbf{S}}_{21}\mathbf{w} + \underline{\mathbf{S}}_{22}\underline{\mathbf{K}}\mathbf{y} \Leftrightarrow \\ \mathbf{y} - \underline{\mathbf{S}}_{22}\underline{\mathbf{K}}\mathbf{y} &= \underline{\mathbf{S}}_{21}\mathbf{w} \Leftrightarrow \\ (\mathbf{1} - \underline{\mathbf{S}}_{22}\underline{\mathbf{K}})\mathbf{y} &= \underline{\mathbf{S}}_{21}\mathbf{w} \Leftrightarrow \\ \mathbf{y} &= (\mathbf{1} - \underline{\mathbf{S}}_{22}\underline{\mathbf{K}})^{-1}\underline{\mathbf{S}}_{21}\mathbf{w} \end{aligned} \quad (5.6)$$

Inserting (5.6) and (5.5) in (5.3) yields

$$\begin{aligned} \mathbf{z} &= \underline{\mathbf{S}}_{11}\mathbf{w} + \underline{\mathbf{S}}_{12}\underline{\mathbf{K}}(\mathbf{1} - \underline{\mathbf{S}}_{22}\underline{\mathbf{K}})^{-1}\underline{\mathbf{S}}_{21}\mathbf{w} \\ \mathbf{z} &= \underbrace{\left(\underline{\mathbf{S}}_{11} + \underline{\mathbf{S}}_{12}\underline{\mathbf{K}}(\mathbf{1} - \underline{\mathbf{S}}_{22}\underline{\mathbf{K}})^{-1}\underline{\mathbf{S}}_{21} \right)}_{\underline{\mathbf{F}}_l(\underline{\mathbf{S}}, \underline{\mathbf{K}})} \mathbf{w}. \end{aligned} \quad (5.7)$$

Here $\underline{\mathbf{F}}_l(\underline{\mathbf{S}}, \underline{\mathbf{K}})$ is denoted the lower linear fractional transformation (LFT) of $\underline{\mathbf{S}}$, with $\underline{\mathbf{K}}$ being a parameter. Using \mathcal{H}_∞ controller synthesis, which minimises the transfer function

from \mathbf{w} to \mathbf{z} w.r.t. the largest singular value [Clausen, Andersen & Stoustrup 1998, page 64], yields the minimisation problem

$$\min \|\underline{\mathbf{F}}_l(P, K)\|_\infty. \quad (5.8)$$

Several methods for solving this problem exists and in this report an LMI based solution will be used, as the description of the uncertainty system is implemented in an intuitive and manageable manner.

5.3.1 Linear Matrix Inequalities

A Linear Matrix Inequality (LMI) is a mathematical expression that advantageously can be used in analysis and control theory applications on dynamical systems, and has appeared to be an efficient way to formulate a controller synthesis. On these grounds the development of a robust controller for the angular velocity will be synthesised using LMIs, which is why the following introduction to LMIs is given with a basis in [Stepen Boyd, Laurent El Ghaoui, Eric Feron & Venkataraman Balakrisnan 1994].

The history of LMIs in the analysis of dynamical systems reaches back to about 1890, when Lyapunov published his seminal work, introducing what is now called Lyapunov theory. He showed that the differential equation $\frac{d}{dt}\mathbf{x}(t) = \underline{\mathbf{A}}\mathbf{x}(t)$ is stable, i.e., all trajectories converge to zero, if and only if there exists a positive definite matrix $\underline{\mathbf{P}}$, such that

$$\underline{\mathbf{A}}^T \underline{\mathbf{P}} + \underline{\mathbf{P}} \underline{\mathbf{A}} \prec 0. \quad (5.9)$$

The requirement $\underline{\mathbf{P}} \succ 0$, $\underline{\mathbf{A}}^T \underline{\mathbf{P}} + \underline{\mathbf{P}} \underline{\mathbf{A}} \prec 0$ ¹ is called the Lyapunov inequality on $\underline{\mathbf{P}}$, which is a special form of an LMI. Lyapunov also showed that this first LMI could be explicitly solved. Indeed, for any $\underline{\mathbf{Q}} = \underline{\mathbf{Q}}^T \succ 0$ the solution on $\underline{\mathbf{P}}$, to the linear equation $\underline{\mathbf{A}}^T \underline{\mathbf{P}} + \underline{\mathbf{P}} \underline{\mathbf{A}} = -\underline{\mathbf{Q}}$, guarantees $\underline{\mathbf{P}}$ to be positive definite if the system is stable. In summary, the first LMI used to analyse stability of a dynamical system, was the Lyapunov inequality (5.9), which can be solved analytically (by solving a set of linear equations) by hand, as subsequent LMIs were. This limited their application to small (second, third order) systems. Later it was discovered that the LMIs could be solved not only by analytical means, but also by solving certain Algebraic Riccati Equations (ARE). This in turn lead to the discovery that LMIs had some advantages in computational algorithms, as opposed to the corresponding Riccati equations, as they could be formulated as convex optimisation problems, that vastly eased finding solutions using computer technology. The development of powerful and efficient interior-point methods has made obtaining a solution to the LMIs, that arise in system and control theory, an easier task, and thus LMIs are now a suitable choice for formulations of complex control issues.

An LMI has the form

$$\underline{\mathbf{F}}(\mathbf{x}) \triangleq \underline{\mathbf{F}}_0 + \sum_{i=1}^m x_i \underline{\mathbf{F}}_i \succ 0, \quad (5.10)$$

where $\mathbf{x} \in \mathbb{R}^m$ is the variable and the symmetric matrices $\underline{\mathbf{F}}_i = \underline{\mathbf{F}}_i^T \in \mathbb{R}^{n \times n}$, $i = 0, \dots, m$, are known. The LMI in (5.10) is a convex constraint on \mathbf{x} , i.e., the set $\{\mathbf{x} \mid \underline{\mathbf{F}}(\mathbf{x}) \succ 0\}$ is convex. Although the LMI in (5.10) may seem to have a specialised form, it can represent a wide variety of convex constraints on \mathbf{x} . In particular, linear inequalities, matrix norm

¹ \prec refers to definiteness. See the nomenclature on page 167.

inequalities, and constraints that arise in control theory, such as Lyapunov and convex quadratic matrix inequalities, can all be cast in the form of an LMI.

Furthermore, multiple LMIs, $\underline{\mathbf{F}}^{(1)}(\mathbf{x}) \succ 0, \dots, \underline{\mathbf{F}}^{(p)}(\mathbf{x}) \succ 0$, can be expressed in a single LMI, as

$$\begin{aligned} \text{blockdiagonal}(\underline{\mathbf{F}}^{(1)}(\mathbf{x}) \succ 0, \dots, \underline{\mathbf{F}}^{(p)}(\mathbf{x}) \succ 0) &= \\ \left[\begin{array}{cccc} \underline{\mathbf{F}}^{(1)}(\mathbf{x}) & \underline{\mathbf{0}} & \dots & \underline{\mathbf{0}} \\ \underline{\mathbf{0}} & \underline{\mathbf{F}}^{(2)}(\mathbf{x}) & \dots & \underline{\mathbf{0}} \\ \vdots & \vdots & \ddots & \underline{\mathbf{0}} \\ \underline{\mathbf{0}} & \dots & \dots & \underline{\mathbf{F}}^{(p)}(\mathbf{x}) \end{array} \right] &\succ 0. \end{aligned} \quad (5.11)$$

Therefore, no distinction will be made between a set of LMIs and a single LMI. When the matrices $\underline{\mathbf{F}}_i$ are diagonal, the LMI $\underline{\mathbf{F}}(\mathbf{x}) \succ 0$ is just a set of linear inequalities.

5.3.2 LMI Formulation for Robust Feedback Control

To formulate the requirement of robustness to uncertainties, but also the requirement to suppress the effects of input disturbances, the focus is turned to the work done by [Zhou, Khargonekar, Stostrup & Niemann 1995], where linear time-invariant systems with real time-varying parameter uncertainties in compact intervals are considered. The main results they presented, showed that both analysis and state feedback synthesis problems, can be reduced to a finite-dimensional convex programming problem. In essence, *Theorem 4* in [Zhou et al. 1995] states that considering the uncertain system

$$\begin{aligned} \dot{\mathbf{x}} &= \underline{\mathbf{A}}_{\Delta}\mathbf{x} + \underline{\mathbf{B}}_{\Delta}\mathbf{w} + \underline{\mathbf{B}}_{2\Delta}\mathbf{u}, \quad \Delta \in \underline{\Delta} \\ \mathbf{z} &= \underline{\mathbf{C}}_{\Delta}\mathbf{x} + \underline{\mathbf{D}}_{\Delta}\mathbf{w} + \underline{\mathbf{D}}_{2\Delta}\mathbf{u} \\ \mathbf{y} &= \mathbf{x}, \end{aligned} \quad (5.12)$$

and supposing that there exists a dynamic state feedback controller $\mathbf{u} = \underline{\mathbf{F}}(s)\mathbf{y}$, such that the closed loop system satisfies the strongly robust \mathcal{H}_{∞} performance criterion. Then there exists a real matrix $\underline{\mathbf{K}}$, such that, with the static controller $\mathbf{u} = \underline{\mathbf{K}}\mathbf{y}$, the closed loop system satisfies the strongly robust \mathcal{H}_{∞} performance criterion. This necessarily implies that the system is quadratically (Lyapunov) stable. The matrix $\underline{\Delta}$ denotes the real-time varying uncertainty region given by

$$\underline{\Delta} = \{\text{blockdiagonal}([\delta_1(t)\underline{\mathbf{1}}_{k_1}, \dots, \delta_m(t)\underline{\mathbf{1}}_{k_m}]) : \delta_i(t) \in [\delta_{i_{\min}}, \delta_{i_{\max}}]\}\}. \quad (5.13)$$

The vertex set of $\underline{\Delta}$ is denoted

$$\underline{\Delta}_{\text{vex}} = \{\text{blockdiagonal}([\delta_1\underline{\mathbf{1}}_{k_1}, \dots, \delta_m\underline{\mathbf{1}}_{k_m}]) : \delta_i = \delta_{i_{\min}} \vee \delta_i = \delta_{i_{\max}}\}, \quad (5.14)$$

where it can be noticed that there are 2^m vertices in $\underline{\Delta}_{\text{vex}}$.

Using *Theorem 9* in [Zhou et al. 1995], it is possible to formulate the requirements into an LMI. *Theorem 9* states that there exists a state feedback controller, such that the closed loop system in (5.12) satisfies the strongly robust \mathcal{H}_{∞} performance criterion, if and only if $\underline{\mathbf{R}}_{\Delta} \triangleq \underline{\mathbf{1}} - \underline{\mathbf{D}}_{\Delta}^T \underline{\mathbf{D}}_{\Delta} \succ 0, \forall \Delta \in \underline{\Delta}_{\text{vex}}$ and there exists a matrix $\underline{\mathbf{W}}$ and a matrix

$\underline{\mathbf{Y}} = \underline{\mathbf{Y}}^T \succ 0$, such that

$$\begin{bmatrix} \underline{\mathbf{Y}}\underline{\mathbf{A}}_{\Delta}^T + \underline{\mathbf{A}}_{\Delta}\underline{\mathbf{Y}} + \underline{\mathbf{W}}^T\underline{\mathbf{B}}_{2\Delta}^T + \underline{\mathbf{B}}_{2\Delta}\underline{\mathbf{W}} & \underline{\mathbf{B}}_{\Delta} + \underline{\mathbf{Y}}\underline{\mathbf{C}}_{\Delta}^T\underline{\mathbf{D}}_{\Delta} + \underline{\mathbf{W}}^T\underline{\mathbf{D}}_{2\Delta}^T\underline{\mathbf{D}}_{\Delta} & \underline{\mathbf{Y}}\underline{\mathbf{C}}_{\Delta}^T + \underline{\mathbf{W}}^T\underline{\mathbf{D}}_{2\Delta}^T \\ \underline{\mathbf{B}}_{\Delta}^T + \underline{\mathbf{D}}_{\Delta}^T\underline{\mathbf{C}}_{\Delta}\underline{\mathbf{Y}} + \underline{\mathbf{D}}_{\Delta}^T\underline{\mathbf{D}}_{2\Delta}\underline{\mathbf{W}} & -\underline{\mathbf{R}}_{\Delta} & \underline{\mathbf{0}} \\ \underline{\mathbf{C}}_{\Delta}\underline{\mathbf{Y}} + \underline{\mathbf{D}}_{2\Delta}\underline{\mathbf{W}} & \underline{\mathbf{0}} & -\underline{\mathbf{1}} \end{bmatrix} \prec 0$$

$\forall \Delta \in \underline{\Delta}_{\text{vex}}$. (5.15)

Moreover, the feedback controller can be found as a constant gain by

$$\underline{\mathbf{K}} = \underline{\mathbf{W}}\underline{\mathbf{Y}}^{-1}. (5.16)$$

The condition $\underline{\mathbf{R}}_{\Delta} \succ 0$ ensures that the direct feed-through of the disturbances is less than one, i.e., $\|\underline{\mathbf{D}}_{\Delta}\| < 1$.

Using *Theorem 9* will ensure the stability and strongly robust performance of the uncertain disturbed angular velocity system. However, a requirement for the closed loop system is, furthermore, that the system should have a restricted bandwidth. This can be ensured by restraining the real part of the closed loop left half plane poles to be no less than a certain limit, η . This is achieved by including another constraint in the LMI in (5.15).

According to [Chilali & Gahinet 1996, eq. (18)] bounding eigenvalues in a matrix $\underline{\mathbf{A}}$ to lie above a specified lower limit, as depicted in Figure 5.5, can be expressed in an LMI as

$$2\eta\underline{\mathbf{P}} - \underline{\mathbf{A}}^T\underline{\mathbf{P}} - \underline{\mathbf{P}}\underline{\mathbf{A}} \prec 0, (5.17)$$

where η is the boundary distance from the imaginary axis along the negative real axis, if and only if there exists a symmetric matrix $\underline{\mathbf{P}} \succ 0 \in \mathbb{R}^{n \times n}$. It is desired, instead of bounding the eigenvalues in the matrix $\underline{\mathbf{A}}$, to bound the poles in the closed loop system, whereby the matrix $\underline{\mathbf{A}}$ is substituted with the dynamics of the closed loop, i.e., $\underline{\mathbf{A}} = \underline{\mathbf{A}}_{\Delta} + \underline{\mathbf{B}}_{2\Delta}\underline{\mathbf{K}}$. Substituting $\underline{\mathbf{A}}$ yields

$$\begin{aligned} 2\eta\underline{\mathbf{P}} - (\underline{\mathbf{A}}_{\Delta} + \underline{\mathbf{B}}_{2\Delta}\underline{\mathbf{K}})^T\underline{\mathbf{P}} - \underline{\mathbf{P}}(\underline{\mathbf{A}}_{\Delta} + \underline{\mathbf{B}}_{2\Delta}\underline{\mathbf{K}}) &\prec 0 \\ \Updownarrow \\ 2\eta\underline{\mathbf{P}} - \underline{\mathbf{A}}_{\Delta}^T\underline{\mathbf{P}} - \underline{\mathbf{K}}^T\underline{\mathbf{B}}_{2\Delta}^T\underline{\mathbf{P}} - \underline{\mathbf{P}}\underline{\mathbf{A}}_{\Delta} - \underline{\mathbf{P}}\underline{\mathbf{B}}_{2\Delta}\underline{\mathbf{K}} &\prec 0. \end{aligned} (5.18)$$

This problem is not in LMI form, due to the terms which contain the products of $\underline{\mathbf{K}}$ and $\underline{\mathbf{P}}$. These terms are non-linear, and as they are products of two variables, they are said to be bi-linear. Multiplying with $\underline{\mathbf{P}}^{-1}$ in (5.18), and using $\underline{\mathbf{Y}} \triangleq \underline{\mathbf{P}}^{-1}$, yields

$$\begin{aligned} \underline{\mathbf{P}}^{-1}(2\eta\underline{\mathbf{P}} - \underline{\mathbf{A}}_{\Delta}^T\underline{\mathbf{P}} - \underline{\mathbf{K}}^T\underline{\mathbf{B}}_{2\Delta}^T\underline{\mathbf{P}} - \underline{\mathbf{P}}\underline{\mathbf{A}}_{\Delta} - \underline{\mathbf{P}}\underline{\mathbf{B}}_{2\Delta}\underline{\mathbf{K}})\underline{\mathbf{P}}^{-1} &\prec 0 \\ \Updownarrow \\ 2\eta\underline{\mathbf{Y}} - \underline{\mathbf{Y}}\underline{\mathbf{A}}_{\Delta}^T - \underline{\mathbf{Y}}\underline{\mathbf{K}}^T\underline{\mathbf{B}}_{2\Delta}^T - \underline{\mathbf{A}}_{\Delta}\underline{\mathbf{Y}} - \underline{\mathbf{B}}_{2\Delta}\underline{\mathbf{K}}\underline{\mathbf{Y}} &\prec 0, \end{aligned} (5.19)$$

which is a new matrix inequality dependent on the variables $\underline{\mathbf{Y}} \succ 0$ and $\underline{\mathbf{K}}$, but still non-linear. Defining $\underline{\mathbf{W}} = \underline{\mathbf{K}}\underline{\mathbf{Y}}$ remedies this, as (5.19) becomes an LMI described by

$$2\eta\underline{\mathbf{Y}} - \underline{\mathbf{Y}}\underline{\mathbf{A}}_{\Delta}^T - \underline{\mathbf{W}}^T\underline{\mathbf{B}}_{2\Delta}^T - \underline{\mathbf{A}}_{\Delta}\underline{\mathbf{Y}} - \underline{\mathbf{B}}_{2\Delta}\underline{\mathbf{W}} \prec 0. (5.20)$$

Thus an LMI feasibility problem² has been obtained in the new variables $\underline{\mathbf{Y}} \succ 0$ and $\underline{\mathbf{W}} \in \mathbb{R}^{m \times n}$. This can now be augmented to the LMI in (5.15), yielding an LMI formulation

²Problems for which a solution is sought, which might not be unique or optimal.

ensuring both strongly robust \mathcal{H}_∞ performance and a bounded bandwidth, by restricting the variables in (5.15). Since $\underline{\mathbf{Y}}^T = \underline{\mathbf{Y}}$ the feedback matrix, $\underline{\mathbf{K}}$, can now be recovered analogously to (5.16) by

$$\underline{\mathbf{W}} = \underline{\mathbf{K}} \underline{\mathbf{Y}} \Rightarrow \underline{\mathbf{K}} = \underline{\mathbf{W}} \underline{\mathbf{Y}}^{-1}. \quad (5.21)$$

Bounding the poles to lie to the left of the imaginary axis is still handled by the LMI in (5.15).

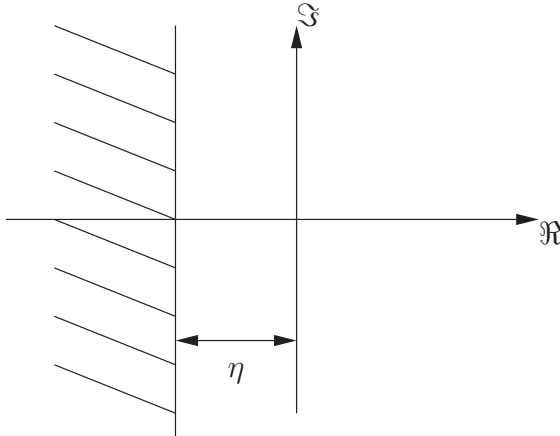


Figure 5.5: Illustration of the desired pole placement boundary for the closed loop system, which is used in the LMI design. The hatched area describes the area in which no poles must be placed.

An LMI feasibility problem, ensuring the bandwidth bounded closed loop stability and performance of an uncertain disturbed system, has now been formulated. Referring to Section 5.3.1 it is now possible to include several uncertain systems in one collective LMI. As the entire uncertainty region is defined as $\underline{\Delta}$, and is linear, it is possible to ensure the inclusion of all uncertainties in the uncertainty region, by simply defining a collective LMI containing an LMI for each of the vertices in $\underline{\Delta}_{\text{vex}}$ in the diagonal.

5.3.3 Angular Controller Design

To design an angular velocity controller, the angular velocity system described in Section 4.2.1 is considered and appended with uncertainties and disturbances, in accordance with the uncertainty system described in (5.12). As stated earlier the disturbance, considered in this report, is the environmental disturbance torque residual, which enters the system in a similar manner as the control torques, i.e., the only difference is a change of sign

$$\underline{\mathbf{B}}_{\text{dist}} = -\underline{\mathbf{B}}_{\text{ctrl}}. \quad (5.22)$$

The uncertainty considered is imprecise knowledge of the values in the diagonal of the inertia matrix, which is estimated to vary $\pm 5\%$, i.e.,

$$\underline{\mathbf{I}}_\Delta = \underline{\mathbf{I}}_{\text{sat}} \pm 0.05 \cdot \underline{\mathbf{I}}_{\text{sat}}. \quad (5.23)$$

This is a simplification as realistic uncertainties in the inertia of the satellite would yield a cross correlation in the inertia matrix. However, for reasons of simplicity (5.23) is used.

The objective of the controller is to minimise the angular velocity of the satellite, such that it is possible to obtain pictures of the North Sea. As the camera is located on the z-axis, rotation around the z-axis is not as critical as around the x and y-axes. Therefore, z is chosen to be ω_1 and ω_2 , yielding the uncertainty system

$$\dot{\omega} = \underbrace{\underline{I}_\Delta \underline{S}(\bar{h}_{mw})}_{\underline{A}_\Delta} \omega + \underbrace{\underline{I}_\Delta}_{\underline{B}_\Delta} N_{dist} - \underbrace{\underline{I}_\Delta}_{\underline{B}_{2\Delta}} N_{mw} \quad (5.24)$$

$$z = \underbrace{\begin{bmatrix} \underline{1}_{2 \times 2} & \underline{0}_{2 \times 1} \end{bmatrix}}_{\underline{C}_\Delta} \omega + \underbrace{\underline{0}_{2 \times 3}}_{\underline{D}_\Delta} N_{dist} + \underbrace{\underline{0}_{2 \times 3}}_{\underline{D}_{2\Delta}} N_{mw}, \quad (5.25)$$

which is exactly on the form presented in (5.12).

YALMIP is used to formulate the LMI presented in the previous section, for all of the vertices in Δ_{vex} . The problem is solved using SeDuMi, which is a solver used by YALMIP. As the inertia matrix contains three parameters, the uncertainty region will become a box as illustrated in Figure 5.6.

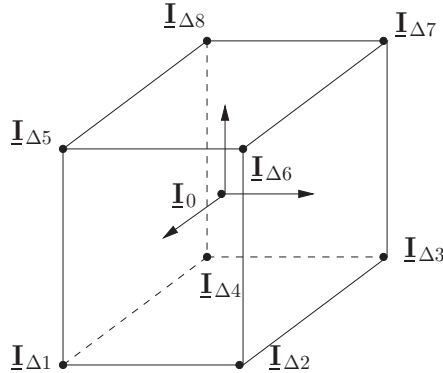


Figure 5.6: Uncertainty region when three parameters are considered.

The LMI used assumes the objective is to obtain a \mathcal{H}_∞ norm less than one, but it is desirable to define a value, γ , such that the \mathcal{H}_∞ norm is less than γ , and then iterate to obtain the smallest possible \mathcal{H}_∞ norm, yielding a near optimal solution of the LMI feasibility problem. This is incorporated by considering $\|\underline{\mathbf{F}}_l(\underline{\mathbf{P}}, \underline{\mathbf{K}})\|_\infty$, which yields

$$\begin{aligned} \|\underline{\mathbf{F}}_l(\underline{\mathbf{P}}, \underline{\mathbf{K}})\|_\infty &< \gamma \\ \left\| \frac{1}{\gamma} \underline{\mathbf{F}}_l(\underline{\mathbf{P}}, \underline{\mathbf{K}}) \right\|_\infty &< 1 \end{aligned} \quad (5.26)$$

Combining this with the system defined in (5.25), yields a scaling of \underline{B}_Δ with $\frac{1}{\gamma}$. From an iterative process it is found that $\gamma = 20$ [.] yields feasibility of the LMI.

As stated earlier the bandwidth of the angular velocity controller should be 0.2 [Hz] or less, i.e., the real values of the closed loop poles should reside between $0.2 \cdot 2\pi$ [rad/s] and 0 [rad/s]. The boundary in the pole-limiting LMI is therefore chosen to be $\eta = 0.2 \cdot 2\pi$ [rad/s], as η is defined positively in the LMI.

The combined LMI is implemented and solved in an m-file and yields a state feedback

controller defined as

$$\underline{\mathbf{K}}_{\text{ang}} = \begin{bmatrix} 0.0506 & -0.0001 & -0.0003 \\ -0.0001 & 0.0506 & -0.0003 \\ -0.0003 & -0.0001 & 0.0340 \end{bmatrix}. \quad (5.27)$$

Closing the loop with this state feedback controller, yields the poles depicted in Figure 5.7, where it is noticed that the poles are all above the limit of $-0.2 \cdot 2 \approx -1.256$ [rad/s]. The Δ marks the poles of the nominal system, and the \times marks the poles of the closed loop system, at each of the vertices of the uncertainty region.

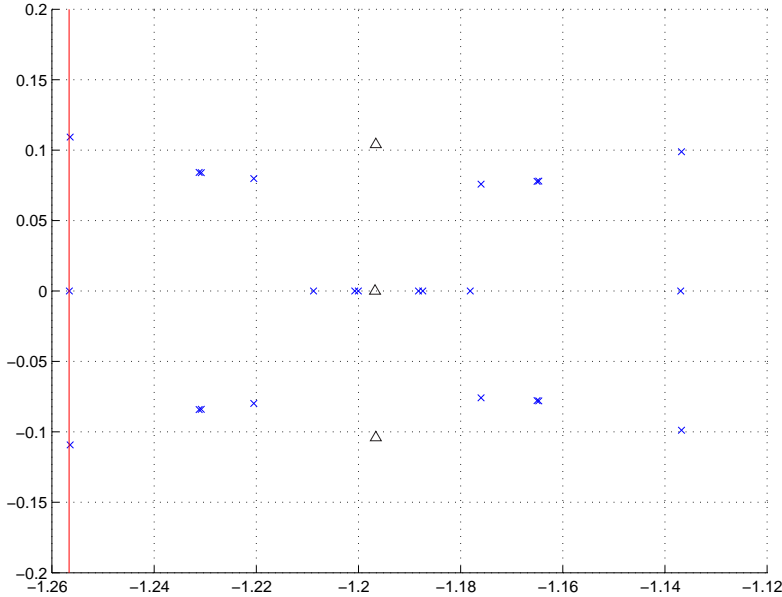


Figure 5.7: Pole locations of the closed loop system with the robust state feedback controller.

The angular velocity controller, including the disturbance estimator, has been designed in `ang_robust_control.m` and `kalman_estimator.m` and has been implemented in SIMULINK. Simulations are used to verify that the design conforms to the requirements.

5.4 Evaluation

From Section 4.3 it is known that the state feedback matrix must be positive definite. Examining (5.27) it is evident that this is the case. The following evaluations indicate the same tendency for stability.

The angular velocity controller was evaluated in Appendix K, where the angular velocity of the satellite, under the influence of the environmental disturbance torques, was considered. The angular velocity controller was also evaluated w.r.t. changes in the inertia matrix, disturbance torque and initial attitude, using a Monte Carlo simulation. Figure 5.8 depicts the angular velocity during an entire orbit, and the angular velocity settles at approximately zero within 14 [s] from an initial velocity, $\omega_{\text{init}} [0.0021 \ -0.0021 \ 0.0021]$ [rad/s].

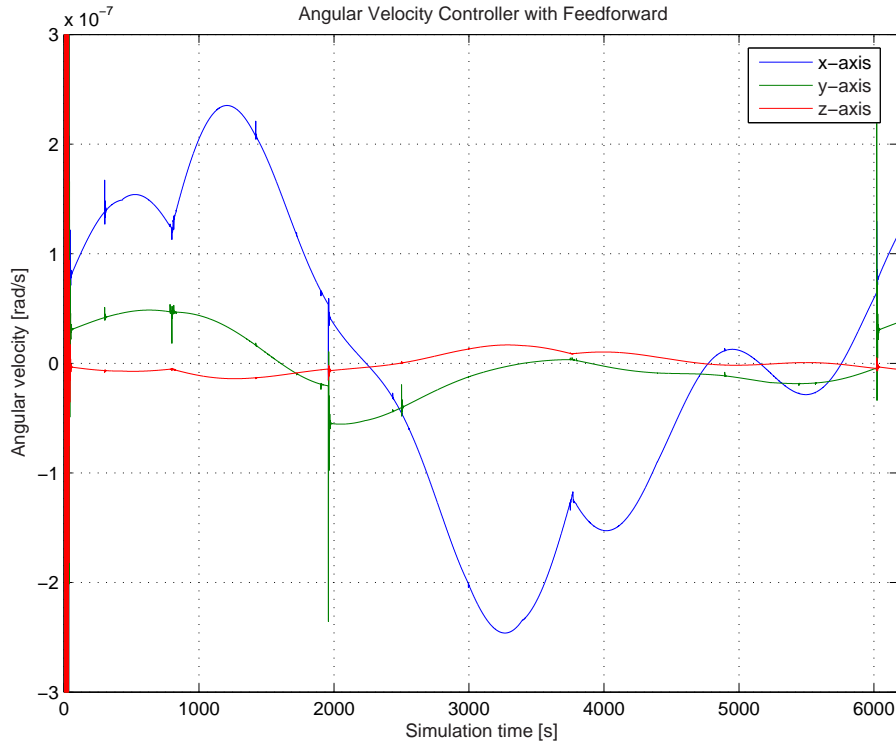


Figure 5.8: Angular velocity from a simulation of a complete orbit using the disturbance estimation and feedforward. After initial settling, the angular velocity is within $\pm 0.25 \cdot 10^{-6}$ [rad/s]. The settling of the angular velocity is dependent on the estimation and feedforward and is approximately 60 seconds. The spikes in the angular velocity is assumed to be caused by the estimator settling and feedforward, as the satellite exits eclipse at approximately $t = 2000$ [s] and enters eclipse in the end of the simulation.

The angular velocity controller without estimation and feedforward is capable of attenuating the disturbance torques. However, the introduction of the estimation and feedforward improves the controller's ability to attenuate the disturbance torques with a factor six, such that the mean angular velocity of the satellite is

$$\boldsymbol{\mu}_{\omega_{\text{est}}} = [600 \ 95 \ -14.7] \cdot 10^{-12} \text{ [rad/s].} \quad (5.28)$$

This value is obtained from 270 simulations, where the inertia matrix, initial attitude and disturbance parameters are changed. Furthermore, the angular velocity is capable of following a reference signal and is, therefore, assumed to allow for attitude control.

CHAPTER 6

Desaturation Control

This chapter describes the design of the desaturation controller for the NSO. It is addressed to the reader with interest in the essential theory and design, regarding the method developed for desaturation of the NSO momentum wheels.

When using the NSO momentum wheels for attitude control, the momentum wheels will eventually reach their saturation limit. This is due to the fact that the momentum wheels suppress the disturbance torques by transferring angular momentum from the satellite frame to the flywheels. Furthermore, when applying control torques to the momentum wheels, the accumulated angular momentum will increase or decrease further, until the momentum wheels either spin at maximum velocity or come to a complete rest.

Due to the accumulation of angular momentum it is desirable to design a controller, which can transfer the angular momentum from the momentum wheels to an external object. This can be performed by the NSO magnetorquers, which basically transfer the angular momentum to the Earth, when interacting with the Earth's geomagnetic field. The method for transferring angular momentum, is referred to as magnetic desaturation control.

As presented in Section 3.1 the desaturation mode should operate in parallel with the pointing controller. This means that the desaturation controller should transfer angular momentum from the momentum wheels, while the pointing controller maintains stability of the satellite. The control structure combining the desaturation controller, and the angular velocity controller is depicted in Figure 6.1. The angular velocity controller contained in the dashed box is explained in Chapter 5.

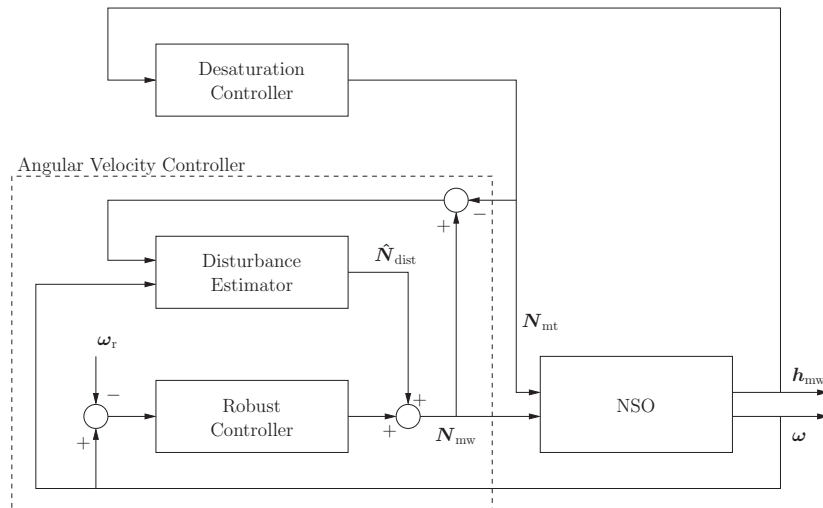


Figure 6.1: Control structure for the desaturation controller including the angular velocity controller.

It should be noticed that the desaturation controller uses the angular momentum of the momentum wheels as an input, to produce an output to the magnetorquers. This torque is subtracted from the feedback to the disturbance estimator, since the torque from the magnetorquers is exerted in the opposite direction of torque from the momentum wheels.

6.1 Controller Choice

Research regarding design of desaturation controllers has been conducted earlier. In [Steyn 1995] the author designed four controllers for desaturation. The designs include an energy optimal controller, two performance optimal controllers and a method denoted the Common Cross Product Law (CCPL). Since no power budget has been outlined in this project, only the performance optimal controllers and the CCPL, are considered.

LQR: Designing the LQR desaturation controller it is assumed that the geomagnetic field changes over time. Therefore, the controller becomes a time-varying finite time LQR controller. Given this type of LQR controller, the optimal solution is obtained by solving the Differential Riccati Equation (DRE) with regards to a performance function [Franklin, Powell & Workman 1998, page 364-371].

ILQR: In this design the geomagnetic field is assumed slowly varying and therefore approximated as being time invariant. This assumption facilitates the possibility of designing an time invariant infinite time LQR (ILQR) desaturation controller. The optimal controller is obtained by solving the Algebraic Riccati Equation (ARE), the optimal controller becomes the steady state solution to the ARE, since the terminal time $t_f \rightarrow \infty$.

CCPL: This design uses the difference between the current angular momentum of the momentum wheels and the angular momentum bias. The cross product between the error in angular momentum and the geomagnetic field vector, yields a magnetic dipole moment for the magnetorquers.

The desaturation controllers, considered above, were evaluated in [Steyn & Chen 1998], which indicated that the CCPL controller performance is initially best, but is with time inferior to the performance of the optimal controllers. The energy consumption was also evaluated, which showed that the LQR controller uses the least energy of the three considered, while the CCPL controller uses the most. Regardlessly, for reasons of simplicity, the CCPL controller will be used in the control of the NSO.

6.2 The Common Cross Product Law

To design the CCPL controller, the necessary theory will be outlined in this section. The control signal, calculated via the CCPL, is defined as the cross product between the error in the angular momentum and the geomagnetic field vector, i.e.,

$$\mathbf{M}_{\text{mt}} = C_{\text{desat}} (\mathbf{h}_{\text{mw}_{\text{err}}} \times \mathbf{B}), \quad (6.1)$$

where C_{desat} is a constant and $\mathbf{h}_{\text{mw}_{\text{err}}}$ is defined as

$$\mathbf{h}_{\text{mw}_{\text{err}}} = \mathbf{h}_{\text{mw}} - \mathbf{h}_{\text{mw}_{\text{bias}}}. \quad (6.2)$$

Notice that the CCPL controller is a simple proportional gain controller. The cross product in (6.1) yields the magnetic dipole moment, that should be produced by the magnetorquers in order to desaturate the momentum wheels.

Figure 6.2 depicts the control law for the desaturation controller. It should be noticed that it is not possible to desaturate the momentum wheels completely, unless $\mathbf{h}_{\text{mw}} - \mathbf{h}_{\text{mw}_{\text{bias}}}$, yields a $\mathbf{h}_{\text{mw}_{\text{err}}}$ in the plane perpendicular to \mathbf{B} . This is due to the fact that the magnetorquers do not provide complete spatial actuation, cf. Section 4.2.2.

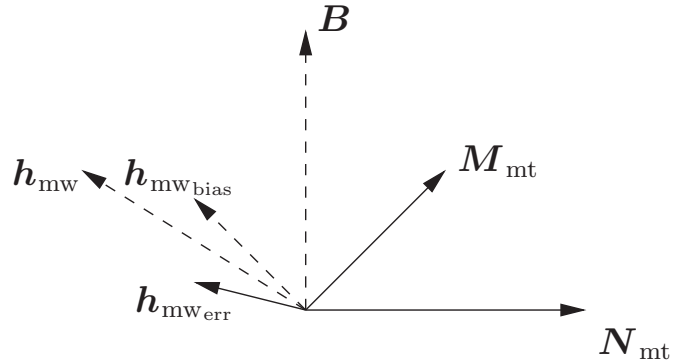


Figure 6.2: Illustration of the Common Cross Product Law, where \mathbf{N}_{mt} is given as the cross product between \mathbf{M}_{mt} and \mathbf{B} .

If the length of the angular momentum vector and the bias vector are equal, the torque from the magnetorquers will be in the opposite direction of the error in the angular momentum. Thus, it is possible to entirely desaturate the momentum wheels.

From (6.1) it should be noticed that the magnetic dipole moment is dependent on the strength of the geomagnetic field. By dividing the geomagnetic field vector in (6.1), by its length, the unit vector, $\hat{\mathbf{B}}$, is obtained. Thus the magnetic dipole moment becomes independent of the strength of the geomagnetic field. This gives the expression

$$\mathbf{M}_{\text{mt}} = C_{\text{desat}} (\mathbf{h}_{\text{mw}_{\text{err}}} \times \hat{\mathbf{B}}). \quad (6.3)$$

Due to the fact that the desaturation control utilises the magnetorquers, actuation is not always possible, as stated in 4.2.2. Dividing the expression obtained in (6.3) by $\|\mathbf{B}\|$, ensures that the controller gain will be large when the strength of the geomagnetic field is small, and vice versa. This hereby ensures that the control system has the same step response at all times. Thus the CCPL becomes

$$\mathbf{M}_{\text{mt}} = \frac{C_{\text{desat}}}{\|\mathbf{B}\|} (\mathbf{h}_{\text{mw}_{\text{err}}} \times \hat{\mathbf{B}}). \quad (6.4)$$

As the analysis in [Steyn & Chen 1998] states, the CCPL desaturation controller uses the most energy of the considered controllers. However, during the simulation performed by [Steyn & Chen 1998] the desaturation controllers were always active.

6.3 Controller Design

The proportional gain constant, C_{desat} , is chosen as 1, as this yields an acceptable response from the desaturation controller.

In order to conserve energy it is decided to introduce the trigger action for the desaturation control as indicated in Figure 3.1. It would be possible to consider the periodicity of the disturbances and use a form of model predictive control (MPC) as trigger method. However, this would require on-board models of the disturbances. Instead, it has been decided to use a simple trigger method on

$$\mathcal{T}_{\text{desat}} = \|\mathbf{h}_{\text{mw_err}} \times \hat{\mathbf{B}}\| = \|\mathbf{h}_{\text{mw_err}}\| \sin(\alpha), \quad (6.5)$$

where α is the angle between the error in angular momentum and the geomagnetic field vector. This method ensures that when the error in angular momentum for one momentum wheel reaches a threshold, the desaturation control will be activated. Furthermore, by including $\hat{\mathbf{B}}$, the desaturation controller is only activated if actuation with the magnetorquers is possible.

In Figure 6.3 an illustration of the activation of the desaturation controller is depicted. As noticed the controller should be activated before one of the momentum wheels reaches its saturation limit. The difference between the saturation limit, $d_{\mathcal{T}_{\text{sat}}}$, and the threshold for activation of the desaturation controller, $d_{\mathcal{T}_{\text{on}}}$, is denoted κ . The threshold for deactivation of the desaturation controller is denoted $d_{\mathcal{T}_{\text{off}}}$.

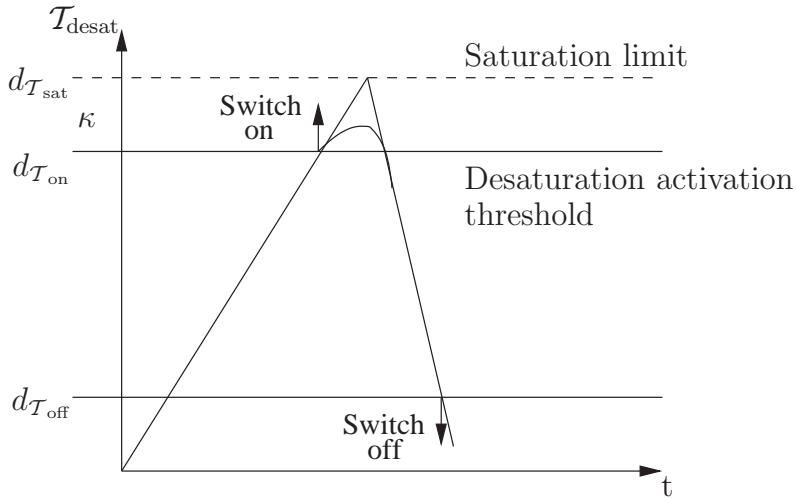


Figure 6.3: Illustration of the trigger method. When $d_{\mathcal{T}_{\text{on}}}$ is reached, the desaturation controller is switched on. Once $\mathcal{T}_{\text{desat}}$ becomes lower than $d_{\mathcal{T}_{\text{off}}}$ the desaturation controller switches off.

In (6.5) $\mathcal{T}_{\text{desat}}$, depicted in Figure 6.3, is shown to be dependent on the angle α . Therefore, $d_{\mathcal{T}_{\text{sat}}}$ is expressed as

$$d_{\mathcal{T}_{\text{sat}}} = h_{\text{mw_bias}} \sin(\alpha), \quad (6.6)$$

where $h_{\text{mw_bias}}$ is the bias point for one momentum wheel. In order to design an activation threshold, the attitude controllability of the magnetorquers have to be considered. Since

the magnetorquers does not provide complete spatial actuation, κ should be large enough to ensure that none of the momentum wheels reach saturation if actuation around a specific axis is not possible. It is estimated that actuation is not possible if the angle between the plane of actuation and the axis, around which actuation is desired, is less than $2 [^\circ]$. Therefore, the maximum time with no actuation around an axis is

$$t_{na} = \frac{t_{orbit}}{360} \cdot 2 \Rightarrow t_{na} = \frac{6174}{360} \cdot 2 = 34.3 [\text{s}]. \quad (6.7)$$

The value of κ can be calculated once the maximum inclination of $\mathcal{T}_{\text{desat}}$ in Figure 6.3, has been calculated. A mathematical expression for the maximum inclination of $\mathcal{T}_{\text{desat}}$, is given by

$$\max(\dot{\mathcal{T}}_{\text{desat}}) = \mathbf{h}_{\text{mw}_{\text{err}}} \perp \mathbf{B}. \quad (6.8)$$

This means that the maximum inclination of $\mathcal{T}_{\text{desat}}$ is equal to the maximum change in $\|\mathbf{h}_{\text{mw}_{\text{err}}}\|$. In order for the momentum wheels to suppress the external disturbances the expression

$$\mathbf{N}_{\text{mw}} = \mathbf{N}_{\text{dist}} \Leftrightarrow \dot{\mathbf{h}}_{\text{mw}} = \mathbf{N}_{\text{dist}} \Rightarrow \|\dot{\mathbf{h}}_{\text{mw}_{\text{err}}}\| = \|\mathbf{N}_{\text{dist}}\| \quad (6.9)$$

must be valid. The maximum disturbance torque exerted on one axis is $1599 \cdot 10^{-9} [\text{Nm}]$. Therefore, using at safety factor of 2, the minimum value of κ is given as

$$\begin{aligned} \kappa &= 2 \|\dot{\mathbf{h}}_{\text{mw}_{\text{err}}}\| t_{na} \Rightarrow \\ \kappa &= 2 \cdot 1599 \cdot 10^{-9} \cdot 34.3 = 1.096 \cdot 10^{-4} [\text{kgm}^2/\text{s}], \end{aligned} \quad (6.10)$$

Using (6.5), (6.6) and Figure 6.3 an expression for activation of the desaturation controller, is given as

$$\begin{aligned} \mathcal{T}_{\text{desat}} &\geq d_{\mathcal{T}_{\text{on}}} \Rightarrow \\ \mathcal{T}_{\text{desat}} &\geq d_{\mathcal{T}_{\text{sat}}} - \kappa \Rightarrow \\ \|\mathbf{h}_{\text{mw}_{\text{err}}}\| \sin(\alpha) &\geq h_{\text{mw}_{\text{bias}}} \sin(\alpha) - \kappa. \end{aligned} \quad (6.11)$$

The threshold for deactivation of the desaturation controller, is expressed in the same way as for the activation limit. However, the limit for deactivation is designed to be a constant limit. Thus, $d_{\mathcal{T}_{\text{off}}}$ is given by

$$d_{\mathcal{T}_{\text{off}}} = h_{\text{mw}_{\text{bias}}} \sin(2^\circ). \quad (6.12)$$

The angle of $2 [^\circ]$ corresponds to the estimated minimum angle required to facilitate actuation. A more formal expression for the trigger method is given by

$$d_{\text{on/off}} = \begin{cases} 1 & \text{if } \mathcal{T}_{\text{desat}} \geq d_{\mathcal{T}_{\text{on}}} \\ 0 & \text{if } \mathcal{T}_{\text{desat}} < d_{\mathcal{T}_{\text{off}}} \end{cases}. \quad (6.13)$$

The control design presented in Section 6.2, and the trigger method presented above, have been implemented in SIMULINK and simulations are used to evaluated the design.

6.4 Evaluation

Since the desaturation controller is active while the robust pointing controller maintains the attitude, the stability analysis of the desaturation controller is conducted by examining the

stability of the robust pointing controller. This is feasible as the desaturation controller only uses the magnetorquers for actuation, and therefore it can be regarded as a disturbance, which is handled by the angular velocity controller.

The desaturation controller was evaluated in Appendix K, where the satellite was subjected to the worst case disturbance torque on one axis. The result of a simulation with maximum disturbance torque on the x-axis is depicted in Figure 6.4.

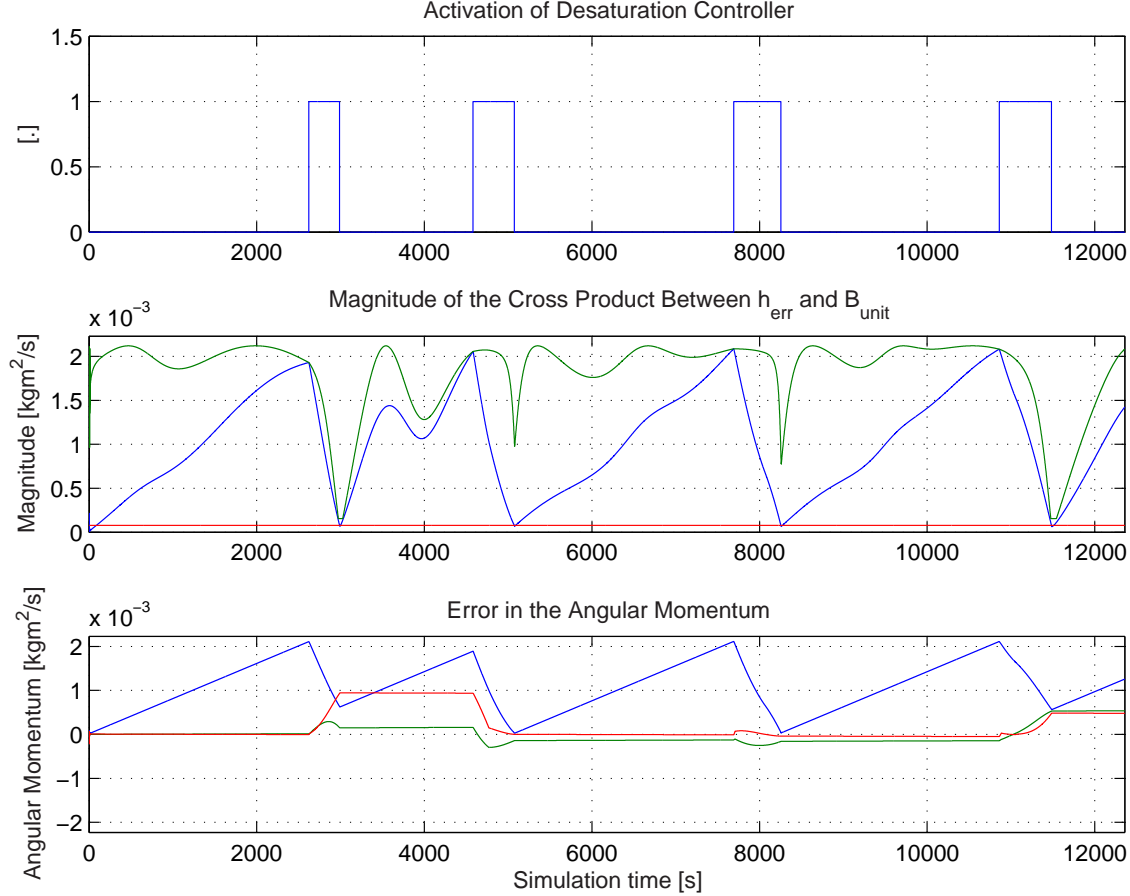


Figure 6.4: The top plot shows the activations and deactivations of the desaturation controller. Middle plot depicts upper and lower limits for desaturation and $\mathcal{T}_{\text{desat}}$. Bottom plot shows the error in the angular momentum.

The evaluation indicates that the desaturation controller is capable of desaturating the momentum wheels using the magnetorquers, once the activation level is reached, e.g., at $t \approx 2500$ [s]. A simulation using the modeled disturbance torques was performed, to evaluate the energy consumption of the desaturation controller with the implemented trigger method, as opposed to continuous actuation. It was evident that the trigger method conserves energy, as the desaturation controller is not activated, when the modeled disturbance torques are used. This suggests that the momentum wheels are overdimensioned, however no attitude manoeuvres were conducted during the simulation. Moreover, when the momentum wheels reach saturation the controller is capable of removing angular momentum, and attitude control is deemed possible.

CHAPTER 7

Attitude Control

This chapter describes the design of the attitude controller, which incorporates optimal control theory. It is addressed to the reader with interest in the theory and design of the attitude controller designed for the NSO, and is considered essential reading.

The control structure in Section 3.2 shows that the attitude controller should be capable of generating an angular velocity as reference to the angular velocity controller. Therefore, the attitude controller should be slower than the angular velocity controller, i.e. the bandwidth should be less than 0.2 [Hz], as stated in Section 4.1.

As stated in Section 4.2.2, regarding attitude controllability, the momentum wheels reach their saturation limit if the attitude manoeuvre is larger than 45 [$^{\circ}$]. This could be handled by designing the attitude controller slow enough to ensure, that the desaturation controller will have time to desaturate the momentum wheels. However, doing so would have an impact on the performance of the attitude controller, in the case of attitude manoeuvres smaller than 45 [$^{\circ}$]. Furthermore, a supervisor controller could also be considered, which should handle attitude manoeuvres beyond 45 [$^{\circ}$]. This is not considered in the design. However, when evaluating the attitude controller it will be subjected to attitude manoeuvres beyond 45 [$^{\circ}$], to determine whether further investigation is necessary. It is decided to design an optimal controller for the attitude of the NSO. This yields an optimal reference for the angular velocity controller, given the attitude reference.

7.1 Optimal Control

Since the system, on which the optimal controller is designed, is time-invariant it is desirable to design an infinite time LQR (ILQR) attitude controller. The design of such an optimal controller, implies calculating a controller gain, which minimises a performance index defined as

$$\mathcal{J} = \int_0^\tau (\mathbf{x}^T(t) \underline{\mathbf{Q}} \mathbf{x}(t) + \mathbf{u}^T(t) \underline{\mathbf{R}} \mathbf{u}(t)) \quad (7.1)$$

where $\underline{\mathbf{Q}}$ is a weight matrix that punishes large states, $\underline{\mathbf{R}}$ is a control weighting matrix, that punishes large control signals and τ denotes the control horizon. Both $\underline{\mathbf{Q}}$ and $\underline{\mathbf{R}}$ are square matrices and must be positive definite and positive semi-definite respectively [Andersen 2006]. Given a linear system in the form

$$\dot{\mathbf{x}}(t) = \underline{\mathbf{A}}\mathbf{x}(t) + \underline{\mathbf{B}}\mathbf{u}(t), \quad (7.2)$$

the optimal control problem can be expressed as calculating a controller gain, which minimises the performance index in (7.1), subjected to the constraints given by the system in

(7.2). It is possible to show that the optimal steady state controller gain can be obtained by solving the Algebraic Riccati Equation (ARE) [Andersen 2006]

$$\underline{\mathbf{Q}} + \underline{\mathbf{A}}^T \underline{\mathbf{P}}_{AC} + \underline{\mathbf{P}}_{AC} \underline{\mathbf{A}} - \underline{\mathbf{P}}_{AC} \underline{\mathbf{B}} \underline{\mathbf{R}}^{-1} \underline{\mathbf{B}}^T \underline{\mathbf{P}}_{AC} = \underline{\mathbf{0}}, \quad (7.3)$$

where $\underline{\mathbf{P}}_{AC}$ is a steady state solution to the ARE. Once the solution to (7.3) is obtained, the optimal steady state feedback gain matrix for the control law $\mathbf{u}(t) = -\underline{\mathbf{K}}\mathbf{x}(t)$, is given by

$$\underline{\mathbf{K}} = \underline{\mathbf{R}}^{-1} \underline{\mathbf{B}}^T \underline{\mathbf{P}}_{AC}. \quad (7.4)$$

The performance of the optimal controller is dependent on the weight matrices $\underline{\mathbf{Q}}$ and $\underline{\mathbf{R}}$ given in (7.1).

7.2 Controller Design

In order to design an ILQR attitude controller, the closed loop system, of the angular velocity controller presented in Section 3.2, is needed to describe the system subject to design. The control structure for the attitude controller is, therefore, constituted as depicted in Figure 7.1, where ω_r is the angular velocity reference, also depicted in Figure 5.1.

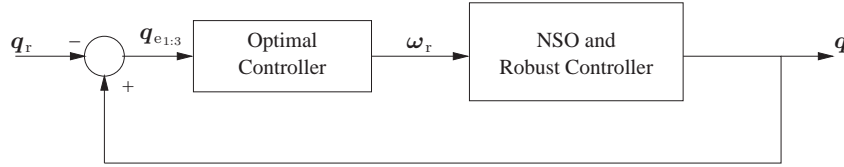


Figure 7.1: Control structure for the attitude controller.

It should be noticed that the summation is not valid when using quaternions. Instead the summation represents the calculation of the error quaternion, cf. Appendix C. Furthermore, the attitude controller will be implemented using positive feedback. The righthand block in Figure 7.1 incorporates the closed system of the inner control loop, which is comprised of

$$\begin{aligned} \underline{\mathbf{A}}_{AC} &= \underline{\mathbf{A}}_{sat} + \underline{\mathbf{B}}_{sat} \underline{\mathbf{K}}_{ang} \\ \underline{\mathbf{B}}_{AC} &= \underline{\mathbf{B}}_{sat} \underline{\mathbf{K}}_{ang} \\ \underline{\mathbf{C}}_{AC} &= \underline{\mathbf{C}}_{sat}. \end{aligned} \quad (7.5)$$

Here $\underline{\mathbf{A}}_{sat}$, $\underline{\mathbf{B}}_{sat}$ and $\underline{\mathbf{C}}_{sat}$ are the inner loop system matrix, input matrix and output matrix respectively, cf. Section 2.6. The matrix $\underline{\mathbf{K}}_{ang}$ is the state feedback gain matrix for the angular velocity controller. A preliminary implementation of the control structure in Figure 7.1 has indicated the requirement for an integral action in the LQR design, due to a steady state error in the attitude.

In order to design the optimal controller, including the integral action, a system description of the outer loop is derived using the linearised system obtained in (2.53) and the control structure presented in Figure 7.1. Augmenting the state vector to include an integral state

vector, yields

$$\begin{aligned} \begin{bmatrix} \dot{\mathbf{q}}_{1:3} \\ \dot{\boldsymbol{\omega}} \\ \dot{\mathbf{x}}_i \end{bmatrix} &= \begin{bmatrix} \underline{\mathbf{0}}_{3 \times 3} & \frac{1}{2}\underline{\mathbf{1}}_{3 \times 3} & \underline{\mathbf{0}}_{3 \times 3} \\ \underline{\mathbf{0}}_{3 \times 3} & \underline{\mathbf{A}}_{AC} & \underline{\mathbf{0}}_{3 \times 3} \\ \underline{\mathbf{1}}_{3 \times 3} & \underline{\mathbf{0}}_{3 \times 3} & \underline{\mathbf{0}}_{3 \times 3} \end{bmatrix} \begin{bmatrix} \mathbf{q}_{1:3} \\ \boldsymbol{\omega} \\ \mathbf{x}_i \end{bmatrix} + \begin{bmatrix} \underline{\mathbf{0}}_{3 \times 3} \\ \underline{\mathbf{B}}_{AC} \\ \underline{\mathbf{0}}_{3 \times 3} \end{bmatrix} \boldsymbol{\omega}_r \\ \mathbf{y} &= \begin{bmatrix} \underline{\mathbf{1}}_{3 \times 3} & \underline{\mathbf{0}}_{3 \times 3} & \underline{\mathbf{0}}_{3 \times 3} \\ \underline{\mathbf{0}}_{3 \times 3} & \underline{\mathbf{C}}_{AC} & \underline{\mathbf{0}}_{3 \times 3} \\ \underline{\mathbf{0}}_{3 \times 3} & \underline{\mathbf{0}}_{3 \times 3} & \underline{\mathbf{1}}_{3 \times 3} \end{bmatrix} \begin{bmatrix} \mathbf{q}_{1:3} \\ \boldsymbol{\omega} \\ \mathbf{x}_i \end{bmatrix}. \end{aligned} \quad (7.6)$$

Regarding the reference, depicted in Figure 7.1, as input to the system, then $\dot{\mathbf{x}}_i = \underline{\mathbf{1}}_{3 \times 3} \mathbf{q}_{e_{1:3}}$.

Given the system description in (7.6) the ILQR can be designed using the MATLAB function `lqr`. Furthermore, the design parameters specified in the symmetric weighting matrices $\underline{\mathbf{Q}}_{AC}$ and $\underline{\mathbf{R}}_{AC}$ should also be included. Seemingly, this yields a high number of design parameters. If $\underline{\mathbf{Q}}_{AC}$ and $\underline{\mathbf{R}}_{AC}$ are an $\mathbb{R}^{n \times n}$ and an $\mathbb{R}^{m \times m}$ matrix respectively, the number of design parameters is exactly $\frac{1}{2}n(n+1) + \frac{1}{2}m(m+1)$. However, it is possible to choose $\underline{\mathbf{Q}}_{AC}$ and $\underline{\mathbf{R}}_{AC}$ as diagonal matrices complying with the definiteness of the weighting matrices, thereby decreasing the number of design parameters to $n+m$ [Franklin, Powell & Workman 1998, page 365]. This means that $\underline{\mathbf{Q}}_{AC}$ becomes a 9×9 diagonal matrix and $\underline{\mathbf{R}}_{AC}$ becomes a 3×3 diagonal matrix, i.e.,

$$\underline{\mathbf{Q}}_{AC} = \begin{bmatrix} C_q \underline{\mathbf{1}}_{3 \times 3} & \underline{\mathbf{0}}_{3 \times 3} & \underline{\mathbf{0}}_{3 \times 3} \\ \underline{\mathbf{0}}_{3 \times 3} & C_\omega \underline{\mathbf{1}}_{3 \times 3} & \underline{\mathbf{0}}_{3 \times 3} \\ \underline{\mathbf{0}}_{3 \times 3} & \underline{\mathbf{0}}_{3 \times 3} & C_{int} \underline{\mathbf{1}}_{3 \times 3} \end{bmatrix} \quad \underline{\mathbf{R}}_{AC} = C_u \underline{\mathbf{1}}_{3 \times 3}, \quad (7.7)$$

where C_q , C_ω , C_{int} and C_u are scalar values. It is observed that decreasing the value of C_q brings the poles of the \mathbf{q} and $\boldsymbol{\omega}$ states closer together, and decreases the influence of the \mathbf{q} states on the controller output, by decreasing the bandwidth of the \mathbf{q} value and increasing the bandwidth on the $\boldsymbol{\omega}$ states, and vice versa. Analogously; decreasing the value of C_ω brings the poles of the $\boldsymbol{\omega}$ and \mathbf{x}_i states together and decreases the influence that the $\boldsymbol{\omega}$ states have on the control output and a decrease in C_{int} entails that the $\boldsymbol{\omega}$ and \mathbf{q} poles moves further apart, and it entails less influence of the \mathbf{x}_i states on the control output.

The value C_u punishes the control signals, and decreasing this value increases the bandwidth of the \mathbf{x}_i states. Furthermore, the influence of all the states on the control output is increased.

The weighting of the states and input have been obtained through empiric design. This empiric design has been a necessity, in order to comply with the requirement regarding the bandwidth. Thus, the weighting matrices are defined as

$$\underline{\mathbf{Q}}_{AC} = \begin{bmatrix} 0.00552 \cdot \underline{\mathbf{1}}_{3 \times 3} & \underline{\mathbf{0}}_{3 \times 3} & \underline{\mathbf{0}}_{3 \times 3} \\ \underline{\mathbf{0}}_{3 \times 3} & 0.0008 \cdot \underline{\mathbf{1}}_{3 \times 3} & \underline{\mathbf{0}}_{3 \times 3} \\ \underline{\mathbf{0}}_{3 \times 3} & \underline{\mathbf{0}}_{3 \times 3} & 0.000045 \cdot \underline{\mathbf{1}}_{3 \times 3} \end{bmatrix} \quad \underline{\mathbf{R}}_{AC} = \underline{\mathbf{1}}_{3 \times 3}. \quad (7.8)$$

Using the matrices specified, the MATLAB function `lqr` yields the optimal steady state feedback gain matrix defined as

$$\underline{\mathbf{K}}_{att} = \begin{bmatrix} 0.0881 & 0.0024 & -0.0026 & 0.0336 & 0.000007 & -0.000023 \\ -0.0024 & 0.0881 & 0.0026 & 0.000007 & 0.0336 & 0.000036 \\ 0.0026 & -0.0026 & 0.0853 & -0.000035 & 0.000054 & 0.0322 \\ 0.0067 & 0.00020 & -0.00020 & & & \\ -0.00020 & 0.0067 & 0.00020 & & & \\ 0.00020 & -0.00020 & 0.0067 & & & \end{bmatrix} \quad (7.9)$$

When implementing an integrator action it also entails the introduction of an anti-integrator windup, such that the error quaternion does not entail saturation of the momentum wheels. Using the law of conservation of angular momentum, the maximum change in angular momentum of the momentum wheels, must be equal to the maximum change in angular momentum of the satellite, i.e.

$$\Delta h_{\text{mw}_{\text{max}}} = \Delta h_{\text{sat}} \Leftrightarrow h_{\text{mw}_{\text{bias}}} = \Delta I_{\text{sat}} \Delta \omega_{\text{sat}} \Rightarrow \Delta \omega_{\text{sat}} = \Delta I_{\text{sat}}^{-1} h_{\text{mw}_{\text{bias}}}. \quad (7.10)$$

Thus the minimum value of the angular velocity is obtained when ΔI_{sat} is maximum. This means that the upper and lower limits, on the anti-integrator windup, should be 0.053 and -0.053 , respectively. However, the upper limit is decreased to 0.01, while the lower limit is increased to -0.01 , to further limit the effect of the integral action.

The attitude controller has been designed in `att_control_with_integrator.m` and implemented in SIMULINK to verify and evaluate the design.

7.3 Evaluation

The attitude controller was evaluated in Appendix K, where 30 random attitude manoeuvres were simulated. Each attitude reference was calculated in such a manner, that it was ensured that the angular momentum vector of the momentum wheels, never left the 1st octant of the SBRF. Six of the 30 simulations are depicted in Figure 7.2, and they show that the attitude controller is capable of changing the attitude of the satellite, without any indication of instability.

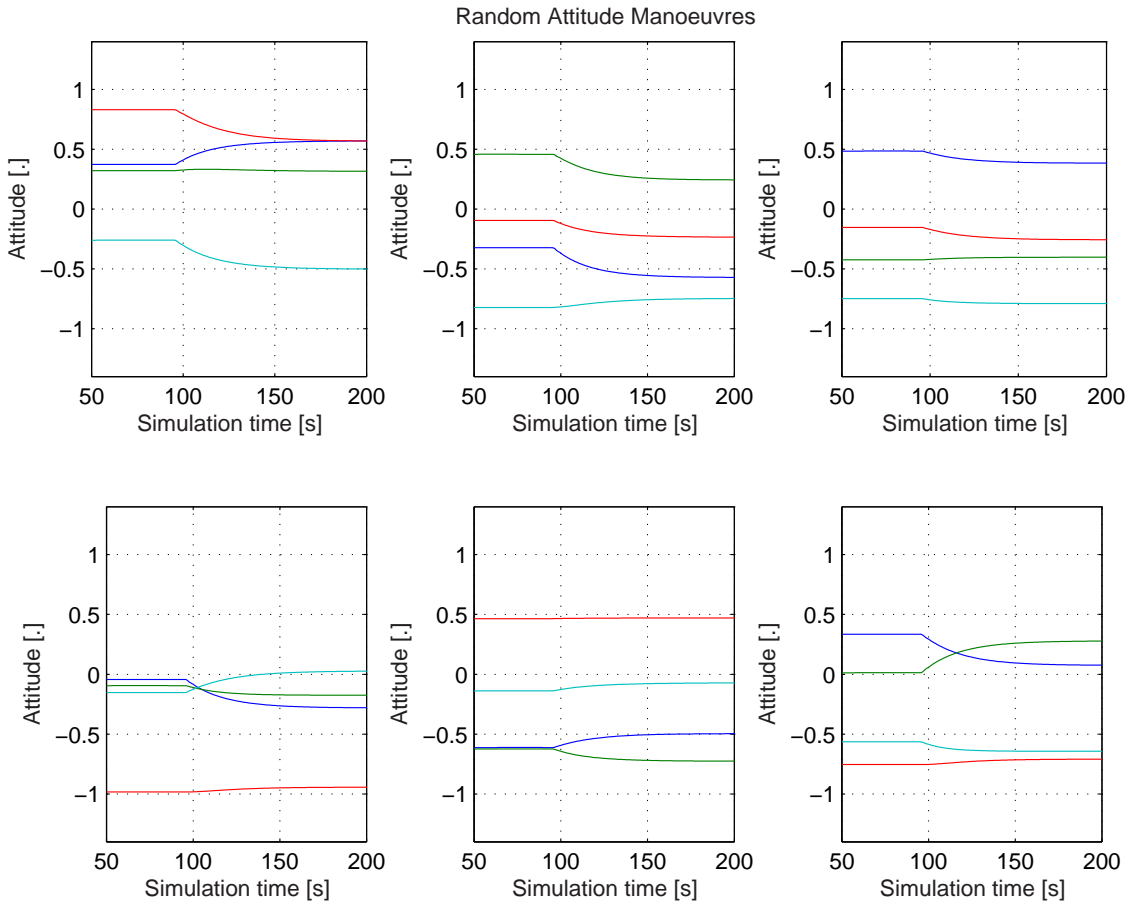


Figure 7.2: Six randomly generated attitude manoeuvres, which show that reference attitudes are obtained by the satellite.

However, a simulation with an attitude manoeuvre requiring the angular momentum vector of the momentum wheels to leave the 1st octant, indicated that this kind of attitude manoeuvre will result in instability. The cause is attributed to the limited desaturation capabilities of the desaturation controller. Therefore, a managing algorithm must be implemented, however, this is not pursued further in this report, and only attitude manoeuvres complying to the restriction will be used in further evaluations.

CHAPTER 8

Pointing Controller

This chapter describes how the reference input for the attitude controller can be generated, such that a specific location on the Earth can be tracked. This chapter is addressed to the reader with interest in the development of the Earth location tracking control and is an essential part of this report.

The attitude controller described in Chapter 7 allows for following a reference attitude quaternion, \mathbf{q}_{ref} . However, to point towards a given location on the Earth, as stated in the requirement in Section 1.3, the reference signal must constantly change as the satellite is moving around the Earth, i.e., a pointing manoeuvre. This chapter will describe how the reference signal will be calculated from a ground coordinate, and how this is combined with the previous described control structure. The control structure for the pointing controller is depicted in Figure 8.1. As noticed the pointing controller utilises input from on-board

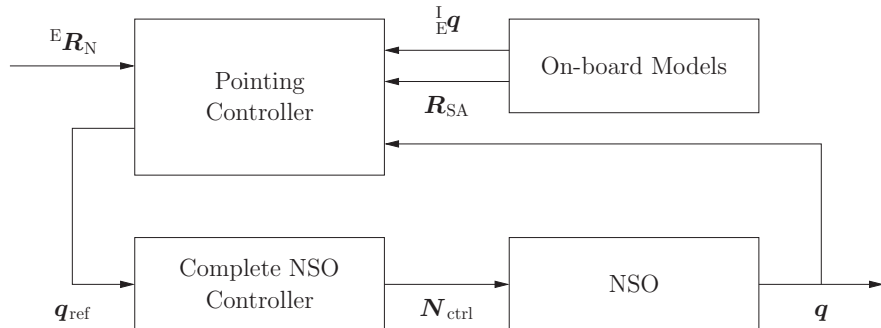


Figure 8.1: Control structure including the reference generator for the NSO satellite.

models, more specific the ephemeris models. Furthermore, a vector, describing the target location and the actual attitude of the satellite, is needed. Given these input the pointing controller generates continuous attitude references for the attitude controller.

8.1 Attitude Reference Calculation

To obtain the reference signal for the attitude controller, a vector describing the direction to the target area, from a satellite point of view, is needed. To calculate this the satellite position and attitude, as well as the position of the target area, must be known in the ECI. Figure 8.2 depicts the position of the satellite, ${}^I \mathbf{R}_{SA}$, the position of the target area, ${}^I \mathbf{R}_N$, and the vector from the satellite to the target location on the Earth, ${}^I \mathbf{R}_{SN}$.

As the target is fixed on the surface of the Earth the location can be described by the

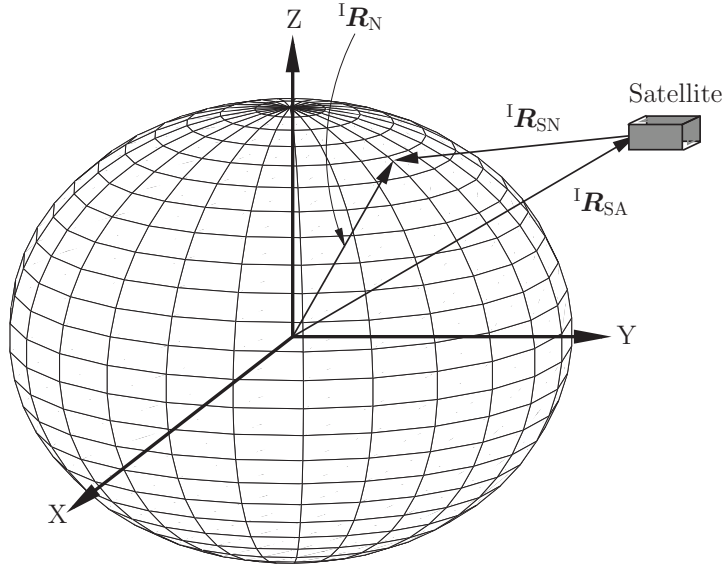


Figure 8.2: Position of the satellite in orbit and the target area on the Earth.

latitude and longitude in the ECEF, and then rotated to the ECI using $\underline{\mathbf{C}}_E^I$, i.e.,

$$\mathbf{R}_N^I = \underline{\mathbf{C}}_E^I \mathbf{R}_N^E, \quad (8.1)$$

where $\underline{\mathbf{C}}_E^I$ is a rotation matrix. The vector from the satellite to the target area can now be calculated as

$$\begin{aligned} \mathbf{R}_N^I &= \mathbf{R}_{SA}^I + \mathbf{R}_{SN}^I \Leftrightarrow \\ \mathbf{R}_{SN}^I &= \mathbf{R}_N^I - \mathbf{R}_{SA}^I \\ &= \underline{\mathbf{C}}_E^I \mathbf{R}_N^E - \mathbf{R}_{SA}^I. \end{aligned} \quad (8.2)$$

Here \mathbf{R}_{SA}^I and $\underline{\mathbf{C}}_E^I$ are output from ephemeris models, and are assumed known, as they must be obtained from on-board models.

As the camera on the NSO is located on the z-axis, the objective is to find a rotation that align the z-axis of the NSO, $\hat{\mathbf{z}}_{SA}$, with $\hat{\mathbf{R}}_{SN}$. At this point, the notion of unit vectors is introduced to avoid large numbers in further calculations. The quaternion describing the error between the two can be found by rotating $\hat{\mathbf{R}}_{SN}$ to SBRF, such that the z-axis and $\hat{\mathbf{R}}_{SN}$ are in the same frame. The quaternion, \mathbf{q}_{err} , describing the rotation of $\hat{\mathbf{z}}_{SA}$ to $\hat{\mathbf{R}}_{SN}$ is described by the Euler eigenaxis, $\hat{\mathbf{e}}$, and the rotation angle, θ , as depicted in Figure 8.3.

Thus, the quaternion, \mathbf{q}_{err} , is found as

$$\begin{aligned} \mathbf{q}_{err} &= \left[\begin{array}{c} \hat{\mathbf{e}} \sin \frac{\theta}{2} \\ \cos \frac{\theta}{2} \end{array} \right] \Rightarrow \\ &= \left[\begin{array}{c} (\hat{\mathbf{R}}_{SN}^S \times \hat{\mathbf{z}}_{SA}^S) \sin \frac{\theta}{2} \\ \cos \frac{\theta}{2} \end{array} \right] \Rightarrow \\ &= \left[\begin{array}{c} (\underline{\mathbf{C}}_I^S \hat{\mathbf{R}}_{SN}^I \times \hat{\mathbf{z}}_{SA}^S) \sin \frac{\theta}{2} \\ \cos \frac{\theta}{2} \end{array} \right], \end{aligned} \quad (8.3)$$

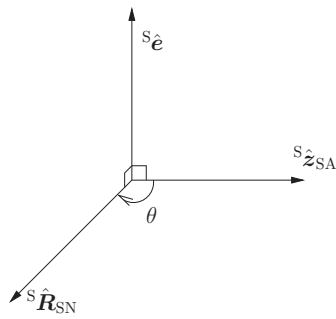


Figure 8.3: Euler eigenaxis and angle for rotating the z-axis of the NSO to point towards the target location.

where $\theta = \arccos(\hat{\mathbf{R}}_{\text{SN}}^T \hat{\mathbf{z}}_{\text{SA}})$. The reference quaternion for the attitude controller can then be calculated as

$$\mathbf{q}_{\text{ref}} = \mathbf{q}_{\text{att}} \mathbf{q}_{\text{err}}, \quad (8.4)$$

but as the error quaternion is calculated in the attitude controller as

$$\mathbf{q}_{\text{err}} = \mathbf{q}_{\text{att}}^{-1} \mathbf{q}_{\text{ref}}, \quad (8.5)$$

it is possible to omit the multiplication by \mathbf{q}_{att} in (8.4), and feed the error quaternion directly into the attitude controller, \mathbf{K}_{att} . Thus, the feedback is moved to the pointing controller, as depicted in Figure 8.1.

8.2 Implementation Assumptions and Limitations

Some of the values needed for calculating the error quaternion, such as the rotation from ECEF to ECI, and the position of the satellite, are based on output from ephemeris models. Furthermore, the attitude of the satellite is used in the calculation to obtain \mathbf{R}_{SN} in the SBRF. These values will be estimated from on-board models and by the ADS, which is why the precision of the reference signal is dependent on the accuracy of the before mentioned. However, this will not be considered further in this report, and therefore the on-board models are assumed to be identical to the ones used in the NSO model, and the satellite attitude quaternion is assumed to be accurate.

8.3 Evaluation

The evaluation of the pointing controller requires the complete control structure for the NSO satellite and will, therefore, be performed during the system evaluation in the following chapter.

System Evaluation

In this chapter the complete robustly controlled system designed in this report is evaluated. The results obtained are compared to the results obtained by using a similar control structure, but with simple substitutions in each of the controllers in the structure. This chapter is addressed to the reader with interest in the final evaluation of the developed control structure, on which the final conclusions will be drawn.

To have a subject for comparison a simple control system is introduced. Simple control will, from hereon, imply an attitude controller with a proportional gain and an angular velocity controller, with state feedback designed using pole placement. The poles in the simple angular velocity controller closed loop, are placed in $-1.254 [.]$, $-1.255 [.]$ and $-1.256 [.]$ respectively, to accommodate the bandwidth requirement described in the model analysis in Chapter 4. Moreover, the proportional gain in the attitude controller is adjusted to $0.06555 [.]$ on each term in $\mathbf{q}_{1:3}$, to comply with that same requirement, and to obtain the same bandwidth of the closed loop system, as for the robustly controlled system. The controller bandwidths are increased as much as possible, with a small margin, to ensure a reasonable performance. Furthermore, the desaturation controllers in the two configurations will be identical, but the estimator in the simple control configuration is a linear estimator designed using pole placement and tuned to similar performance as the designed Kalman filter.

A complete evaluation with all resulting plots and values can be found in Appendix K. Here a more detailed description of each performed evaluation is also presented and all resulting values are present. Only the most protruding results and plots will be presented and concluded upon in this chapter. If values used in conclusions are considered of direct importance, when considering the requirements in Section 1.3, they will be stated in relation to that conclusion.

9.1 Attitude Manoeuvres

To investigate the effects of attitude manoeuvres, and the effects of uncertainties in the inertia matrix, an evaluation is performed on each of the two control configurations. Two random attitudes are used to create consecutive attitude manoeuvres. However, the random attitude quaternions does not rotate the angular momentum of the momentum wheels outside the 1st octant. A short period of settling is required for the estimators, which is why no attitude manoeuvres is executed before $t = 100 [\text{s}]$ in the simulations. Two simulations were performed with a nominal inertia matrix and a perturbed inertia matrix in an extremity of the uncertainty region, respectively.

Plotting the results obtained from the simulations, yielded the results showed in Figure 9.1. As can be seen the robust controller configuration yields a faster settle of the error angle. The angle has settled enough to certify an acceptable attitude manoeuvre, within approximately 100 [s], as opposed to the 160 [s] seconds with the simple controller configuration. The same tendency is evident for the rise-time to an acceptable attitude in the two configurations. However, no significant change in performance can be seen from the nominal and perturbed scenario.

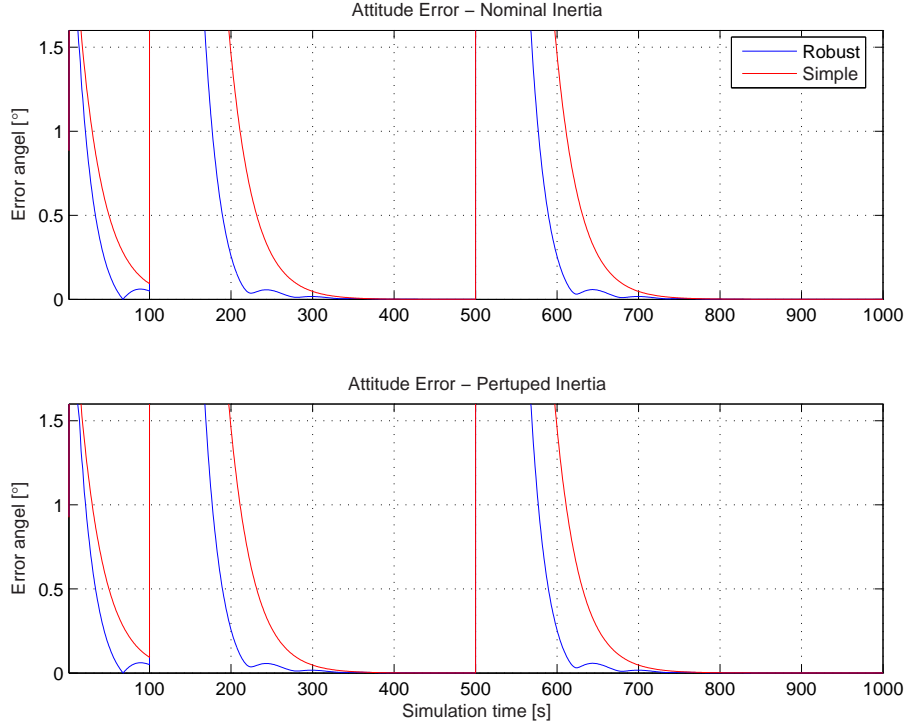


Figure 9.1: Plots of the angular errors in attitude on the z-axis for both controller configurations with a nominal (topmost) and a perturbed (bottom) inertia matrix. Notice that the rise- and settle-time for the simply controlled system is significantly longer than for the robustly controlled system. No significant change in performance can be seen from the nominal and perturbed scenario.

The angular velocities of the two controller configurations are plotted in Figure 9.2. The same tendency for a faster settling-time is evident. Also noticeable is the slight overshoot in the angular velocities in the robust controlled configuration. When reexamining Figure 9.1 this is also evident in the slight increase in the error angle, after the initial rise for the robust control configuration.

The bandwidth of the closed loop systems in each configuration were identical (0.19958 [Hz]) for the nominal system, but differed in the perturbed case. The robust control configuration was still within the requirement, with a bandwidth of 0.19974 [Hz], but the simply controlled closed loop system had a bandwidth of 0.20133 [Hz].

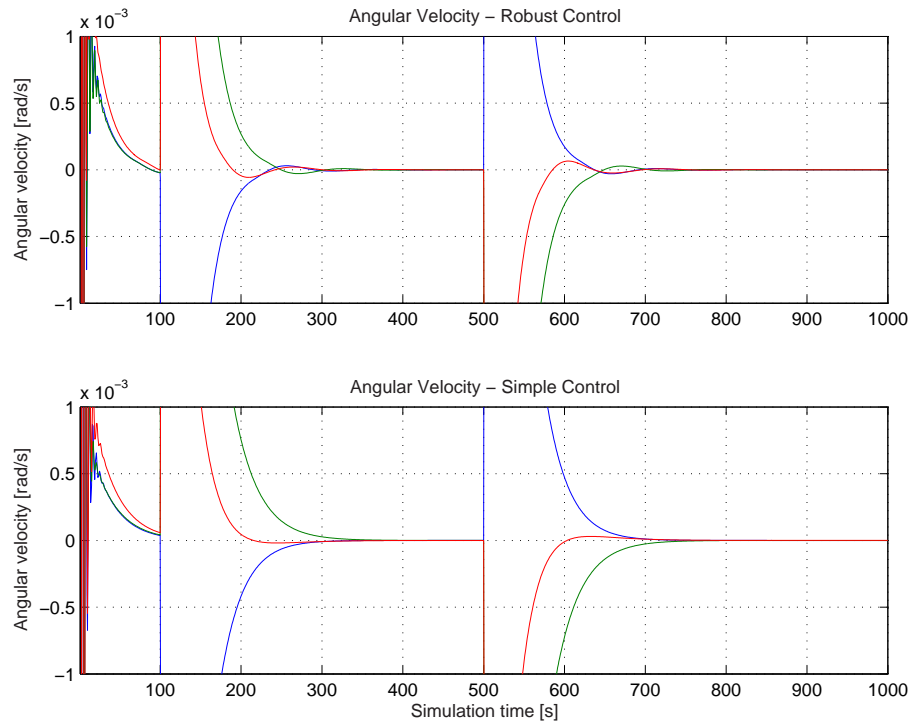


Figure 9.2: Plots of the resulting changes in angular velocity arising from attitude manoeuvres with a perturbed inertia matrix. The topmost plot shows the angular velocity on the robustly controlled system, whereas the bottom plot show the simply controlled system. The robustly controlled system performs better, but has a slight overshoot.

9.1.1 Conclusion

The plots from the simulations of the attitude manoeuvres, show that both controller configurations were able to control the attitude of the NSO. However, when comparing the two control configurations, the robust controller configuration did prove overwhelmingly faster at acquiring the designated attitude. A slight overshoot was, however present, in the robustly controlled closed loop. This could be relevant for the power consumption of the ACS, if it was more prominent. It is, however, deemed unimportant on account of the small nature, and could be attenuated by tuning the LQR attitude controller. An examination of the difference in performances reveals, that it is the LQR control design that makes the difference. Therefore, it is concluded that this is the preferred method for designing a controller for the attitude.

Another noticeable fact is that the performance in both configurations did not differ significantly, when introduced to uncertainties in the inertia matrix. However, the bandwidth requirement of ≤ 0.2 [Hz] was not met for the simply controlled system when introduced to uncertainties, but remained virtually unchanged for the robustly controlled system. This implies that the bandwidth requirement cannot be guaranteed with a simple state feedback on the angular velocity, and must be reviewed for each uncertainty vertex. This will not be the case for the angular velocity controller designed in this report. Having stated this it must be remarked that the failure to meet the requirement is not that crucial as the overstep of the bandwidth is minimal, and would, therefore, probably still work in practice. However, designing the robust controller ensuring the requirement to the bandwidth

is met, requires little additional calculations, and is therefore preferred.

The uncertainty variation in the inertia matrix is not compliant with the real uncertainty variations as they would probably yield cross correlations, and thus not only change the diagonal. Therefore, further investigation into this subject is required.

9.2 Reliability

It is desired to investigate, whether the controlled systems meet the requirements to the ACS concerning the ability to hold an attitude. This is done using a Monte Carlo simulation, where the two controlled systems for each iteration are simulated for an entire orbit given the initial attitude, a drag coefficient and an air density. The ability to maintain the initial attitude is investigated over 30 different initial attitudes, drag coefficients and air densities. This is done only for every vertex of the inertia uncertainty region, and for the nominal inertia matrix, to reduce the computational load of the simulation. This combination yields 270 different simulations of each system. The first 150 [s] of each simulation is circumvented to allow for the settling of the estimators.

The Monte Carlo simulation results were used to extract information concerning the mean and standard deviation for the attitude error angle, and for the angular velocities for both controller configurations. The values for each of the systems are presented in Table K.1. In Figure 9.3 a histogram, for the sampling distribution of the angular error on the z-axis for the robustly controlled configuration, is depicted.

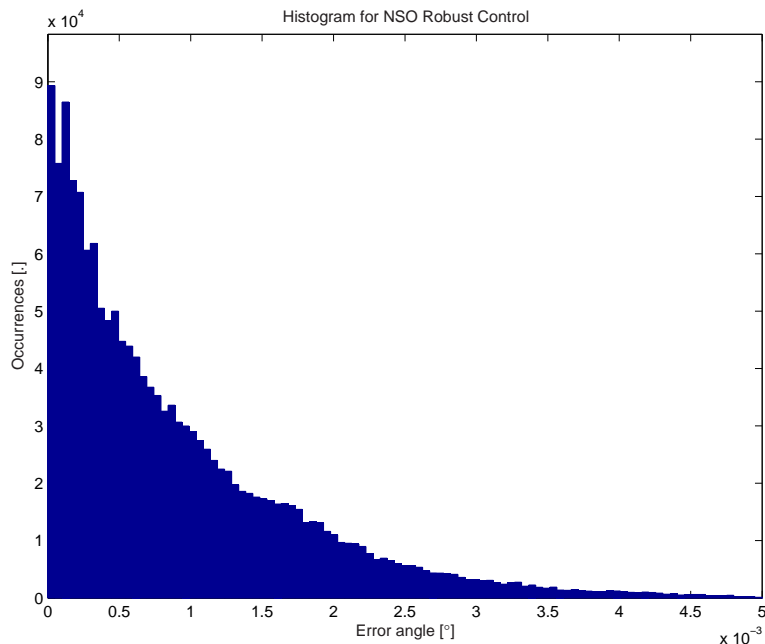


Figure 9.3: Distribution of samples of the angular error on the z-axis for the robustly controlled system. The number of samples is 1649060.

9.2.1 Conclusion

The controlled system needs to be verified for its accordance with the demands for the ACS to an angular error lower than or equal to $0.57 [^\circ]$, within a 95 [%] confidence interval. This could be done by using the exact values in the sample distribution, but to yield a more realistic and conservative result, the calculations will instead be based on the distribution tendency.

The 1649060 samples of the error angle for the robustly controlled system, depicted in Figure 9.3, are not uniformly distributed. As the angle is never negative, a one sided distribution is required to examine the results. When examining Figure 9.3 it is intuitive to approximate with an exponential distribution.

The cumulative probability of obtaining an error value for an exponential random variable, x , of less than or equal to a specific value of x , denoted x_0 , is expressed as

$$P(x \leq x_0) = 1 - \exp\left(\frac{-x_0}{\mu}\right), \quad (9.1)$$

where μ is the mean value of the sample set [Anderson, Sweeney & Williams 2003]. Inserting the mean value of $0.0058 [^\circ]$ and the confidence interval of 95 [%], yields

$$\begin{aligned} 0.95 &= 1 - \exp\left(\frac{-x_0}{0.0058}\right) \Rightarrow \\ x_0 &= 0.0174 [^\circ]. \end{aligned} \quad (9.2)$$

This means that the angular error with 95 [%] certainty will be less than or equal to $0.0174 [^\circ]$. Comparing this to the requirement of $0.57 [^\circ]$ the designed control system is deemed in compliance, thus proving the control system feasibility. Using a confidence interval of 99.9 [%], the designed control system guarantees an error of no more than $0.0401 [^\circ]$. In comparison the simply designed controller configuration only guarantees an error angle less than $0.1761 [^\circ]$ for a confidence interval of 95 [%], which, however, is still within the requirement.

9.3 Target Acquisition

To evaluate the NSO's ability to track a specific location on the Earth using the pointing controller, the controller is given the location of Aalborg as input and the reference attitude from the pointing controller is fed to the attitude controller. The simulation result is depicted in Figure 9.4, where the error between the desired z-axis direction and the actual z-axis direction is shown.

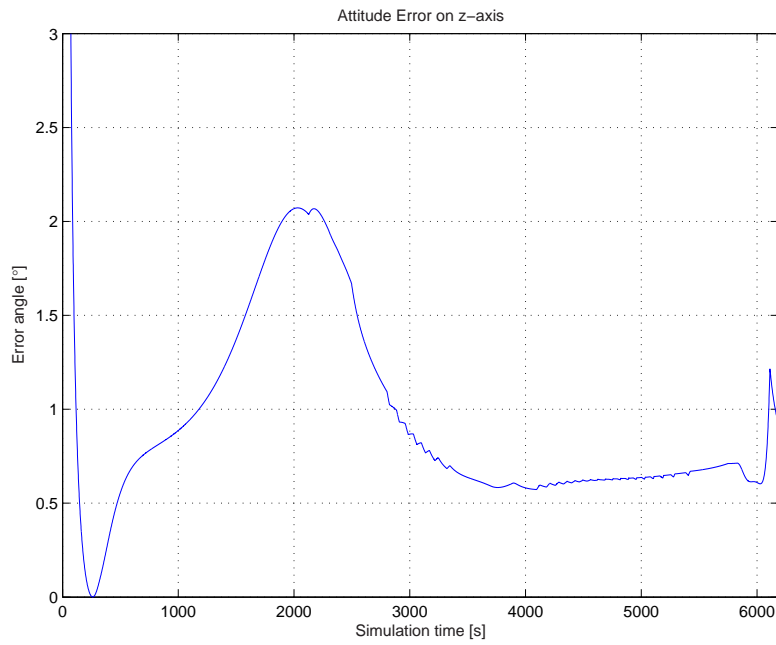


Figure 9.4: The error angle during a simulation with the pointing controller. At $t = 2000$ [s] the NSO is directly above its target, which is Aalborg, Denmark.

9.3.1 Conclusion

Figure 9.4 reveals that the NSO is capable of tracking a fixed location on the Earth, which can be observed in Figure K.19 in Appendix K or by viewing the video on the enclosed CD (see Appendix M). However, a z-axis error angle of 2 [$^{\circ}$] at $t = 2000$ [s], when the satellite is above the target location, is present. As the attitude controller is capable of maintaining an attitude within 0.0174 [deg], the error is assumed to be caused by a demand in the rate change of the attitude and might be resolved increasing the bandwidth of the closed loop system. This would, in turn, require a higher sample rate, but further investigation into this subject is needed, but cannot be completed within the project time frame.

CHAPTER 10

Closure

This chapter presents conclusions on the results obtained in the project and discusses perspectives concerning future projects on robust disturbance rejecting control for small satellites like the NSO, and is addressed to any reader.

10.1 Conclusion

This report has dealt with the development of a robust disturbance rejecting Attitude Control System (ACS) for a small satellite called the North Sea Observer (NSO). In particular the subjects on designing a functional control structure for a satellite pointing controller.

The NSO features a high resolution camera payload, which is to be used to monitor shipping routes in the North Sea, and search for oil spills from seagoing vessels in these waters. By correlating with shipping trajectories it will be possible to identify the leaking vessel. Also included in the payload is an experimental deployable solar cell array, which will enhance on-board power production. It is a student satellite project and complies with the pico-satellite triple CubeSat configuration. To enable attitude effecting actuation in space, the NSO utilises three momentum wheels and three magnetorquers, whereas no orbital manoeuvres are possible.

10.1.1 Requirements

The requirements to the NSO ACS were derived from preliminary estimates of the on-board camera specifications, and a set of tasks defined from known attitude control issues. As the collective capability to acquire and maintain a specified attitude is dependent on on-board attitude determination, the requirements for the ACS stems from initial requirements stated for the unified Attitude Determination and Control System (ADCS). According to Section 1.3 the requirements to the ACS for the satellite maximum attitude error on the camera axis is $0.57 [^\circ]$, which shall be met within a $95 [\%]$ confidence interval.

10.1.2 Modeling

To facilitate simulation and evaluation of the ACS, a simulation environment, using quaternions for attitude representations, was developed. The simulation environment was based on models developed from a previous ADS project group [Group 05gr833 2005]. However, some models were found either inaccurate or incorrect, which is why significant efforts were made to remodel certain aspects in the space environment. Also more accurate modeling

of the actuators was pursued, but found negligible and time consuming in simulations. The models were implemented in SIMULINK facilitating an environment for designing and evaluating the controllers developed in this report.

A general control structure was designed and the model was analysed in light of this choice. The structure included a robust disturbance rejecting controller on the angular velocity of the satellite, an optimal attitude controller, an independent momentum wheel desaturation controller and a camera pointing algorithm. The model analysis included analysis of the accuracy of the linearised model compared to the non-linear, which yielded some additional requirements to the bandwidth of the controllers included in the control structure. Furthermore, the system controllability was examined, which proved system controllability, but emphasised some limitations in the actuator capabilities. Also the requirements for stability for the controllers in the control structure was examined, using Lyapunov stability analysis, which, e.g., determined that a state feedback gain matrix for the angular velocity controller was required to be positive definite.

10.1.3 Controller Design

The angular velocity controller was developed using robust design to handle disturbances on the input to the satellite system and simple uncertainties in the satellite inertia matrix. The robust design of the angular controller was performed using a linear matrix inequality (LMI) feasibility problem, ensuring strongly robust \mathcal{H}_∞ performance, developed by [Zhou et al. 1995]. The feasibility problem was augmented with a pole bounding LMI to ensure the bandwidth requirement to the controller was met. The feasibility problem was then solved as a convex optimisation problem for each vertex in a defined uncertainty region, using a toolbox for MATLAB called YALMIP, and a solver called SeDuMi. To limit the magnitude of the disturbances that the robust controller should suppress, a Kalman filter was introduced to estimate the collective disturbance, which was then fed forward to the satellite.

The momentum wheel desaturation controller was designed using a slightly modified Common Cross Product Law (CCPL) handling the change in the Earth's magnetic field. This controller was also fitted with a trigger algorithm to conserve energy.

To enable the control structure to follow and maintain a reference attitude, an optimal LQR controller was developed. To ensure a steady state gain of zero, this controller was expanded to include integral action.

The ability to track a specified reference location on the Earth's surface, is handled by a developed pointing controller, which was designed with use of mathematical models of the physical relation between the orbiting NSO, and the target location.

10.1.4 Results

The different controllers were individually evaluated and an evaluation of the entire system was subsequently performed, wherein the results were compared to other simpler choices for the individual controller designs.

The introduction of a Kalman filter, estimating the disturbances, in conjunction with the robust controller, indicated a significant reduction on the effects of the disturbances on the angular velocities, and the controller proved able to follow a reference velocity. Furthermore, the desaturation controller was able to dissipate excess angular momentum from the momentum wheels, and the trigger algorithm showed a reduction in power consumption. The optimal attitude controller proved able to execute changes in the attitude. However, if given a reference attitude, requiring the angular momentum vector of the momentum wheels to leave the 1st octant of the SBRF, instability occurs, thus implying the need for a managing algorithm.

Simulating attitude manoeuvres indicated that the designed control structure was faster at acquiring the designated attitude, than the simple substitutions. This can decisively be attributed to the LQR control design. A noticeable fact is that the performance in both configurations did not differ significantly, when introduced to uncertainties in the inertia matrix. However, the bandwidth of the simple control system, when introduced to uncertainties, changed noticeably, but remained virtually unchanged for the robustly controlled system. Therefore, designing a robust controller, as described in this report, is recommended, as the design of such a controller is not significant impediment.

Through Monte Carlo simulations it was found that the designed control structure was able to maintain a reference attitude with an accuracy of 0.0174 [°], within a 95 [%] confidence interval. In comparison the simple substitutions guarantees an error angle of less than 0.1761 [°] for a 95 [%] confidence interval. However, both configurations are still within the requirement, but on account of a vastly better performance and a robustness to uncertainties, the designed control structure is deemed preferable to simpler substitutions.

A qualitative evaluation of the pointing controllers ability to track a fixed location on the Earth, revealed that it did not do so to a satisfactory degree. The angular error on the camera axis exceeded the limit in the requirements by as much as 1.5 [°], whereby further evaluations were deemed futile. The relatively large error is assumed to be caused by the need for fast attitude manoeuvres directly above the target location. This issue might be resolved by increasing the bandwidth of the closed loop system, which would in turn require a higher sample rate. To ensure the demand of the camera tracking ability further investigation into this subject is needed, but could not be completed within the project time frame.

10.2 Discussion

To conclude the project work, presented in this report, a few subjects should be emphasised, which have been the highlights of our work. Firstly, it is desired to point out that the project has proven to be challenging and far-ranging, as the areas included in designing an ACS for a satellite are extensive, which is why certain areas were chosen for further investigation. It is regrettable, to some extent, that we did not chose to make this thesis an extended final project, such that an additional six months would be available to pursue the remaining aspects described in the following section.

The control structure, presented in this report, is considered a great advantage as opposed to designing a singular controller, as this enables designers to be more specific in the design

criteria for the individual controller, also it enables the division of tasks between the project group. However, it proved more challenging to formulate controller requirements.

What proved the most challenging aspect in this project, was the development of the angular velocity controller. A lot of different methods for designing the robustness in the controller were investigated, but the use of LMI problem formulation proved to be very efficient and intuitive to formulate, once the initial \mathcal{H}_∞ LMI formulation was discovered. Bounding the poles in the angular velocity controller, and designing the desaturation controller trigger, were also challenging.

In hindsight not nearly as much effort would be desirable to invest into the modeling, as the interesting part was the controller designs. However, an accurate model is essential to achieve valid evaluations, and we hope that the work put into this subject will be used in later projects. A number of issues in the modeling and dimensioning of the actuators were also reasons for redesigns in applications in the AAUSAT-II project.

The use of quaternions caused a lot of tedious problems. They are not directly comprehensible, and the task of defining usable quaternions, was a task we could have been without. For example if an error quaternion does not have a precise norm bound it can cause errors in the attitude that can be perceived as attitude steady state errors. None the less they ease calculations and modeling considerably, whereby the use of quaternions is recommended.

A number of sources used, especially in the modeling, did prove contradicting. For example the work done by previous groups had to be reevaluated, which proved to be worth the effort. Also the values used in the modeling were multiply defined in different sources, which was why our attention was turned to the values and models in use at ESA. Especially the values preliminarily used in the modeling, were taken from [Wertz 1978], which proved to be outdated, however, the actual models were still valid.

Certainly the NSO project is a student satellite project worth finishing, as it would then be a completely unique achievement.

10.3 Future Work

For future projects on robust disturbance rejecting attitude control systems, the subjects described in this section, would be considered suitable areas for further investigation.

Pointing Control To complete a feasible pointing controller design, which allows for pointing manoeuvres, the need to increase the sampling rate must be investigated. If this is not found feasible, the design of the pointing controller, presented in this report, must be rethought.

Attitude Manoeuvre Manager To allow for larger attitude manoeuvres, which requires the angular momentum vector to leave the 1st octant of the SBRF, a managing algorithm must be developed. This could also be done with a redesign of the attitude controller, but requires further investigation.

Operational Mode Completion It is necessary, for the satellite to function, to design controllers for the remaining locations in the operational mode diagram in Section 3.1.

Suggestions for the design of each controller is given in the related description of each location.

Uncertainty Modeling The uncertainty variation in the inertia matrix considered in this report is not compliant with realistic uncertainty variations, as these would probably yield cross correlations, and thus not only change the diagonal. A different approach to the representations of uncertainties in the inertia matrix should therefore be investigated.

Desaturation Trigger Optimisation It is desirable to find some form of optimisation of the desaturation trigger method, as this could increase the conservation of energy. Here the focus might be turned to the use of modern Model Predictive Control (MPC), as actuation might be more feasible to perform earlier in an orbit, than is presently the case. This requires information about the Earth's magnetic field to be accessible.

Desaturation Performance Enhancement Another enhancement to the desaturation controller could be a complete redesign using optimal control, as this is assumed to increase the performance of the controller. This would also enhance the attitude controllers ability to perform attitude manoeuvres where the angular momentum vector would leave the 1st octant of the SBRF, when using the CCPL controller. Another possible subject for investigation into this area could be the exploitation of the disturbances to desaturate the momentum wheels.

Hybrid Lyapunov Stability Analysis An interesting subject for further investigation is also the use of hybrid system analysis to analyse the Lyapunov stability of the complete system with momentum wheel effects.

Bibliography

- Adams, Douglas. 1978. *The Hitchhiker's Guide to the Galaxy*. Ballantine Books.
ISBN: 0-345-39180-2
- Adaweb. 2006. *Land Records Glossary : Centroid*.
<http://www.adaweb.net/departments/assessor/LandRecordsGlossary.asp>.
- Andersen, Palle. 2006. *Optimal Control*.
<http://www.control.auc.dk/~pa/kurser/Optimal/optnote.pdf>.
- Anderson, David R., Dennis J. Sweeney & Thomas A. Williams. 2003. *Modern Business Statistics with Microsoft Excel*. South Western.
ISBN: 0-324-12174-1
- Angus P. Andrews, Mohinder S. Grewal. 2001. *Kalman Filtering: Theory and Practice - Using MATLAB*. John Wiley & Sons, Inc.
ISBN: 0-471-26638-8
- Arianespace. 2004. *VEGA User's Manual*.
<http://www.arianespace.com/site/images/VEGAUsersManual2.pdf>.
- Bak, Thomas. 1999. *Spacecraft Attitude Determination - a Magnetometer Approach, Ph.D Thesis*. Department of Control Engineering - Aalborg University.
ISBN: 87-90664-03-5
- Bøgh, Søren Abildsten, Rafal Wisniewski & Thomas Bak. 1998. "Autonomous Attitude Control System for the Ørsted Satellite.".
- California Polytechnic State University. 2005. *CubeSat Program*.
http://cubesat.calpoly.edu/_new/index.html.
- California Polytechnic State University. 2006. *CubeSat Specifications*.
<http://littonlab.atl.calpoly.edu/media/Documents/Developers/CDS\%20R9%.pdf>.
- Chilali, Mahmoud & Pascal Gahinet. 1996. " H_∞ Design with Pole Placement Constraints: An LMI Approach." *Automatic Control* 41(3):358–367.
- Chou, Jack C. K. 1992. "Quaternion kinematic and dynamic differential equations." *IEEE Transactions on Robotics and Automation* Vol.8(1):53 –64.
- Clausen, Steen Tøffner, Palle Andersen & Jacob Stoustrup. 1998. "Robust Processreguler- ing - 3. udgave."

BIBLIOGRAPHY

- ELFA Elektronik A/S. 2006. *ELFA-katalog 2006*.
- ESTEC, Requirements & Standards Division ESA. April 1996. *Space Project Management - Project Phasing and Planning*.
[http://www.ecss.nl/forums/ecss/dispatch.cgi/standards/showFile/100073%/d20010105224553/No/ECSS-M-30A%20Project%20phasing%20and%20planning%20\(19%20April%201996\).pdf](http://www.ecss.nl/forums/ecss/dispatch.cgi/standards/showFile/100073%/d20010105224553/No/ECSS-M-30A%20Project%20phasing%20and%20planning%20(19%20April%201996).pdf).
- ESTEC, Requirements & Standards Division ESA. January 2000. *Space Environment*.
[http://www.ecss.nl/forums/ecss/dispatch.cgi/standards/showFile/100092%/d20020625115630/No/ECSS-E-10-04A%20Space%20environment%20\%5Bpage\%201-112%\%5D%20\(21\%20January\%202000\).pdf](http://www.ecss.nl/forums/ecss/dispatch.cgi/standards/showFile/100092%/d20020625115630/No/ECSS-E-10-04A%20Space%20environment%20\%5Bpage\%201-112%\%5D%20(21\%20January\%202000).pdf).
- Franklin, Gene F., J David Powell & Abbas Emami-Naeini. 2002. *Feedback Control of Dynamic Systems*. Prentice-Hall, Inc.
ISBN: 0-13-098041-2
- Franklin, Gene F., J. David Powell & Michael Workman. 1998. *Digital Control of Dynamic Systems*. Addison Wesley Longman, Inc.
ISBN: 0-201-82054-4
- Graversen, Torben, Michael Kvist Frederiksen & Søren Vejlgaard Vedstesen. 2002. *Attitude Control system for AAU CubeSat*.
- Group 04gr830a. 2004. *Attitude Control System for AAUSAT-II*. Aalborg University.
<http://www.aausatii.auc.dk/>
- Group 05gr833. 2005. *Attitude Determination System for AAUSAT-II*. Aalborg University.
- Hughes, Peter C. 1986. *Spacecraft Attitude Dynamics*. Wiley and Sons, Inc.
ISBN: 0-471-81842-9
- Khalil, Hassan K. 2002. *Nonlinear Systems*. 3rd edition Prentice Hall.
ISBN: 0-13-067389-7
- Kuipers, Jack B. 2002. *Quaternions and Rotation Sequences: A Primer with Applications to Orbits, Aerospace, and Virtual Reality*. Princeton University Press.
- Kwon, Young-Hoo. 2006. *Transformation of the Inertia Tensor*.
<http://kwon3d.com/theory/moi/triten.html>.
- Maxon Motor. April 2005. *Maxon DC motor RE-10 data sheet*.
http://www.maxonmotor.com/docsx/Download/catalog_2005/Pdf/05_053_e.pdf.
- National Semiconductor. Downloaded March 2005. *LM628/LM629 Precision Motion Controller*.
<http://www.national.com/ds.cgi/LM/LM628.pdf>.
- Navigation Center. 2005. *Automatic ID System*.
<http://www.navcen.uscg.gov/enav/ais/default.htm>.
- Peck, Mason A. 2003. *Uncertainty Models for Physically Realizable Inertia Dyadics*. Presented at the 2003 Flight Mechanics Symposium, Goddard Space Flight Center.
http://mae.cornell.edu/mpeck/documents/Papers/Inertia_Peck_JAS.pdf.

- Postlethwaite, Sigurd Skogestad & Ian. 2005. *Multivariable Feedback Control - Analysis and Design*. John Wiley and Sons Ltd.
ISBN: 978-0-470-01168-3
- Pulham, John. 2006. *Moments of Inertia*.
http://www.maths.abdn.ac.uk/courses/eg1527/site/pdf/notes/notes10_app%1.pdf.
- Schaten, H. K. 2006. "Solar Activity and the Solar Cycle.".
http://ai-solutions.com/Resources/Papers/cospar-schatten-D1.1-D2.1-E3%.1-0001-05_final.pdf.
- Serway, Raymond A. & Robert J. Beichner. 2000. *Physics For Scientists and Engineers with Modern Physics*. Harcourt College Publishers.
ISBN: 0-03-022657-0
- Stepen Boyd, Laurent El Ghaoui, Eric Feron & Venkataraman Balakrisnan. 1994. *Linear Matrix Inequalities in System and Control Theory*. Society for Industrial and Applied Mathematics.
ISBN: 0-89871-334-X
- Steyn, Willem H. 1995. *A Multi-mode Attitude Determination and Control System for Small Satellites*. University of Stellenbosch.
- Steyn, Willem H. & Xiaojiang Chen. 1998. "Optimal Combined Reaction-Wheel Momentum Management for LEO Earth-Pointing Satellites." *Guidance, Control, and Dynamics*.
- Weisstein, Eric W. Downloaded March 2005. *Cofactor*. MathWorld - A Wolfram Web Resource.
<http://mathworld.wolfram.com/Cofactor.html>.
- Welch, Greg & Gary Bishop. 2001. *An Introduction to the Kalman Filter*.
http://www.cs.unc.edu/~tracker/media/pdf/SIGGRAPH2001_CoursePack_08.pdf
- Wertz, James R. 1978. *Spacecraft Attitude Determination and Control*. Kluwer Academic Publishers.
ISBN: 90-277-0959-9
- Wertz, James R. & Wiley J. Larson. 1999. *Space Mission Analysis*. Microcosm Press and Kluwer Academic Publishers.
ISBN: 1-881883-10-8
- Wie, Bong. 1998. *Space Vehicle Dynamics and Control*. American Institute of Aeronautics and Astronautics, Inc.
ISBN: 1-56347-261-9
- Wikipedia. 2006. *Gamma Ray Bursts*.
<http://www.navcen.uscg.gov/enav/ais/default.htm>.
- Wisniewski, Rafal. 1996. *Satellite Attitude Control Using Only Electromagnetic Actuation*. Department of Control Engineering, Aalborg University.

BIBLIOGRAPHY

Zhou, Kemin, Pramod P. Khargonekar, Jacob Stoustrup & Hans Henrik Niemann. 1995.
“Robust Performance of Systems with Structured Uncertainties in State Space.” *Automatica*, Vol. 31, No.2 pp. 249–255.

APPENDIX A

Inertia Matrix Calculation

This appendix contains the approximated calculation of the inertia matrix of the NSO. The inertia matrix is calculated for two different cases. One where the solar arrays are deployed and one where they have not yet been deployed. It is addressed to the reader with interest in the assumptions and calculation methods used for obtaining the inertia matrix used in the design.

In order to calculate the inertia matrices some assumptions have been made. These are:

- Once the solar arrays are deployed the satellite and the arrays can be perceived as individual objects.
- The deployed solar arrays can be approximated as four solid bricks.
- The satellite body can be approximated as a solid brick.
- When the solar arrays are collapsed the satellite is approximated as a solid brick, with the combined mass of the satellite and the solar arrays.

The solid brick approximations are used since the mass distribution of the satellite is considered even. The inertia matrix is a 3×3 matrix, where the diagonal contains the moments of inertia and the remaining 6 entries are referred to as the products of inertia. In this appendix the following notation for the inertia matrix is used

$$\underline{\mathbf{I}} = \begin{bmatrix} I_{11} & I_{12} & I_{13} \\ I_{21} & I_{22} & I_{23} \\ I_{31} & I_{32} & I_{33} \end{bmatrix}. \quad (\text{A.1})$$

Some facts about the inertia matrix are as follows:

- The moments of inertia must always be positive. The products of inertia can be either positive or negative.
- If the inertia matrix is calculated around the CoM with the principal axis defining the reference frame, the inertia matrix becomes a diagonal matrix containing only the moments of inertia.
- The sum of the moments of inertia are invariant under orientation changes of the reference frame.
- Calculating the eigenvalues of an inertia matrix, yields the principal moments of inertia. Furthermore, the corresponding eigenvectors describes the principal axis.

In the following two sections the inertia matrix is calculated around the CoM.

A.1 Inertia Matrix with the Solar Arrays Deployed

In order to calculate the inertia matrix when the solar arrays are deployed the assumption regarding multiple combined objects is used. First the inertia matrix for each object is calculated around the CoM. In Figure A.1 the locations of the CoM of the 5 objects are shown. The satellite body is referred to as object d_1 and the deployed solar arrays as objects d_2, d_3, d_4 and d_5 .

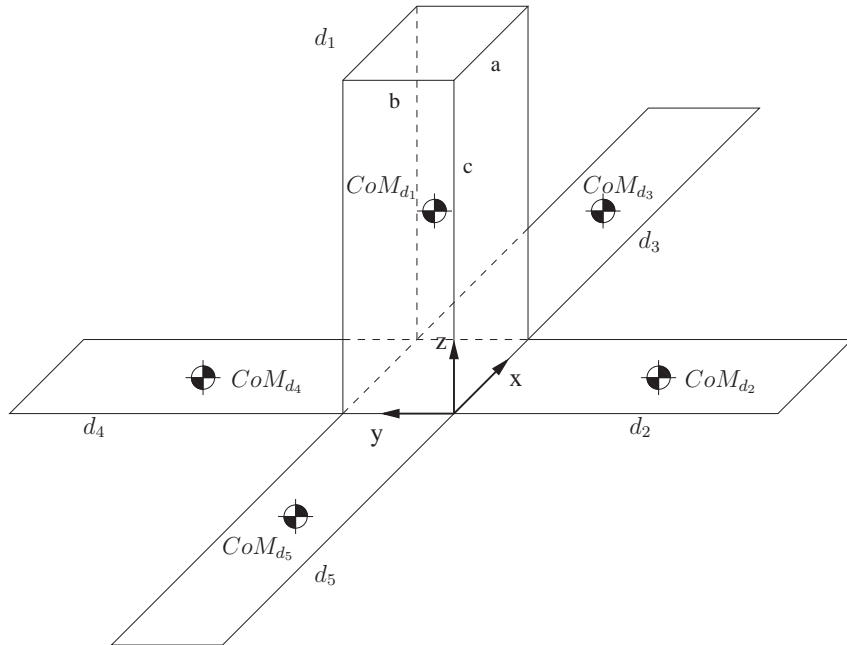


Figure A.1: Location of the CoM for both the satellite and the deployed solar arrays.

Furthermore, Figure A.1 shows the SBRF, which is denoted by the x-, y- and z-axes. In order to calculate the inertia around the CoM of d_1 , this object is considered as a solid brick with mass $m_{body} = 2.5$ [kg]. According to [Pulham 2006] the inertia matrix of a solid brick can be calculated as follows

$$\mathbf{I}_{d_1} = \begin{bmatrix} A & 0 & 0 \\ 0 & B & 0 \\ 0 & 0 & C \end{bmatrix}, \quad (\text{A.2})$$

where A, B and C are given by

$$\begin{aligned} A &= \frac{1}{12}m_{body}(b^2 + c^2) \\ B &= \frac{1}{12}m_{body}(a^2 + c^2) \\ C &= \frac{1}{12}m_{body}(a^2 + b^2). \end{aligned} \quad (\text{A.3})$$

Here a, b and c are the sides of the solid brick, which are depicted in Figure A.1. These are given by the dimensions of the satellite, which are 0.1 [m], 0.1 [m] and 0.3 [m] respectively.

Given all the values (A.2) yields the inertia matrix for the solid brick

$$\underline{\mathbf{I}}_{d_1} = \begin{bmatrix} 0.020833 & 0 & 0 \\ 0 & 0.020833 & 0 \\ 0 & 0 & 0.004167 \end{bmatrix}. \quad (\text{A.4})$$

The inertia matrix of the solar arrays are equal in pairs and can be calculated as object d_1 . The solar arrays are considered as solid bricks with mass $m_{\text{array}} = 0.125$ [kg] and a height of 0.002 [m]. This yields the inertia matrices

$$\underline{\mathbf{I}}_{d_2} = \underline{\mathbf{I}}_{d_4} = \begin{bmatrix} 0.000938 & 0 & 0 \\ 0 & 0.000104 & 0 \\ 0 & 0 & 0.000104 \end{bmatrix} \quad (\text{A.5})$$

$$\underline{\mathbf{I}}_{d_3} = \underline{\mathbf{I}}_{d_5} = \begin{bmatrix} 0.000104 & 0 & 0 \\ 0 & 0.000938 & 0 \\ 0 & 0 & 0.000104 \end{bmatrix}. \quad (\text{A.6})$$

In order to calculate the inertia matrix around the combined CoM of the satellite with deployed solar arrays, it is necessary to calculate the combined CoM. Before this is possible vectors from the origin of the SBRF to each of the CoM's shown in Figure A.1, must be defined. These are expressed as

$$\begin{aligned} \mathbf{p}_1 &= [0.05 \ 0.05 \ 0.15]^T \\ \mathbf{p}_2 &= [0.05 \ -0.15 \ 0]^T \\ \mathbf{p}_3 &= [0.25 \ 0.05 \ 0]^T \\ \mathbf{p}_4 &= [0.05 \ 0.25 \ 0]^T \\ \mathbf{p}_5 &= [-0.15 \ 0.05 \ 0]^T. \end{aligned} \quad (\text{A.7})$$

The defined vectors allow for the calculation of the combined CoM using the expression

$$\mathbf{p}_{\text{CoM}} = \frac{m_{\text{body}}\mathbf{p}_1 + m_{\text{array}}\mathbf{p}_2 + m_{\text{array}}\mathbf{p}_3 + m_{\text{array}}\mathbf{p}_4 + m_{\text{array}}\mathbf{p}_5}{m_{\text{body}} + 4m_{\text{array}}}. \quad (\text{A.8})$$

Inserting the masses m_{body} and m_{array} and the vectors from (A.7), the combined CoM is obtained, yielding

$$\mathbf{p}_{\text{CoM}} = [0.05 \ 0.05 \ 0.125]^T. \quad (\text{A.9})$$

In order to calculate the inertia matrix around the combined CoM the calculated inertia matrices around each CoM, shown in Figure A.1, needs to be translocated to the combined CoM. According to [Kwon 2006] the translocation is given by

$$\underline{\mathbf{I}} = \underline{\mathbf{I}}_{\text{CoM}} + m(\mathbf{p}^T \mathbf{p} \underline{\mathbf{1}}_{3 \times 3} - \mathbf{p} \mathbf{p}^T), \quad (\text{A.10})$$

where $\underline{\mathbf{1}}_{3 \times 3}$ is an identity matrix of the indicated dimension, m is the mass of the combined object and \mathbf{p} is a vector indicating the destination of the translocation. Using (A.10), (A.7),

(A.9) and the masses m_{body} and m_{array} , the following inertia matrices around the combined CoM are obtained:

$$\begin{aligned}\underline{\mathbf{I}}_1 &= \underline{\mathbf{I}}_{d_1} + m_{\text{body}}((\mathbf{p}_{\text{CoM}} - \mathbf{p}_1)^T(\mathbf{p}_{\text{CoM}} - \mathbf{p}_1)\mathbf{1}_{3 \times 3} - (\mathbf{p}_{\text{CoM}} - \mathbf{p}_1)(\mathbf{p}_{\text{CoM}} - \mathbf{p}_1)^T) \\ \underline{\mathbf{I}}_2 &= \underline{\mathbf{I}}_{d_2} + m_{\text{array}}((\mathbf{p}_{\text{CoM}} - \mathbf{p}_2)^T(\mathbf{p}_{\text{CoM}} - \mathbf{p}_2)\mathbf{1}_{3 \times 3} - (\mathbf{p}_{\text{CoM}} - \mathbf{p}_2)(\mathbf{p}_{\text{CoM}} - \mathbf{p}_2)^T) \\ \underline{\mathbf{I}}_3 &= \underline{\mathbf{I}}_{d_3} + m_{\text{array}}((\mathbf{p}_{\text{CoM}} - \mathbf{p}_3)^T(\mathbf{p}_{\text{CoM}} - \mathbf{p}_3)\mathbf{1}_{3 \times 3} - (\mathbf{p}_{\text{CoM}} - \mathbf{p}_3)(\mathbf{p}_{\text{CoM}} - \mathbf{p}_3)^T) \\ \underline{\mathbf{I}}_4 &= \underline{\mathbf{I}}_{d_4} + m_{\text{array}}((\mathbf{p}_{\text{CoM}} - \mathbf{p}_4)^T(\mathbf{p}_{\text{CoM}} - \mathbf{p}_4)\mathbf{1}_{3 \times 3} - (\mathbf{p}_{\text{CoM}} - \mathbf{p}_4)(\mathbf{p}_{\text{CoM}} - \mathbf{p}_4)^T) \\ \underline{\mathbf{I}}_5 &= \underline{\mathbf{I}}_{d_5} + m_{\text{array}}((\mathbf{p}_{\text{CoM}} - \mathbf{p}_5)^T(\mathbf{p}_{\text{CoM}} - \mathbf{p}_5)\mathbf{1}_{3 \times 3} - (\mathbf{p}_{\text{CoM}} - \mathbf{p}_5)(\mathbf{p}_{\text{CoM}} - \mathbf{p}_5)^T)\end{aligned}$$

Adding these 5 inertia matrices, yields the inertia matrix around the combined CoM for the satellite when the solar arrays are deployed, which is given by

$$\begin{aligned}\underline{\mathbf{I}}_{\text{sat}_d} &= \underline{\mathbf{I}}_1 + \underline{\mathbf{I}}_2 + \underline{\mathbf{I}}_3 + \underline{\mathbf{I}}_4 + \underline{\mathbf{I}}_5 \Rightarrow \\ \underline{\mathbf{I}}_{\text{sat}_d} &= \begin{bmatrix} 0.0423 & 0 & 0 \\ 0 & 0.0423 & 0 \\ 0 & 0 & 0.0283 \end{bmatrix}. \quad (\text{A.11})\end{aligned}$$

A.2 Inertia Matrix without Deployment

The calculation of the satellite's inertia matrix when the solar arrays are collapsed is straight forward using the preceding procedure. In Figure A.2 the CoM of the satellite is depicted. Since the solar arrays are not deployed, it is assumed that the satellite has one combined mass of $m_{\text{sat}} = 3 \text{ [kg]}$.

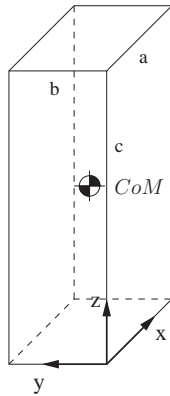


Figure A.2: Location of the CoM of the satellite, without deployment of the solar arrays.

It is therefore possible to calculate the inertia matrix under the assumption that the satellite is a solid brick with the specified mass. Given the dimensions of the satellite, and using (A.2), the following inertia matrix is obtained

$$\underline{\mathbf{I}}_{\text{sat}_c} = \begin{bmatrix} 0.025 & 0 & 0 \\ 0 & 0.025 & 0 \\ 0 & 0 & 0.005 \end{bmatrix}.$$

The calculated inertia matrices in this appendix are used for calculation of various torques which makes the actuator design feasible. Furthermore, the inertia matrices are used in the simulation environment.

APPENDIX B

Tasks and Requirements

This appendix defines and explains the different tasks for the NSO and describes their implications on the ACS. On grounds hereof the requirements for the ACS are stated. It is addressed to the reader with interest in the specified requirements for the ACS of the NSO.

As there are no direct mission objectives for the NSO, this report will only deal with known attitude issues with satellites requiring communication, pointing of a payload and maximising the power input. The requirements will throughout the requirement specification be stated for the entire ADCS, and finally the direct implications for the ACS will be derived.

B.1 Tasks for ADCS

Since the exact orbit height, at which the satellite is released into after deployment, is unknown, the requirements for ADCS on NSO are made for worst case scenarios for orbit heights between 500 [km] and 900 [km], as a 200 [km] deviation from the specified 700 [km] circular polar orbit specified in the VEGA user manual [Arianespace 2004] is considered.

B.1.1 Detumbling

As the satellite leaves the launch vehicle it will be ejected from a separation mechanism, called a P-POD¹. This P-POD utilises a loaded spring to eject the satellite, and this spring cannot be assumed to apply an even force on the satellite. On account of this, it is assumed that the satellite will have an initial angular velocity at the time of separation, which is known as satellite tumbling. The initial worst case single axis angular velocity is assumed to be 0.1 [rad/s], as this is a commonly used value for the initial tumbling rate, but the actual figure is very dependent on the separation mechanism, cf. Annex 1. In order to consider the satellite as detumbled, the angular velocity of the satellite shall be equal to or less than the change in angular rotation, caused by the satellite moving in the magnetic field of the Earth. Hereby it is assumed that a simple attitude controller is present in the NSO in the form of a magnetic dipole. This minimises the risk of constantly having a low antenna gain in the direction of the Earth. The worst case scenario will be if a "blind spot", meaning an antenna gain so low that no signal reaches the ground station, points towards the ground station during an entire pass. This problem has the same properties as the requirements for rotation, which are described in Section B.1.2.

The magnetic field causes the vector field to rotate 2 times during an orbit, as illustrated in Figure B.1.

¹Poly-Picosatellite Orbital Deployer

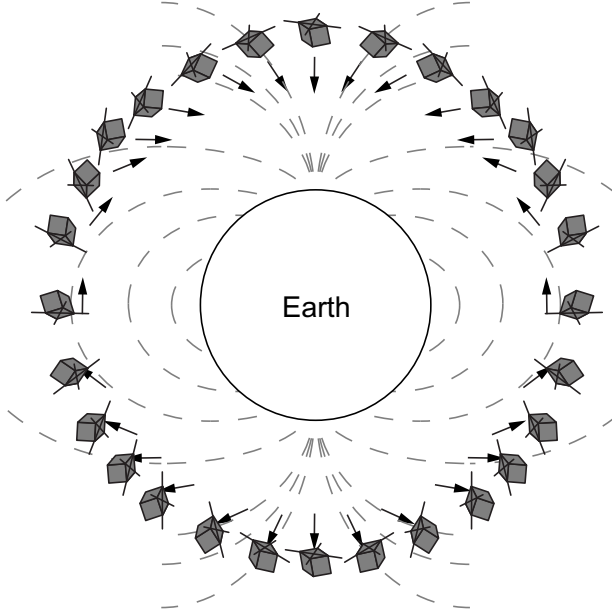


Figure B.1: Rotation of a satellite, in a circular orbit, stabilised by a magnetic dipole.

According to [Wertz & Larson 1999, Earth Satellite Parameters table col:52] the orbit time for a satellite in an orbit height of 900 [km] is 102.99 [min] ≈ 6179.4 [s]. This yields a mean angular velocity of the satellite, $\|\omega\|$, given by

$$\|\omega_{\text{det}}\| = 2 \cdot \frac{2\pi}{6179.4 \text{ [s]}} = 0.00203 \text{ [rad/s]} \approx 0.117 \text{ [°/s].} \quad (\text{B.1})$$

The satellite is considered detumbled, when the mean angular velocity is 0.117 [°/s] or lower. To limit the time that the satellite may be incapable of communication with a ground station, due to extensive tumbling, the required detumbled rate must be obtained within two orbits. According to [Bøgh, Wisniewski & Bak 1998] it should be feasible to obtain the velocity stated in (B.1). This means that satellite tracks the rotation of the geomagnetic field.

B.1.2 Rotation

To ensure higher efficiency during transmission at high data rates, the antenna on the satellite shall point directly towards the ground station, with the direction that ensures maximum gain. Therefore, the satellite shall rotate π [rad] during a pass, which is worst case when an ideal pass, at an orbit height of 500 [km], occurs.

According to Figure B.2 the maximum arch section of the orbit, α , visible from a ground station can be calculated as

$$\begin{aligned} \alpha &= 2 \cdot \arccos \left(\frac{R_E}{R_O} \right) \quad \Rightarrow \\ \alpha &= 2 \cdot \arccos \left(\frac{6378166 \text{ [m]}}{6378166 \text{ [m]} + 500000 \text{ [m]}} \right) \approx 0.7673 \text{ [rad]} \approx 44 \text{ [°].} \end{aligned} \quad (\text{B.2})$$

This gives, using an orbit time of $T_O = 5677.2$ [s] at an orbit height of 500 [km] [Wertz &

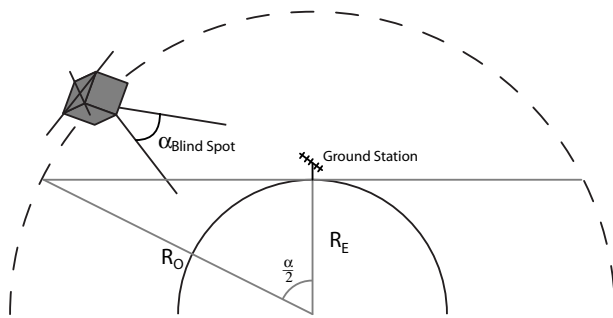


Figure B.2: Satellite during pass of a ground station.

Larson 1999, Earth Satellite Parameters table col: 52], a maximum time in view, T_v , of

$$\begin{aligned} T_v &= \frac{\alpha}{2\pi} \cdot T_O \quad \Rightarrow \\ T_v &= \frac{0.7673 \text{ [rad]}}{2\pi \text{ [rad]}} \cdot 5677.2 \text{ [s]} = 693 \text{ [s]}, \end{aligned} \quad (\text{B.3})$$

which yields a minimum angular velocity of the satellite of

$$\omega_{\min} = \frac{\pi}{693 \text{ [s]}} = 0.0045 \text{ [rad/s]} \approx 0.26 \text{ [°/s]}. \quad (\text{B.4})$$

The satellite shall be able to maintain an angular velocity of minimum 0.26 [°/s] during a pass, to ensure a stable communication line with maximum antenna gain.

In order to clarify the problem with a "blind spot", that was mentioned in Section B.1.1, the inequality in (B.5) is calculated when the satellite is detumbled. This yields the smallest angle, for which communication would be a problem,

$$\begin{aligned} \alpha_{\text{Blind spot}} &< T_v \cdot \omega_{\det} \quad \Rightarrow \\ \alpha_{\text{Blind spot}} &< 693 \text{ [s]} \cdot 0.00203 \text{ [rad/s]} = 1.4068 \text{ [rad]} \approx 81 \text{ [°]}. \end{aligned} \quad (\text{B.5})$$

If the measurements for the antenna gain turns out to have "blind spots" that, according to the link budget, are larger than 84 [°], the demands for the ADCS regarding detumbling must be reevaluated.

B.1.3 Payload

The on-board camera has to point at a certain location on the Earth's surface, which must be done with a certain accuracy to ensure that the picture taking is of the designated area. This is called a pointing demand.

If an oil spill is thought to be found at a certain location in the sea, the ADCS shall be accurate enough to ensure that the oil spill is included in the picture taken. As indicated in Section 1.1.4 the pointing demand for the entire ADCS system is to point the camera axis at the desired location, within an accuracy of 1.57 [°].

The regularly used orbit parameters (TLE's)² might not be sufficient, as they could be off by around 20 [km] [Bak 1999]. Therefore, it might be necessary to use other position

²Two Line Elements

describing methods, such as GPS. This is, however, not investigated further in this project, as this project mainly deals with attitude control.

B.1.4 Sun Pointing

Similarly to the pointing demand for the camera payload, there will be a pointing demand for the satellite to point the deployed solar arrays towards the Sun when possible. In [Group 05gr833 2005] a model of a solar cell was developed as a simple cosine dependence. Therefore, when regarding the solar arrays as being in the same plane when deployed, the power output from the solar arrays will not be degraded substantially for small deviations from the optimal sun-pointing direction. Hereby, if the maximal normalised output from a solar cell, pointed perfectly at the Sun, is 1 [.], then a pointing deviation of 5 [$^{\circ}$] would yield a normalised power output of 0.996 [.], whereby a deviation of 5 [$^{\circ}$] is considered acceptable. As this requirement is lower than the requirement for payload pointing, the payload requirement is considered the requirement in effect.

B.2 System Requirements

The following requirements to the ADCS shall be met with a 95 [%] confidence interval:

1. The ADCS shall be able to detumble the satellite from $0.1 \text{ [rad/s]} \approx 5.73 \text{ [} ^{\circ}/\text{s} \text{]}$ to $0.117 \text{ [} ^{\circ}/\text{s} \text{]}$ or below, within two orbits.
2. The ADCS shall be able to rotate the satellite at an angular velocity of at least $0.26 \text{ [} ^{\circ}/\text{s} \text{]}.$
3. The ADCS shall be able to point the camera at a location on the Earth or the solar arrays at the Sun center, with a maximum deviation from the correct direction of $1.57 \text{ []}.$

B.2.1 Requirements for ACS

From the requirements to ADCS the requirements for ACS shall now be derived. According to [Group 05gr833 2005] the ADS can ensure a maximum deviance of $3.37 \text{ []},$ within a 95.44 [%] confidence interval. This number has since the finalisation of [Group 05gr833 2005] been improved, such that a maximum deviation of under $1 \text{ [} ^{\circ} \text{]}$ is ensured. This is, however, not documented due to the fact that the project group 05gr833 has been split up to pursue other projects. Their word is, therefore, used as reference, and the sub-degree performance of the ADS is adopted. This means that the before stated requirements reduce to

1. unchanged when regarding the detumbling capability.
2. unchanged when regarding the rotational capability.
3. reduced to a demand of a maximum deviation from the optimal direction of 0.57 [] within a 95 [%] confidence interval.

APPENDIX C
Quaternions

Since the kinematics of the satellite, for calculation purposes, are best expressed in quaternion form, this appendix includes quaternion definitions and describes the fundamental algebraic properties of quaternions. As sources for this appendix [Wertz 1978, page 758-759] and [Chou 1992] are used. This appendix is addressed to the reader requiring knowledge about the quaternions used throughout the report.

C.1 Quaternion Definitions

A quaternion is a hyper complex number, and can be defined as

$$\mathbf{q} = \hat{\mathbf{i}}q_1 + \hat{\mathbf{j}}q_2 + \hat{\mathbf{k}}q_3 + q_4, \quad (\text{C.1})$$

where the hyperimaginary numbers $\hat{\mathbf{i}}$, $\hat{\mathbf{j}}$ and $\hat{\mathbf{k}}$ satisfy the conditions,

$$\begin{aligned}\hat{\mathbf{i}}^2 &= \hat{\mathbf{j}}^2 = \hat{\mathbf{k}}^2 = -1 \\ \hat{\mathbf{i}}\hat{\mathbf{j}} &= -\hat{\mathbf{j}}\hat{\mathbf{i}} = \hat{\mathbf{k}} \\ \hat{\mathbf{j}}\hat{\mathbf{k}} &= -\hat{\mathbf{k}}\hat{\mathbf{j}} = \hat{\mathbf{i}} \\ \hat{\mathbf{k}}\hat{\mathbf{i}} &= -\hat{\mathbf{i}}\hat{\mathbf{k}} = \hat{\mathbf{j}}.\end{aligned} \quad (\text{C.2})$$

In (C.1) the parameter q_4 is also known as the real part, or the scalar part. The first three terms in (C.1) are normally denoted the imaginary part or vector part. By defining the vector part as

$$\mathbf{q}_{1:3} = \hat{\mathbf{i}}q_1 + \hat{\mathbf{j}}q_2 + \hat{\mathbf{k}}q_3, \quad (\text{C.3})$$

it is possible to introduce the following representation of (C.1)

$$\mathbf{q} = (\mathbf{q}_{1:3}, q_4). \quad (\text{C.4})$$

When quaternions are used for attitude descriptions, and general rotations of objects, the four parameters (q_1, q_2, q_3, q_4) are defined as

$$q_1 = e_1 \sin(\theta/2) \quad (\text{C.5})$$

$$q_2 = e_2 \sin(\theta/2) \quad (\text{C.6})$$

$$q_3 = e_3 \sin(\theta/2) \quad (\text{C.7})$$

$$q_4 = \cos(\theta/2), \quad (\text{C.8})$$

where $e_1^2 + e_2^2 + e_3^2 = 1$. This implies that $\|\mathbf{q}\| = 1$, and further that the use of this subset of quaternions performs rotations while preserving lengths. In Figure C.1 the vector and the angle, used to express the quaternion, are depicted.

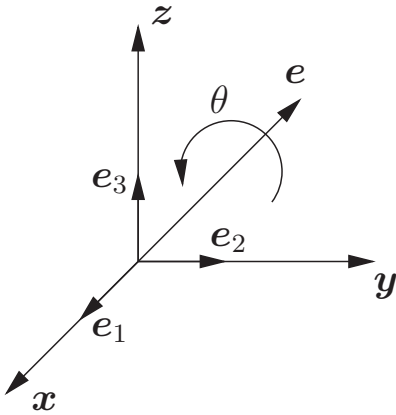


Figure C.1: Components of the quaternion depicted in a coordinate system.

The difference between two quaternions, i.e. the attitude error can be calculated as

$$\mathbf{q}_{\text{err}} = \mathbf{q}_{\text{att}}^{-1} \mathbf{q}_{\text{ref}}, \quad (\text{C.9})$$

where \mathbf{q}_{att} is the calculated attitude quaternion and \mathbf{q}_{ref} is the reference attitude quaternion [Wertz 1978, page 605]. Therefore, an error quaternion of the composition $[0 \ 0 \ 0 \ 1]^T$ means that the two compared attitudes are identical.

C.2 Quaternion Algebra

The fundamental mathematical operations, that will be described in this section, are addition and subtraction of quaternions, the norm and inverse of quaternions and multiplication of quaternions.

C.2.1 Addition and Subtraction

The addition and subtraction of quaternions obey the associative and commutative laws and are defined as

$$\mathbf{q}_A \pm \mathbf{q}_B = (\mathbf{q}_{A1:3} \pm \mathbf{q}_{B1:3}) + (q_{A4} \pm q_{B4}). \quad (\text{C.10})$$

Quaternions are added and subtracted as normal complex numbers or vectors.

C.2.2 Norm and Inverse

The norm of a quaternion is calculated as the norm of a complex number, and is defined as

$$\|\mathbf{q}\| = \sqrt{q_1^2 + q_2^2 + q_3^2 + q_4^2}. \quad (\text{C.11})$$

The inverse of a quaternion is defined as

$$\mathbf{q}^{-1} = \frac{\mathbf{q}^*}{\|\mathbf{q}\|}, \quad (\text{C.12})$$

where \mathbf{q}^* is the complex conjugate of \mathbf{q} , which is defined as

$$\mathbf{q} = -\hat{\mathbf{i}}q_1 - \hat{\mathbf{j}}q_2 - \hat{\mathbf{k}}q_3 + q_4 = (-\mathbf{q}_{1:3} + q_4). \quad (\text{C.13})$$

From (C.12) it should be noticed that when the norm of a quaternion is 1, the inverse of that quaternion is equal to the complex conjugate of that same quaternion.

C.2.3 Multiplication

Quaternion multiplication is performed in the same way as multiplication of complex numbers. However, the order of operation must be taken into account as quaternion multiplication does not obey the commutative law, i.e., $\mathbf{q}_A \mathbf{q}_B \neq \mathbf{q}_B \mathbf{q}_A$.

The following expression defines the multiplication of two quaternions, \mathbf{q}_A and \mathbf{q}_B .

$$\mathbf{q}_C = \mathbf{q}_A \mathbf{q}_B = (\hat{\mathbf{i}}q_{A_1} + \hat{\mathbf{j}}q_{A_2} + \hat{\mathbf{k}}q_{A_3} + q_{A_4})(\hat{\mathbf{i}}q_{B_1} + \hat{\mathbf{j}}q_{B_2} + \hat{\mathbf{k}}q_{B_3} + q_{B_4}). \quad (\text{C.14})$$

Using (C.2) it is possible to express (C.14) as

$$\begin{aligned} \mathbf{q}_C = \mathbf{q}_A \mathbf{q}_B &= \hat{\mathbf{i}}(q_{A_1}q_{B_4} + q_{A_2}q_{B_3} - q_{A_3}q_{B_2} + q_{A_4}q_{B_1}) \\ &+ \hat{\mathbf{j}}(-q_{A_1}q_{B_3} + q_{A_2}q_{B_4} + q_{A_3}q_{B_1} + q_{A_4}q_{B_2}) \\ &+ \hat{\mathbf{k}}(q_{A_1}q_{B_2} - q_{A_2}q_{B_1} + q_{A_3}q_{B_4} + q_{A_4}q_{B_3}) \\ &+ (-q_{A_1}q_{B_1} - q_{A_2}q_{B_2} - q_{A_3}q_{B_3} + q_{A_4}q_{B_4}). \end{aligned} \quad (\text{C.15})$$

In matrix form (C.15) becomes

$$\begin{bmatrix} q_{C_1} \\ q_{C_2} \\ q_{C_3} \\ q_{C_4} \end{bmatrix} = \begin{bmatrix} q_{B_4} & q_{B_3} & -q_{B_2} & q_{B_1} \\ -q_{B_3} & q_{B_4} & q_{B_1} & q_{B_2} \\ q_{B_2} & -q_{B_1} & q_{B_4} & q_{B_3} \\ -q_{B_1} & -q_{B_2} & -q_{B_3} & q_{B_4} \end{bmatrix} \begin{bmatrix} q_{A_1} \\ q_{A_2} \\ q_{A_3} \\ q_{A_4} \end{bmatrix}. \quad (\text{C.16})$$

Given two successive rotations \mathbf{q}_A and \mathbf{q}_B , (C.16) gives the components of the quaternion that describes the combined rotation, \mathbf{q}_C .

C.3 Quaternion Rotation

Rotation of a vector, \mathbf{p} from reference frame A to B described by a quaternion, ${}^B_A \mathbf{q}$ yields

$$\begin{bmatrix} {}^B \mathbf{p} \\ 0 \end{bmatrix} = {}^B_A \mathbf{q}^{-1} \begin{bmatrix} {}^A \mathbf{p} \\ 0 \end{bmatrix} {}^B_A \mathbf{q}, \quad (\text{C.17})$$

where ${}^B \mathbf{p}$ is the vector, \mathbf{p} , in the B reference frame.

APPENDIX D

Worst Case Disturbance Torques

This appendix deals with calculation of worst case disturbance torques, which are used to dimension the satellite actuators. The disturbance torques are calculated for both collapsed and deployed solar arrays. This appendix is addressed to the reader with interest in the calculations of the worst case disturbance torques.

The CoM of the satellite with collapsed solar arrays must be within 2 [cm] of the geometric center to comply with the CubeSat specifications [California Polytechnic State University 2006]. When the solar arrays are deployed the CoM is calculated assuming that the combined mass of the solar arrays is 0.5 [kg] and the mass of the satellite body is 2.5 [kg].

D.1 Aerodynamic Torque

The aerodynamic torque can be calculated as

$${}^S\mathbf{N}_A = {}^S\mathbf{R}_{Acp} \times {}^S\mathbf{F}_A, \quad (\text{D.1})$$

where ${}^S\mathbf{R}_{Acp}$ is a vector from the CoM to the geometrical center and ${}^S\mathbf{F}_A$ is calculated as

$${}^S\mathbf{F}_A = -\frac{1}{2}\rho_{air} C_D A \|{}^S\mathbf{V}\|^2 {}^S\hat{\mathbf{V}}, \quad (\text{D.2})$$

where ${}^S\hat{\mathbf{V}}$ is the unit vector in the direction of the translational velocity, \mathbf{V} , of the satellite, ρ_{air} is the worst case atmospheric density, $C_D = 2$ is the drag coefficient and A is the total exposed area of the satellite, which is measured in a plane perpendicular to the translational motion. The atmospheric density can be found from the $F10.7$ value using SPENVIS. The NSO is expected to be launched late 2007 or early 2008 which according to [Schatten 2006] is in the beginning of solar cycle 24, where $F10.7 = 70$ is expected. However, the models used in [Schatten 2006] has previously been offset approximately one year, and therefore a value of 120 is used instead. $F10.7 = 120$ yields an atmospheric density of $\rho_{air} \approx 730 \cdot 10^{-15} [\frac{\text{kg}}{\text{m}^3}]$. According to [ESTEC January 2000, page 74] seasonal variations can cause changes in the air density up to $6.5 \cdot 10^{-12} [\frac{\text{kg}}{\text{m}^3}]$, and a density of $\rho_{air} = 7.23 \cdot 10^{-12} [\frac{\text{kg}}{\text{m}^3}]$ is therefore used in the calculations.

As the torque is dependent of the exposed area and the cross product between the velocity vector and the vector from the CoM to the geometrical center, which both change as the satellite's attitude changes. The calculations have been performed in the m-file, `aerodynamic_drag_worst.m` (see Appendix M). The maximum aerodynamic torques is calculated to $365.2 \cdot 10^{-9} [\text{Nm}]$ when the solar arrays are collapsed and $1549.2 \cdot 10^{-9} [\text{Nm}]$ with deployed solar arrays.

D.2 Radiation Torque

The radiation torque is calculated using

$${}^S\mathbf{N}_R = {}^S\mathbf{R}_{Rcp} \times {}^S\mathbf{F}_R, \quad (\text{D.3})$$

where ${}^S\mathbf{R}_{Rcp}$ is a vector from the satellite CoM to the CoP of the radiation and ${}^S\mathbf{F}_R$ is defined as

$${}^S\mathbf{F}_R = C_R A P {}^S\hat{\mathbf{S}}, \quad (\text{D.4})$$

where $C_R = 1.5$ is a constant depending on how light is reflected on the satellite surface, A is the cross sectional area of the satellite perpendicular to the sun vector and P is the momentum flux from the Sun, given by $P = 4.4 \cdot 10^{-6} [\text{kg/ms}^2]$. Due to the similarities between radiation torque and aerodynamic torque, as the cross sectional area and vector from the CoM to the geometrical center, the maximum radiation torque has been calculated using the m-file, `radiation_worst_case.m`, which is similar to the aerodynamic torque calculations (see Appendix M). The maximum radiation torque is $5.8 \cdot 10^{-9} [\text{Nm}]$, when the solar arrays are collapsed, and $24.4 \cdot 10^{-9} [\text{Nm}]$ when the solar arrays are deployed.

D.3 Gravity Gradient Torque

The gravity gradient torque is calculated as

$$\mathbf{N}_{GG} = \frac{3Gm_E}{\|\mathbf{R}\|^3} \left[\hat{\mathbf{R}} \times (\underline{\mathbf{I}} \hat{\mathbf{R}}) \right], \quad (\text{D.5})$$

where $G = 66.726 \cdot 10^{-12} [\frac{\text{Nm}^2}{\text{kg}^2}]$ is the gravitational constant, $m_E = 5.9742 [\text{kg}]$ is the mass of the Earth, \mathbf{R} is a vector from the center of the Earth to the satellite and $\underline{\mathbf{I}}_{sat}$ is the moment of inertia matrix. Assuming $\underline{\mathbf{I}}_{sat}$ is diagonal it is possible to calculate the cross product using the determinant and defining three vectors, \mathbf{e}_1 , \mathbf{e}_2 , and \mathbf{e}_3 , which describes the axis of a right-handed coordinate system. This yields

$$\begin{aligned} \hat{\mathbf{R}} \times (\underline{\mathbf{I}}_{sat} \hat{\mathbf{R}}) &= \begin{vmatrix} \hat{\mathbf{e}}_1 & \hat{\mathbf{e}}_2 & \hat{\mathbf{e}}_3 \\ R_1 & R_2 & R_3 \\ I_{sat_{11}}R_1 & I_{sat_{22}}R_2 & I_{sat_{33}}R_3 \end{vmatrix} \\ &= \begin{bmatrix} R_2I_{sat_{33}}R_3 - R_3I_{sat_{22}}R_2 \\ R_3I_{sat_{11}}R_1 - R_1I_{sat_{33}}R_3 \\ R_1I_{sat_{22}}R_2 - R_2I_{sat_{11}}R_1 \end{bmatrix} = \begin{bmatrix} (I_{sat_{33}} - I_{sat_{22}})R_2R_3 \\ (I_{sat_{11}} - I_{sat_{33}})R_3R_1 \\ (I_{sat_{22}} - I_{sat_{11}})R_1R_2 \end{bmatrix}. \end{aligned} \quad (\text{D.6})$$

Assuming $I_{sat_{11}} > I_{sat_{22}} > I_{sat_{33}}$, the largest gravity gradient torque appears when $R_2 = 0$ and R_3R_1 assumes the largest possible value with in the constraint $R_1^2 + R_3^2 = 1$. This can be solved using Lagrange multipliers, which yields $R_1 = R_3 = \frac{\sqrt{2}}{2}$. Rotating $\hat{\mathbf{R}} = [\frac{\sqrt{2}}{2}, 0, \frac{\sqrt{2}}{2}]$ to the SBRF and inserting it in (2.9), along with the inertia matrix and μ , yield a gravity gradient torque of $36.8 \cdot 10^{-9} [\text{Nm}]$ when the solar arrays are collapsed, and $25.5 \cdot 10^{-9} [\text{Nm}]$ with deployed solar arrays. The calculations have been performed in the m-file, `gravity_gradient_worst_case.m` (see Appendix M)

D.4 Total Disturbance Torque

Table D.1 summarises the worst case torques due to disturbances.

Disturbance	Collapsed torque	Deployed torque
Aerodynamic torque	$365.2 \cdot 10^{-9}$ [Nm]	$1549.2 \cdot 10^{-9}$ [Nm]
Radiation torque	$5.8 \cdot 10^{-9}$ [Nm]	$24.4 \cdot 10^{-9}$ [Nm]
Gravity gradient torque	$36.8 \cdot 10^{-9}$ [Nm]	$25.5 \cdot 10^{-9}$ [Nm]
Total	$407.5 \cdot 10^{-9}$ [Nm]	$1599.1 \cdot 10^{-9}$ [Nm]

Table D.1: Worst case disturbance torques due to aerodynamic torque, radiation torque and gravity gradient torque.

APPENDIX E

Magnetotorquer Model

In this appendix the modeling of the magnetotorquers on the NSO is performed. First a model of the magnetotorquers will be derived and then the coil dimensioning will be described yielding the final magnetotorquer parameters. It is addressed to the reader with interest in a comprehensive modeling and design of the magnetotorquers.

The magnetotorquers used on the NSO are rectangular coils with the sides S_{α_1} , S_{α_2} , S_{β_1} , S_{β_2} , as shown in Figure E.1. The arrows indicate the direction of the current in the coil. When placed in a magnetic field, the force, \mathbf{F} , acting on each side of the coil, can be described by [Serway & Beichner 2000, page 912]

$$\mathbf{F}_i = ni_{mt} \mathbf{S}_i \times \mathbf{B}, \quad i = \{\alpha_1, \alpha_2, \beta_1, \beta_2\}, \quad (\text{E.1})$$

where n is the number of windings in the coil, i_{mt} is the current in the coil and \mathbf{B} is the magnetic field vector. The resulting force, \mathbf{F}_{res} , can, therefore, be described by

$$\mathbf{F}_{\text{res}} = \sum_i ni_{mt} \mathbf{S}_i \times \mathbf{B}, \quad i = \{\alpha_1, \alpha_2, \beta_1, \beta_2\}. \quad (\text{E.2})$$

Figure E.1 shows the magnetotorquer placed in a magnetic field and the forces acting on each side of the coil.

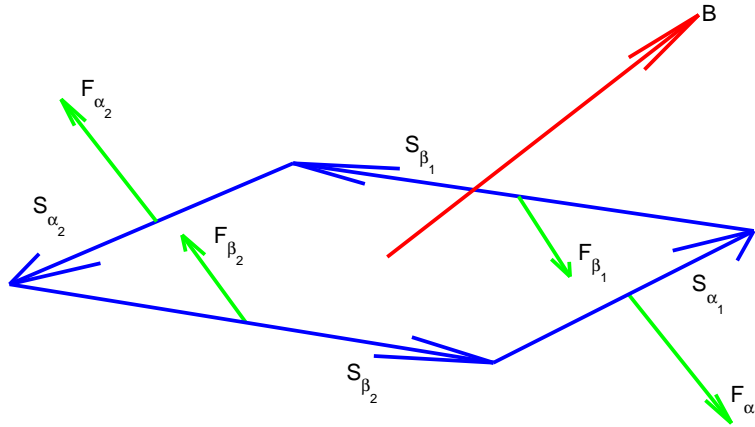


Figure E.1: Representational diagram of a magnetotorquer showing the resulting forces created by applying a current to the coil in a magnetic field, represented by the vector \mathbf{B} .

Because the current loops in the coil the resulting force will be equal to zero. Hereby it is assumed that the coil elements are of equal length in pairs, which also implies that the forces are of equal magnitude in pairs, yielding

$$\mathbf{F}_{i_1} = -\mathbf{F}_{i_2}, \quad i = \{\alpha, \beta\}, \quad (\text{E.3})$$

As \mathbf{F}_{res} is zero the orbit of the satellite cannot be changed by the magnetorquer. It can, however, create a torque as the forces are acting on the sides of the coil, which are non-collocated with the CoM. The resulting torque can be used to change the attitude of the satellite.

The resulting torque exerted on the satellite by two parallel coil elements, is given by a force acting on one of the parallel coil elements crossed with a perpendicular coil element ending in the origin of the coil element, on which the force acted. This can be formulated as

$$\mathbf{N}_i = \mathbf{F}_i \times \mathbf{S}_{i+}, \quad i = \{\alpha, \beta\}, \quad (\text{E.4})$$

where $i+$ indicates the perpendicular coil element with the desired properties.

This is true for all satellites where the CoM projected onto the coil plane lies within the area spanned by the coil elements, i.e., not outside the satellite encasing. As the NSO has deployable elements situated in one extremity of the satellite, this property might not apply. However, as the camera on the satellite is situated on the opposing extremity, the mass is considered adequately distributed along the longitudinal axis for this property to apply.

To deduce the collective torque exerted on the entire coil it is useful to view the coil as having two sides parallel to the magnetic field vector. If the two sides parallel to the magnetic field were the α -sides, no forces would be exerted on these as $\mathbf{B} \times \mathbf{S}_\alpha = \mathbf{0}$. Moreover, the force exerted on a β -side would be defined as

$$\mathbf{F}_\beta = ni_{\text{mt}} \mathbf{S}_\beta \times \mathbf{B}. \quad (\text{E.5})$$

The total torque exerted on the coil will now be described by

$$\begin{aligned} \mathbf{N}_{\text{Total}} &= ni_{\text{mt}} \mathbf{S}_{\beta_1} \times \mathbf{B} \times \frac{\mathbf{S}_{\alpha_1}}{2} + ni_{\text{mt}} \mathbf{S}_{\beta_2} \times \mathbf{B} \times \frac{\mathbf{S}_{\alpha_2}}{2} \\ &= ni_{\text{mt}} A_{\text{mt}} \hat{\mathbf{n}} \times \mathbf{B}, \end{aligned} \quad (\text{E.6})$$

where $\hat{\mathbf{n}}$ is a unit normal vector to the coil plane, which direction is determined by using the right-hand rule and A_{mt} is the area spanned by the coil. The term $ni_{\text{mt}} A_{\text{mt}} \hat{\mathbf{n}}$ is often expressed as the magnetic dipole moment, \mathbf{M}_{mt} .

Although the torque was obtained for a particular orientation of \mathbf{B} with respect to the current loop, (E.6) is valid for any orientation and for any loop shape [Serway & Beichner 2000].

To take into account the electro mechanic properties of the coil and simultaneously facilitate the possibility of impressing a voltage to the magnetorquer to produce the desired torque, a transfer function for the coil is introduced. This can be described by

$$\begin{aligned} v_{\text{mt}} &= R_{\text{mt}} i_{\text{mt}} + L_{\text{mt}} \frac{di_{\text{mt}}}{dt} \quad \Rightarrow \\ \frac{i_{\text{mt}}(s)}{v_{\text{mt}}(s)} &= \frac{1}{R_{\text{mt}} + L_{\text{mt}} s}, \end{aligned} \quad (\text{E.7})$$

where R_{mt} and L_{mt} are the coil resistance and coil self inductance respectively. The coil resistance is dependent on the coil temperature, which is assumed consistent with the satellite internal temperature. The coil resistance is given by

$$R_{\text{mt}} = \frac{nC\sigma_{0_{\text{cu}}}(1 + \alpha_{0_{\text{cu}}}(T - T_0))}{A_{\text{wire}}}, \quad (\text{E.8})$$

where $\sigma_{0_{\text{cu}}} = 1.7 \cdot 10^{-8} [\Omega\text{m}]$ is the resistivity of copper at 293 [K], $\alpha_{0_{\text{cu}}} = 3.9 \cdot 10^{-3} [\text{K}^{-1}]$ is the resistivity temperature coefficient, C is the circumference of the coil, T is the temperature, T_0 is the resistivity base temperature and A_{wire} is the wire cross sectional area.

Dimensioning

To determine the coil parameters the maximum values of external torque requirements are used. Each coil must be able to produce a torque greater than the torque required to detumble the satellite, and also overcome the maximum collective disturbance torque exerted on the satellite. The maximum torque required to detumble the satellite is given from the requirements in Section B.1.1 by

$$\begin{aligned} \max(N_{\text{det}}) &= \max \left(C_{\underline{\mathbf{I}}_{\text{sat}_d}} \frac{(C_{\omega_{\text{tumble}_{\text{init}}}} - C_{\omega_{\text{tumble}_{\text{det}}}})}{O_{\text{det}} t_{\text{orbit}}} \right) \Rightarrow \\ &= \max \left(\begin{bmatrix} 0.0423 & 0 & 0 \\ 0 & 0.0423 & 0 \\ 0 & 0 & 0.0283 \end{bmatrix} \cdot \begin{bmatrix} 1 \\ 1 \\ 1 \end{bmatrix} \cdot \frac{0.1 - 0.00203}{2 \cdot 5677.2} \right) \\ &= 364.98 \cdot 10^{-9} [\text{Nm}], \end{aligned} \quad (\text{E.9})$$

where $C_{\underline{\mathbf{I}}_{\text{sat}_d}}$ is the inertia matrix of the satellite in the deployed state, $C_{\omega_{\text{tumble}_{\text{init}}}}$ is the initial tumble rate vector of the satellite, $C_{\omega_{\text{tumble}_{\text{det}}}}$ is the rate at which detumbling has been achieved, O_{det} is the number of orbits, in which detumbling must be achieved and t_{orbit} is the orbit time in seconds at a worst case orbit height of 500 [km]. Furthermore, \max denotes the maximum value of the calculated torque vector. From (E.9) and Table D.1 the collective maximum required torque is acquired, whereby the required magnetic dipole moment magnitude is

$$\begin{aligned} M_{\text{mt}_{\text{req}}} &\geq 2 \cdot \frac{N_{\text{det}} + N_{\text{dist}}}{B_{\min}} \Rightarrow \\ M_{\text{mt}_{\text{req}}} &\geq 2 \cdot \frac{(364.98 + 1599.1) \cdot 10^{-9}}{30 \cdot 10^{-6}} \\ &\geq 130.94 \cdot 10^{-3} [\text{Am}^2], \end{aligned} \quad (\text{E.10})$$

when using a safety factor of two and a minimum magnetic field strength, B_{\min} , of $30 \cdot 10^{-6} [\text{T}]$ [Group 04gr830a 2004], which is at the equator.

The coils will be rectangular and the dimensions guesstimated to be $70 [\text{mm}] \times 70 [\text{mm}]$ for the coil on the z -side and $210 [\text{mm}] \times 70 [\text{mm}]$ for the remaining two sides, if feasible with the final satellite mechanics. The coil dimensions are chosen to maximise the coil area in order to reduce the magnitude of the current required in the coil. The coil material is chosen to be copper wire with a diameter of $0.2 [\text{mm}]$. The coil parameter calculations are performed in Appendix F to refrain from going astray from the subject at hand. In Appendix F the parameters for the magnetorquers in Table E.1 are found, and additional properties are concluded upon. The calculation of the coil inductances are based on the work done by [Group 04gr830a 2004], with a number of modifications.

With the given dimensions the rectangular magnetorquers are capable of producing a magnetic dipole moment of $202.97 \cdot 10^{-3} [\text{Am}^2]$ in a worst case scenario, and the quadratic magnetorquer one of $135.31 \cdot 10^{-3} [\text{Am}^2]$. As stated in Appendix F the mass and power

Parameter	Symbol	Value
Windings in rectangular coils	n_{xy}	435 [.]
Windings in quadratic coil	n_z	865 [.]
Self inductance in rectangular coils	$L_{mw_{xy}}$	$25.956 \cdot 10^{-3}$ [H]
Self inductance in quadratic coil	L_{mw_z}	$59.256 \cdot 10^{-3}$ [H]

Table E.1: Parameters used in the magnetorquer modeling.

consumption of the magnetorquers are considered feasible with preliminary budgets, but will have to be reevaluated at a later stage.

A preliminary implementation of the magnetorquers in SIMULINK shows that the effect of the coil inductance significantly prolongs simulations. This is not considered acceptable, which is why the error produced from leaving out the coil inductance is examined by comparing the model with and without the inductance. Only the magnetic dipole moment is examined to leave out the influence of the changing magnetic field. The results can be seen in Figure E.2, where it is evident that the error is significantly small to justify leaving out the inductance in the model. This is on account of a very short large deviation of only 1.5 [ms] immediately after a pulse signal is applied on the input at $t = 1$ [s], and that the error after this large deviation is only around 1 [%].

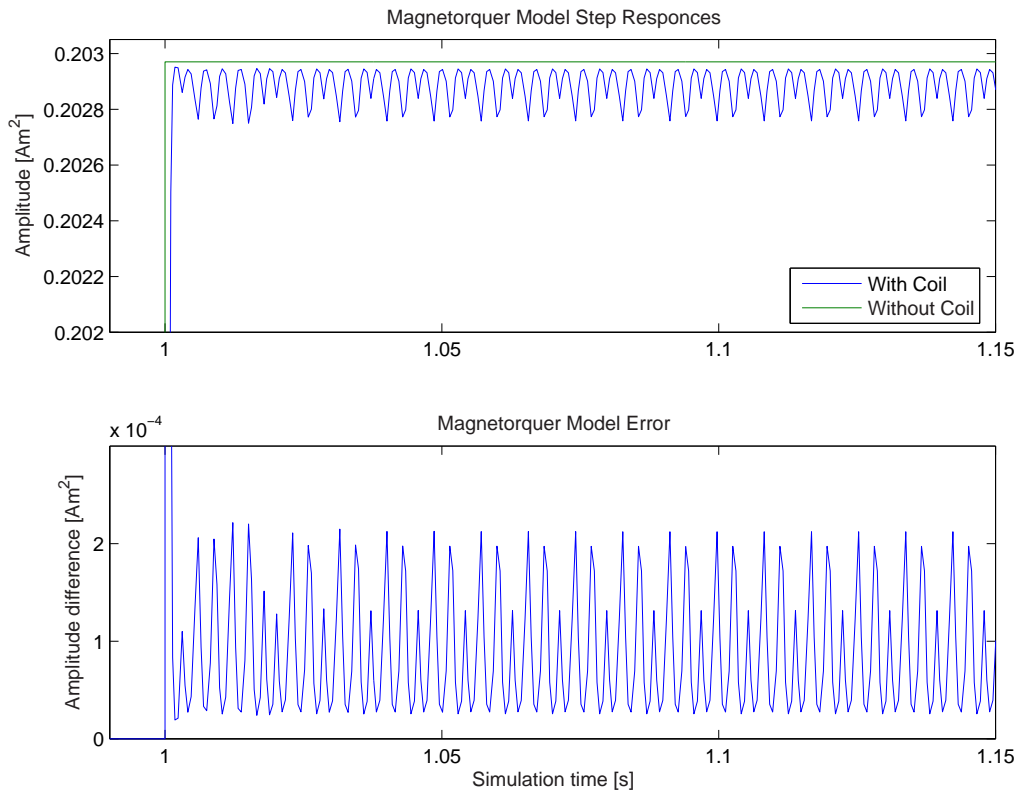


Figure E.2: Magnetorquer modeling errors. The inductance is found negligible.

Using the magnetorquer parameters the finalised model of the magnetorquers has been implemented in SIMULINK as depicted in Figure L.6 in Appendix L.

APPENDIX F

Magnetorquer Design

In this appendix the dimensioning of the magnetorquers is performed. The procedure followed is based on the work done by [Group 04gr830a 2004], however some erroneous equations are corrected and correct values for copper material properties are used. It is addressed to the reader with interest in the specific design of the magnetorquers.

F.1 Prerequisites and Assumptions

The following are the prerequisites used in the magnetorquer dimensioning:

- From Appendix E it is known that the required magnetic dipole moment from a magnetorquer is $130.94 \cdot 10^{-3} [\text{Am}^2]$.
- The material used in the coil is copper wire. Copper has a nominal mass density of $\rho_{\text{cu}} = 8.92 \cdot 10^{-3} [\text{kg/m}^3]$ and a resistivity of $\sigma_{0,\text{cu}} = 1.7 \cdot 10^{-8} [\Omega\text{m}]$ at 293 [K], with a resistivity temperature coefficient of $\alpha_{0,\text{cu}} = 3.9 \cdot 10^{-3} [\text{K}^{-1}]$
- The maximum mean voltage delivered to the coil terminals is 5 [V] from the ADCS PCB.
- The magnetic vacuum permeability is $\mu_0 = 4\pi \cdot 10^{-7} [\text{Wb/Am}]$.
- The xy -coils are rectangular with the dimensions 210 [mm] \times 70 [mm] and the z -coil is square with the dimensions 70 [mm] \times 70 [mm].

All constants are found in [Serway & Beichner 2000]. Furthermore, the following assumptions are made for the worst cases:

- The worst case temperature for the resistance in the coils, when looking for the maximum magnetic dipole moment, is guesstimated to be 343 [K] internally in the satellite.
- The worst case temperature for the resistance in the coil, when looking for the maximum current in the coils, is guesstimated to be 248 [K] internally in the satellite.
- The flux density is considered constant, when calculating the inductance of the coil.
- The rectangular coils on the x and y axes can be approximated by a square coil with side length $l_{xy} = \sqrt{A_{xy}} \Rightarrow l_{xy} = \sqrt{0.21 \cdot 0.07} = 0.121 [\text{m}]$.

F.2 Formulas

To provide an overview of the formulas used in the dimensioning of the magnetorquers, they are successively listed and the individual parameters are explained.

$$R_{\text{mt}} = \frac{nC\sigma_{0\text{cu}}(1 + \alpha_{0\text{cu}}(T - T_0))}{A_{\text{wire}}} \quad (\text{F.1})$$

$$P_{\text{mt}} = v_{\text{mt}} I_{\text{mt}} = i_{\text{mt}}^2 R_{\text{mt}} \quad (\text{F.2})$$

$$m_{\text{mt}} = V_{\text{mt}} \rho_{\text{cu}} = nCA_{\text{wire}} \rho_{\text{cu}} \quad (\text{F.3})$$

$$M_{\text{mt}} = nI_{\text{mt}} A_{\text{mt}} \quad (\text{F.4})$$

$$B_{\text{mt}} = \frac{\mu_0 2\sqrt{2}nI_{\text{mt}}}{\pi l} \quad (\text{F.5})$$

$$\Phi_{\text{mt}} = B_{\text{mt}} A_{\text{mt}} \quad (\text{F.6})$$

$$L_{\text{mt}} = \frac{n\Phi_{\text{mt}}}{I_{\text{mt}}} = \frac{\mu_0 2\sqrt{2}n^2 A_{\text{mt}}}{\pi l}, \quad (\text{F.7})$$

where

- R_{mt} : Resistance in the coil [Ω].
- n : Number of windings in the coil [.].
- C : Circumference of the coil [m].
- T : Temperature of material [K].
- T_0 : Resistivity base temperature [K].
- A_{wire} : Cross sectional area of wire [m^2].
- P_{mt} : Coil power consumption [W].
- v_{mt} : Coil terminal voltage [V].
- i_{mt} : Coil current [A].
- m_{mt} : Mass of the coil (assuming coil volume valid at 273 [K]) [Kg].
- V_{mt} : Volume of the coil [m^3].
- M_{mt} : Magnetic moment generated by the coil [Am^2].
- B_{mt} : Magnetic field strength [T].
- Φ_{mt} : Magnetic flux [Wb].
- L_{mt} : Self inductance of the coil [H].
- l : Side length of the quadratic coil [m].

Calculations are performed with the intent to achieve the required magnetic dipole moment at maximum mean voltage from the ADCS hardware. The initial parameter, upon which the coil dimensioning is performed, is the number of windings in the coil. The coil properties are checked for compliance with the magnetic dipole moment requirement and also the coil's capability to cope with a maximum impressed terminal voltage. The latter is dependent on the wire thickness, which determines the amount of current the wire is able to carry. The data for the current carrying capability of a wire is acquired from a catalog from ELFA Elektronik A/S [ELFA Elektronik A/S 2006] and divided by two, as the value provided are based on Earth applications. The wire thickness is chosen to be 0.2 [mm] or AWG¹ 32.

¹ American Wire Gauge

Upon adjustment of the number of windings in the coils, the parameters for the coils were as stated in Table F.1.

Parameter	xy-coils	z-coil
Windings [.]	435	865
Worst case current [A]	$46.005 \cdot 10^{-3}$	$46.271 \cdot 10^{-3}$
Worst case power consumption [W]	$333.39 \cdot 10^{-3}$	$335.32 \cdot 10^{-3}$
Mass [kg]	$68.264 \cdot 10^{-3}$	$67.872 \cdot 10^{-3}$
Magnetic moment [Am^2]	$202.97 \cdot 10^{-3}$	$135.31 \cdot 10^{-3}$
Self inductance [H]	$25.956 \cdot 10^{-3}$	$59.256 \cdot 10^{-3}$

Table F.1: Magnetorquer parameters.

As can be seen from Table F.1 the required magnetic dipole moment is acquired and the worst case power consumptions are considered within reasonable limits. However, this will have to be reevaluated when more is known about the satellite power budget. Likewise is valid for the mass of the magnetorquers, when considering the unknown mass budget.

The calculations for the magnetorquer dimensioning is performed in a MATLAB m-file, where also all constants are stated. The m-file can be found on the enclosed CD-ROM, of which the content is described in Appendix M.

APPENDIX G

Momentum Wheel Model

In this appendix the modeling of the momentum wheels on the NSO is performed. First an electrical model of the motor used will be derived and then the effects of the inherent mechanical properties. The final parameters of the momentum wheel is then obtained from calculations and the design of a hardware controller present on the ADCS PCB. It is addressed to the reader with interest in a detailed modeling and design of the momentum wheels.

The NSO is equipped with three momentum wheels consisting of a flywheel mounted on a DC-motor. When the flywheel is accelerated by the motor the change in angular momentum generates a torque, which makes the satellite rotate. The momentum wheels are aligned parallel to the axes of the SBRF. This section is based on [Franklin, Powell & Emami-Naeini 2002].

The DC-motor chosen for the momentum wheels, is similar to the ones used on AAUSAT-II being a Maxon RE 10 (Order No. 256086) [Maxon Motor April 2005]. It runs at a nominal voltage of 3 [V] and is available in a space qualified version.

Electrical Model

The torque of the DC-motor is generated by moving a conductor in a magnetic field. Since the orientation of the conductors is approximately orthogonal to the magnetic field, the torque of the motor, N_m , is proportional to the current, i_{mw} , with the motor torque constant, C_t , as the proportionality factor. Hence the torque of the motor is given by

$$N_m = C_t i_{mw}. \quad (\text{G.1})$$

When a conductor is moved in a magnetic field an electromotive force, e_{mw} , is generated. It is approximated by a linear combination of the angular velocity of the rotor, ω_{mw} , and the motor speed constant, C_s . Thus, the electromotive force can be approximated by

$$e_{mw} \approx C_s \omega_{mw}. \quad (\text{G.2})$$

Figure G.1 illustrates the electrical equivalent diagram of a DC-motor. From this diagram it is possible to derive the relation between the armature voltage, v_{mw} , the motor current, i_{mw} , and the angular velocity, ω_{mw} . The armature voltage is given by

$$v_{mw} = R_{mw} i_{mw} + L_{mw} \frac{di_{mw}}{dt} + e_{mw} = R_{mw} i_{mw} + L_{mw} \frac{di_{mw}}{dt} + C_s \omega_{mw}, \quad (\text{G.3})$$

where R_{mw} is the resistance in the motor coils and L_{mw} is the inductance of the coils. R_{mw} is considered independent of the temperature.

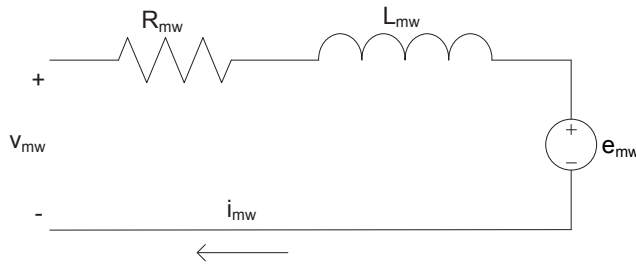


Figure G.1: Electrical equivalent diagram of a DC-motor.

Mechanical Model

With the attachment of a flywheel to the motor axel, the momentum wheel will also have to include a mechanical model. Figure G.2 illustrates a free body diagram of the motor and load, i.e., the flywheel. N_m is the torque generated by the motor and N_f is the torque generated due to friction.

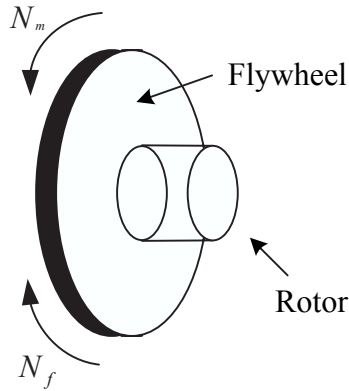


Figure G.2: Free body diagram of the motor and load. N_m is the torque generated by the motor and N_f is the torque generated on account of friction.

From the free body diagram and Euler's law of rotational motion it is possible to derive the torque of the momentum wheel as

$$N_{mw} = I_{mw} \frac{d\omega_{mw}}{dt} = (I_r + I_{fw}) \frac{d\omega_{mw}}{dt} = N_m - N_f, \quad (\text{G.4})$$

where I_{mw} is the moment of inertia of the momentum wheel given by the sum of the moment of inertia of the rotor, I_r , and the moment of inertia of the load, I_{fw} .

In order to utilise a linear model and avoid unnecessary wear of the motors, they will be actuated around a bias point, thus never crossing a zero operation voltage. Therefore, only viscous friction is included in the model.

The torque generated by friction, N_f , is proportional to the angular velocity, ω_{mw} , with the viscous friction coefficient, μ_f , as the proportionality factor, yielding

$$N_f = \mu_f \omega_{mw}. \quad (\text{G.5})$$

From (G.1), (G.4) and (G.5) follows that the torque of the momentum wheel can be expressed as

$$N_{\text{mw}} = I_{\text{mw}} \frac{d\omega_{\text{mw}}}{dt} = C_t i_{\text{mw}} - \mu_f \omega_{\text{mw}}. \quad (\text{G.6})$$

In Figure L.7 in Appendix L the SIMULINK implementation of the momentum wheel model is illustrated. A voltage saturation has been inserted to ensure that the motor cannot exceed operational limits.

Dimensioning

As the motor for the momentum wheel model is reused from the AAUSAT-II satellite the dimensioning needed for the momentum wheel is only the flywheel inertia. The momentum wheels must be able to suppress the disturbances exerted on the satellite. From Table D.1 the maximum collective disturbance torque is found to be $1599.1 \cdot 10^{-9}$ [Nm]. Furthermore, the momentum wheels must be capable for storing the angular momentum generated by the disturbances, for at least the time the satellite must point towards a location in the North Sea, which is 693 [s] as stated in the requirements in Section B.1.2. Using a safety factor of two the required angular momentum is therefore

$$h_{\text{mw max}} = 2 \cdot 1599.1 \cdot 10^{-9} \cdot 693 = 2.2 \cdot 10^{-3} [\text{kgm}^2/\text{s}]. \quad (\text{G.7})$$

Thus, when introducing the bias on the angular velocity, the inertia required for the flywheel is calculated as

$$\begin{aligned} I_{\text{mw}} &\geq \frac{h_{\text{mw max}}}{\omega_{\text{max}}/2} \quad \Rightarrow \\ I_{\text{fw}} &\geq \frac{2h_{\text{mw max}}}{\omega_{\text{max}}} - I_r \quad \Rightarrow \quad I_{\text{fw}} \geq \frac{2 \cdot 2.2 \cdot 10^{-3}}{1.0786 \cdot 10^3} - 6.7 \cdot 10^{-9} \\ &\geq 4.073 \cdot 10^{-6} [\text{kgm}^2], \end{aligned} \quad (\text{G.8})$$

when defining $\omega_{\text{max}} = 1.0786 \cdot 10^3$ [rad/s] as the no load speed [Maxon Motor April 2005]. The calculated inertia corresponds to a cylindrical flywheel of steel with a radius of 16.0 [mm] and a height of 5 [mm], as stainless 18Cr-8Ni steel has a density of $\rho_{\text{steel}} = 8.03 \cdot 10^3$ [kg/m³]. These dimensions result in an inertia of the steel flywheel of $4.133 \cdot 10^{-6}$ [kgm²], thus yielding a collective inertia of the momentum wheel of $4.139 \cdot 10^{-6}$ [kgm²].

The final parameters used in the momentum wheel model are stated in Table G.1, and all, with the exception of the flywheel inertia, are derived form the motor datasheet [Maxon Motor April 2005].

The viscous friction coefficient is calculated from the no load speed, the no load current and the torque constant. The no load values are, however, measured in the effects of gravity and will, therefore, not yield a true value. However, the calculated coefficient is still considered a good estimate.

Hardware Controller

The motor for the momentum wheel is locally controlled by a hardware PID-controller on the ADCS subsystem PCB. This controller must be included in the model of the momentum

Parameter	Symbol	Value
Armature resistance	R_{mw}	8 [Ω]
Armature inductance	L_{mw}	$0.07 \cdot 10^{-3}$ [H]
Momentum wheel inertia	I_{mw}	$4.139 \cdot 10^{-6}$ [kgm ²]
Torque constant	C_t	$2.67 \cdot 10^{-3}$ [Nm/A]
Speed constant	C_s	0.0027 [$\frac{\text{V}}{\text{rad/s}}$]
Friction coefficient	μ_f	$39.606 \cdot 10^{-9}$ [$\frac{\text{Nm}}{\text{rad/s}}$]

Table G.1: Parameters used in the momentum wheel modeling.

wheel, in order to get a realistic simulation result. The Laplace transformed transfer function for the momentum wheel is given by

$$\begin{aligned} \frac{\omega_{\text{mw}}(s)}{v_{\text{mw}}(s)} &= \frac{\frac{C_t}{I_{\text{mw}}L_{\text{mw}}s^2 + (I_{\text{mw}}R_{\text{mw}} + \mu_f L_{\text{mw}})s + \mu_f R_{\text{mw}}}}{1 + C_s \frac{C_t}{I_{\text{mw}}L_{\text{mw}}s^2 + (I_{\text{mw}}R_{\text{mw}} + \mu_f L_{\text{mw}})s + \mu_f R_{\text{mw}}}} \\ &= \frac{C_t}{I_{\text{mw}}L_{\text{mw}}s^2 + (I_{\text{mw}}R_{\text{mw}} + \mu_f L_{\text{mw}})s + \mu_f R_{\text{mw}} + C_t C_s}, \end{aligned} \quad (\text{G.9})$$

From a preliminary implementation of the momentum wheel model, it is known that the inherent second order dynamics in the momentum wheel system requires significant long computation time. Therefore, the possibility of excluding the coil influence in the motor model has been investigated using the parameters in Table G.1, and the results found are illustrated in Figure G.3.

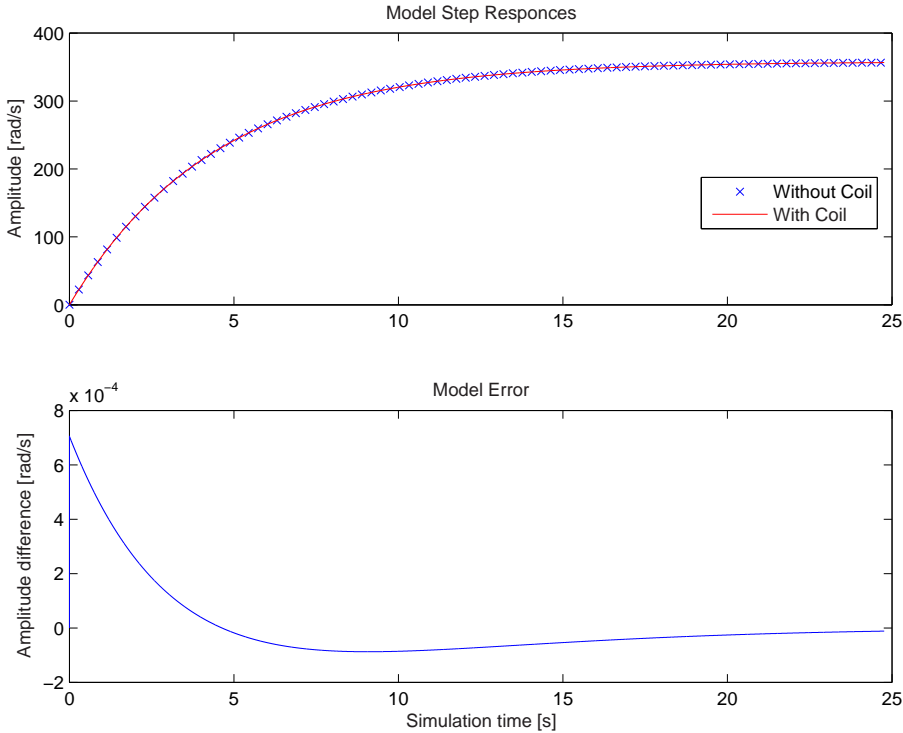


Figure G.3: Plot of momentum wheel step responses with and without motor coil influence. Bottom plot visualises the difference between the two models.

As seen in Figure G.3 the difference in the momentum wheel models are insignificant with

a maximum deviation of $0.70528 \cdot 10^{-3}$ [rad/s] for a short period of time. This is due to a coefficient in second order dynamics of only $289.8 \cdot 10^{-12}$ [,], and the difference is expected to be even smaller with the introduction of a hardware controller. On these grounds the effect of the motor coil is excluded from the momentum wheel model and the transfer function is reduced to

$$\frac{\omega_{\text{mw}}(s)}{v_{\text{mw}}(s)} = \frac{C_t}{I_{\text{mw}}R_{\text{mw}}s + \mu_f R_{\text{mw}} + C_t C_s}. \quad (\text{G.10})$$

The motor system without the influence of the motor inductance has a DC-gain of

$$\begin{aligned} g_{\text{mw}} &= \frac{C_t}{\mu_f R_{\text{mw}} + C_s C_t} \Rightarrow \\ &= \frac{2.67 \cdot 10^{-3}}{39.606 \cdot 10^{-9} \cdot 8 + 0.0027 \cdot 2.67 \cdot 10^{-3}} = 357.97 [.]. \end{aligned} \quad (\text{G.11})$$

A PID-controller's transfer function is [Franklin, Powell & Emami-Naeini 2002, Page 218]

$$\frac{C_d s^2 + C_p s + C_i}{s}. \quad (\text{G.12})$$

The discrete PID-controller is equipped with a $5 \cdot 10^6$ [Hz] clock, and therefore the sample rate is

$$f_s = \frac{f_{\text{clk}}}{2048} \Rightarrow f_s = \frac{5 \cdot 10^6}{2048} = 2.441 \cdot 10^3 \text{ [Hz]}, \quad (\text{G.13})$$

according to [National Semiconductor Downloaded March 2005, Page 9]. The sampling theorem requires that $f_s > 2f_b$ [Franklin, Powell & Workman 1998, Page 450], where f_b is the closed loop system bandwidth, in order to get a stable system. However, to achieve an acceptable smooth time response the sampling multiple must be $\frac{f_s}{f_b} \geq 20$ as a rule of thumb. Therefore, the maximum bandwidth of the system must be 122 [Hz].

Since the DC-gain of the motor model is 357.97 [] the initial gain for the hardware controller is set to $\frac{1}{357.97} []$ in order to achieve a closed loop unit gain. The frequency response of the closed loop system with unit gain is plotted in Figure G.4.

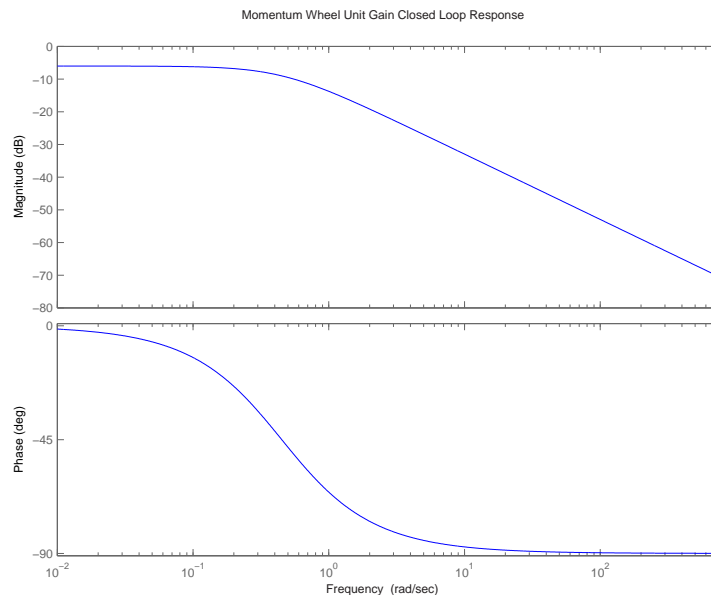


Figure G.4: Frequency response of the momentum wheel with a hardware PI-controller ensuring closed loop unit gain.

As the gain at the bandwidth frequency is -70.6442 [dB] the hardware controller gain is increased by the positive equivalent value, thus maintaining an acceptable smooth time response system. This protrudes as a bit much, but none the less the effect will be studied. The hardware controller proportional gain is therefore

$$C_p = 10^{\frac{70.6442}{20}} \cdot \frac{1}{357.97} = 9.514 [.] \quad (\text{G.14})$$

A pure P-controller has a small DC-error and hence an integrator is introduced. The I-gain is determined using a rule of thumb, stating the gain as $C_i = \frac{1}{10}$ of the P-gain. The resulting frequency response is shown in Figure G.5. The system bandwidth now is 122 [Hz], which yields a acceptable smooth time response.

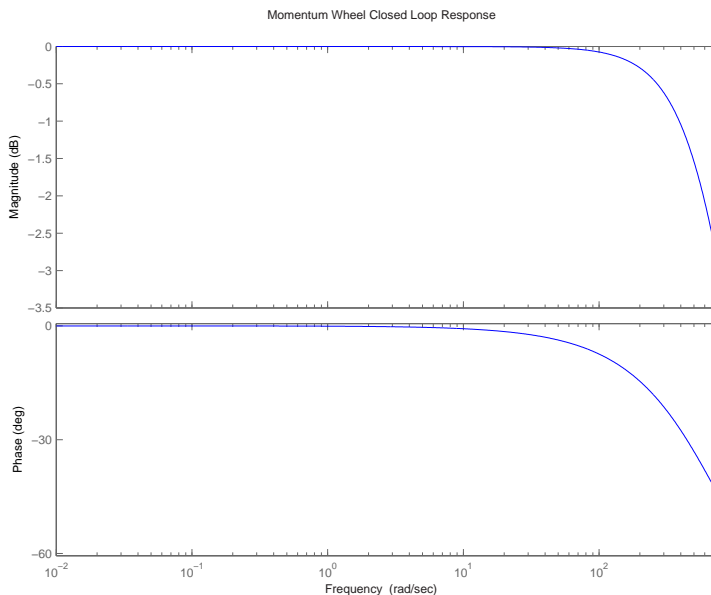


Figure G.5: Frequency response of the momentum wheel with a hardware PI-controller ensuring maximum closed loop gain.

A continuous PID-controller is inserted into the momentum wheel model as a discrete implementation involves a slower simulation time and the difference is minimal with the high sample rate. However, implementation indicates that the gain of the controller, as expected, is far to large, when introduced to the implemented motor with actuator saturation, as the input voltage is switched very fast between upper and lower limit of the input. It is desired to keep the motor at either a positive or negative input voltage and never reaching the voltage limitations, when running at a constant speed. Therefore, the proportional gain is tuned by iteration to achieve an acceptable response, where a final value of $C_p = 0.4$ is adopted, thus yielding a bandwidth of approximately 5 [Hz]. The C_i term is kept at a tenth of the proportional gain. No differential term is introduced to limit the noise susceptibility of the control loop.

As the motor model includes a non-linear voltage saturation the PID-controller used is also expanded to include anti-integrator wind-up. The wind-up limits are set to ± 3 to correlate with the non-linear motor voltage saturation. To implement the hardware controller on the ADCS PCB the function C2D in MATLAB can be utilised, thus finalising the design by emulation approach. This is considered outside the project scope.

APPENDIX H

Rotations

This appendix explains different rotation methods, such as direction cosine matrix denoted attitude matrix, Euler angles and Euler's eigenaxis rotation theorem. Furthermore, this appendix deals with the derivation of the kinematic differential equation for the attitude matrix and is based on [Kuipers 2002] and [Wie 1998, page 307-329]. It is addressed to the reader with interest in a detailed description of various rotation forms.

H.1 Direction Cosine

In the following two reference frames, A and B, will be used, which are both right handed and have bases formed by the orthogonal sets of unit vectors $(\hat{\mathbf{a}}_1, \hat{\mathbf{a}}_2, \hat{\mathbf{a}}_3)$ and $(\hat{\mathbf{b}}_1, \hat{\mathbf{b}}_2, \hat{\mathbf{b}}_3)$ respectively. A rotation matrix rotating A into B can be found by expressing the basis of B in terms of A as

$$\hat{\mathbf{b}}_1 = C_{11}\hat{\mathbf{a}}_1 + C_{12}\hat{\mathbf{a}}_2 + C_{13}\hat{\mathbf{a}}_3 \quad (\text{H.1})$$

$$\hat{\mathbf{b}}_2 = C_{21}\hat{\mathbf{a}}_1 + C_{22}\hat{\mathbf{a}}_2 + C_{23}\hat{\mathbf{a}}_3 \quad (\text{H.2})$$

$$\hat{\mathbf{b}}_3 = C_{31}\hat{\mathbf{a}}_1 + C_{32}\hat{\mathbf{a}}_2 + C_{33}\hat{\mathbf{a}}_3. \quad (\text{H.3})$$

Following (H.1), (H.2) and (H.3) can be written in matrix notation as

$$\begin{bmatrix} \hat{\mathbf{b}}_1 \\ \hat{\mathbf{b}}_2 \\ \hat{\mathbf{b}}_3 \end{bmatrix} = \begin{bmatrix} C_{11} & C_{12} & C_{13} \\ C_{21} & C_{22} & C_{23} \\ C_{31} & C_{32} & C_{33} \end{bmatrix} \begin{bmatrix} \hat{\mathbf{a}}_1 \\ \hat{\mathbf{a}}_2 \\ \hat{\mathbf{a}}_3 \end{bmatrix} = {}^B_A\underline{\mathbf{C}} \begin{bmatrix} \hat{\mathbf{a}}_1 \\ \hat{\mathbf{a}}_2 \\ \hat{\mathbf{a}}_3 \end{bmatrix}, \quad (\text{H.4})$$

where ${}^B_A\underline{\mathbf{C}}$ is called the attitude matrix. As each element is calculated by projection,

$${}^B_A\underline{\mathbf{C}} = \begin{bmatrix} \hat{\mathbf{b}}_1 \cdot \hat{\mathbf{a}}_1 & \hat{\mathbf{b}}_1 \cdot \hat{\mathbf{a}}_2 & \hat{\mathbf{b}}_1 \cdot \hat{\mathbf{a}}_3 \\ \hat{\mathbf{b}}_2 \cdot \hat{\mathbf{a}}_1 & \hat{\mathbf{b}}_2 \cdot \hat{\mathbf{a}}_2 & \hat{\mathbf{b}}_2 \cdot \hat{\mathbf{a}}_3 \\ \hat{\mathbf{b}}_3 \cdot \hat{\mathbf{a}}_1 & \hat{\mathbf{b}}_3 \cdot \hat{\mathbf{a}}_2 & \hat{\mathbf{b}}_3 \cdot \hat{\mathbf{a}}_3 \end{bmatrix}, \quad (\text{H.5})$$

where ${}^B_A C_{ij} = \hat{\mathbf{b}}_i \cdot \hat{\mathbf{a}}_j = \cos(\alpha_{ij})$, as the basis¹ of A and B consists of unit vectors and α_{ij} is the angle between the two elements. Analogously the rotation from B to A can be found as

$$\begin{bmatrix} \hat{\mathbf{a}}_1 \\ \hat{\mathbf{a}}_2 \\ \hat{\mathbf{a}}_3 \end{bmatrix} = {}^A_B\underline{\mathbf{C}} \begin{bmatrix} \hat{\mathbf{b}}_1 \\ \hat{\mathbf{b}}_2 \\ \hat{\mathbf{b}}_3 \end{bmatrix}, \quad (\text{H.6})$$

¹Hence the commonly used notion direction cosine matrix.

where

$${}^A_B \underline{\mathbf{C}} = \begin{bmatrix} \hat{\mathbf{a}}_1 \cdot \hat{\mathbf{b}}_1 & \hat{\mathbf{a}}_1 \cdot \hat{\mathbf{b}}_2 & \hat{\mathbf{a}}_1 \cdot \hat{\mathbf{b}}_3 \\ \hat{\mathbf{a}}_2 \cdot \hat{\mathbf{b}}_1 & \hat{\mathbf{a}}_2 \cdot \hat{\mathbf{b}}_2 & \hat{\mathbf{a}}_2 \cdot \hat{\mathbf{b}}_3 \\ \hat{\mathbf{a}}_3 \cdot \hat{\mathbf{b}}_1 & \hat{\mathbf{a}}_3 \cdot \hat{\mathbf{b}}_2 & \hat{\mathbf{a}}_3 \cdot \hat{\mathbf{b}}_3 \end{bmatrix}. \quad (\text{H.7})$$

H.2 Euler Angles

There exist three special forms of the attitude matrix, which each rotate the reference frame about one of its axes. These are called elementary rotations. Rotation around the third axes as depicted in Figure H.1, yields the transformation matrix

$$\underline{\mathbf{C}}_3 = \begin{bmatrix} \hat{\mathbf{b}}_1 \cdot \hat{\mathbf{a}}_1 & \hat{\mathbf{b}}_1 \cdot \hat{\mathbf{a}}_2 & \hat{\mathbf{b}}_1 \cdot \hat{\mathbf{a}}_3 \\ \hat{\mathbf{b}}_2 \cdot \hat{\mathbf{a}}_1 & \hat{\mathbf{b}}_2 \cdot \hat{\mathbf{a}}_2 & \hat{\mathbf{b}}_2 \cdot \hat{\mathbf{a}}_3 \\ \hat{\mathbf{b}}_3 \cdot \hat{\mathbf{a}}_1 & \hat{\mathbf{b}}_3 \cdot \hat{\mathbf{a}}_2 & \hat{\mathbf{b}}_3 \cdot \hat{\mathbf{a}}_3 \end{bmatrix}, \quad (\text{H.8})$$

rotating frame B to A.

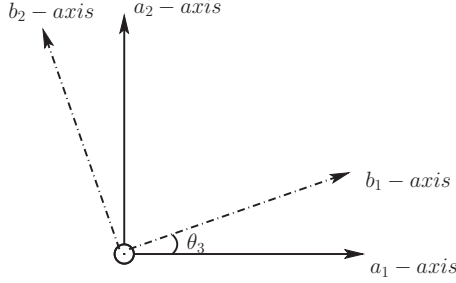


Figure H.1: Example of Euler rotation around the z-axis.

The two reference frames have a mutual third-axis and the three axes are orthogonal, hence $\hat{\mathbf{b}}_1 \cdot \hat{\mathbf{a}}_3 = \hat{\mathbf{b}}_2 \cdot \hat{\mathbf{a}}_3 = \hat{\mathbf{b}}_3 \cdot \hat{\mathbf{a}}_1 = \hat{\mathbf{b}}_3 \cdot \hat{\mathbf{a}}_2 = 0$ and $\hat{\mathbf{b}}_3 \cdot \hat{\mathbf{a}}_3 = 1$. This yields

$$\underline{\mathbf{C}}_3 = \begin{bmatrix} \hat{\mathbf{b}}_1 \cdot \hat{\mathbf{a}}_1 & \hat{\mathbf{b}}_1 \cdot \hat{\mathbf{a}}_2 & 0 \\ \hat{\mathbf{b}}_2 \cdot \hat{\mathbf{a}}_1 & \hat{\mathbf{b}}_2 \cdot \hat{\mathbf{a}}_2 & 0 \\ 0 & 0 & 1 \end{bmatrix}. \quad (\text{H.9})$$

The remaining dot products can be calculated by inspecting the projection of $\hat{\mathbf{a}}_1$ and $\hat{\mathbf{a}}_2$ on the $\hat{\mathbf{b}}_1$ and $\hat{\mathbf{b}}_2$, which yields

$$\underline{\mathbf{C}}_3 = \begin{bmatrix} \cos(\theta_3) & \sin(\theta_3) & 0 \\ -\sin(\theta_3) & \cos(\theta_3) & 0 \\ 0 & 0 & 1 \end{bmatrix}. \quad (\text{H.10})$$

Similar calculations for the second- and first-axis yields

$$\underline{\mathbf{C}}_2 = \begin{bmatrix} \cos(\theta_2) & 0 & -\sin(\theta_2) \\ 0 & 1 & 0 \\ \sin(\theta_2) & 0 & \cos(\theta_2) \end{bmatrix} \quad \text{and} \quad \underline{\mathbf{C}}_1 = \begin{bmatrix} 1 & 0 & 0 \\ 0 & \cos(\theta_1) & \sin(\theta_1) \\ 0 & -\sin(\theta_1) & \cos(\theta_1) \end{bmatrix}. \quad (\text{H.11})$$

Note that the sign of the sine terms are opposite when rotating about the second axis, due to the properties of the righthanded coordinate system.

By combining three Euler rotations, without having two successive rotations around the same axis, it is possible to obtain any arbitrary rotation. Thus, there exists 12 possible sets of Euler rotations.

H.3 Euler's Eigenaxis Rotation Theorem

Euler's eigenaxis rotation theorem uses a vector fixed in one reference frame during rotation, rather than one of the axes. Consider a reference frame B rotated an angle of θ around the unit vector \hat{e} , to coincide with reference frame A, where

$$\hat{e} = e_1\hat{a}_1 + e_2\hat{a}_2 + e_3\hat{a}_3 \quad (\text{H.12})$$

$$= e_1\hat{b}_1 + e_2\hat{b}_2 + e_3\hat{b}_3. \quad (\text{H.13})$$

As \hat{e} is fixed in reference frame A, (H.12) and (H.13) can be expressed as an attitude matrix,

$$\begin{bmatrix} e_1 \\ e_2 \\ e_3 \end{bmatrix} = \begin{bmatrix} C_{11} & C_{12} & C_{13} \\ C_{21} & C_{22} & C_{23} \\ C_{31} & C_{32} & C_{33} \end{bmatrix} \begin{bmatrix} e_1 \\ e_2 \\ e_3 \end{bmatrix} = \underline{\mathbf{C}} \begin{bmatrix} e_1 \\ e_2 \\ e_3 \end{bmatrix}. \quad (\text{H.14})$$

The rotation matrix $\underline{\mathbf{C}}$ can be expressed as three successive rotations. First A is rotated to the point where the unit vector \hat{a}_1 is aligned with \hat{e} thus constructing a new reference frame A'. This is done using the rotation matrix

$$\underline{\mathbf{R}} = \begin{bmatrix} e_1 & e_2 & e_3 \\ R_{21} & R_{22} & R_{23} \\ R_{31} & R_{32} & R_{33} \end{bmatrix}. \quad (\text{H.15})$$

Secondly the reference frames A and A' are rotated around \hat{e} by an angle of θ . After this rotation the A frame will be aligned with the B frame, and A' will construct a new reference frame A'' using the rotation matrix

$${}_{A'}^{\text{A}''}\underline{\mathbf{C}} = \begin{bmatrix} 1 & 0 & 0 \\ 0 & \cos \theta & \sin \theta \\ 0 & -\sin \theta & \cos \theta \end{bmatrix}. \quad (\text{H.16})$$

It is important to notice that relative rotation of B to A'' is equal to the rotation from A to A' i.e. ${}_{B}^{\text{A}''}\underline{\mathbf{C}} = {}_{A'}^{\text{A}''}\underline{\mathbf{C}} = \underline{\mathbf{R}}$.

The third of the three successive rotations needs to align the reference frame A'' with B. This is done by rotating A'' through an inverse matrix $\underline{\mathbf{R}}^{-1} = \underline{\mathbf{R}}^T$, since ${}_{A''}^{\text{B}}\underline{\mathbf{C}} = \underline{\mathbf{R}}^{-1}$. It is now possible to describe the rotation from A to B by the attitude matrix ${}_{A}^{\text{B}}\underline{\mathbf{C}}$ expressed as

$${}_{A}^{\text{B}}\underline{\mathbf{C}} = {}_{A''}^{\text{B}}\underline{\mathbf{C}} {}_{A'}^{\text{A}''}\underline{\mathbf{C}} {}_{A}^{\text{A}'}\underline{\mathbf{C}}. \quad (\text{H.17})$$

By inserting (H.15) and (H.16) in (H.17), the elements of the matrix ${}_{A}^{\text{B}}\underline{\mathbf{C}}$ can be expressed as

$$\begin{aligned} C_{11} &= e_1^2 + (R_{21}^2 + R_{31}^2) \cos(\theta) \\ C_{12} &= e_1 e_2 + (R_{21} R_{22} + R_{31} R_{32}) \cos(\theta) + (R_{21} R_{32} - R_{22} R_{31}) \sin(\theta) \\ C_{13} &= e_1 e_3 + (R_{21} R_{23} + R_{31} R_{33}) \cos(\theta) + (R_{21} R_{33} - R_{23} R_{31}) \sin(\theta) \\ &\vdots \\ C_{33} &= e_3^2 + (R_{23}^2 + R_{33}^2) \cos(\theta). \end{aligned} \quad (\text{H.18})$$

Utilising the orthonormality condition $\underline{\mathbf{R}}^T \underline{\mathbf{R}} = \mathbf{I}$, yields

$$\begin{aligned} e_1^2 + R_{21}^2 + R_{31}^2 &= 1 \\ e_2^2 + R_{22}^2 + R_{32}^2 &= 1 \\ e_3^2 + R_{23}^2 + R_{33}^2 &= 1 \\ e_1 e_2 + R_{21} R_{22} + R_{31} R_{32} &= 0 \\ e_2 e_3 + R_{22} R_{23} + R_{32} R_{33} &= 0 \\ e_1 e_3 + R_{21} R_{23} + R_{31} R_{33} &= 0, \end{aligned}$$

and calculating the cofactor of each of the elements (e_1, e_2, e_3) in (H.15) [Weisstein Downloaded March 2005],

$$\begin{aligned} e_1 &= R_{22} R_{33} - R_{32} R_{23} \\ e_2 &= R_{23} R_{31} - R_{21} R_{33} \\ e_3 &= R_{21} R_{32} - R_{31} R_{22}, \end{aligned}$$

it is possible to obtain the rotation matrix

$${}^B_A \underline{\mathbf{C}} = \begin{bmatrix} c\theta + e_1^2(1 - c\theta) & e_1 e_2(1 - c\theta) + e_3 s\theta & e_1 e_3(1 - c\theta) - e_2 s\theta \\ e_2 e_1(1 - c\theta) - e_3 s\theta & c\theta + e_2^2(1 - c\theta) & e_2 e_3(1 - c\theta) + e_1 s\theta \\ e_3 e_1(1 - c\theta) + e_2 s\theta & e_3 e_2(1 - c\theta) - e_1 s\theta & c\theta + e_3^2(1 - c\theta) \end{bmatrix}, \quad (\text{H.19})$$

where $c\theta \triangleq \cos(\theta)$, $s\theta \triangleq \sin(\theta)$ and e_i are the direction cosines of the Euler axis. The parameters (e_1, e_2, e_3) are not independent, but constrained by $e_1^2 + e_2^2 + e_3^2 = 1$.

H.4 Direction Cosine and Kinematics

In order to derive the kinematic differential equation, two reference frames, A and B, are used. A time varying angular velocity vector in the reference frame B is denoted as $\boldsymbol{\omega}$. This vector can also be expressed in terms of the unit vectors of reference frame B, which yields

$$\boldsymbol{\omega} = \hat{\omega}_1 \hat{\mathbf{b}}_1 + \hat{\omega}_2 \hat{\mathbf{b}}_2 + \hat{\omega}_3 \hat{\mathbf{b}}_3. \quad (\text{H.20})$$

In (H.4) the attitude matrix ${}^B_A \underline{\mathbf{C}}$ was defined such that

$$\begin{bmatrix} \hat{\mathbf{b}}_1 \\ \hat{\mathbf{b}}_2 \\ \hat{\mathbf{b}}_3 \end{bmatrix} = {}^B_A \underline{\mathbf{C}} \begin{bmatrix} \hat{\mathbf{a}}_1 \\ \hat{\mathbf{a}}_2 \\ \hat{\mathbf{a}}_3 \end{bmatrix}. \quad (\text{H.21})$$

Because the attitude matrix ${}^B_A \underline{\mathbf{C}}$ is an orthonormal matrix, (H.21) can be rewritten to

$$\begin{bmatrix} \hat{\mathbf{a}}_1 \\ \hat{\mathbf{a}}_2 \\ \hat{\mathbf{a}}_3 \end{bmatrix} = {}^B_A \underline{\mathbf{C}}^T \begin{bmatrix} \hat{\mathbf{b}}_1 \\ \hat{\mathbf{b}}_2 \\ \hat{\mathbf{b}}_3 \end{bmatrix}. \quad (\text{H.22})$$

Since the two reference frames, A and B, are rotating relative to each other, the attitude matrix and its elements C_{ij} are time dependent. Taking the time derivative of (H.22) in

A yields the following equation

$$\begin{bmatrix} 0 \\ 0 \\ 0 \end{bmatrix} = {}^B_A\dot{\underline{\mathbf{C}}}^T \begin{bmatrix} \hat{\mathbf{b}}_1 \\ \hat{\mathbf{b}}_2 \\ \hat{\mathbf{b}}_3 \end{bmatrix} + {}^B_A\underline{\mathbf{C}}^T \begin{bmatrix} \dot{\hat{\mathbf{b}}}_1 \\ \dot{\hat{\mathbf{b}}}_2 \\ \dot{\hat{\mathbf{b}}}_3 \end{bmatrix}. \quad (\text{H.23})$$

Because the unit vectors $\hat{\mathbf{b}}_i$, fixed in reference frame B, are rotating relative to A, the rate of change in $\hat{\mathbf{b}}_i$ is only caused by $\boldsymbol{\omega}$. This means that the time derivative of the unit vector $\dot{\hat{\mathbf{b}}}_i$, must be normal to both $\hat{\mathbf{b}}_i$ and $\boldsymbol{\omega}$. Thus, (H.23) can be expressed as

$$\begin{bmatrix} 0 \\ 0 \\ 0 \end{bmatrix} = {}^B_A\dot{\underline{\mathbf{C}}}^T \begin{bmatrix} \hat{\mathbf{b}}_1 \\ \hat{\mathbf{b}}_2 \\ \hat{\mathbf{b}}_3 \end{bmatrix} + {}^B_A\underline{\mathbf{C}}^T \begin{bmatrix} \boldsymbol{\omega} \times \hat{\mathbf{b}}_1 \\ \boldsymbol{\omega} \times \hat{\mathbf{b}}_2 \\ \boldsymbol{\omega} \times \hat{\mathbf{b}}_3 \end{bmatrix}. \quad (\text{H.24})$$

By introducing the skew symmetric matrix

$$\underline{\mathbf{S}}(\boldsymbol{\omega}) = \begin{bmatrix} 0 & -\omega_3 & \omega_2 \\ \omega_3 & 0 & -\omega_1 \\ -\omega_2 & \omega_1 & 0 \end{bmatrix}, \quad (\text{H.25})$$

it is possible to substitute the cross product in (H.24) with a multiplication [Hughes 1986, page 524], and rewrite (H.23) to

$$\begin{bmatrix} 0 \\ 0 \\ 0 \end{bmatrix} = \left[{}^B_A\dot{\underline{\mathbf{C}}}^T - {}^B_A\underline{\mathbf{C}}^T \underline{\mathbf{S}}(\boldsymbol{\omega}) \right] \begin{bmatrix} \hat{\mathbf{b}}_1 \\ \hat{\mathbf{b}}_2 \\ \hat{\mathbf{b}}_3 \end{bmatrix}, \quad (\text{H.26})$$

which is again rewritten to

$$\underline{\mathbf{0}} = {}^B_A\dot{\underline{\mathbf{C}}}^T - {}^B_A\underline{\mathbf{C}}^T \underline{\mathbf{S}}(\boldsymbol{\omega}). \quad (\text{H.27})$$

By transposing both sides of (H.26) and utilising the relationship $\underline{\mathbf{S}}^T(\boldsymbol{\omega}) = -\underline{\mathbf{S}}(\boldsymbol{\omega})$, the kinematic differential equation for the direct cosine matrix

$$\underline{\mathbf{0}} = {}^B_A\dot{\underline{\mathbf{C}}} + \underline{\mathbf{S}}(\boldsymbol{\omega}) {}^B_A\underline{\mathbf{C}}, \quad (\text{H.28})$$

is obtained.

APPENDIX I

Linearisation

This appendix describes the linearisation of the kinematic and dynamic differential equations for the satellite. Furthermore, the models of the momentum wheels and the magnetorquers will be included in the system equations, which are presented at the end of this appendix. It addresses the reader with interest in the detailed linearisation of the system equations used in this report.

The non-linear expression of the dynamic and kinematic equations are shown in (I.1). These two equations can be derived using Newton's laws of motion and Euler's laws of angular motion. In order to use these equations in, e.g., optimal control, the non-linear expression

$$\begin{bmatrix} \dot{\boldsymbol{\omega}} \\ \dot{\boldsymbol{q}} \end{bmatrix} = \begin{bmatrix} \underline{\mathbf{I}}_{\text{sat}}^{-1}(\mathbf{N}_{\text{ext}} + \mathbf{N}_{\text{ctrl}} - \underline{\mathbf{S}}(\boldsymbol{\omega})(\underline{\mathbf{I}}\boldsymbol{\omega} + \mathbf{h}_{\text{mw}})) \\ \frac{1}{2}\underline{\boldsymbol{\Omega}}\boldsymbol{q} \end{bmatrix}, \quad (\text{I.1})$$

is linearised and expressed in state space. A linear description of (I.1) is obtained by linearising around an operating point. In this appendix the linearised equations are given as general expressions, which means that the operating point can be changed dependent on the controller design.

I.1 Linearisation of the Satellite Kinematic Equation

The satellite kinematic equation is expressed as

$$\dot{\boldsymbol{q}} = \frac{1}{2}\underline{\boldsymbol{\Omega}}\boldsymbol{q}. \quad (\text{I.2})$$

Linearisation of quaternions are used in order to linearise (I.2). This linearisation introduces utilisation of quaternion properties, which are described in Appendix C. The quaternion can hereby be expressed as

$$\boldsymbol{q} = \boldsymbol{q}(t + \Delta t) = \boldsymbol{q}(t)\boldsymbol{q}(\Delta t) = \bar{\boldsymbol{q}}\tilde{\boldsymbol{q}}, \quad (\text{I.3})$$

where $\bar{\boldsymbol{q}}$ is the quaternion in the operating point and $\tilde{\boldsymbol{q}}$ is the small signal quaternion, representing a small change in attitude. Using the quaternion property, $\boldsymbol{q}^{-1} = \boldsymbol{q}^*$, then $\tilde{\boldsymbol{q}}$ in (I.3) can be derived as

$$\tilde{\boldsymbol{q}} = \bar{\boldsymbol{q}}^*\boldsymbol{q}. \quad (\text{I.4})$$

Where $\bar{\boldsymbol{q}}^*$ is the complex conjugate of $\bar{\boldsymbol{q}}$.

It is possible to rewrite the kinematic equation of the satellite in (I.2) as a multiplication of two quaternions, by using the multiplicative properties of a quaternion. This is expressed

as

$$\begin{aligned} \mathbf{q}\mathbf{q}_\omega &= (q_4 + q_1\hat{\mathbf{i}} + q_2\hat{\mathbf{j}} + q_3\hat{\mathbf{k}}) \cdot (0 + \omega_1\hat{\mathbf{i}} + \omega_2\hat{\mathbf{j}} + \omega_3\hat{\mathbf{k}}) \\ &= \underbrace{\begin{bmatrix} 0 & \omega_3 & -\omega_2 & \omega_1 \\ -\omega_3 & 0 & \omega_1 & \omega_2 \\ \omega_2 & -\omega_1 & 0 & \omega_3 \\ -\omega_1 & -\omega_2 & \omega_3 & 0 \end{bmatrix}}_{\underline{\Omega}} \underbrace{\begin{bmatrix} q_1 \\ q_2 \\ q_3 \\ q_4 \end{bmatrix}}_{\mathbf{q}}. \end{aligned} \quad (\text{I.5})$$

Inserting (I.5) into (I.2) the kinematic equation is given as

$$\dot{\mathbf{q}} = \frac{1}{2}\mathbf{q}\mathbf{q}_\omega, \quad (\text{I.6})$$

where \mathbf{q}_ω is defined as

$$\mathbf{q}_\omega = \begin{bmatrix} \mathbf{0}_{3 \times 1} \\ 0 \end{bmatrix} = \begin{bmatrix} \bar{\boldsymbol{\omega}}_{3 \times 1} + \tilde{\boldsymbol{\omega}}_{3 \times 1} \\ 0 \end{bmatrix} = \bar{\mathbf{q}}_\omega + \tilde{\mathbf{q}}_\omega. \quad (\text{I.7})$$

Taking the derivative of (I.4) with respect to time, and utilising (I.6), along with the quaternion properties $(\mathbf{q}\mathbf{q}_\omega)^* = \mathbf{q}_\omega^*\mathbf{q}^*$ and $\mathbf{q}_\omega^* = -\mathbf{q}_\omega$, yields

$$\begin{aligned} \dot{\tilde{\mathbf{q}}} &= \dot{\mathbf{q}}^*\mathbf{q} + \bar{\mathbf{q}}^*\dot{\mathbf{q}} \\ &= \frac{1}{2}[(\bar{\mathbf{q}}\bar{\mathbf{q}}_\omega)^*\mathbf{q} + \bar{\mathbf{q}}^*(\mathbf{q}\mathbf{q}_\omega)] \\ &= \frac{1}{2}[(\bar{\mathbf{q}}\bar{\mathbf{q}}_\omega)^*\mathbf{q} + \tilde{\mathbf{q}}\mathbf{q}_\omega] \\ &= \frac{1}{2}[\bar{\mathbf{q}}_\omega^*\bar{\mathbf{q}}^*\mathbf{q} + \tilde{\mathbf{q}}\mathbf{q}_\omega] \\ &= \frac{1}{2}[-\bar{\mathbf{q}}_\omega\tilde{\mathbf{q}} + \tilde{\mathbf{q}}\mathbf{q}_\omega]. \end{aligned} \quad (\text{I.8})$$

Inserting (I.7) into (I.8) yields

$$\begin{aligned} \dot{\tilde{\mathbf{q}}} &= \frac{1}{2}[-\bar{\mathbf{q}}_\omega\tilde{\mathbf{q}} + \tilde{\mathbf{q}}\bar{\mathbf{q}}_\omega + \tilde{\mathbf{q}}\tilde{\mathbf{q}}_\omega] \\ &= \frac{1}{2}[-\bar{\mathbf{q}}_\omega\tilde{\mathbf{q}} + \tilde{\mathbf{q}}\bar{\mathbf{q}}_\omega] + \frac{1}{2}\tilde{\mathbf{q}}\tilde{\mathbf{q}}_\omega. \end{aligned} \quad (\text{I.9})$$

When calculating the quaternion products in (I.9), $\bar{\mathbf{q}}_\omega\tilde{\mathbf{q}}$ can be obtained as

$$\begin{aligned} \bar{\mathbf{q}}_\omega\tilde{\mathbf{q}} &= \begin{bmatrix} -\underline{\mathbf{S}}(\tilde{\mathbf{q}}_{1:3}) + \tilde{q}_4\mathbf{1}_{3 \times 3} & \tilde{\mathbf{q}}_{1:3} \\ -\tilde{\mathbf{q}}_{1:3}^T & \tilde{q}_4 \end{bmatrix} \begin{bmatrix} \bar{\boldsymbol{\omega}} \\ 0 \end{bmatrix} \\ &= \begin{bmatrix} \underline{\mathbf{S}}(\bar{\boldsymbol{\omega}})\tilde{\mathbf{q}}_{1:3} + \tilde{q}_4\mathbf{1}_{3 \times 3}\bar{\boldsymbol{\omega}} \\ -\tilde{\mathbf{q}}_{1:3}^T\bar{\boldsymbol{\omega}} \end{bmatrix}. \end{aligned} \quad (\text{I.10})$$

Note that $\underline{\mathbf{S}}(\boldsymbol{\omega})$ is the skew symmetric matrix and that the mathematical property $\underline{\mathbf{S}}(\boldsymbol{\omega})\mathbf{q}_{1:3} = -\underline{\mathbf{S}}(\mathbf{q}_{1:3})\boldsymbol{\omega}$ is used. The multiplication of $\tilde{\mathbf{q}}\bar{\mathbf{q}}_\omega$ can be found as

$$\begin{aligned} \tilde{\mathbf{q}}\bar{\mathbf{q}}_\omega &= \begin{bmatrix} -\underline{\mathbf{S}}(\bar{\boldsymbol{\omega}}) & \bar{\boldsymbol{\omega}} \\ -\bar{\boldsymbol{\omega}}^T & 0 \end{bmatrix} \begin{bmatrix} \tilde{\mathbf{q}}_{1:3} \\ \tilde{q}_4 \end{bmatrix} \\ &= \begin{bmatrix} -\underline{\mathbf{S}}(\bar{\boldsymbol{\omega}})\tilde{\mathbf{q}}_{1:3} + \bar{\boldsymbol{\omega}}\tilde{q}_4 \\ -\bar{\boldsymbol{\omega}}^T\tilde{\mathbf{q}}_{1:3} \end{bmatrix}. \end{aligned} \quad (\text{I.11})$$

Finally the multiplication of $\tilde{\mathbf{q}}\tilde{\mathbf{q}}\omega$ must be derived. In this case note that each quaternion represents a rotation and it has a vector part, $\mathbf{q}_{1:3}$, with dimensions 3×1 and a scalar part, q_4 . Therefore, small rotations yield

$$\lim_{\text{rotation} \rightarrow 0} \mathbf{q} = \lim_{\theta \rightarrow 0} \begin{bmatrix} \mathbf{q}_{1:3} \\ q_4 \end{bmatrix} = \lim_{\theta \rightarrow 0} \begin{bmatrix} e_1 \sin\left(\frac{\theta}{2}\right) \\ e_2 \sin\left(\frac{\theta}{2}\right) \\ e_3 \sin\left(\frac{\theta}{2}\right) \\ \cos\left(\frac{\theta}{2}\right) \end{bmatrix} = \begin{cases} \tilde{\mathbf{q}}_{1:3} \rightarrow 0 \\ \tilde{q}_4 \rightarrow 1 \end{cases}. \quad (\text{I.12})$$

Therefore, $\tilde{\mathbf{q}}\tilde{\mathbf{q}}\omega$ can be approximated with $\tilde{\mathbf{q}}\omega$ as shown in (I.13).

$$\begin{aligned} \tilde{\mathbf{q}}\tilde{\mathbf{q}}\omega &= \begin{bmatrix} -\underline{\mathbf{S}}(\bar{\omega}) & \bar{\omega} \\ -\bar{\omega}^T & 0 \end{bmatrix} \begin{bmatrix} \tilde{\mathbf{q}}_{1:3} \\ \tilde{q}_4 \end{bmatrix} = \begin{bmatrix} -\underline{\mathbf{S}}(\bar{\omega})\tilde{\mathbf{q}}_{1:3} + \bar{\omega}\tilde{q}_4 \\ -\bar{\omega}^T\tilde{\mathbf{q}}_{1:3} + 0\tilde{q}_4 \end{bmatrix} \\ &\approx \begin{bmatrix} \begin{bmatrix} 0 \\ 0 \\ 0 \\ 0 \end{bmatrix} \\ \begin{bmatrix} \tilde{\omega}_1 \\ \tilde{\omega}_2 \\ \tilde{\omega}_3 \\ 0 \end{bmatrix} \end{bmatrix} + \begin{bmatrix} \tilde{\omega}_1 \\ \tilde{\omega}_2 \\ \tilde{\omega}_3 \\ 0 \end{bmatrix} \tilde{q}_4 = \begin{bmatrix} \tilde{\omega}_1 \\ \tilde{\omega}_2 \\ \tilde{\omega}_3 \\ 0 \end{bmatrix} \\ &= \tilde{\mathbf{q}}\omega. \end{aligned} \quad (\text{I.13})$$

The linear expression for the kinematic differential equation of the satellite is obtainable by substituting (I.10), (I.11) and (I.13) into (I.9), which yields

$$\begin{aligned} \dot{\tilde{\mathbf{q}}} &= \frac{1}{2} \left(- \begin{bmatrix} \underline{\mathbf{S}}(\bar{\omega})\tilde{\mathbf{q}}_{1:3} + \tilde{q}_4 \mathbf{1}_{3 \times 3} \bar{\omega} \\ -\tilde{\mathbf{q}}_{1:3}^T \bar{\omega} \end{bmatrix} + \begin{bmatrix} -\underline{\mathbf{S}}(\bar{\omega})\tilde{\mathbf{q}}_{1:3} + \tilde{q}_4 \mathbf{1}_{3 \times 3} \bar{\omega} \\ -\bar{\omega}^T \tilde{\mathbf{q}}_{1:3} \end{bmatrix} \right) + \frac{1}{2} \tilde{\mathbf{q}}\tilde{\mathbf{q}}\omega \\ &= \begin{bmatrix} -\underline{\mathbf{S}}(\bar{\omega}) \\ \mathbf{0}_{1 \times 3} \end{bmatrix} \tilde{\mathbf{q}}_{1:3} + \frac{1}{2} \tilde{\mathbf{q}}\tilde{\mathbf{q}}\omega \\ &\approx \begin{bmatrix} -\underline{\mathbf{S}}(\bar{\omega}) \\ \mathbf{0}_{1 \times 3} \end{bmatrix} \tilde{\mathbf{q}}_{1:3} + \frac{1}{2} \tilde{\mathbf{q}}\omega, \end{aligned} \quad (\text{I.14})$$

due to the fact that $\mathbf{a}^T \mathbf{b} = \mathbf{b}^T \mathbf{a}$ applies. It should be noted that the derivative of q_4 is zero, and can, therefore, be omitted in the linearised expression of the kinematic equation.

I.2 Linearisation of Satellite Dynamic Equation

The dynamic differential equation of the satellite, which describes how torques acting on the satellite influence the rotational acceleration of the satellite, is expressed as

$$\dot{\omega} = \underline{\mathbf{I}}_{\text{sat}}^{-1} [\mathbf{N}_{\text{ext}} + \mathbf{N}_{\text{ctrl}} - \underline{\mathbf{S}}(\omega)(\underline{\mathbf{I}}_{\text{sat}}\omega + \mathbf{h}_{\text{mw}})]. \quad (\text{I.15})$$

To linearise the dynamic equation, it is necessary to choose an operating point $\bar{\omega}$ for the system. The change in angular velocity is modeled with the small signal $\tilde{\omega}$ around the operating point. This yields

$$\omega = \omega(t + \Delta t) = \bar{\omega} + \tilde{\omega}. \quad (\text{I.16})$$

The time derivative of (I.16) yields

$$\dot{\omega} = \dot{\bar{\omega}} + \dot{\tilde{\omega}}. \quad (\text{I.17})$$

Taking (I.15) into consideration, it is possible to assume \mathbf{N}_{ext} as constant around the operating point, within the time frame Δt . Therefore, $\dot{\boldsymbol{\omega}}$ becomes a function of $\boldsymbol{\omega}$, \mathbf{N}_{ctrl} and \mathbf{h}_{mw} . (I.15) is linearised using first order Taylor Expansion.

$$\begin{aligned}\dot{\boldsymbol{\omega}}(\boldsymbol{\omega}, \mathbf{h}_{\text{mw}}, \mathbf{N}_{\text{ctrl}}) &\approx -\underline{\mathbf{I}}_{\text{sat}}^{-1} \frac{d}{d\boldsymbol{\omega}} \underline{\mathbf{S}}(\boldsymbol{\omega})(\underline{\mathbf{I}}_{\text{sat}}\boldsymbol{\omega} + \mathbf{h}_{\text{mw}}) \Big|_{\boldsymbol{\omega}=\bar{\boldsymbol{\omega}}, \mathbf{h}_{\text{mw}}=\bar{\mathbf{h}}_{\text{mw}}} \tilde{\boldsymbol{\omega}} \\ &\quad - \underline{\mathbf{I}}_{\text{sat}}^{-1} \frac{d}{d\mathbf{h}_{\text{mw}}} \underline{\mathbf{S}}(\boldsymbol{\omega})(\underline{\mathbf{I}}_{\text{sat}}\boldsymbol{\omega} + \mathbf{h}_{\text{mw}}) \Big|_{\boldsymbol{\omega}=\bar{\boldsymbol{\omega}}, \mathbf{h}_{\text{mw}}=\bar{\mathbf{h}}_{\text{mw}}} \tilde{\mathbf{h}}_{\text{mw}} \\ &\quad + \underline{\mathbf{I}}_{\text{sat}}^{-1} \frac{d}{d\mathbf{N}_{\text{ctrl}}} \mathbf{N}_{\text{ctrl}} \Big|_{\mathbf{N}_{\text{ctrl}}=\bar{\mathbf{N}}_{\text{ctrl}}} \tilde{\mathbf{N}}_{\text{ctrl}}.\end{aligned}\quad (\text{I.18})$$

By rewriting the $\tilde{\boldsymbol{\omega}}$ term and expanding the $\tilde{\mathbf{N}}_{\text{ctrl}}$ and $\tilde{\mathbf{h}}_{\text{mw}}$ terms, (I.18) can be expressed in the form

$$\begin{aligned}\dot{\boldsymbol{\omega}} &= -\underline{\mathbf{I}}_{\text{sat}}^{-1} \left[\frac{d}{d\boldsymbol{\omega}} \underline{\mathbf{S}}(\boldsymbol{\omega}) \Big|_{\boldsymbol{\omega}=\bar{\boldsymbol{\omega}}} \underline{\mathbf{I}}_{\text{sat}}\bar{\boldsymbol{\omega}} + \underline{\mathbf{S}}(\bar{\boldsymbol{\omega}}) \frac{d}{d\boldsymbol{\omega}} \underline{\mathbf{I}}_{\text{sat}}\boldsymbol{\omega} \Big|_{\boldsymbol{\omega}=\bar{\boldsymbol{\omega}}} + \frac{d}{d\boldsymbol{\omega}} \underline{\mathbf{S}}(\boldsymbol{\omega}) \Big|_{\boldsymbol{\omega}=\bar{\boldsymbol{\omega}}} \bar{\mathbf{h}}_{\text{mw}} \right] \tilde{\boldsymbol{\omega}} \\ &\quad - \underline{\mathbf{I}}_{\text{sat}}^{-1} \frac{d}{d\mathbf{h}_{\text{mw}}} \mathbf{h}_{\text{mw}} \Big|_{\mathbf{h}_{\text{mw}}=\bar{\mathbf{h}}_{\text{mw}}} \underline{\mathbf{S}}(\bar{\boldsymbol{\omega}})\tilde{\mathbf{h}}_{\text{mw}} + \underline{\mathbf{I}}_{\text{sat}}^{-1} \tilde{\mathbf{N}}_{\text{ctrl}}.\end{aligned}\quad (\text{I.19})$$

Using the fact that $\underline{\mathbf{S}}(\boldsymbol{\omega})\underline{\mathbf{I}}_{\text{sat}}\bar{\boldsymbol{\omega}} = -\underline{\mathbf{S}}(\underline{\mathbf{I}}_{\text{sat}}\bar{\boldsymbol{\omega}})\boldsymbol{\omega}$ then (I.19) can be expressed as

$$\begin{aligned}\dot{\boldsymbol{\omega}} &= \underline{\mathbf{I}}_{\text{sat}}^{-1} \left[\underline{\mathbf{S}}(\underline{\mathbf{I}}_{\text{sat}}\bar{\boldsymbol{\omega}}) \frac{d}{d\boldsymbol{\omega}} \boldsymbol{\omega} \Big|_{\boldsymbol{\omega}=\bar{\boldsymbol{\omega}}} - \underline{\mathbf{S}}(\bar{\boldsymbol{\omega}}) \frac{d}{d\boldsymbol{\omega}} \underline{\mathbf{I}}_{\text{sat}}\boldsymbol{\omega} \Big|_{\boldsymbol{\omega}=\bar{\boldsymbol{\omega}}} + \underline{\mathbf{S}}(\bar{\mathbf{h}}_{\text{mw}}) \frac{d}{d\boldsymbol{\omega}} \boldsymbol{\omega} \Big|_{\boldsymbol{\omega}=\bar{\boldsymbol{\omega}}} \right] \tilde{\boldsymbol{\omega}} \\ &\quad - \underline{\mathbf{I}}_{\text{sat}}^{-1} \underline{\mathbf{S}}(\bar{\boldsymbol{\omega}})\tilde{\mathbf{h}}_{\text{mw}} + \underline{\mathbf{I}}_{\text{sat}}^{-1} \tilde{\mathbf{N}}_{\text{ctrl}}.\end{aligned}\quad (\text{I.20})$$

From (I.20) the linearised dynamic differential equation is obtained as

$$\dot{\boldsymbol{\omega}} = \underline{\mathbf{I}}_{\text{sat}}^{-1} [\underline{\mathbf{S}}(\underline{\mathbf{I}}_{\text{sat}}\bar{\boldsymbol{\omega}}) - \underline{\mathbf{S}}(\bar{\boldsymbol{\omega}})\underline{\mathbf{I}}_{\text{sat}} + \underline{\mathbf{S}}(\bar{\mathbf{h}}_{\text{mw}})] \tilde{\boldsymbol{\omega}} - \underline{\mathbf{I}}_{\text{sat}}^{-1} \underline{\mathbf{S}}(\bar{\boldsymbol{\omega}})\tilde{\mathbf{h}}_{\text{mw}} + \underline{\mathbf{I}}_{\text{sat}}^{-1} \tilde{\mathbf{N}}_{\text{ctrl}}. \quad (\text{I.21})$$

I.3 Linear Equation for the Satellite Attitude

Based on the linearisations of the kinematic and dynamic differential equations, it is possible to obtain the linear system equation for the satellite attitude, which is expressed as

$$\begin{aligned}\begin{bmatrix} \dot{\tilde{\mathbf{q}}}_{1:3} \\ \dot{\tilde{\boldsymbol{\omega}}} \\ \dot{\tilde{\mathbf{h}}}_{\text{mw}} \end{bmatrix} &= \begin{bmatrix} -\underline{\mathbf{S}}(\bar{\boldsymbol{\omega}}) & \frac{1}{2}\underline{\mathbf{1}}_{3\times 3} & \underline{\mathbf{0}}_{3\times 3} \\ \underline{\mathbf{0}}_{3\times 3} & \underline{\mathbf{I}}_{\text{sat}}^{-1} [\underline{\mathbf{S}}(\underline{\mathbf{I}}_{\text{sat}}\bar{\boldsymbol{\omega}}) - \underline{\mathbf{S}}(\bar{\boldsymbol{\omega}})\underline{\mathbf{I}}_{\text{sat}} + \underline{\mathbf{S}}(\bar{\mathbf{h}}_{\text{mw}})] & -\underline{\mathbf{I}}_{\text{sat}}^{-1} \underline{\mathbf{S}}(\bar{\boldsymbol{\omega}}) \\ \underline{\mathbf{0}}_{3\times 3} & \underline{\mathbf{0}}_{3\times 3} & \underline{\mathbf{0}}_{3\times 3} \end{bmatrix} \begin{bmatrix} \tilde{\mathbf{q}}_{1:3} \\ \tilde{\boldsymbol{\omega}} \\ \tilde{\mathbf{h}}_{\text{mw}} \end{bmatrix} \\ &\quad + \begin{bmatrix} \underline{\mathbf{0}}_{3\times 3} & \underline{\mathbf{0}}_{3\times 3} \\ \underline{\mathbf{I}}_{\text{sat}}^{-1} & -\underline{\mathbf{I}}_{\text{sat}}^{-1} \\ \underline{\mathbf{0}}_{3\times 3} & \underline{\mathbf{1}}_{3\times 3} \end{bmatrix} \begin{bmatrix} \tilde{\mathbf{N}}_{\text{mt}} \\ \tilde{\mathbf{N}}_{\text{mw}} \end{bmatrix}.\end{aligned}\quad (\text{I.22})$$

Here $\underline{\mathbf{S}}(\bar{\boldsymbol{\omega}})$ and $\underline{\mathbf{S}}(\bar{\mathbf{h}}_{\text{mw}})$ are constant in their operating points and they are calculated in each operating point using the measurements from the gyros and the tachometers on the momentum wheels. $\tilde{\mathbf{N}}_{\text{mt}}$ and $\tilde{\mathbf{N}}_{\text{mw}}$ are small changes in the torques exerted by the actuators, within the Δt time frame. However, the dynamics given in (I.22), does not include the dynamics of the actuators. In order to design controllers, which consider the dynamics of the entire system, the system equation in (I.22) will be expanded to include the dynamics of the actuators.

I.4 Momentum Wheels

In this section the dynamics of the momentum wheels are presented and expressed in a manner facilitating the inclusion of them in the overall system equation. The expression is given for one momentum wheel, which is used in general to include all three momentum wheels. In (2.20) on page 22 the dynamics of the momentum wheel are stated. However, the transfer function in (2.20) needs to be extended so the reference becomes the angular acceleration to facilitate augmentation of (I.22). This is depicted in Figure I.1, where $T(s)$ denotes the closed loop transfer function obtained in (2.20).

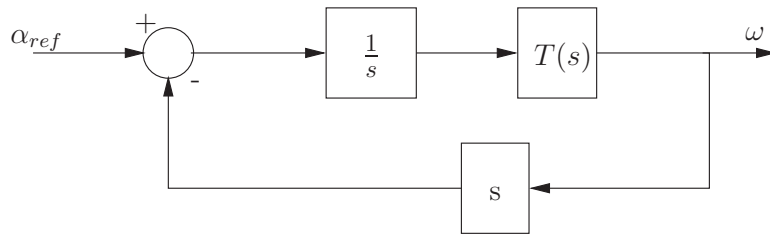


Figure I.1: Block diagram illustrating the extension of the transfer function for a momentum wheel.

Calculating the closed loop transfer function for the system in Figure I.1 yields

$$\begin{aligned}
 \frac{\omega_{\text{mw}}(s)}{\alpha_{\text{mw ref}}(s)} &= \frac{b_2 s^2 + b_3 s + b_4}{s^4 + a_1 s^3 + a_2 s^2 + a_3 s}, \quad \text{where} \\
 b_2 &= \frac{C_p C_t}{I_{\text{mw}} R_{\text{mw}}} \\
 b_3 &= \frac{C_p C_t (\mu_f R_{\text{mw}} + C_t C_s) + C_i C_t I_{\text{mw}} R_{\text{mw}}}{I_{\text{mw}}^2 R_{\text{mw}}^2} \\
 b_4 &= \frac{C_i C_t (\mu_f R_{\text{mw}} + C_t C_s)}{I_{\text{mw}}^2 R_{\text{mw}}^2} \\
 a_0 &= 1 \\
 a_1 &= \frac{2C_p C_t + 2(\mu_f R_{\text{mw}} + C_t C_s)}{I_{\text{mw}} R_{\text{mw}}} \\
 a_2 &= \frac{2C_p C_t (\mu_f R_{\text{mw}} + C_t C_s) + 2C_i C_t I_{\text{mw}} R_{\text{mw}} + \mu_f^2 R_{\text{mw}}^2}{I_{\text{mw}}^2 R_{\text{mw}}^2} \\
 &\quad + \frac{C_t^2 C_s^2 + 2\mu_f R_{\text{mw}} C_t C_s}{I_{\text{mw}}^2 R_{\text{mw}}^2} \\
 a_3 &= \frac{C_i C_t (\mu_f R_{\text{mw}} + C_t C_s)}{I_{\text{mw}}^2 R_{\text{mw}}^2}.
 \end{aligned}$$

According to [Franklin, Powell & Emami-Naeini 2002, page 497] the transfer function in (I.23), can be expressed in state space, with the matrices given in canonical form, as

$$\begin{aligned}
 \underline{\mathbf{A}}_{\text{mw}_x} &= \begin{bmatrix} -a_1 & -a_2 & -a_3 & 0 \\ 1 & 0 & 0 & 0 \\ 0 & 1 & 0 & 0 \\ 0 & 0 & 1 & 0 \end{bmatrix}, \quad \underline{\mathbf{B}}_{\text{mw}_x} = \begin{bmatrix} 1 \\ 0 \\ 0 \\ 0 \end{bmatrix} \text{ and} \\
 \underline{\mathbf{C}}_{\text{mw}_x} &= [0 \ b_2 \ b_3 \ b_4].
 \end{aligned} \tag{I.23}$$

Because each momentum wheel has a four dimensional state vector, three vectors containing the state variables are defined to ease notation. These are \mathbf{x}_{mw_x} , \mathbf{x}_{mw_y} and \mathbf{x}_{mw_z} . Defining a matrix, which contains the dynamics of all three momentum wheels, yields

$$\underline{\mathbf{A}}_{\text{mw}} = \begin{bmatrix} \underline{\mathbf{A}}_{\text{mw}_x} & \underline{\mathbf{0}}_{4 \times 4} & \underline{\mathbf{0}}_{4 \times 4} \\ \underline{\mathbf{0}}_{4 \times 4} & \underline{\mathbf{A}}_{\text{mw}_y} & \underline{\mathbf{0}}_{4 \times 4} \\ \underline{\mathbf{0}}_{4 \times 4} & \underline{\mathbf{0}}_{4 \times 4} & \underline{\mathbf{A}}_{\text{mw}_z} \end{bmatrix}. \quad (\text{I.24})$$

From (I.22) it is noticed that the momentum wheels influence the change in angular velocity, $\dot{\boldsymbol{\omega}}$. Furthermore, the torque generated by the momentum wheels is proportional to the change in angular momentum, $\dot{\mathbf{h}}$. As for the dynamics these influences will be specified for one momentum wheel, and then augmented to include all three momentum wheels. According to (I.22) the influence, from the momentum wheel along the x-axis, on $\dot{\boldsymbol{\omega}}$ is given as

$$-I_{\text{sat}11}^{-1} \tilde{N}_{\text{mw}_x} = -I_{\text{sat}11}^{-1} I_{\text{mw}_x} \alpha_{\text{mw}_x} \quad (\text{I.25})$$

The angular acceleration, α , is given as the derivative of the angular velocity. Using $\underline{\mathbf{C}}_{\text{mw}_x}$ in (I.23), the angular velocity can be expressed as

$$\omega_{\text{mw}_x} = \underline{\mathbf{C}}_{\text{mw}_x} \mathbf{x}_{\text{mw}_x} = [0 \ b_2 \ b_3 \ b_4] \begin{bmatrix} x_1 \\ x_2 \\ x_3 \\ x_4 \end{bmatrix} = b_2 x_2 + b_3 x_3 + b_4 x_4. \quad (\text{I.26})$$

Taking the time derivative of (I.26) yields

$$\dot{\omega}_{\text{mw}_x} = \alpha_{\text{mw}_x} = b_2 \dot{x}_2 + b_3 \dot{x}_3 + b_4 \dot{x}_4. \quad (\text{I.27})$$

Using the canonical form of $\underline{\mathbf{A}}_{\text{mw}_x}$ in (I.23), the angular acceleration can be expressed as

$$\alpha_{\text{mw}_x} = b_2 x_1 + b_3 x_2 + b_4 x_3. \quad (\text{I.28})$$

Inserting (I.28) into (I.25) yields

$$-I_{\text{sat}11}^{-1} I_{\text{mw}_x} [b_2 \ b_3 \ b_4 \ 0] \mathbf{x}_{\text{mw}_x} = -I_{\text{sat}11}^{-1} I_{\text{mw}_x} \mathbf{b} \mathbf{x}_{\text{mw}_x}. \quad (\text{I.29})$$

As noticed in (I.22), the only difference between the influence of the momentum wheels on $\dot{\boldsymbol{\omega}}$ and $\dot{\mathbf{h}}$, is a multiplication by the inverse inertia matrix of the satellite. Thus, defining a matrix containing the influences for all three momentum wheels yields

$$\underline{\mathbf{A}}_{\text{torque}_{\text{mw}}} = \left[\begin{array}{c} -\underline{\mathbf{I}}_{\text{sat}}^{-1} \begin{bmatrix} I_{\text{mw}_x} \mathbf{b} & \underline{\mathbf{0}}_{1 \times 4} & \underline{\mathbf{0}}_{1 \times 4} \\ \underline{\mathbf{0}}_{1 \times 4} & I_{\text{mw}_y} \mathbf{b} & \underline{\mathbf{0}}_{1 \times 4} \\ \underline{\mathbf{0}}_{1 \times 4} & \underline{\mathbf{0}}_{1 \times 4} & I_{\text{mw}_z} \mathbf{b} \end{bmatrix} \\ I_{\text{mw}_x} \mathbf{b} \begin{bmatrix} \underline{\mathbf{0}}_{1 \times 4} & \underline{\mathbf{0}}_{1 \times 4} & \underline{\mathbf{0}}_{1 \times 4} \\ \underline{\mathbf{0}}_{1 \times 4} & I_{\text{mw}_y} \mathbf{b} & \underline{\mathbf{0}}_{1 \times 4} \\ \underline{\mathbf{0}}_{1 \times 4} & \underline{\mathbf{0}}_{1 \times 4} & I_{\text{mw}_z} \mathbf{b} \end{bmatrix} \end{array} \right]. \quad (\text{I.30})$$

I.5 Magnetorquers

The dynamics of the magnetorquers also need to be included in the overall system equation. However, in (E.7) in Appendix E the inductance of the magnetorquers have been omitted,

which means that the voltage to the magnetorquers is proportional to the current, with the inverse resistance. Due to the fact that there are no dynamics in the magnetorquer transfer function, the torque contributed by the magnetorquers is included in the input matrix for the overall system.

From (I.22) it is noticed that the magnetorquers only influence the change in angular velocity, $\dot{\omega}$. The small signal torque vector, \tilde{N}_{mt} , can be expressed as

$$\tilde{N}_{\text{mt}} = {}^C \mathbf{M}_{\text{mt}} \times {}^C \mathbf{B} = {}^C \mathbf{M}_{\text{mt}} \times {}_S^C \underline{\mathbf{C}}(\mathbf{q}) {}^S \mathbf{B}, \quad (\text{I.31})$$

where ${}^S \mathbf{B}$ is the magnetic field measured in the SBRF, ${}^C \mathbf{M}_{\text{mt}}$ is the magnetic dipole moment generated by the magnetorquers and ${}_S^C \underline{\mathbf{C}}(\mathbf{q})$ is the attitude matrix describing the rotation from SBRF to CRF, which is constant. Utilising mathematical properties for cross products and the fact that the magnetic dipole moment is given by (2.17) on page 21, (I.31) can be expressed as

$$\tilde{N}_{\text{mt}} = -\underline{\mathbf{S}}({}_S^C \underline{\mathbf{C}}(\mathbf{q}) {}^S \mathbf{B}) \underline{\mathbf{n}} \underline{\mathbf{A}}_{\text{area}} \underline{\mathbf{i}}_{\text{mt}}, \quad (\text{I.32})$$

where $\underline{\mathbf{n}}$ is a diagonal matrix containing the number of windings of each coil, $\underline{\mathbf{A}}_{\text{area}}$ is a diagonal matrix containing the area spanned by each coil and $\underline{\mathbf{i}}_{\text{mt}}$ is a vector containing the current in the different coils. Since the input vector to the overall system, contains the voltage to each coil a diagonal matrix containing the inverse resistance in each coil is defined as

$$\underline{\mathbf{R}}_{\text{mt}} = \begin{bmatrix} \frac{1}{R_{\text{mt}x}} & 0 & 0 \\ 0 & \frac{1}{R_{\text{mt}y}} & 0 \\ 0 & 0 & \frac{1}{R_{\text{mt}z}} \end{bmatrix}. \quad (\text{I.33})$$

Hereby a matrix including the influence that all three magnetorquers have on $\dot{\omega}$, can be expressed as

$$\underline{\mathbf{B}}_{\text{mt}} = -\underline{\mathbf{I}}_{\text{sat}}^{-1} \underline{\mathbf{S}}({}_S^C \underline{\mathbf{C}}(\mathbf{q}) {}^S \mathbf{B}) \underline{\mathbf{n}} \underline{\mathbf{A}}_{\text{area}} \underline{\mathbf{R}}_{\text{mt}}, \quad (\text{I.34})$$

where $\underline{\mathbf{I}}_{\text{sat}}^{-1}$ is included according to (I.22). The matrix $\underline{\mathbf{B}}_{\text{mt}}$ describes the influence of the magnetorquer control output on the satellite, as linear combinations of the voltage to each coil, which are included in the input vector.

I.6 System Equation Including Actuator Dynamics

This section presents the overall system equation in state space. The state vector, given in (I.22), is augmented to include the vectors \mathbf{x}_{mw_x} , \mathbf{x}_{mw_y} and \mathbf{x}_{mw_z} . Thus the system matrix can be expressed as

$$\underline{\mathbf{A}}_{\text{sat}_{\text{act}}} = \left[\begin{array}{c|c} \underline{\mathbf{A}}_{\text{sat}} & \underline{\mathbf{0}}_{3 \times 12} \\ \hline \underline{\mathbf{0}}_{12 \times 9} & \underline{\mathbf{A}}_{\text{torque}_{\text{mw}}} \\ \hline & \underline{\mathbf{A}}_{\text{mw}} \end{array} \right], \quad (\text{I.35})$$

where $\underline{\mathbf{A}}_{\text{sat}}$ is the system matrix given in (I.22). As stated the input to the momentum wheels is the angular acceleration and given the transfer function for the magnetorquers, it

is noticed that the input here is the voltage. Thus using (I.23) and (I.34) the input matrix can be written as

$$\underline{\mathbf{B}}_{\text{sat}_{\text{act}}} = \left[\begin{array}{cc|c} \underline{\mathbf{0}}_{3 \times 3} & \underline{\mathbf{0}}_{3 \times 3} & \\ \underline{\mathbf{B}}_{\text{mt}} & \underline{\mathbf{0}}_{3 \times 3} & \\ \hline \underline{\mathbf{0}}_{3 \times 3} & \underline{\mathbf{0}}_{3 \times 3} & \\ \hline \underline{\mathbf{0}}_{4 \times 3} & 1 & 0 & 0 \\ & \underline{\mathbf{0}}_{3 \times 3} & & \\ \underline{\mathbf{0}}_{4 \times 3} & 0 & 1 & 0 \\ & \underline{\mathbf{0}}_{3 \times 3} & & \\ \underline{\mathbf{0}}_{4 \times 3} & 0 & 0 & 1 \\ & \underline{\mathbf{0}}_{3 \times 3} & & \end{array} \right]. \quad (\text{I.36})$$

None of the states describing the dynamics of either the momentum wheels or the magnetorquers are measurable in the system. Thus, the output matrix can be expressed as

$$\underline{\mathbf{C}}_{\text{sat}_{\text{act}}} = \left[\begin{array}{ccc|c} \underline{\mathbf{1}}_{3 \times 3} & \underline{\mathbf{0}}_{3 \times 3} & \underline{\mathbf{0}}_{3 \times 3} & \\ \underline{\mathbf{0}}_{3 \times 3} & \underline{\mathbf{1}}_{3 \times 3} & \underline{\mathbf{0}}_{3 \times 3} & \underline{\mathbf{0}}_{9 \times 12} \\ \hline \underline{\mathbf{0}}_{3 \times 3} & \underline{\mathbf{0}}_{3 \times 3} & \underline{\mathbf{1}}_{3 \times 3} & \\ \hline \underline{\mathbf{0}}_{12 \times 9} & & & \underline{\mathbf{0}}_{12 \times 12} \end{array} \right]. \quad (\text{I.37})$$

Now (I.35), (I.36) and (I.37) can be combined to present the system equations in state space,

$$\begin{aligned} \dot{\underline{\mathbf{x}}} &= \underline{\mathbf{A}}_{\text{sat}_{\text{act}}} \underline{\mathbf{x}} + \underline{\mathbf{B}}_{\text{sat}_{\text{act}}} \underline{\mathbf{u}} \\ \underline{\mathbf{y}} &= \underline{\mathbf{C}}_{\text{sat}_{\text{act}}} \underline{\mathbf{x}}, \end{aligned} \quad (\text{I.38})$$

where $\underline{\mathbf{x}}$ and $\underline{\mathbf{u}}$ are given as

$$\begin{aligned} \underline{\mathbf{x}} &= [\tilde{q}_{1:3} \ \tilde{\omega} \ \tilde{h}_{\text{mw}} \ \underline{\mathbf{x}}_{\text{mw}_x} \ \underline{\mathbf{x}}_{\text{mw}_y} \ \underline{\mathbf{x}}_{\text{mw}_z}]^T \\ \underline{\mathbf{u}} &= [v_{\text{mt}_x} \ v_{\text{mt}_y} \ v_{\text{mt}_z} \ \alpha_{\text{ref}_x} \ \alpha_{\text{ref}_y} \ \alpha_{\text{ref}_z}]^T. \end{aligned} \quad (\text{I.39})$$

APPENDIX J

Kalman Filter

This appendix is based on [Welch & Bishop 2001] and describes the Kalman filter, which can both estimate the internal states and filter the measurements of a linear system. This appendix should provide the reader with basic understanding of the Kalman filter.

A Kalman filter essentially consists of a set of recursive equations divided into two groups; prediction and correction. Figure J.1 depicts a block diagram of a Kalman filter, where the predictor estimates the next state, $\hat{x}_{k|k-1}$, which is used to predict the next measurement, \hat{z}_k . This is compared with the actual noisy measurement to generate a residual, \tilde{z}_k , which is used in the Kalman gain to correct the state estimate. The Kalman gain is calculated with consideration to the process noise and the measurement noise, such that the state error is minimised.

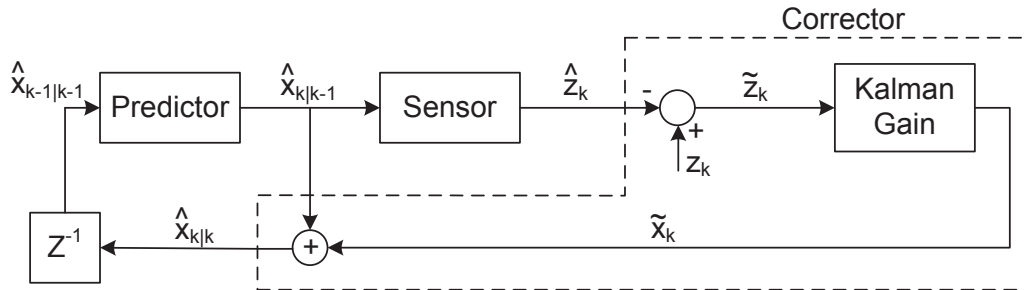


Figure J.1: Block diagram of a Kalman filter.

The Kalman filter is designed to produce a state estimation, \hat{x} of a system described as

$$\mathbf{x}_k = \Phi \mathbf{x}_{k-1} + \Gamma \mathbf{u}_k + \mathbf{W} \mathbf{w}_{k-1} \quad (\text{J.1})$$

$$\mathbf{z}_k = \mathbf{H} \mathbf{x}_k + \mathbf{V} \mathbf{v}_k, \quad (\text{J.2})$$

where \mathbf{w} is a random variable representing the noise introduced by the system¹ and \mathbf{v} is a random variable representing the noise introduced in the measurements. Both are assumed to be zero-mean Gaussian noise, i.e.,

$$\begin{aligned} p(\mathbf{w}) &\sim N(\mathbf{0}, \underline{\mathbf{Q}}) \\ p(\mathbf{v}) &\sim N(\mathbf{0}, \underline{\mathbf{R}}), \end{aligned}$$

where $\underline{\mathbf{Q}}$ and $\underline{\mathbf{R}}$ are referred to as the process noise covariance and measurement noise covariance matrices respectively.

¹This noise is usually caused by modeling inaccuracies

By defining the a-priori estimation error, $\mathbf{e}_{k|k-1}$, and the a posteriori estimation error, $\mathbf{e}_{k|k}$, as

$$\mathbf{e}_{k|k-1} = \mathbf{x}_k - \hat{\mathbf{x}}_{k|k-1} \quad (\text{J.3})$$

$$\mathbf{e}_{k|k} = \mathbf{x}_k - \hat{\mathbf{x}}_{k|k} \quad (\text{J.4})$$

it is possible to calculate the a-priori and the a-posteriori estimation covariances,

$$\underline{\mathbf{P}}_{k|k-1} = E \left[\mathbf{e}_{k|k-1} \mathbf{e}_{k|k-1}^T \right] \quad (\text{J.5})$$

$$\underline{\mathbf{P}}_{k|k} = E \left[\mathbf{e}_{k|k} \mathbf{e}_{k|k}^T \right], \quad (\text{J.6})$$

which must be minimised to perform optimal estimation.

The prediction error, \mathbf{e}_k , can be estimated from the measurement residual, as the system is linear. The estimate of the prediction error is denoted $\tilde{\mathbf{x}}_k$ and calculated as

$$\tilde{\mathbf{x}}_k = \underline{\mathbf{K}}_k \tilde{\mathbf{z}}_k, \quad (\text{J.7})$$

where $\underline{\mathbf{K}}_k$ is the Kalman gain. This yields the new state estimate

$$\begin{aligned} \hat{\mathbf{x}}_{k|k} &= \hat{\mathbf{x}}_{k|k-1} + \underline{\mathbf{K}}_k \tilde{\mathbf{z}}_k \\ &= \hat{\mathbf{x}}_{k|k-1} + \underline{\mathbf{K}}_k (\mathbf{z}_k - \hat{\mathbf{z}}_k) \\ &= \hat{\mathbf{x}}_{k|k-1} + \underline{\mathbf{K}}_k (\mathbf{z}_k - \underline{\mathbf{H}} \hat{\mathbf{x}}_{k|k-1}), \end{aligned} \quad (\text{J.8})$$

where $\underline{\mathbf{K}}_k$ according to [Welch & Bishop 2001, page 29] can be calculated by minimising (J.6). Using the orthogonality principle [Angus P. Andrews 2001, page 118], yields

$$E \left[\mathbf{e}_{k|k} \tilde{\mathbf{z}}_k^T \right] = 0, \quad (\text{J.9})$$

which by insertion of (J.4), (J.2) and (J.8), yields

$$\begin{aligned} 0 &= E \left[[\mathbf{x}_k - (\hat{\mathbf{x}}_{k|k-1} + \underline{\mathbf{K}}_k (\underline{\mathbf{H}} \mathbf{x}_k + \underline{\mathbf{V}} \mathbf{v}_k - \underline{\mathbf{H}} \hat{\mathbf{x}}_{k|k-1}))] [\underline{\mathbf{H}} \mathbf{x}_k + \underline{\mathbf{V}} \mathbf{v}_k - \underline{\mathbf{H}} \hat{\mathbf{x}}_{k|k-1}]^T \right] \\ 0 &= E \left[[\mathbf{x}_k - \hat{\mathbf{x}}_{k|k-1} - \underline{\mathbf{K}}_k \underline{\mathbf{H}} (\mathbf{x}_k - \hat{\mathbf{x}}_{k|k-1}) - \underline{\mathbf{K}}_k \underline{\mathbf{V}} \mathbf{v}_k] [\underline{\mathbf{H}} (\mathbf{x}_k - \hat{\mathbf{x}}_{k|k-1}) + \underline{\mathbf{V}} \mathbf{v}_k]^T \right] \\ 0 &= E \left[[\mathbf{e}_{k|k-1} - \underline{\mathbf{K}}_k \underline{\mathbf{H}} \mathbf{e}_{k|k-1} - \underline{\mathbf{K}}_k \underline{\mathbf{V}} \mathbf{v}_k] [\underline{\mathbf{H}} \mathbf{e}_{k|k-1} + \underline{\mathbf{V}} \mathbf{v}_k]^T \right]. \end{aligned} \quad (\text{J.10})$$

Now (J.10) can be reduced by utilising the fact that the a-priori state estimate and process noise are uncorrelated, i.e.,

$$\begin{aligned} 0 &= E \left[\mathbf{e}_{k|k-1} \underline{\mathbf{H}}^T \mathbf{e}_{k|k-1}^T - \underline{\mathbf{K}}_k \underline{\mathbf{H}} \mathbf{e}_{k|k-1} \underline{\mathbf{H}}^T \mathbf{e}_{k|k-1}^T - \underline{\mathbf{K}}_k \underline{\mathbf{V}} \mathbf{v}_k \underline{\mathbf{H}}^T \mathbf{e}_{k|k-1}^T \right. \\ &\quad \left. + \mathbf{e}_{k|k-1} \underline{\mathbf{V}}^T \mathbf{v}_k^T - \underline{\mathbf{K}}_k \underline{\mathbf{H}} \mathbf{e}_{k|k-1} \underline{\mathbf{V}}^T \mathbf{v}_k^T - \underline{\mathbf{K}}_k \underline{\mathbf{V}} \mathbf{v}_k \underline{\mathbf{V}}^T \mathbf{v}_k^T \right] \\ 0 &= E \left[\mathbf{e}_{k|k-1} \mathbf{e}_{k|k-1}^T \right] \underline{\mathbf{H}}^T - \underline{\mathbf{K}}_k \underline{\mathbf{H}} E \left[\mathbf{e}_{k|k-1} \mathbf{e}_{k|k-1}^T \right] \underline{\mathbf{H}}^T - \underline{\mathbf{K}}_k \underline{\mathbf{V}} E \left[\mathbf{v}_k \mathbf{v}_k^T \right] \underline{\mathbf{V}}^T \\ 0 &= \underline{\mathbf{P}}_{k|k-1} \underline{\mathbf{H}}^T - \underline{\mathbf{K}}_k \underline{\mathbf{H}} \underline{\mathbf{P}}_{k|k-1} \underline{\mathbf{H}}^T - \underline{\mathbf{K}}_k \underline{\mathbf{V}} \underline{\mathbf{R}}_k \underline{\mathbf{V}}^T. \end{aligned}$$

Solving for $\underline{\mathbf{K}}_k$ yields

$$\underline{\mathbf{K}}_k = \underline{\mathbf{P}}_{k|k-1} \underline{\mathbf{H}}^T (\underline{\mathbf{H}} \underline{\mathbf{P}}_{k|k-1} \underline{\mathbf{H}}^T + \underline{\mathbf{V}} \underline{\mathbf{R}}_k \underline{\mathbf{V}}^T)^{-1}. \quad (\text{J.11})$$

The a-priori prediction error covariance, $\underline{\mathbf{P}}_{k|k-1}$, is calculated using (J.5) and (J.1), yielding

$$\begin{aligned}
 \underline{\mathbf{P}}_{k|k-1} &= E \left[[\mathbf{x}_k - \underline{\Phi} \hat{\mathbf{x}}_{k-1|k-1}] [\mathbf{x}_k - \underline{\Phi} \hat{\mathbf{x}}_{k-1|k-1}]^T \right] \\
 \underline{\mathbf{P}}_{k|k-1} &= E \left[[\underline{\Phi} \mathbf{x}_{k-1} + \underline{\mathbf{W}} \mathbf{w}_{k-1} - \underline{\Phi} \hat{\mathbf{x}}_{k-1|k-1}] [\underline{\Phi} \mathbf{x}_{k-1} + \underline{\mathbf{W}} \mathbf{w}_{k-1} - \underline{\Phi} \hat{\mathbf{x}}_{k-1|k-1}]^T \right] \\
 \underline{\mathbf{P}}_{k|k-1} &= E \left[[\underline{\Phi} \mathbf{e}_{k-1|k-1} + \underline{\mathbf{W}} \mathbf{w}_{k-1}] [\underline{\Phi} \mathbf{e}_{k-1|k-1} + \underline{\mathbf{W}} \mathbf{w}_{k-1}]^T \right] \\
 \underline{\mathbf{P}}_{k|k-1} &= \underline{\Phi} E[\mathbf{e}_{k-1|k-1} \mathbf{e}_{k-1|k-1}^T] \underline{\Phi}^T + \underline{\mathbf{W}} E[\mathbf{w}_{k-1} \mathbf{w}_{k-1}^T] \underline{\mathbf{W}}^T \\
 \underline{\mathbf{P}}_{k|k-1} &= \underline{\Phi} \underline{\mathbf{P}}_{k-1|k-1} \underline{\Phi}^T + \underline{\mathbf{W}} \underline{\mathbf{Q}} \underline{\mathbf{W}}^T,
 \end{aligned} \tag{J.12}$$

as the estimation error is independent of the process noise. The a-posteriori prediction error covariance can be found in a similar manner, which yields

$$\underline{\mathbf{P}}_{k|k} = (\mathbf{I} - \underline{\mathbf{K}}_k \underline{\mathbf{H}}_k) \underline{\mathbf{P}}_{k|k-1}. \tag{J.13}$$

As $\underline{\mathbf{P}}_{k|k-1}$ and $\underline{\mathbf{P}}_{k|k}$ is independent of the measurement vector it is possible to calculate a steady state value of these and thus the Kalman gain, $\underline{\mathbf{K}}_k$. The noise descriptions $\underline{\mathbf{Q}}$ and $\underline{\mathbf{R}}$ are usually empirically estimated and later fine tuned, based on simulations.

APPENDIX K

Evaluation

This appendix presents an evaluation of the different controllers developed in this project. Firstly, the general specifications for the simulation environment are presented. Hereafter, the different controllers are evaluated in individual sections. The final section constitutes an evaluation of the entire control structure including desaturation control. It is addressed to reader with interest in an elaborated explanation of the evaluations conducted on the entire control structure.

The different controllers evaluated in this appendix are the angular velocity controller, the desaturation controller and the attitude controller. However, the controllers are dependent on each other, e.g., in order to evaluate the desaturation controller the angular velocity controller is needed as well. The requirements to the overall system are stated in Appendix B and will be appropriately evaluated during the evaluation of the individual controllers. Furthermore, each section contains a description of the different simulations conducted in the evaluation, a presentation of the results obtained and a conclusion outlining important aspects of the evaluation.

All the evaluations utilise the simulation environment presented in Appendix L. However, it is possible to configure the simulation environment in numerous ways by specifying individual parameters. The following listing describes the standard configuration of the important parameters used in the evaluations.

- The start time for the simulation environment is 2452315.56 [JD]. This entails that the simulation starts with the satellite in sunlight.
- The orbit propagation uses a Two Line Element (TLE), and in the simulations the Ørsted TLE is used.
- Initial attitude i.e., the quaternion denoting the rotation from ECI to SBRF, is randomly generated. This is feasible since the satellite can point in any direction upon separation from the launch vehicle.
- The disturbances have been enabled.
- The air density is set $\rho_{\text{air}} = 925 \cdot 10^{-15} [\text{kg}/\text{m}^3]$.
- There is no measured value for the drag coefficient. Therefore, a $C_D = 2 [.]$ is used.
- At all times the solar arrays are deployed.
- The initial velocity is $[0 \ 0 \ 0] [\text{rad}/\text{s}]$

If any of these standard configurations are changed in an evaluation, it is elaborated in the description of the corresponding simulation.

K.1 Angular Velocity Controller

This section describes an evaluation of the developed angular velocity controller. First an evaluation of the disturbance estimator is performed, and then the robust angular velocity controller is evaluated.

K.1.1 Disturbance Estimator

The disturbance estimator is evaluated w.r.t. the estimation error, i.e., the difference between the modeled disturbance torque and estimated torque. The evaluation is performed by simulating one orbit using a random inertia matrix, within 5% of the nominal inertia matrix, and a random attitude air density and drag coefficient. The orbit is simulated using 30 different initial attitudes, air densities, drag coefficients and inertia matrices, and no control torques are applied.

Results

The mean estimation error is calculated using `mean` in MATLAB, and yields

$$\mu_\omega = [-31.21 \ 31.12 \ 0.28] \cdot 10^{-9} [\text{rad/s}]. \quad (\text{K.1})$$

The standard deviation, minimum, and maximum are found using `std`, `max`, and `min` in MATLAB, and yields

$$\begin{aligned} \sigma_\omega &= [-50.15 \ 50.19 \ 17.07] \cdot 10^{-9} [\text{rad/s}], \\ \omega_{\max} &= [-373.7 \ 413.6 \ 231.7] \cdot 10^{-9} [\text{rad/s}], \text{ and} \\ \omega_{\min} &= [-372 \ -358.7 \ -185.1] \cdot 10^{-9} [\text{rad/s}]. \end{aligned} \quad (\text{K.2})$$

Conclusion

The estimation error from one of the simulations is depicted in Figure K.1. The estimation error on the z-axis is smaller than the x- and y-axes, and the cause of this is assumed to be that the large solar array area only influence the aerodynamic torque around the x- and y-axes. The small oscillations are assumed to be caused by the angular momentum bias in the momentum wheels. The mean estimation error is approximately 2% of the worst case disturbance torque, when considering different attitudes, air densities, drag coefficients and inertia matrices, and a feedforward should, therefore yield a smaller input disturbance to the system.

K.1.2 Robust Angular Velocity Controller

The evaluation of the robust angular velocity controller is divided into the four different cases described below.

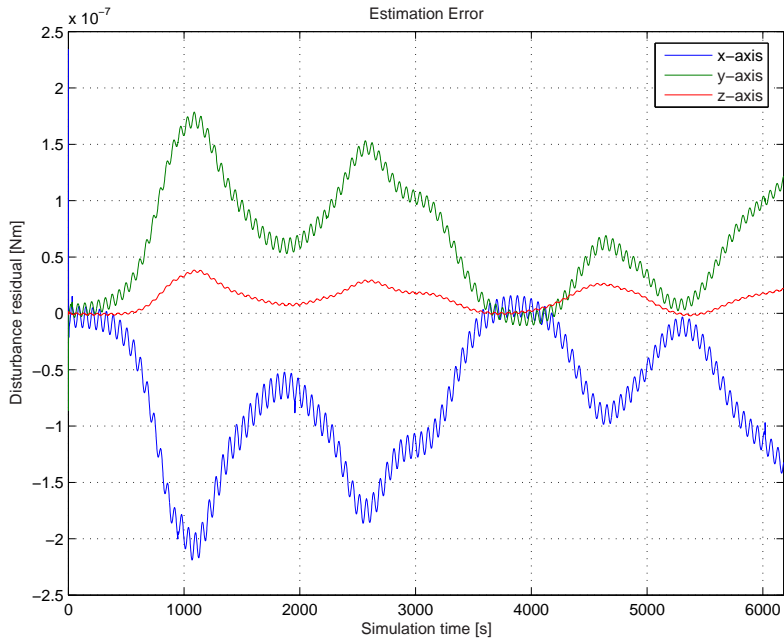


Figure K.1: The estimation error between the modeled disturbance torque and the estimated torque, during one of the simulations. The small oscillations are assumed to be caused by the momentum wheel bias.

1. The initial angular velocity is above the detumbled angular velocity, i.e., 0.0021 [rad/s] on each axis. This is used to evaluate whether the angular velocity controller can stabilise the attitude after detumbling has been performed. The actuator dynamics in the momentum wheels are omitted.
2. Initial angular velocity is set to detumbled angular velocity as in the previous evaluation, however, the actuator dynamics are included to yield a more realistic result. This simulation is performed both with and without the disturbance estimation and feedforward.
3. As the angular velocity controller is in the inner loop of the control structure it needs to be able to follow a reference generated by the outer loop. The initial angular velocity is set to 0 [rad/s] on each axis. At $t = 300$ [s] the reference input is set to 0.0045 [rad/s], and at $t = 2500$ [s] the reference input returns to zero.
4. To evaluate the angular velocity controller, w.r.t. different inertia matrices, a Monte Carlo simulation is used. The inertia matrix is changed, such that each of the vertices in the uncertainty region is evaluated. Furthermore, 30 random attitudes are simulated at each vertex. The initial angular velocity is set to zero, and the evaluation is performed both with and without disturbance estimation.

Results

The results obtained from the four different evaluations are presented in the following.

Case 1 A simulation with the initial angular velocity, is depicted in Figure K.2. The angular velocity settles to zero within approximately 6 [s], however, the momentum wheel

dynamics are not included as this simulation is performed to verify that the controller operates as designed.

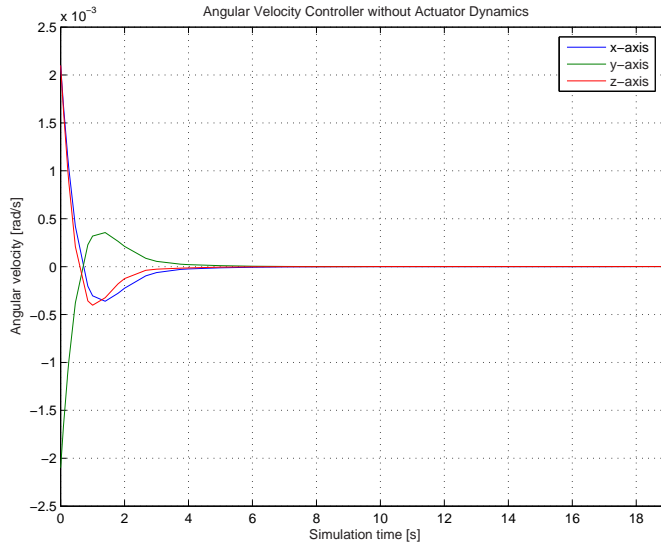


Figure K.2: Simulation results using the angular velocity controller without estimation, feedforward and actuator dynamics. Observe that the angular velocity has settled at zero within approximately 6 [s].

Case 2 When the momentum wheel dynamics are included the settling is not as smooth as without the momentum wheel dynamics, and the settling time is also prolonged to approximately 14 [s], as shown in Figure K.3.

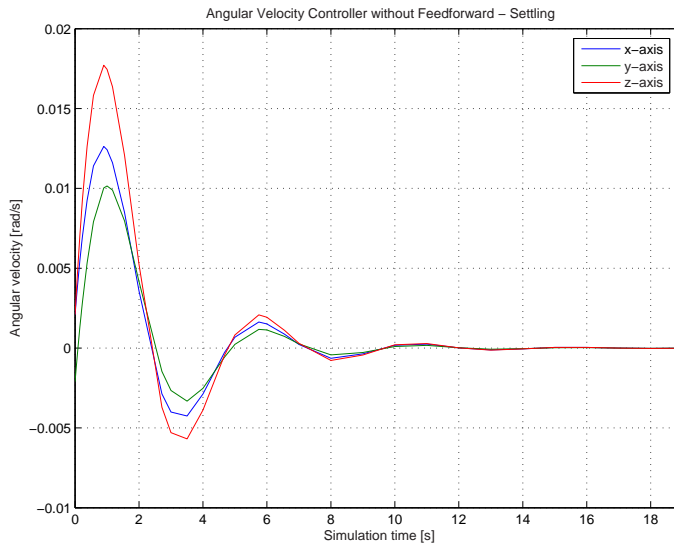


Figure K.3: Plot of the angular velocity settling at zero from an initial angular velocity, when including the actuator dynamics. The settling time is approximately 14 [s].

However, during an orbit the disturbance torques are counteracted and the angular velocity is below $1.5 \cdot 10^{-6}$ [rad/s]. This result is obtained without feeding the disturbance estimate

forward and the angular velocity is depicted in Figure K.4.

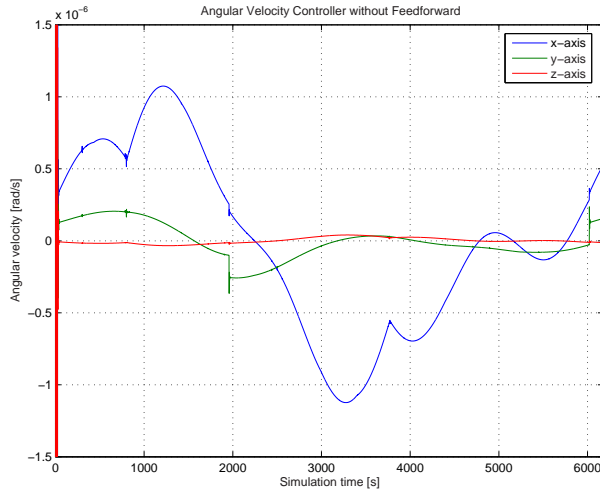


Figure K.4: Simulation result from a complete orbit using the angular velocity controller without estimation and feedforward of the disturbance torques. The angular velocity is after settling within $\pm 1.5 \cdot 10^{-6}$ [rad/s], during the entire orbit.

Figure K.5 shows that once the disturbance estimator is enabled the angular velocity controller is capable of reducing the angular velocity below $0.25 \cdot 10^{-6}$ [rad/s] on the axis introduced to the largest torque. However, the settling of the estimator yields fluctuations in the angular velocity for approximately 60 [s].

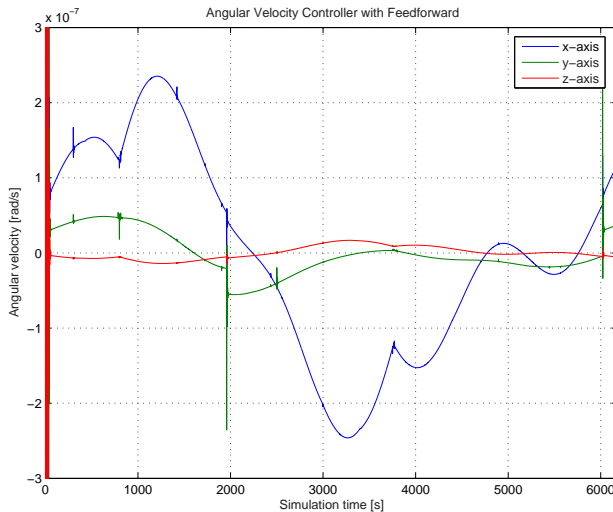


Figure K.5: Angular velocity from a simulation of an entire orbit using the disturbance estimation and feedforward. The angular velocity is, after settling, within $\pm 0.25 \cdot 10^{-6}$ [rad/s]. The settling of the angular velocity is dependent on the estimation and feedforward, and is approximately 60 [s]. The spikes in the angular velocity is assumed to be caused by the estimator settling and feedforward, as the satellite exits eclipse at approximately $t = 2000$ [s] and enters eclipse again in the end of the simulation.

Case 3 Figure K.6 depicts the resulting angular velocity from the simulation where the reference input to the angular controller is changed. The topmost plot in Figure K.6 shows that once the angular velocity controller receives a reference signal, it is able to obtain the specified angular velocity.

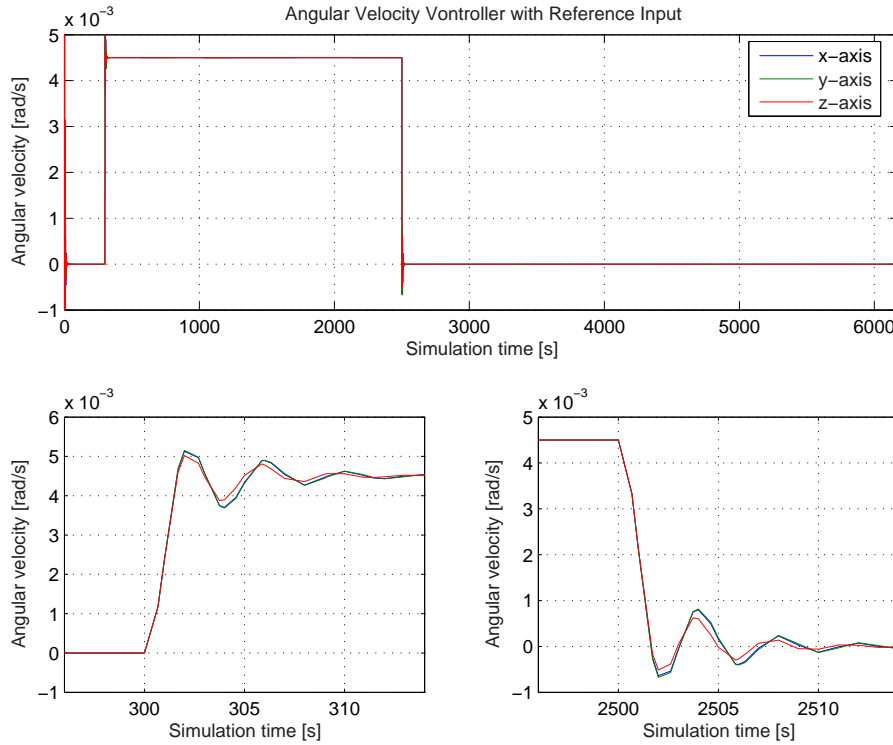


Figure K.6: Simulation results from an orbit with step on the reference input. The top plot depicts the angular velocity during the entire orbit. In the bottom left plot, the step up is shown. The step down is depicted in the bottom right plot.

As noticed from the bottom left and bottom right plots the angular velocity controller obtains the desired references within approximately 15 [s].

Case 4 The inertia matrix is changed within the uncertainty region and a new random attitude is used every orbit, yielding 270 simulations. Furthermore, this simulation has been performed both with and without the disturbance estimation and feedforward. Without estimation and feedforward

$$\boldsymbol{\mu}_{\omega_{\text{no_est}}} = [-9.38 \ -16.8 \ 0.36] \cdot 10^{-9} [\text{rad/s}] \quad (\text{K.3})$$

$$\boldsymbol{\sigma}_{\omega_{\text{no_est}}} = [434 \ 400 \ 36] \cdot 10^{-9} [\text{rad/s}] \quad (\text{K.4})$$

was obtained. Enabling the disturbance estimation and feedforward reduced these values to

$$\boldsymbol{\mu}_{\omega_{\text{est}}} = [600 \ 95 \ -14.7] \cdot 10^{-12} [\text{rad/s}] \quad (\text{K.5})$$

$$\boldsymbol{\sigma}_{\omega_{\text{est}}} = [6.01 \ 4.96 \ 0.54] \cdot 10^{-9} [\text{rad/s}]. \quad (\text{K.6})$$

The reason the z-axis values are smaller than the x- and y-axes is assumed to be the solar array, which yields a larger aerodynamic torque around the x- and y-axes.

Conclusion

The angular velocity controller is capable of reducing the angular velocity to less than $1.5 \cdot 10^{-6} [\text{rad/s}]$ from an initial velocity equivalent to the detumbled angular velocity. The feedforward of the estimated disturbance torques reduces the influence of environmental torques with a factor of 6. Furthermore, the angular velocity is capable of following reference input of at least $0.26 [\text{^o/s}]$ as stated in the requirements. From a Monte Carlo simulation it is established that the angular velocity controller can reduce the angular velocity caused by the environmental disturbance torques. The angular velocity controller is at this point assumed to be sufficient to facilitate the requirement for the attitude error angle.

K.2 Desaturation Controller

This section describes the evaluation of the desaturation controller designed to handle the unloading of angular momentum of the momentum wheels once the limit for activation of the controller is reached. In order to evaluate the desaturation controller the angular velocity controller has been included in the simulations. However, this evaluation only considers results regarding the performance of the desaturation controller. A description of the evaluations performed follows.

1. The maximum disturbance torque of $1599.1 \cdot 10^{-9} [\text{Nm}]$, is exerted on the x-axis of the satellite. This entails that the momentum wheel on the x-axis spins towards saturation, while the change in angular momentum for the other momentum wheels should be significantly less. Thus, it should be possible to show that the desaturation controller functions as intended.
2. The designed trigger method is evaluated w.r.t. conservation of energy and is compared to an implementation where the desaturation controller is constantly active. In this simulation the modeled disturbances are exerted on the satellite, and both simulations are performed over two orbits.

K.2.1 Results

The results of the two evaluations are presented in the following.

Case 1 Figure K.7 depicts the results from the first simulation. The top plot shows the activation and deactivation of the desaturation controller. The middle plot depicts the upper and lower limits for activation and deactivation respectively, and the magnitude of the cross product between the error in angular momentum and the geomagnetic field vector. The bottom plot shows the error in angular momentum for each momentum wheel. From the middle figure it is noticed that the upper bound for activation changes dynamically according to the change in the geomagnetic field.

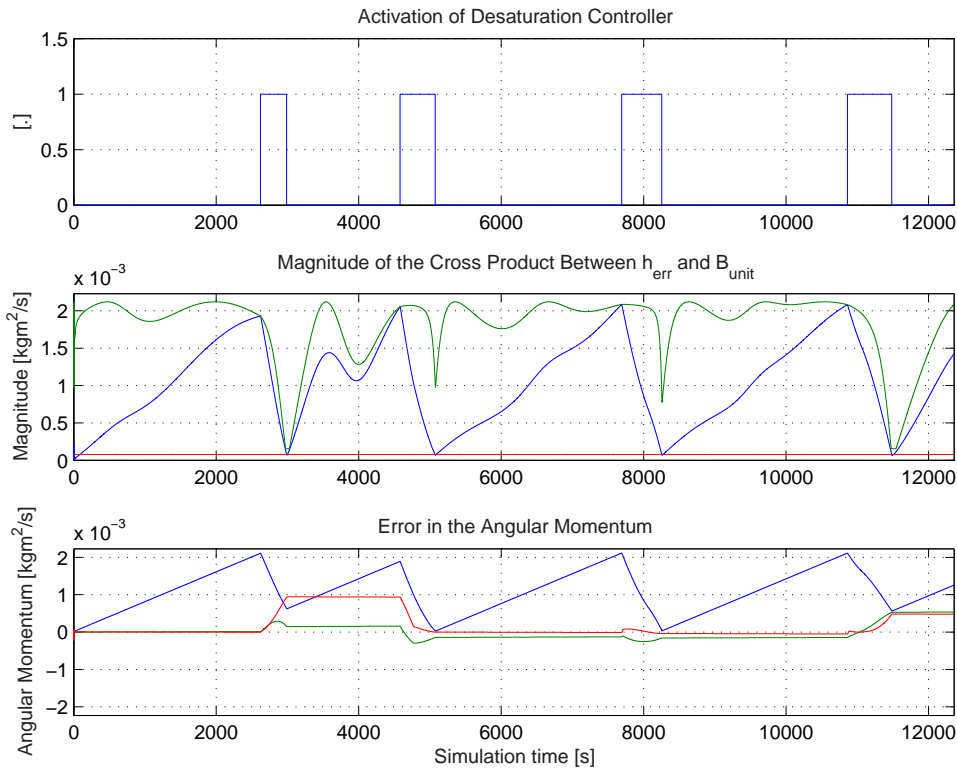


Figure K.7: Simulation results for the desaturation controller. The top plot depicts the trigger output and the middle plot depicts the trigger level and \mathcal{T}_{desat} . The bottom plot depicts the angular momentum of each of the momentum wheels.

Once \mathcal{T}_{desat} crosses the upper limit the activation of the desaturation controller is triggered, which is also shown in the top plot as the function switches from zero to one. From the bottom plot it is noticed that the error in angular momentum, on the momentum wheel along the x-axis, increases until the desaturation controller is activated. After activation the desaturation controller uses the magnetorquers to decrease the error back towards $\mathbf{h}_{mw_{bias}}$, which corresponds to zero in the bottom plot.

Case 2 The power consumption of the desaturation controller is investigated and reveals that when using the trigger method no power is consumed by the magnetorquers. Figure K.8 depicts T_{desat} and the activation limits. As seen in the figure the magnitude of the cross product never exceeds the upper limit, thus the desaturation controller is never switched on. This is caused by the fact that a near constant attitude is maintained and the sum of environmental torques during an entire orbit adds to approximately zero, i.e., the disturbance torques are used to both accumulate and dissipate angular momentum.

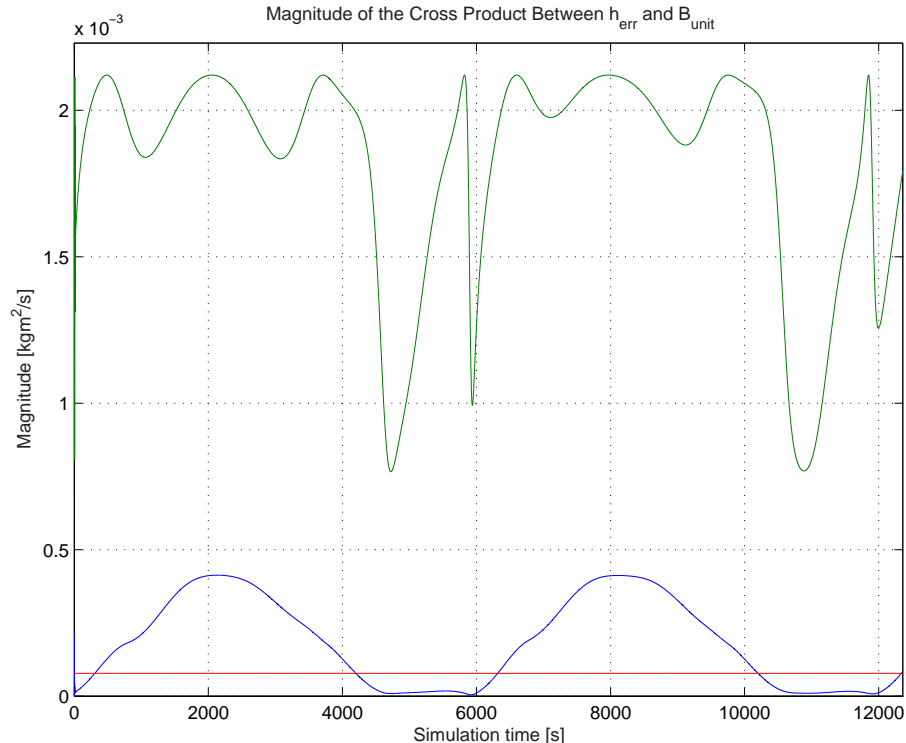


Figure K.8: Simulation results from a simulation using the modeled disturbance torques. Notice that the desaturation controller is never activated.

Figure K.9 depicts the power consumption from the same simulation with a constantly activated desaturation controller. In the considered situation it is, therefore, possible to conserve energy by using the trigger method.

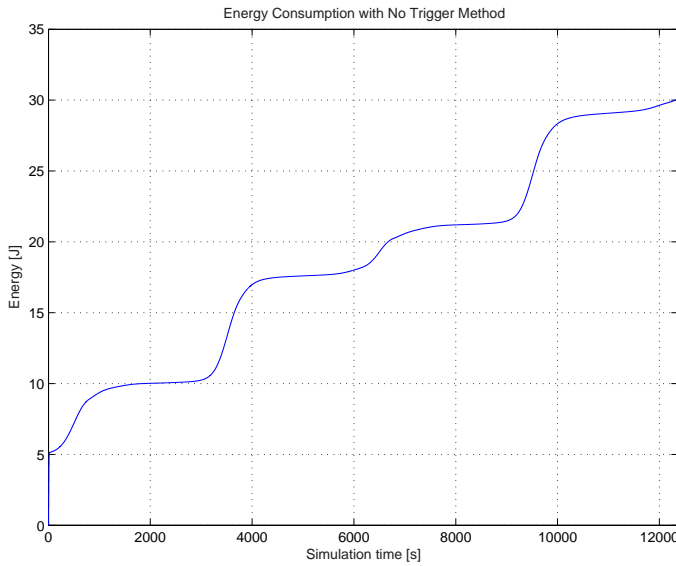


Figure K.9: Energy consumption of the magnetotorquers during a simulation of two orbits. The desaturation controller is constantly activated.

K.2.2 Conclusion

The desaturation controller is capable of removing angular momentum from the momentum wheels, which is accumulated from disturbance torques and attitude manoeuvres. However, Figure K.8 indicates that the momentum wheels might be slightly overdimensioned as the desaturation controller is never activated, when the modeled disturbances are enabled. The trigger method implemented conserves energy compared to a constantly activated desaturation controller. Thus the desaturation controller functions as intended.

K.3 Attitude Controller

In order to evaluated the attitude controller the simulations include the desaturation controller and the angular velocity controller. However, this evaluation only includes results regarding the performance of the attitude controller.

1. A total of 30 simulations have been executed, each with a simulation time of one orbit and randomly generated initial and reference quaternions. The reference quaternions are generated in such a manner, that a rotation of the angular momentum vector of the momentum wheels by the error quaternion, still yields an angular momentum vector in the 1st octant of the SBRF. The objective of this evaluation is to show that the attitude controller is capable of producing a reference signal for the angular velocity controller, which entails that the satellite reaches the desired reference attitude. The reference quaternion is fed to the attitude controller 100 [s] after the simulation is initiated to allow the Kalman filter to settle.
2. A simulation is executed with a simulation time of one orbit, where the attitude controller is fed a reference quaternion, which entails that the error quaternion rotates

the angular momentum vector outside the 1st octant of the SBRF. The objective of this simulation is to show that once the angular momentum vector of the momentum wheels leaves the 1st octant the attitude becomes unstable.

K.3.1 Results

The results of the two evaluations are presented in the following.

Case 1 Of the 30 simulations conducted with randomly generated initial and reference quaternions six are depicted in Figure K.10. All of the 30 simulations showed that the attitude controller is capable of producing the necessary reference for the angular velocity controller, in order for the satellite to obtain the specified reference attitude.

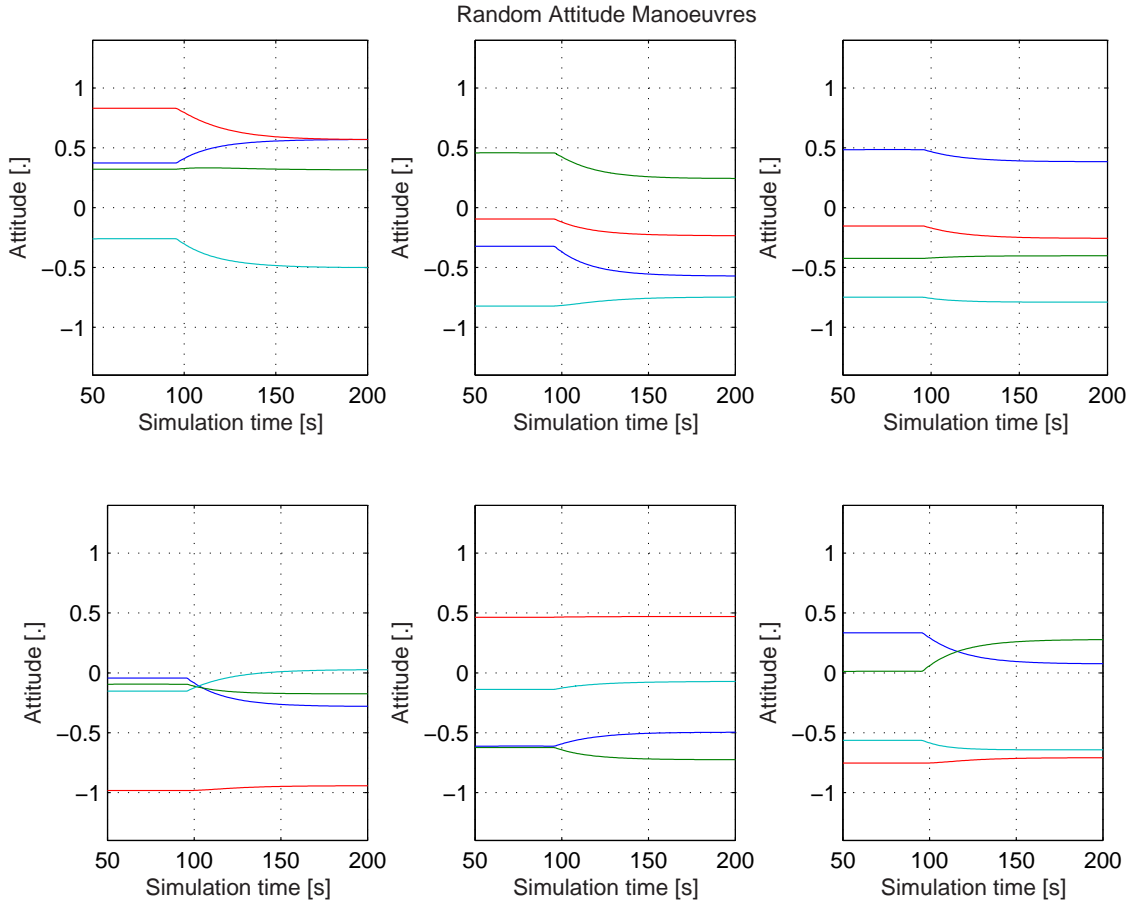


Figure K.10: Six randomly generated attitude manoeuvres, which show that reference attitudes are obtained by the satellite.

Case 2 Figure K.11 depicts the attitude quaternion of the satellite, when the attitude controller is fed a quaternion, which corresponds to the error quaternion rotating the angular momentum vector of the momentum wheels outside the 1st octant of the SBRF.

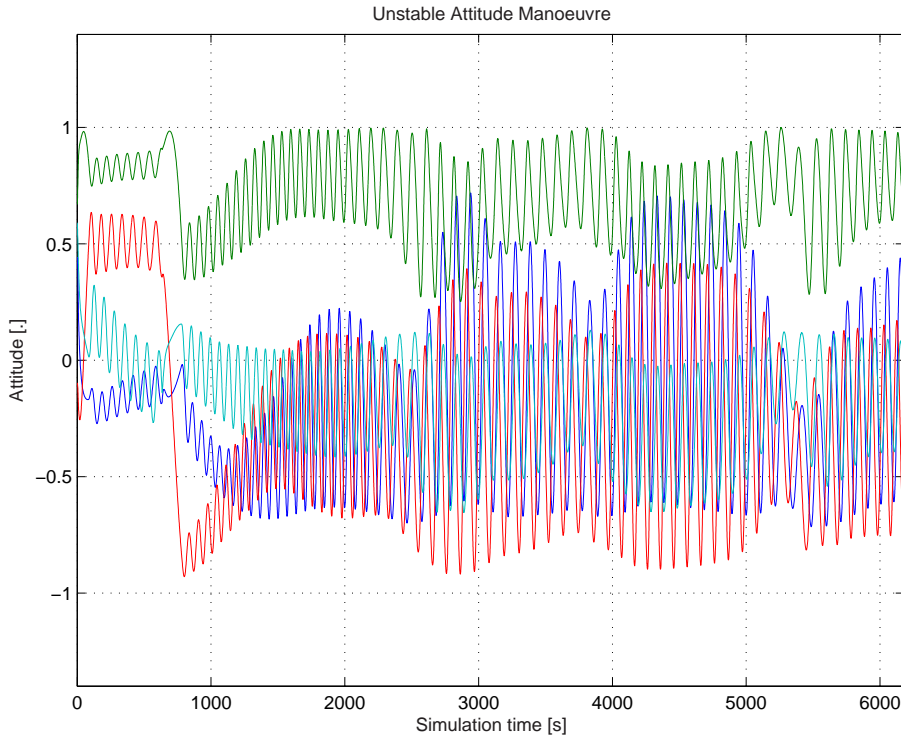


Figure K.11: Unstable attitude manoeuvre. It is not possible to obtain the desired attitude, due to the fact that one or more momentum wheels reach their saturation limit.

K.3.2 Conclusion

The attitude controller is capable of producing the necessary reference signal for the angular velocity controller, given that the angular momentum of the momentum wheels is not rotated outside the 1st octant of the SBRF. Should the angular momentum of the momentum wheels leave the 1st octant the attitude of the satellite cannot be obtained, thus if the attitude becomes unstable.

K.4 Complete Control System

In this section the complete robustly controlled system designed in this report is evaluated. The results obtained are compared to the results obtained by using a similar control structure, but with simple substitutions in each of the controllers in the control structure, which will from hereon be referred to as "simple control".

Simple control implies an attitude controller with a proportional gain and an angular velocity controller, with state feedback, designed using pole placement. The poles in the simple angular velocity controller closed loop are placed in $-1.254 [.]$, $-1.255 [.]$ and $-1.256 [.]$ respectively to accommodate the bandwidth requirement described in the model analysis in Chapter 4. Moreover, the proportional gain in the attitude controller is adjusted to $0.06555 [.]$ on each term in $\mathbf{q}_{1:3}$, to comply with that same requirement, and to obtain the same bandwidth of the closed loop system as for the robust control system. The con-

trollers are made nearly as fast as possible, with a small margin, to ensure a reasonable performance. Furthermore, the desaturation controllers in the two configurations will be identical, but the estimator in the simple control configuration is a linear estimator designed using pole placement and tuned to similar performance as the designed Kalman filter.

The evaluation of the complete control system is divided into three cases.

1. The random initial attitude $\mathbf{q}_{\text{init}} = [-0.1166 \ -0.4432 \ 0.4313 \ -0.7771]^T$ will be used, from which to step to $\mathbf{q}_{\text{ref}} = [-0.1059 \ -0.7028 \ 0.2078 \ -0.6721]^T$, the random reference attitude, at the start of the simulation at $t = 100$ [s], thus leaving the first 100 [s] for the estimators to settle. At $t = 500$ [s] the reference attitude is stepped back to the initial attitude. Two simulations are performed with these attributes: One with the nominal inertia matrix (a) and one with an uncertain inertia matrix (b), with the diagonal being 95 [%] of nominal on each element, i.e, a vertex in the uncertainty region. This evaluation is performed to investigate the effects of attitude manoeuvres, and the effects of uncertainties in the inertia matrix in each of the two control configurations.
2. From a random initial attitude it is desired to investigate, whether the controlled systems meet the requirements to the ACS. This is done using a Monte Carlo simulation, where the two controlled systems for each iteration are simulated for an entire orbit given the initial attitude, a drag coefficient and an air density. The ability to maintain the initial attitude is investigated over 30 different initial attitudes, drag coefficients and air densities. This is done only for every vertex of the inertia uncertainty region, and for the nominal inertia matrix, to reduce the computational load of the simulation. This yields 270 different simulations of each system. The first 150 [s] of each simulation is circumvented to allow for the settling of the estimators.
3. The designed pointing controller is given a location on the Earth's surface to track with the camera, more precisely Aalborg, Denmark. The NSO is commanded to point towards this location for an entire orbit. The results are meant to indicate the pointing controller's ability to keep the satellite pointed at a specified location.

K.4.1 Results

The simulations previously described yielded the results subsequently described. All mean, standard deviations, minima and maxima, are calculated using corresponding functions in MATLAB.

Case 1a Plotting the results obtained when simulating attitude manoeuvres with a nominal inertia matrix, yielded the results showed in Figure K.12 and Figure K.13. As can be seen in Figure K.12 the robust controller configuration yields a faster settle of the error angle. The angle has settled enough to certify an acceptable attitude manoeuvre within approximately 100 [s] as opposed to the 160 [s] with the simple controller. The same tendency is evident for the rise-time in the two configurations.

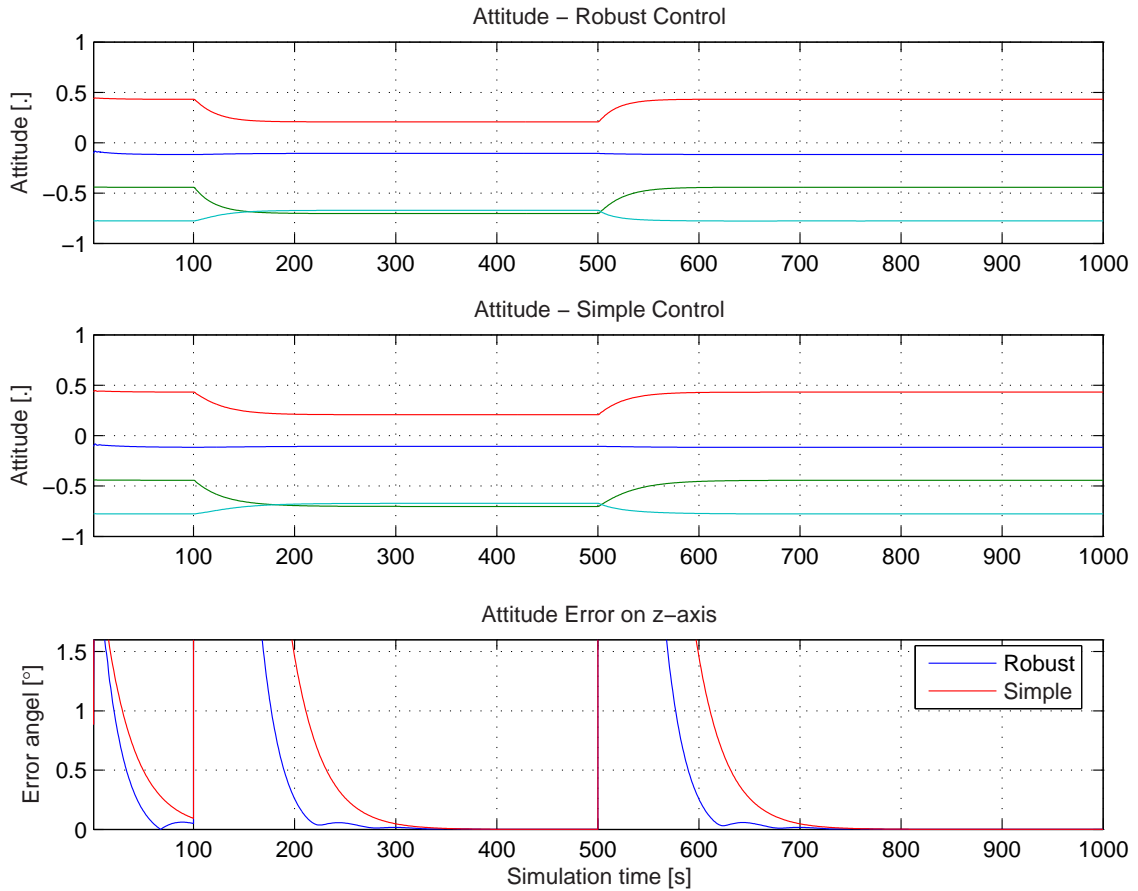


Figure K.12: Plots of the resulting changes in attitude with a nominal inertia matrix. The two topmost plots show the attitude for both the robustly controlled and the simply controlled system. The bottom plot shows the angular errors in attitude on the z-axis for both controller configurations. Notice that the rise- and settle-time for the simply controlled system is significantly longer than for the robustly controlled system.

Keeping in mind the results seen in Figure K.12 it is noticeable to see the same tendency for the settling-time in the plots of the angular velocities in Figure K.13. Also noticeable is the slight overshoot in the angular velocities in the robust control configuration. When reexamining Figure K.12 this is evident in the slight increase in the error angle for the robust control configuration after the initial rise.

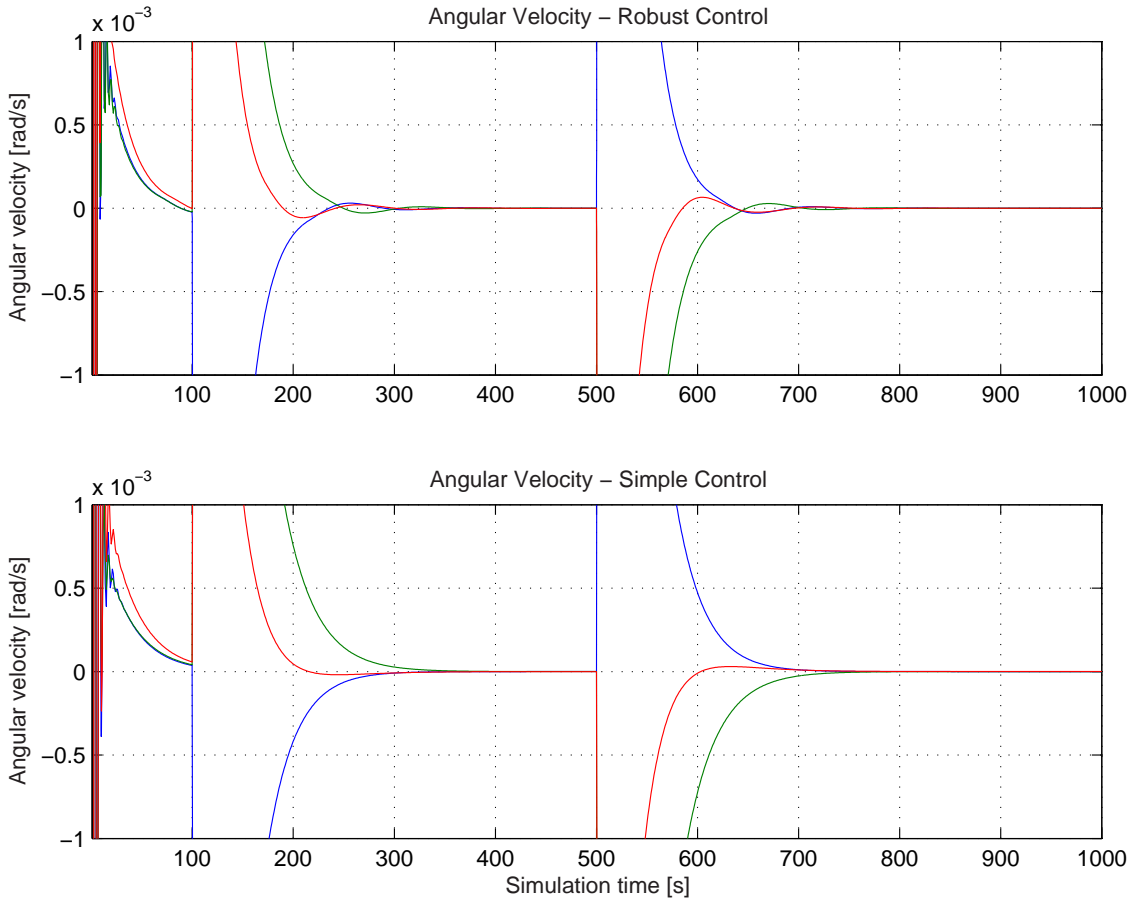


Figure K.13: Plots of the resulting changes in angular velocity arising from attitude manoeuvres with a nominal inertia matrix. The topmost plot shows the angular velocity on the robustly controlled system, whereas the bottom plot show the simply controlled system. Notice the better performance and slight overshoot in the robust control configuration.

The bandwidth of the closed loop systems in each configuration were identical and had a value of 0.19958 [Hz]. The jitter in the attitude and velocity, at the start of each the simulations, is attributed to the settling of the estimators.

Case 1b The perturbed inertia matrix yielded little change in the performance of each of the two configurations. Plots similar to the ones in case 1a are successively presented in Figure K.14 and Figure K.15. If anything should be noticed it will be the slightly longer settling time in the simple control configuration in the plot of the angular velocities in Figure K.15.

An interesting fact is found when examining the resulting bandwidths of each system. The robust control configuration is still within the requirement, with a bandwidth of 0.19974 [Hz], but the simply controlled closed loop system now has a bandwidth of 0.20133 [Hz].

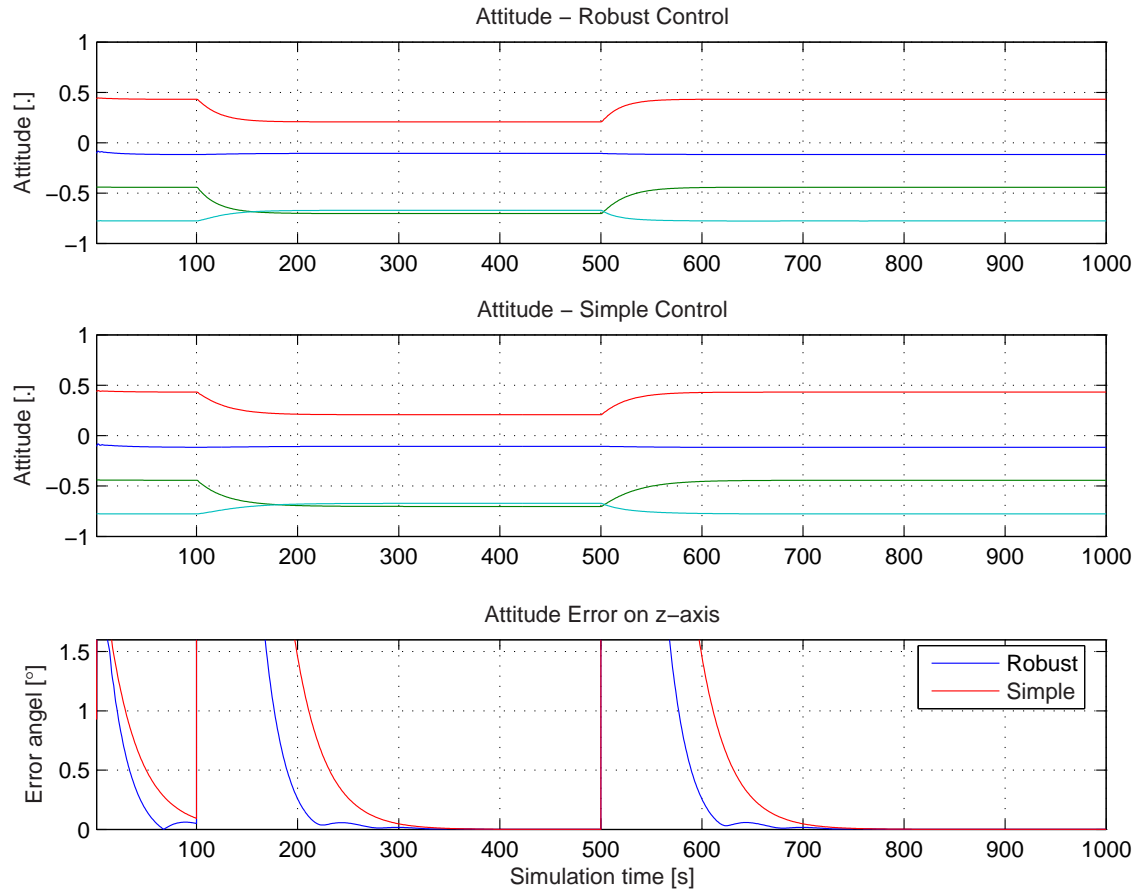


Figure K.14: Plots of the resulting changes in attitude with a perturbed inertia matrix. The two topmost plots show the attitude for both the robustly controlled and the simply controlled system. The bottom plot shows the angular errors in attitude on the z-axis for both controller configurations. The rise- and settle-time for the simply controlled system is significantly longer than for the robustly controlled system.

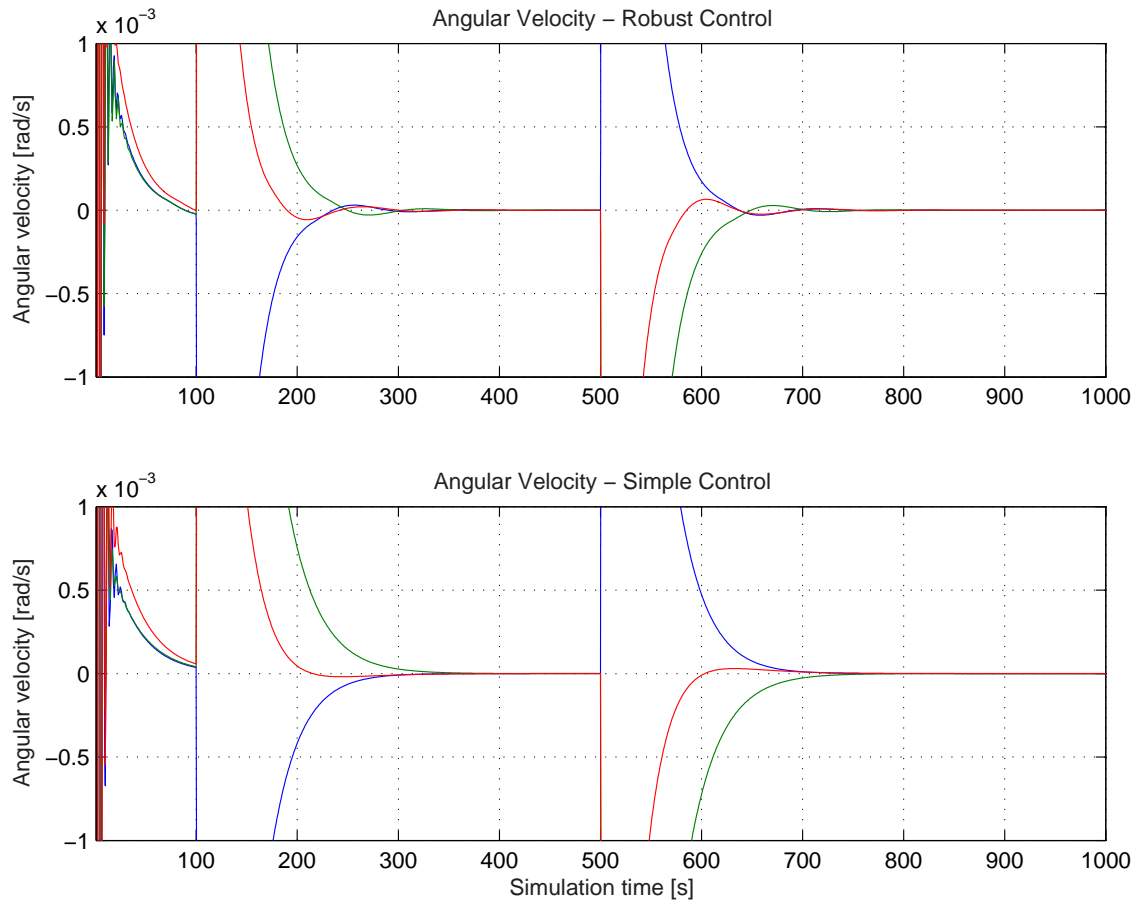


Figure K.15: Plots of the resulting changes in angular velocity arising from attitude manoeuvres with a perturbed inertia matrix. The topmost plot shows the angular velocity on the robustly controlled system, whereas the bottom plot show the simply controlled system. The robust control configuration performs better and has a slight overshoot.

Case 2 From the Monte Carlo simulation the mean and standard deviation for the attitude error angle and for the angular velocity, were obtained for both configurations. The values for each of the configurations are presented in Table K.1, along with maximum and minimum values. The error angle is for simplicity denoted ϑ . The sampling distribution for the angular error on the z-axis for both control configurations, is depicted in the histogram in Figure K.16. A total of 1649060 angles were sampled in each configuration.

Entity	Robust Control	Simple Control	Unit
Error Angle on z-axis (ϑ)			
μ_ϑ	0.0058	0.0588	[$^\circ$]
σ_ϑ	0.0467	0.0599	[$^\circ$]
ϑ_{\max}	0.99	1.0672	[$^\circ$]
ϑ_{\min}	0	0	[$^\circ$]
Angular Velocity			
μ_ω	$[36.487 \ 33.521 \ 36.41] \cdot 10^{-9}$	$[30.504 \ 38.458 \ 49.16] \cdot 10^{-9}$	[rad/s]
σ_ω	$[604.94 \ 537.67 \ 627.78] \cdot 10^{-9}$	$[310.74 \ 383.04 \ 498.13] \cdot 10^{-9}$	[rad/s]
ω_{\max}	$[8.89 \ 7.98 \ 8.96] \cdot 10^{-6}$	$[6.61 \ 7.90 \ 10.43] \cdot 10^{-6}$	[rad/s]
ω_{\min}	$[-2.68 \ -2.24 \ -5.53] \cdot 10^{-6}$	$[-0.27 \ -0.27 \ -0.07] \cdot 10^{-6}$	[rad/s]

Table K.1: Resulting mean and standard deviations, along with maximum and minimum values, for the results obtained in the Monte Carlo simulation of the two controller configurations.

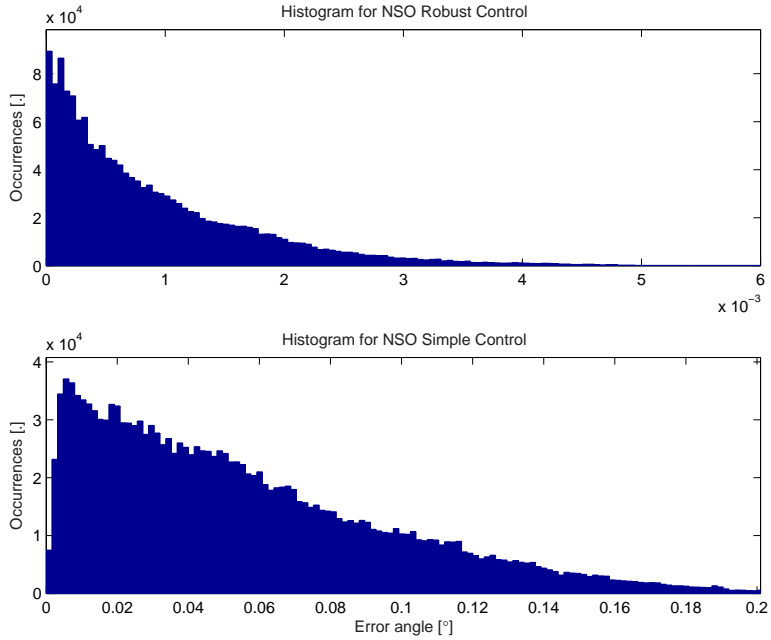


Figure K.16: Distribution of angular error samples on the z-axis for both the robustly controlled system and the system controlled by simple controllers. The number of samples is 1649060. Note that the scale is different in the two histograms.

Case 3 The z-axis error angle during an entire orbit is depicted in Figure K.17, and reveals that the error is approximately $2 [^\circ]$ at $t = 2000 [\text{s}]$. At that time the NSO is above the target location and the attitude reference is assumed to change rapidly. This

is verified by inspecting the attitude and angular velocity of the NSO, which is depicted in Figure K.18. It is noticed that the attitude changes during the entire orbit, which is expected as the reference location is constant.

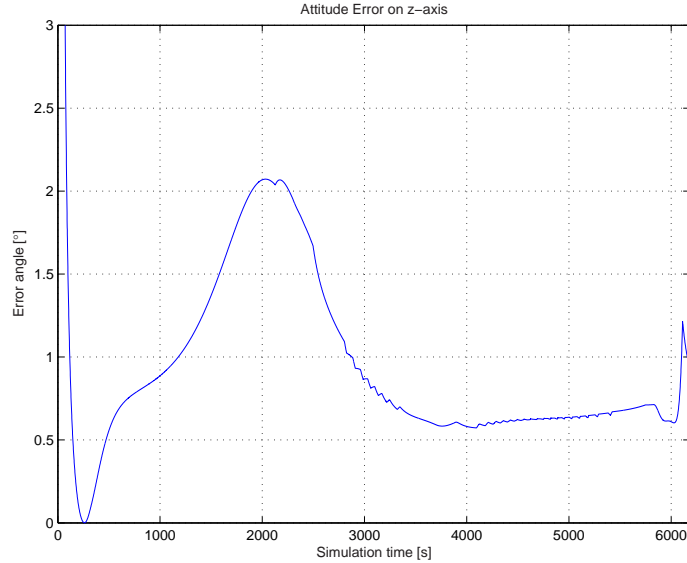


Figure K.17: The error angle during a simulation with the pointing controller. At $t = 2000$ [s] the NSO is directly above its target, which is Aalborg, Denmark.

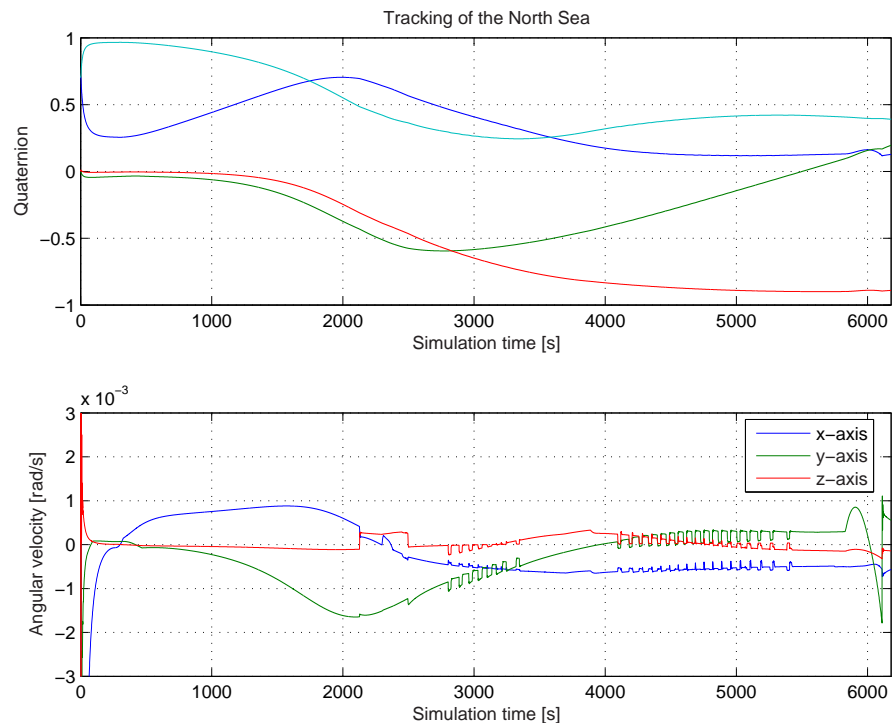


Figure K.18: The attitude changes constantly during the simulation of the pointing controller and the angular velocity is largest when the NSO is above the target location at $t = 2000$ [s].

This is also depicted in Figure K.19 where the satellite's position and attitude during the pass of Denmark is depicted. Furthermore, a video of this pass can be found on the enclosed CD (see Appendix M).

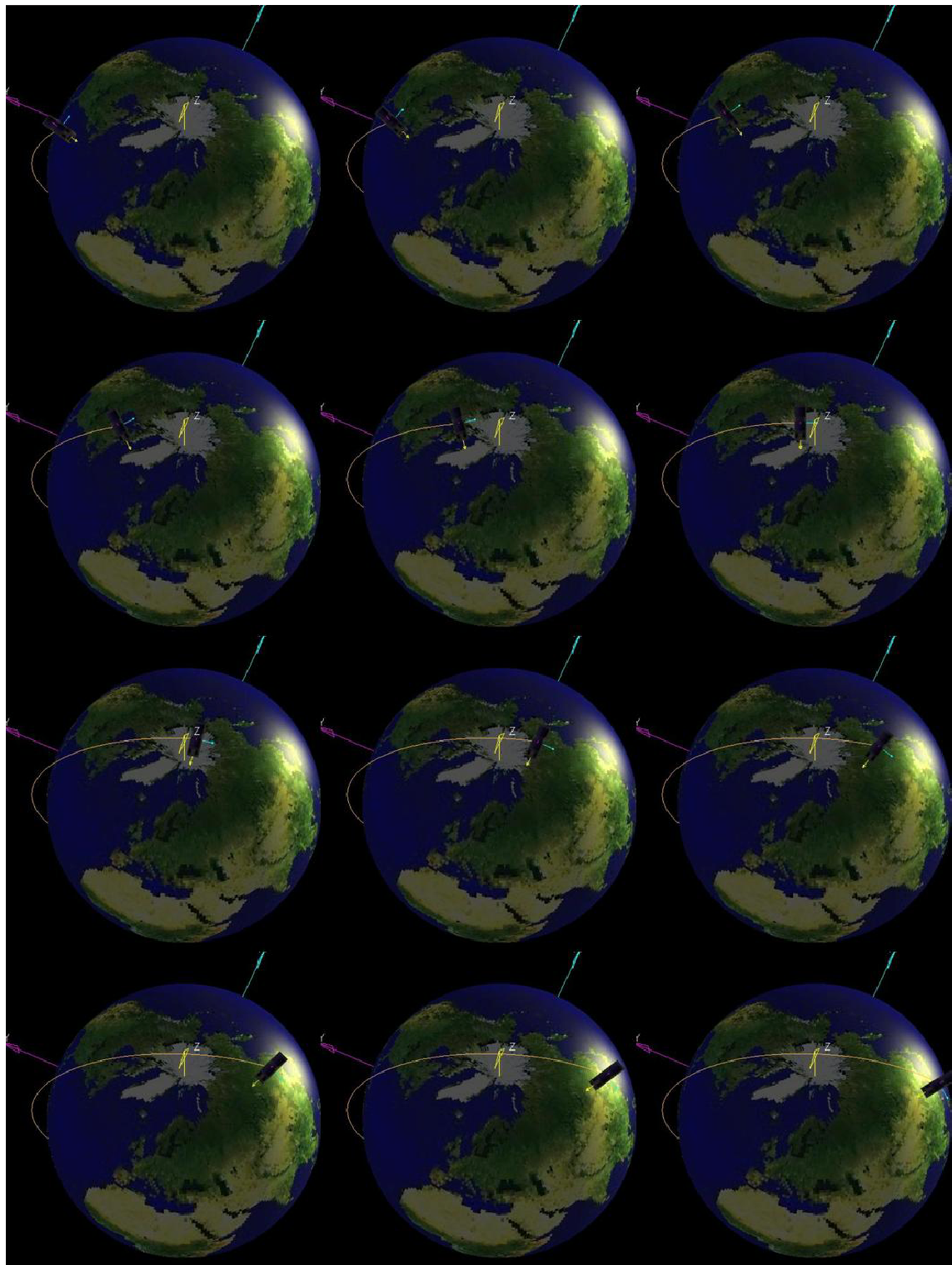


Figure K.19: The position and attitude of the NSO during a pass of Denmark.

K.4.2 Conclusion

The simulations of the attitude manoeuvres showed that both controller configurations were able to control the attitude of the NSO. However, the robust controller configuration did prove overwhelmingly faster at acquiring the designated attitude than the simple control configuration. The simulations did, however, show that a slight overshoot is present in the robustly controlled closed loop. Another noticeable fact is that the performance in both configurations did not differ significantly, when introduced to uncertainties in the inertia matrix. However, the bandwidth requirement was not met for the simply controlled system, but remained virtually unchanged for the robustly controlled system.

Due to the integrator action in the system, inherent in the feedback of the attitude, the angular velocity mean obtained from the Monte Carlo simulation in case 2 was expected to be smaller than what is obtained in the evaluation of the angular velocity controller in Section K.1. This is, however, not the case and is explained by the circumstances of the two simulations, i.e., the angular velocity controller is simulated without the desaturation controller and thus an entire orbit cannot be simulated with the actuator dynamics. Furthermore, in the evaluation of the angular velocity controller the air density was not changed. Therefore, the mean and standard deviation of the complete system is larger.

The Monte Carlo simulation also yielded resulting mean angular errors and standard deviations as presented in Table K.1. It is immediately evident that the robust control configuration is more reliable for pointing in the correct direction, as both the mean and standard deviation are smaller than for the simple control configuration. It is worth noticing that the mean deviation of the z-axis is a factor ten better for the robust control configuration. The angular velocities does, however, not yield similar results as the mean angular velocity is approximately the same in the two configurations. The standard deviation is for the robust configuration larger, which implies that this configuration has a faster response to disturbances.

The 1649060 samples of the error angle, depicted in Figure K.16 for the robustly and simple controlled systems respectively, are not uniformly distributed. As the angle is never negative, a one sided distribution is required to examine the results. When examining Figure K.16 it is intuitive to approximate with an exponential distribution. Preliminary estimates indicate a better performance in the robust controller configuration.

The simulation of the pointing controller showed that a reference attitude can be calculated and introduced to the attitude controller to obtain tracking of a Earth-fixed location. However, when the satellite is located above the reference location a pointing error of $2 [^\circ]$ is present, which is not feasible w.r.t to requirement.

Simulation Environment

This appendix describes the simulator developed for this project. The simulator is implemented in SIMULINK as a means of verifying different controllers. This appendix addresses the reader, which is interested in the simulator structure and seeks a more detailed view of the individual model implementations.

L.1 Simulation Environment

To facilitate further development and expansions the simulator is based on a SIMULINK library implementation and the mask functionality has widely been used to ensure singular definitions of parameters, e.g., the inertia matrix. The different files and libraries used in the simulator are described in the `readMe.txt`-file in the simulator library root. Here one may also find the `startup.m`-file used to ensure that all paths are set up correctly for satellite simulation. This file can be executed with an optional input, e.g. `startup(42)`, to compile the required `mex`-files. This is only required to be done once, as the required compiled files will then be present.

The simulator source files are sorted in designated directories, which name reflects the purpose for which they are used. The different directories are presented in Table L.1.

Directory Name	Content Description
<code>root</code>	Files used to ensure simulation on various versions of MATLAB and the magnetic field model data. Also found are the <code>readMe.txt</code> and <code>startup.m</code> files.
<code>lib</code>	Contains the SIMULINK library with the components of the simulator.
<code>lib/albedo_toolbox</code>	Contains a source model for the albedo toolbox used in the modeling. Developed by M.Sc.E.E., Ph.D., Dan Bhandari, AAU.
<code>lib/pictures</code>	Contains jpeg-files used in different SIMULINK block masks.
<code>lib/utils</code>	Contains <code>mex</code> - and <code>m</code> -files used in the mathematical modeling of the satellite, sorted into subdirectories.
<code>misc</code>	Miscellaneous script files for, e.g., compiling <code>mex</code> -files, printing SIMULINK models or illustrating vectors.
<code>design</code>	Files used to create different controllers.
<code>models</code>	Contains various SIMULINK model files used as templates for test cases.
<code>test</code>	Contains SIMULINK model files with specific controllers used to evaluate the individual controllers.

Table L.1: Description of directories in the simulator.

Generally a description of the `m`-files used in the simulator can also be found in the individual files.

L.2 Satellite Behavior

The satellite behavior implementation is based on orbit models, space environment models and the equations of motion for the satellite. The orbit models and equations of motion are reused from the AAUSAT-II simulation environment [Group 05gr833 2005], however the space environment models have been heavily remodeled and restructured. To provide a brief overview of the satellite behavior implementation, it can be inspected in Figure L.1.

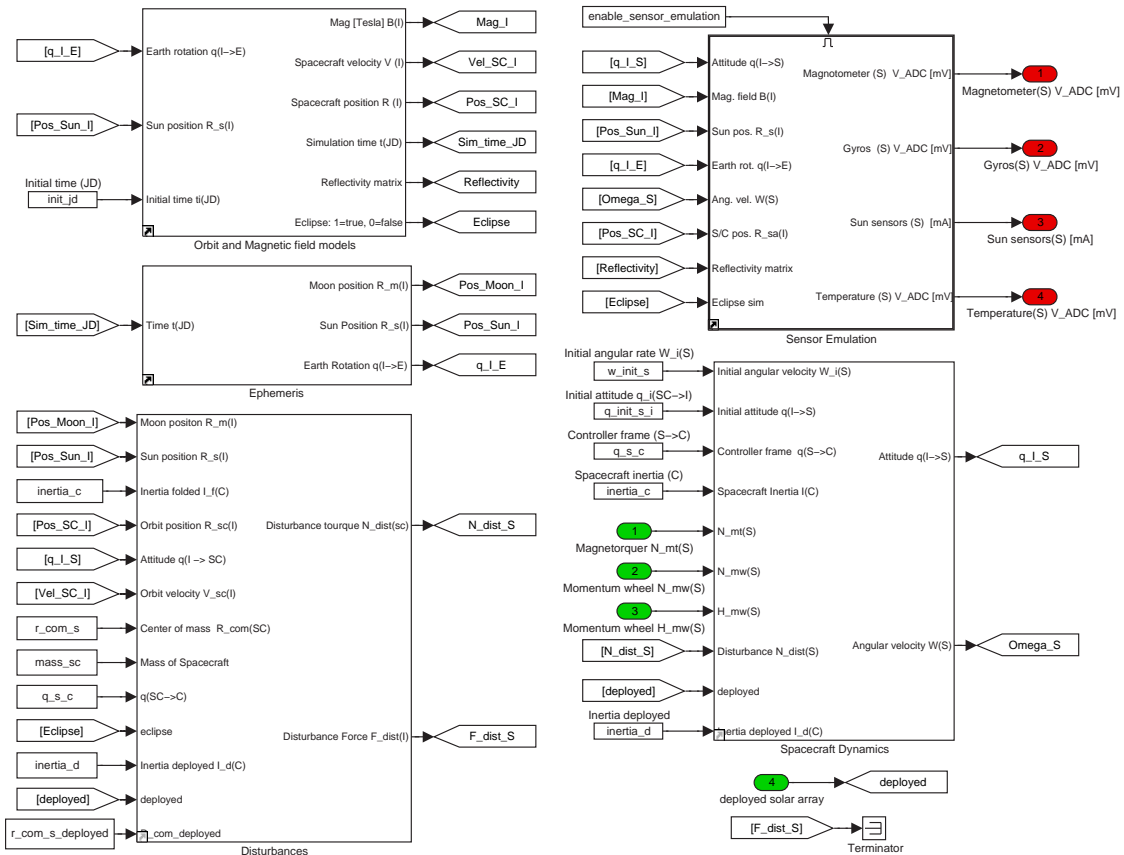


Figure L.1: The satellite behavior implementation.

L.2.1 Environmental Disturbances

The space environment models, which have been greatly remodeled, are the solar radiation, the gravity gradient and the atmospheric drag disturbances as described in Section 2.3 on page 12. These have each been implemented in the simulator separately, and the implementations are illustrated in Figure L.2, Figure L.3 and Figure L.4 respectively.

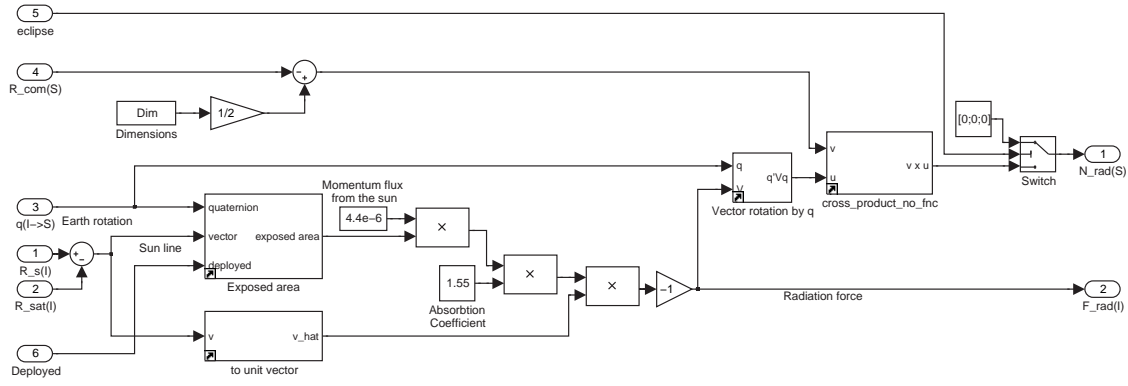


Figure L.2: The solar radiation disturbance implementation.

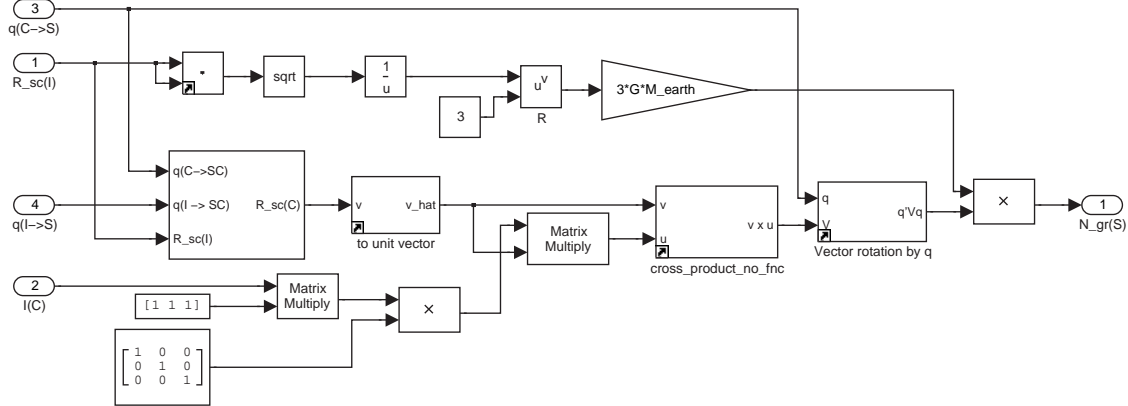


Figure L.3: The gravity gradient disturbance implementation.

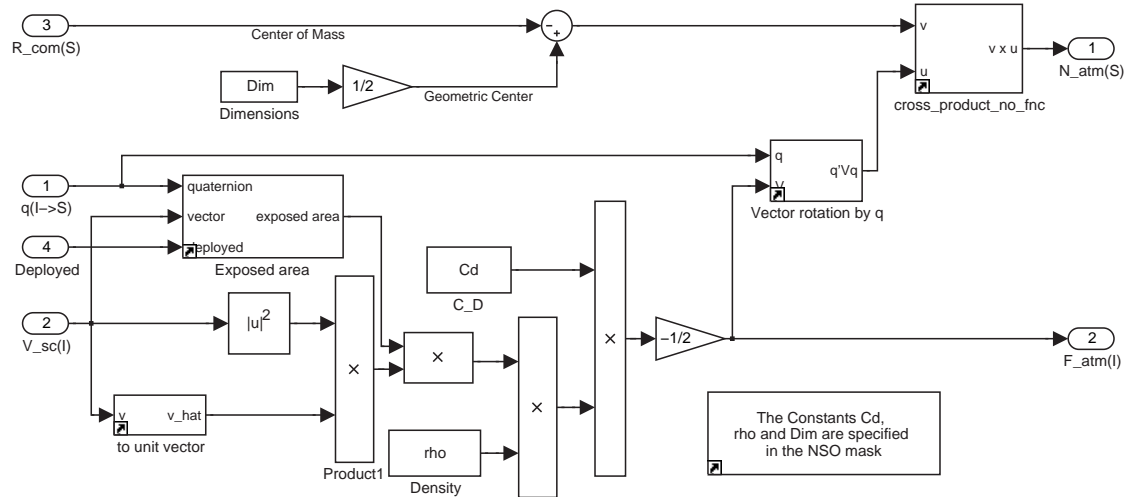


Figure L.4: The atmospheric drag disturbance implementation.

The individual disturbances are joined to form a single disturbance torque, which is dependent on the deployed state of the NSO. This is done as depicted in Figure L.5.

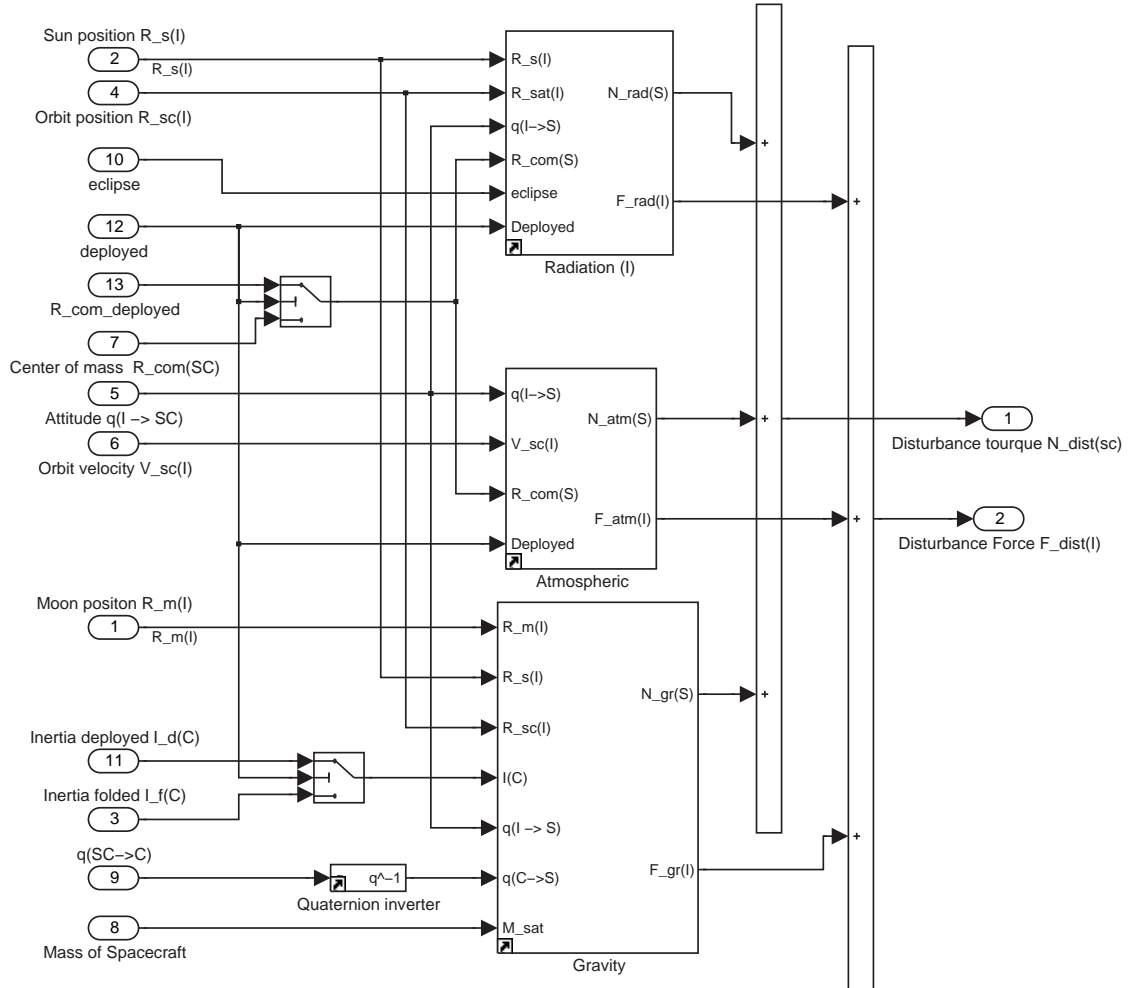


Figure L.5: The implemented environmental disturbances joined to a single disturbance torque.

L.3 Actuator Implementations

The actuator implementations used on the NSO also has their roots in the implementations on AAUSAT-II. However, like the environmental disturbance models they have been subject to substantial remodeling, which is why the implementation of these are described here. The mathematical modeling of the actuators are described in Section 2.4 on page 20.

Magnetorquer The model describing the individual magnetorquer has been implemented in SIMULINK as depicted in Figure L.6, and a model of the complete magnetorquer system is easily available via the SIMULINK library browser.

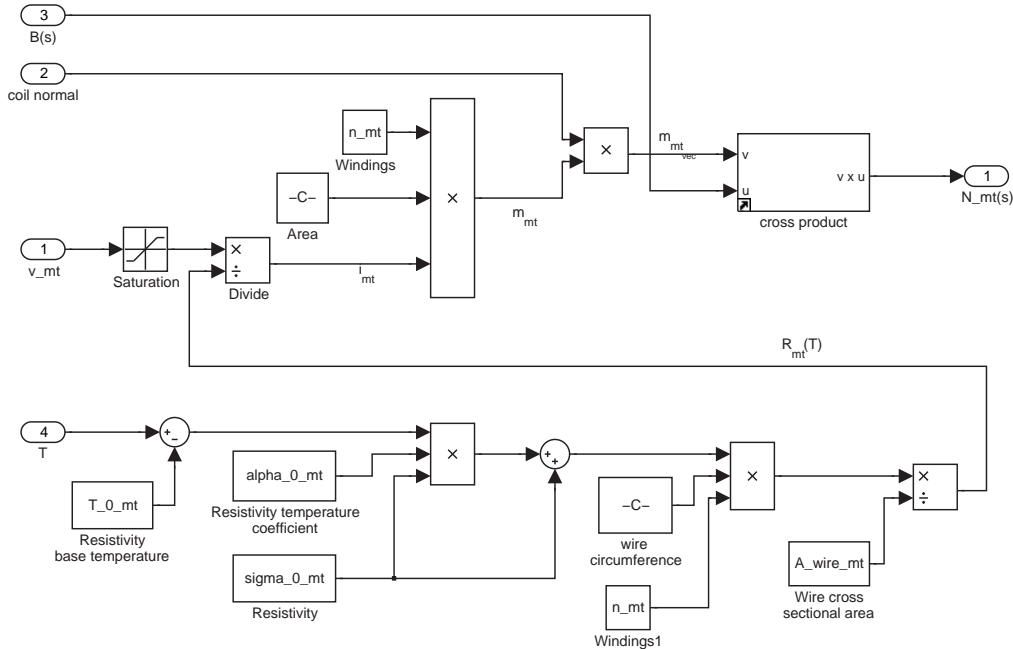


Figure L.6: The implementation of a magnetorquer.

Momentum Wheel The model for the individual momentum wheel is implemented as illustrated in Figure L.7. Furthermore, a continuous version of the momentum wheel hardware controller is augmented to the model as a transfer function, and a complete implementation of the entire momentum wheel system is available analogously to the magnetorquer system.

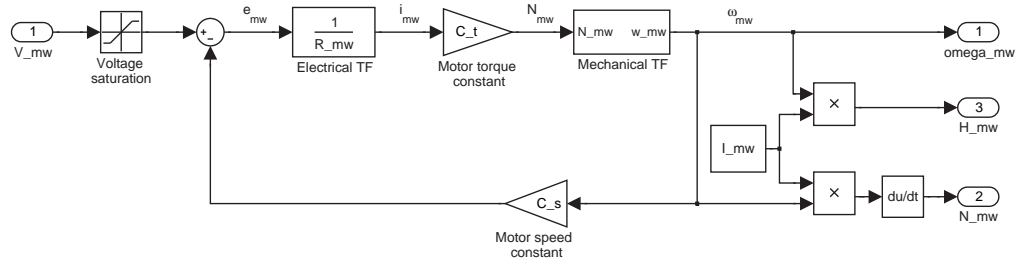


Figure L.7: The implementation of a momentum wheel.

L.4 Basic Implementation Model

To facilitate an easy controller implementation on a standardised model, the notion of a basic implementation model is introduced. In this model the satellite behavior is implemented along with basic output viewing options like the satellite angular velocity and the satellite attitude. Furthermore, the developed actuator models are implemented and also the general control structure, with the option to define the controller design files in the

masks. The controller design files will have to define A,B,C,D matrices for a controller state space system. Thus if the controller is merely a gain matrix only the D-matrix has to contain the controller, and the remaining be zero-matrices. The controller design files are kept in the `design` directory, and the definition of the controller system matrices is the final task in each controller design file. A depiction of the basic implementation model can be seen in Figure L.8.

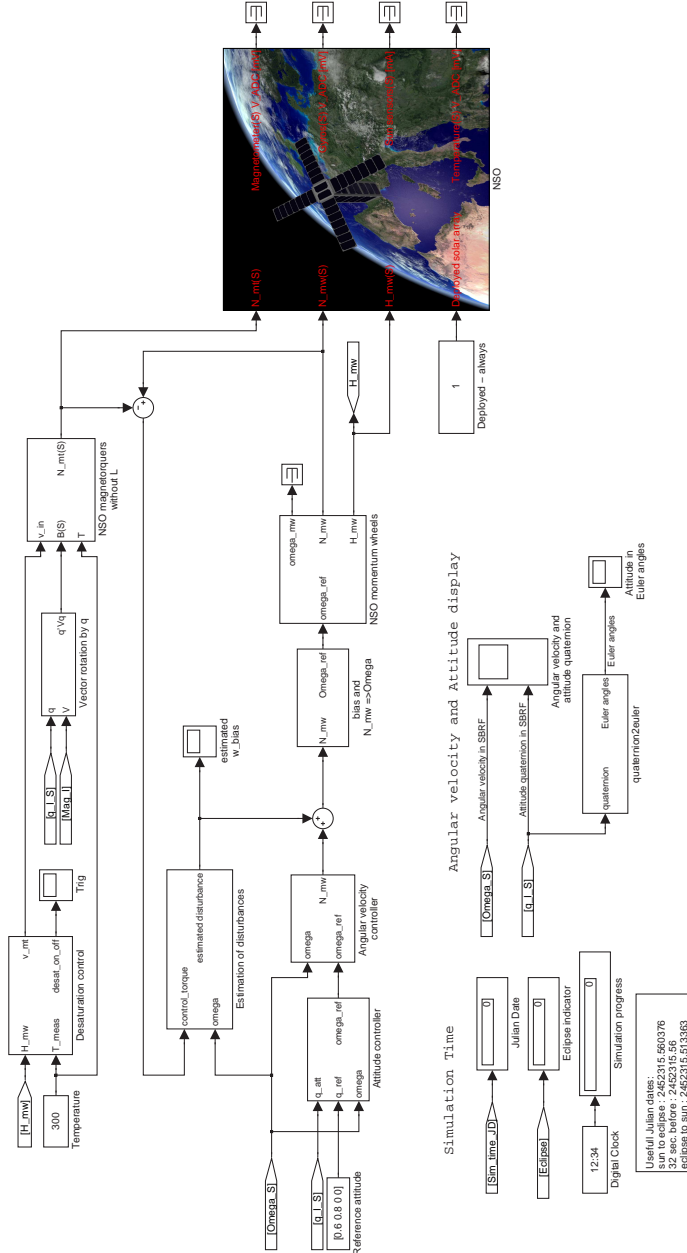


Figure L.8: The basic implementation model.

APPENDIX M

Content of Enclosed CD-ROM

The following entries can be found on the enclosed CD-ROM:

Simulator The simulator developed for this project implemented in SIMULINK. The different files and libraries used in the simulator are described in the `readMe.txt`-file in the simulator library root.

Calculations Contains files used to calculate parameters and dimensions in the modeling.

Movie Is a simulation movie of the NSO tracking Aalborg.

Literature References and documents, used during the project period to develop models and verify theories.

Report A copy of this report in digital form to enable easier copying.

Programs A PDF reader (Adobe Reader).

Email from Neil Melville

Subject: Tumbling rate
From: Neil.Melville@esa.int
Date: Wed, 26 Apr 2006 10:37:57 +0200
To: 06gr1032@control.aau.dk

Good morning,
Regarding the issue you raised in our recent telephone conversation on P-Pod deployment, I would recommend using an initial maximum angular velocity of 0.1 rad/s as the worst case single axis rate for your triple cubesat.

This is due to the fact that the satellite will be deployed from a P-POD, the internal guide-rails of which ensure a relatively low tumble rate, especially for a triple cubesat. The figure is, however, only an estimate based on my experience with similar systems, as I do not have access to actual measurements or simulations on this specific matter.

Feel free to ask me if I can be of further assistance.

Best regards,
Neil

Neil Melville
ESTEC - European Space Agency
Education Department EXR-E
Keplerlaan 1
2201 AZ Noordwijk ZH
The Netherlands
Tel: +31 (0)71 565 6367
Fax: +31 (0)71 565 5590
neil.melville@esa.int

Nomenclature

Generally all symbols are presented with an alphabetical letter describing its physical nature, and if the specified symbol is related to an object or a place of reference, this is indicated in the subscript of the symbol.

Acronyms

<i>ACS</i>	Attitude Control System
<i>ADCS</i>	Attitude Determination and Control System
<i>ADS</i>	Attitude Determination System
<i>ARE</i>	Algebraic Riccati Equation
<i>AS</i>	Asymptotically Stable
<i>CCPL</i>	Common Cross Product Law
<i>CoM</i>	Center of Mass
<i>CoP</i>	Center of Pressure
<i>DRE</i>	Differential Riccati Equation
<i>GAS</i>	Globally Asymptotically Stable
<i>ILQR</i>	Infinite time Linear Quadratic Regulator
<i>LEO</i>	Low Earth Orbit
<i>LMI</i>	Linear Matrix Inequality
<i>LQR</i>	Linear Quadratic Regulator
<i>MPC</i>	Model Predictive Control
<i>NSO</i>	North Sea Observer
<i>OBC</i>	On Board Computer
<i>PCB</i>	Printed Circuit Board
s.t.	such that
w.r.t.	with respect to

List Of Symbols

<i>A</i>	Area
<i>B</i>	Magnetic field
<i>C</i>	Circumference or Constant
<i>e</i>	Electromotive force

F	Force
f	Frequency
G	Gravitational constant
g	Gain
h	Angular momentum
I	Inertia
i	Current
L	Inductance
l or S	Distance
M	Magnetic moment
m	Mass
N	Torque
n	Winding number
P	Momentum flux or Power
R	Resistance or Position Vector
T	Temperature
t	Time
V	Volume or Translational velocity
v	Voltage
α	Resistivity temperature coefficient
ϑ	Angular error of attitude on z-axis
κ	Interval on y-axis
σ	Resistivity
ω	Angular velocity
Φ	Magnetic flux
μ	Friction or Permeability
ρ	Density
τ	Control horizon
\mathcal{V}	Lyapunov candidate function

Reference Frames

ECI Earth Centered Inertial reference frame. Abbreviated I in equations.

ECEF Earth Centered Earth Fixed reference frame. Abbreviated E in equations.

SBRF Satellite Body Reference Frame. Abbreviated S in equations.

CRF Controller Reference Frame. Abbreviated C in equations.

Symbols specified in a specific reference frame is indicated by a preceding superscript.

Notation

Domains

- Time domain signals are indicated by a (t) , or when nothing is specified.
- Frequency domain signals are indicated as a function of the Laplace operator (s) .

Vectors, Matrices and Rotations

- Vectors are typed as \mathbf{v} .
- Unit vectors are typed as $\hat{\mathbf{u}}$.
- Matrices are typed as $\underline{\mathbf{M}}$,

e.g., a 3×3 identity matrix is written as

$$\underline{\mathbf{1}}_{3 \times 3} = \begin{bmatrix} 1 & 0 & 0 \\ 0 & 1 & 0 \\ 0 & 0 & 1 \end{bmatrix}$$

- Rotations (quaternions and matrices) are typed with source frame designation (preceding subscript) and destination frame designation (preceding superscript), e.g.,

$${}^I_S \mathbf{q}, {}^I_C \underline{\mathbf{C}},$$

where ${}^I_S \mathbf{q}$ is a quaternion describing a rotation from SBRF to ECI and ${}^I_C \underline{\mathbf{C}}$ is an attitude matrix describing a rotation from ECI to CRF.

- Vector and quaternion components are typed as

$${}^E \mathbf{v}_x, {}^I \mathbf{q}_{1:3},$$

which denotes the component x of the vector \mathbf{v} in the ECEF, and the components 1 through 3 of the quaternion \mathbf{q} in the ECI.

Signals

- Small signals are typed as $\tilde{\mathbf{q}}$, which denotes the small signal quaternion.
- Working points are typed as $\bar{\mathbf{q}}$, which denotes the quaternion in the working point.

Operators

- In matrix inequalities, rounded inequality signs are used to describe the definiteness, e.g.,

$$\underline{\mathbf{V}} \succ 0,$$

means that the $\underline{\mathbf{V}} \in \mathbb{R}^{n \times n}$ is positive definite, i.e., $\mathbf{u}^T \underline{\mathbf{V}} \mathbf{u} > 0$ for all nonzero $\mathbf{u} \in \mathbb{R}^n$.

List of Tables

3.1	Description of the transitions depicted in Figure 3.1.	28
D.1	Worst case disturbance torques due to aerodynamic torque, radiation torque and gravity gradient torque.	101
E.1	Parameters used in the magnetorquer modeling.	106
F.1	Magnetorquer parameters.	109
G.1	Parameters used in the momentum wheel modeling.	114
K.1	Resulting mean and standard deviations, along with maximum and minimum values, for the results obtained in the Monte Carlo simulation of the two controller configurations.	152
L.1	Description of directories in the simulator.	157

List of Figures

1.1	The North Sea Observer in orbit with the solar arrays deployed. Removing the solar arrays from the figure, illustrates the situation where the solar arrays are collapsed. ©Morten Bisgaard.	2
1.2	Overall system configuration for the NSO Attitude Determination and Control System.	5
2.1	Illustration of orbit parameters for a satellite.	8
2.2	Orthogonal view of a satellite orbit.	8
2.3	The Earth Centered Inertial reference frame.	10
2.4	The Earth Centered Earth Fixed reference frame.	10
2.5	The NSO Satellite Body Reference Frame.	11
2.6	The NSO Controller Reference Frame w.r.t. the principal axes, with the origo placed in the CoM.	12
2.7	Aerodynamic drag force on an infinitesimal surface element of the NSO.	13
2.8	The expected $F10.7$ value during the next solar cycle (cycle 24).	14
2.9	The air density in an orbit height of 500 [km]. This plot is generated by SPENVIS.	14
2.10	Illustration of the satellite body and solar arrays projected onto a plane perpendicular to the velocity vector of the satellite.	16
2.11	The norm of the aerodynamic torque on the NSO with deployed solar arrays as a function of the attitude.	17
2.12	Illustration of the gravity gradient torque.	18
3.1	Operational modes of the ACS.	27
3.2	Control structure for the pointing mode. The attitude controller generates the angular velocity reference for a robust controller, which generates the control signal for the momentum wheels.	30

4.1	Model errors. The topmost plot describes the evolution of the error quaternion, the middle plot the error in the angular velocities and the bottom one the rotation error angle.	32
4.2	The rotation error angle between the two attitudes, from the linear and non-linear model respectively.	32
4.3	Illustration of model deviations with time, and the effect of sampling rate variations. If a higher sampling rate is applied better precision is achieved, but elevation of the processing load is inevitable.	33
4.4	Input-output mapping of a 2×2 system.	35
4.5	Singular values of the angular velocity system as a function of frequency. The spike, at approximately 0.1 [rad/s], is caused by two imaginary system poles.	36
4.6	The angular momentum of the satellite is constant in an inertial coordinate system and the angular momentum of the momentum wheels must reside in the 1 st octant of the SBRF.	37
4.7	The control torques produced by the magnetorquers are always perpendicular to the magnetic field vector (indicated by the circle). Thus, it is not possible to perform three axis control at all times. Note that the magnetic vector field is illustrative and not necessarily correct.	38
4.8	The angular velocity system controlled by a simple untuned state feedback positive definite controller gain matrix. Notice the spiraling tendency, where the trajectory converges towards the equilibrium.	41
5.1	Block diagram of the angular velocity controller with estimation and feed-forward of the external disturbance torques.	44
5.2	Block diagram of a Kalman filter.	44
5.3	The estimation error between the modeled disturbance torque and the estimated torque, during one of the simulations. The small oscillations are assumed to be caused by the momentum wheel bias.	45
5.4	General control structure for cases with model uncertainties.	46
5.5	Illustration of the desired pole placement boundary for the closed loop system, which is used in the LMI design. The hatched area describes the area in which no poles must be placed.	50
5.6	Uncertainty region when three parameters are considered.	51
5.7	Pole locations of the closed loop system with the robust state feedback controller.	52

5.8	Angular velocity from a simulation of a complete orbit using the disturbance estimation and feedforward. After initial settling, the angular velocity is within $\pm 0.25 \cdot 10^{-6}$ [rad/s]. The settling of the angular velocity is dependent on the estimation and feedforward and is approximately 60 seconds. The spikes in the angular velocity is assumed to be caused by the estimator settling and feedforward, as the satellite exits eclipse at approximately $t = 2000$ [s] and enters eclipse in the end of the simulation.	53
6.1	Control structure for the desaturation controller including the angular velocity controller.	55
6.2	Illustration of the Common Cross Product Law, where \mathbf{N}_{mt} is given as the cross product between \mathbf{M}_{mt} and \mathbf{B}	57
6.3	Illustration of the trigger method. When $d_{T_{\text{on}}}$ is reached, the desaturation controller is switched on. Once T_{desat} becomes lower than $d_{T_{\text{off}}}$ the desaturation controller switches off.	58
6.4	The top plot shows the activations and deactivations of the desaturation controller. Middle plot depicts upper and lower limits for desaturation and T_{desat} . Bottom plot shows the error in the angular momentum.	60
7.1	Control structure for the attitude controller.	62
7.2	Six randomly generated attitude manoeuvres, which show that reference attitudes are obtained by the satellite.	65
8.1	Control structure including the reference generator for the NSO satellite. . .	67
8.2	Position of the satellite in orbit and the target area on the Earth.	68
8.3	Euler eigenaxis and angle for rotating the z-axis of the NSO to point towards the target location.	69
9.1	Plots of the angular errors in attitude on the z-axis for both controller configurations with a nominal (topmost) and a perturbed (bottom) inertia matrix. Notice that the rise- and settle-time for the simply controlled system is significantly longer than for the robustly controlled system. No significant change in performance can be seen from the nominal and perturbed scenario.	72
9.2	Plots of the resulting changes in angular velocity arising from attitude manoeuvres with a perturbed inertia matrix. The topmost plot shows the angular velocity on the robustly controlled system, whereas the bottom plot show the simply controlled system. The robustly controlled system performs better, but has a slight overshoot.	73
9.3	Distribution of samples of the angular error on the z-axis for the robustly controlled system. The number of samples is 1649060.	74

9.4	The error angle during a simulation with the pointing controller. At $t = 2000$ [s] the NSO is directly above its target, which is Aalborg, Denmark.	76
A.1	Location of the CoM for both the satellite and the deployed solar arrays.	88
A.2	Location of the CoM of the satellite, without deployment of the solar arrays.	90
B.1	Rotation of a satellite, in a circular orbit, stabilised by a magnetic dipole.	92
B.2	Satellite during pass of a ground station.	93
C.1	Components of the quaternion depicted in a coordinate system.	96
E.1	Representational diagram of a magnetorquer showing the resulting forces created by applying a current to the coil in a magnetic field, represented by the vector \mathbf{B}	103
E.2	Magnetorquer modeling errors. The inductance is found negligible.	106
G.1	Electrical equivalent diagram of a DC-motor.	112
G.2	Free body diagram of the motor and load. N_m is the torque generated by the motor and N_f is the torque generated on account of friction.	112
G.3	Plot of momentum wheel step responses with and without motor coil influence. Bottom plot visualises the difference between the two models.	114
G.4	Frequency response of the momentum wheel with a hardware PI-controller ensuring closed loop unit gain.	115
G.5	Frequency response of the momentum wheel with a hardware PI-controller ensuring maximum closed loop gain.	116
H.1	Example of Euler rotation around the z-axis.	118
I.1	Block diagram illustrating the extension of the transfer function for a momentum wheel.	127
J.1	Block diagram of a Kalman filter.	131
K.1	The estimation error between the modeled disturbance torque and the estimated torque, during one of the simulations. The small oscillations are assumed to be caused by the momentum wheel bias.	137
K.2	Simulation results using the angular velocity controller without estimation, feedforward and actuator dynamics. Observe that the angular velocity has settled at zero within approximately 6 [s].	138

K.3 Plot of the angular velocity settling at zero from an initial angular velocity, when including the actuator dynamics. The settling time is approximately 14 [s].	138
K.4 Simulation result from a complete orbit using the angular velocity controller without estimation and feedforward of the disturbance torques. The angular velocity is after settling within $\pm 1.5 \cdot 10^{-6}$ [rad/s], during the entire orbit.	139
K.5 Angular velocity from a simulation of an entire orbit using the disturbance estimation and feedforward. The angular velocity is, after settling, within $\pm 0.25 \cdot 10^{-6}$ [rad/s]. The settling of the angular velocity is dependent on the estimation and feedforward, and is approximately 60 [s]. The spikes in the angular velocity is assumed to be caused by the estimator settling and feedforward, as the satellite exits eclipse at approximately $t = 2000$ [s] and enters eclipse again in the end of the simulation.	139
K.6 Simulation results from an orbit with step on the reference input. The top plot depicts the angular velocity during the entire orbit. In the bottom left plot, the step up is shown. The step down is depicted in the bottom right plot.	140
K.7 Simulation results for the desaturation controller. The top plot depicts the trigger output and the middle plot depicts the trigger level and T_{desat} . The bottom plot depicts the angular momentum of each of the momentum wheels.	142
K.8 Simulation results from a simulation using the modeled disturbance torques. Notice that the desaturation controller is never activated.	143
K.9 Energy consumption of the magnetorquers during a simulation of two orbits. The desaturation controller is constantly activated.	144
K.10 Six randomly generated attitude manoeuvres, which show that reference attitudes are obtained by the satellite.	145
K.11 Unstable attitude manoeuvre. It is not possible to obtain the desired attitude, due to the fact that one or more momentum wheels reach their saturation limit.	146
K.12 Plots of the resulting changes in attitude with a nominal inertia matrix. The two topmost plots show the attitude for both the robustly controlled and the simply controlled system. The bottom plot shows the angular errors in attitude on the z-axis for both controller configurations. Notice that the rise- and settle-time for the simply controlled system is significantly longer than for the robustly controlled system.	148
K.13 Plots of the resulting changes in angular velocity arising from attitude manoeuvres with a nominal inertia matrix. The topmost plot shows the angular velocity on the robustly controlled system, whereas the bottom plot show the simply controlled system. Notice the better performance and slight overshoot in the robust control configuration.	149

K.14 Plots of the resulting changes in attitude with a perturbed inertia matrix. The two topmost plots show the attitude for both the robustly controlled and the simply controlled system. The bottom plot shows the angular errors in attitude on the z-axis for both controller configurations. The rise- and settle-time for the simply controlled system is significantly longer than for the robustly controlled system.	150
K.15 Plots of the resulting changes in angular velocity arising from attitude ma- noeuvres with a perturbed inertia matrix. The topmost plot shows the angular velocity on the robustly controlled system, whereas the bottom plot show the simply controlled system. The robust control configuration per- forms better and has a slight overshoot.	151
K.16 Distribution of angular error samples on the z-axis for both the robustly con- trolled system and the system controlled by simple controllers. The number of samples is 1649060. Note that the scale is different in the two histograms.	152
K.17 The error angle during a simulation with the pointing controller. At $t =$ 2000 [s] the NSO is directly above its target, which is Aalborg, Denmark. . .	153
K.18 The attitude changes constantly during the simulation of the pointing con- troller and the angular velocity is largest when the NSO is above the target location at $t = 2000$ [s].	153
K.19 The position and attitude of the NSO during a pass of Denmark.	154
L.1 The satellite behavior implementation.	158
L.2 The solar radiation disturbance implementation.	159
L.3 The gravity gradient disturbance implementation.	159
L.4 The atmospheric drag disturbance implementation.	159
L.5 The implemented environmental disturbances joined to a single disturbance torque.	160
L.6 The implementation of a magnetorquer.	161
L.7 The implementation of a momentum wheel.	161
L.8 The basic implementation model.	162

Index

- AAUSAT-II, 1
- ACS, *see* Attitude Control System
- Actuators, *see* Magnetorquers or Momentum wheels
- ADCS, *see* Attitude Determination and Control System
- ADS, *see* Attitude Determination System
- Angular controller design, 50
- Angular velocity system, 34
- Armature voltage, 111
- Attitude
 - Error, 96
 - Matrix, *see* Direction Cosine Matrix
- Attitude Control System, 5
 - Requirements, 6, 94
- Attitude Determination and Control System, 2
 - Modes, 3
 - Requirements, 94
 - Tasks, 91
- Attitude Determination System, 94
- Automatic Identification System, 1
- Calculation of area
 - Satellite body, 15
 - Shadow, 15
 - Solar arrays, 15
- Controllability, 33
 - Attitude controllability, 36
 - Condition number, 35
 - Directional gains, 34
 - Magnetorquers, 37
 - Matrix, 34
 - Momentum wheels, 36
 - Singular value decomposition, 35
- CRF, *see* Reference frames
- CubeSat concept, 1
- Cumulative probability, 75
- Danish National Space Center, 1
- Desaturation, 3, 55
 - Desaturation control, 55
- Common cross product law, 56
- ILQR, 56
- LQR, 56
- Detumbling, 3, 91
- Direction cosine matrix, 117, 120
- Disturbance, 12
 - Aerodynamic, 13
 - Gravity gradient, 17
 - Radiation, 18
 - Worst case torques, 99
- Disturbance estimation, 44, 45
 - Kalman, *see* Kalman filter
- Dynamic differential equations, 22
- ECEF, *see* Reference frames
- ECI, *see* Reference frames
- Electromotive force, 111
- Ephemeris, 7
- Euler angles, 118
 - Elementary rotations, 118
- Euler's eigenaxis rotation theorem, 119
- European Space Agency, 2
- Evaluation, 135
 - Attitude controller, 144
 - Desaturation controller, 141
 - Disturbance estimator, 136
 - Robust angular velocity controller, 136
 - Standard configuration, 135
- Exponential distribution, 75
- Flywheel, 21, 111, 112
 - Inertia, 113
- Gravitational constant, 17
- Gyro, 4
- Inertia matrix, 3, 87
 - Collapsed, 90
 - Deployed, 88
 - Moments of inertia, 87
 - Products of inertia, 87
- Kalman filter, 44, 45, 131, 133

- A posteriori estimation error, 132
A posteriori estimation error covariance, 133
A priori estimation error, 132
A priori prediction error covariance, 133
Gaussian noise, 131
Kalman gain, 132
Kinematic differential equation, 24, 120, 121
Linear matrix inequality, 47–49
 Bounded bandwidth, 50
 Convex optimisation problems, 47
 Lyapunov inequality, 47
 Lyapunov theory, 47
 Strongly robust \mathcal{H}_∞ performance criterion, 48
 Uncertainty region, 48, 51
 Uncertainty system, 51
 Vertex set, 48
Linear model accuracy, 31
Linearisation, 123
 Dynamic equation, 125
 Kinematic equation, 123
 Magnetorquers, 128
 Momentum wheels, 127
 Satellite attitude, 126
 System equations, 26
LMI, *see* Linear matrix inequality
Low Earth Orbit, 2
Lyapunov stability, 38
 Angular velocity system stability, 39
 Asymptotically stable, 39
 Attitude system stability, 41
 Energy function, 39
 Globally asymptotically stable, 39
Magnetic dipole moment, 21, 104, 107
Magnetic field, 103
Magnetic vacuum permeability, 107
Magnetometer, 4
Magnetorquer, 4, 20, 103
 Dimensioning, 105, 108
 Dimensions, 20, 105
 Electro mechanics, 104
 Torque, 104
Momentum wheel, 4, 21, 111
 Dimensioning, 113
 Electrical model, 111
Hardware controller, 113
Mechanical model, 112
Monte Carlo, 52, 74, 79, 137, 147, 155
North Sea Observer, 1
 Actuators, 4
 Sensors, 4
NSO, *see* North Sea Observer
Operational modes, 27
 Detumbling, 28
 Idle momentum wheels on/off, 29
 Point with magnetorquers, 29
 Pointing, 3, 29
 Sun pointing, 4, 29
Optimal control, 61
 Algebraic riccati equation, 62
 Design, 62
 Performance index, 61
 Weight matrices, 61, 63
P-POD, 91
Principal axes, 11
Quaternion, 95
 Addition, 96
 Inverse, 96
 Multiplication, 97
 Norm, 96
 Rotation, 97
 Subtraction, 96
Reference frames, 9
 Controller, 11
 Earth Centered Earth Fixed, 9
 Earth Centered Inertial, 9
 Satellite Body, 10
Reflection
 Absorption, 18
 Diffuse, 18
 Specular, 18
Residual magnetic dipole, 19
Robust control, 45
 General control structure, 45
 Generalised plant, 45
 Linear fractional transformation, 46
 Nominal system, 45
 Uncertainty system, 45
Sampling multiple, 115
Sampling theorem, 115

SBRF, *see* Reference frames
SeDuMi, 51
Simulator, 157
System evaluation, 71, 146
 Attitude manoeuvres, 71
 Reliability, 74
 Target acquisition, 75

Taylor expansion, 126
Two line elements, 93, 135

Validity interval, 31
VEGA, 2
Viscous friction coefficient, 113

YALMIP, 51